PLASMONIC ORGANIC ELECTRONIC DEVICES

by

FENG LIU

A thesis submitted to the Department of Chemistry

In conformity with the requirements for

the degree of Doctor of Philosophy

Queen's University

Kingston, Ontario, Canada

(January, 2012)

Abstract

Surface plasmon is a collective oscillation behavior of electrons in metal nanoparticle induced by the excitation of incident light, which can create an enhanced localized electric field near the surface of metal nanoparticle. To date, metal nanoparticle surface plasmon resonances have been extensively studied in the photoluminescence domain; little work however was devoted to electroluminescent and photovoltaic research.

In this thesis, as a fundamental study we firstly investigated surface plasmon enhanced europium complex luminescence and obtained an increased understanding of the importance of optical spacer in metal enhanced fluorescence phenomenon. Under this guideline, we incorporated metal NPs into organic light emitting diodes (OLED) and organic solar cells, by means of thermal evaporation and wet chemistry. Metal nanoparticles are demonstrated to enhance the efficiency of both OLEDs and solar cells only under tailored device architecture. The surface plasmon enhanced local electric field plays an important and comprehensive role in enhancing device performance. In Alq_3 based OLED we observed increased charge carrier injection by depositing Ag nanoparticles underneath the Al cathode; in $Ir(ppy)_3$ based OLED we gained enhanced luminous efficiency via doping silica functionalized Ag nanoparticles into emitting layer; in P3HT based organic polymer solar cell we noticed an increased polymer absorption by incorporating Ag nanoparticles over the active layer. On the other hand, adverse effects such as metal nanoparticle induced charge carrier recombination and light extinction are also observed. The study of surface plasmon effects in organic optoelectronic devices reveals interesting surface plasmon features and permits to optimize optoelectronic devices from a novel point of view.

Acknowledgements

Firstly I would like to deliver my sincerely appreciation to my supervisor Prof. Jean-Michel Nunzi, who gave me invaluable advice and suggestions in my research projects, guided and encouraged me to access different research areas. It would be impossible for me to accomplish the work covered in this thesis without the help of Prof. Nunzi. His wisdom, kindness, friendliness as well as patience make him such a great master, I am so proud to have been his student in the past four years. Moreover, I would like to offer my special thankfulness to Prof. Nunzi for standing behind my comprehensive exam, it would be also impossible for me to write this PhD thesis without his generous help.

Besides I would like to thank Prof. Buncel for his guidance in chemistry synthesis work and his patience in reading and editing my manuscripts. I am truly grateful to Prof. Dust, Prof. Um, Prof. Buncel and Prof. Nunzi for their unselfish help and harsh training during my comprehensive exam period, it is your help that made me strong and confident. I also appreciate my supervisor committee members Prof. Guojun Liu and Prof. Peter Loock for their precious advice and critiques through my PhD studies.

I am grateful to my colleague Dr. Gabriela Nunzi for her patient guidance in organic synthesis as well as suggestive discussions on my research projects. Bobbara Sanyasi Rao is greatly appreciated for his assistance in time resolved luminescence experiments and valuable discussions in mechanism interpretations. I am also thankful for all the group members Thomas Kraft, Nicole Day, Matthew Schuster, and Konrad Piskorz for your help. I would like to extend my appreciation to all who assisted me with instrumentational help including Prof. Guojun Liu for AFM, Xiaoyu Li for TEM, Prof. Gregory Jerkiewicz for profilemeter, Prof. Jun Gao for AFM and solar simulator, Dr. Francoise Sauriol for NMR, Jessie Sui and Dr. Jiaxi Wang for mass spectroscopy.

I have received unconditional support and endless love from my wife Yu Xiao throughout my PhD studies, you were always being there to accompany and encourage me to stand up from frustration and share the happiness with me, I would specially like to send my sincerely appreciation to you my beloved. The support from my family is always inestimable, I thank my father Mingxin Liu, mother Shizhi Qiu, and elder brother Wei Liu for your constant support, love and encouragement. I would also like to dedicate this thesis to the new family member Alexander T. Liu, welcome to this amazing world!

Last but not least, Annette Keyes and Robert Dumont are appreciated for their assistance in my PhD studies; Queen's University, Chemistry department and NSERC are greatly appreciated for funding the research described in this thesis.

Statement of Originality

I hereby certify that all of the work described within this thesis is the original work of the author under the supervision of Prof. Jean-Michel Nunzi, except for the fluorescence lifetime measurements in **Figure 2.11** and **Figure 3.36** which were done by Bobbara Sanyasi Rao (PhD candidate in Nunzi's group in department of physics); and the time resolved electroluminescence measurement in **Figure 3.43** which was finished by both the author and Bobbara Sanyasi Rao. Any published (or unpublished) ideas and/or techniques from the work of others are fully acknowledged in accordance with the standard referencing practices.

(FENG LIU)

(January, 2012)

Table of Contents

List of Tables

List of Figures

List of Abbreviations

AFM	Atomic Force Microscopy
Alq_3	8-Hydroxyquinoline Aluminum
AM	Air Mass
BCP	Bathocuproine
BHJ	Bulk Heterojunction
BSA	Bovine Serum Albumin
$btp_2Ir(acac)$	Bis(2-(2'-benzothienyl)-pyridinato-N, $C^{3'}$) iridium (acetylacetonate)
CBP	4,4'-N, N'-dicarbazol-biphenyl
CRZ	Charge Recombination Zone
CTAB	Cetyl trimethylammonium Bromide
CuPc	Copper Phthalocyanine
DA	Donor-Acceptor
DPAVBi	4,4'-bis[4-(di-p-tolyamino)styryl]biphenyl
EL	Electroluminescence
E-field	Electric field
E_g	Energy Gap
EQE	External Quantum Efficiency
ETL	Electron Transport Layer
$Eu(fod)_3$	Tris (6,6,7,7, 8, 8, 8-heptafluoro-2, 2-dimethyl-3, 5-octanedionato) europium
FIrpic	Bis(2-(4,6-difluorophenyl)pyridyl-N, $C^{2'}$)iridiumpicolinate
FTIR	Fourier Transform Infrared Spectroscopy
HSA	Human Serum Albumin

HOMO	Highest Occupied Molecular Orbital
HTL	Hole Transport Layer
ICG	Indocyanine Green
$Ir(DPF)_3$	Tris[9,9-dihexyl-2-(pyridinyl-2')fluorene]iridium
$Ir(ppy)_3$	Tris(2-phenylpyridine)iridium (III)
ISC	Intersystem Crossing
I_{SC}	Short Circuit Current
ITO	Indium Tin Oxide
J_{SC}	Short Circuit Current Density
LCD	Liquid Crystal Display
LUMO	Lowest Unoccupied Molecular Orbital
MEF	Metal Enhanced Fluorescence
MEH-PPV	Poly[2-methoxy-5-(2'-ethylhexoxy)-1,4-phenylenevinylene]
MIM	Metal-Insulator-Metal
MPP	Maximum Power Point
Nd-YAG	Neodymium-doped Yttrium Aluminium Garnet
NPs	Nanoparticles
NPB(NPD)	N,N'-di(1-naphthyl)-N,N'-diphenyl-[1,1'-biphenyl]-4,4'-diamine
OC1C10-PPV	Poly[2-methoxy-5-(3',7'-dimethyloctyloxy)-p-phenylenevinylene]
OLED	Organic Light Emitting Diode
OSC	Organic Solar Cell
OXD-7	1,3-bis[5-(p-tert-butylphenyl)-1,3,4-oxadiazol-2-yl]benzene
P3HT	Poly(3-hexyl-thiophene)
PBD	2-(4-Biphenylyl)-5-phenyl-1,3,4-oxadiazole

PCBM	[6,6]-phenyl C_{61} butyric acid methyl ester
PCE	Power Conversion Efficiency
PCPDTBT	Poly[2,1,3-benzothiadiazole-4,7,-diyl[4,4-bis(2-ethylhexyl)-4H-cyclopenta[2,1-b:3, 4-b']dithiophene-2,6-diyl]:
PDOFT	Poly (9,9-dioctylfluorene-alt-thiophene)
PEDOT:PDD	Poly(3,4-ethylenedioxythiophene): Poly (styrenesulfonate)
PHOLED	Phosphorescent Organic Light Emitting Diode
PL	Photoluminescence
PMMA	Polymethyl Methacrylate
$Pt(thpy)_2$	Cis-bis[2-(2-thienyl)pyridine-N, C^3]platinum
Pt(TPBP)	5,10, 15, 20-tetraphenyltetrabenzoporphyrin platinum complex
PTCBI	Perylenetetracarboxylic Bisbenzimidazole
PVA	Polyvinyl Alcohol
PVK	Poly(9-vinylcarbazole)
QE	Quantum Efficiency
RB	Rhodamine B
RE	Rare-Earth
Ref.	Reference
RP	Radiating Plasmons
SERS	Surface Enhanced Raman Scattering
SIF	Silver Island Film
SM-OLED	Small Molecule Organic Light Emitting Diode
SP	Surface Plasmon
SPAD	Single Photon Avalanche Detector
SPR	Surface Plasmon Resoannce

SPRS	Surface Plasmon Resonance Spectroscopy
TCSPC	Time Correlated Single Photon Counting
TEM	Transmission Electron Microscopy
TEOS	Tetraethoxysilane
TPBI	2,2’,2”-(1,3,5-benzenetriyl)tris-[1-phenyl-1H-benzimidazole]
TPD	N,N’-Bis(3-methyl-phenyl)-N,N’-diphenyl-[1,1’-biphenyl]-4,4’-diamine
V_{FB}	Flat Band Voltage
V_{OC}	Open Circuit Voltage

Chapter 1
Introduction and Literature Review

The theme of this thesis is the surface plasmon of noble metal nanoparticles and its applications in photoluminescence, electroluminescence as well as photovoltaics. This chapter mainly covers the introduction to a few important concepts such as surface plasmon theory and surface plasmon enhanced luminescence, which build up the foundation of this thesis. With regard to the practical applications of surface plasmon, more introductions together with literature review have been given to organic optoelectronic devices such as organic light emitting diode and organic solar cell, which are the core of this thesis.

1.1 Surface Plasmon

Surface Plasmon is a collective oscillation behavior of electrons on a metal surface, which can be excited by incident photons. In 1957, R.H. Ritchie first predicted the existence of surface plasmons.[1] Later on, surface plasmon has been extensively studied in the following two decades. So far, the surface plasmon phenomenon has found a rich variety of applications such as Surface Enhanced Raman Scattering (SERS), and Surface Plasmon Resonance Spectroscopy (SPRS).[2]

1.1.1 Surface Plasmon Resonance of Metal Nanoparticles

Figure 1.1 shows the origin of surface plasmon. Free electrons in a metal can travel freely through the material. When the metal nanoparticle (NP) is irradiated under an incident light with wavelength much larger than the particle size, the electrons can oscillate with light in a standing wave resonance condition. [3]

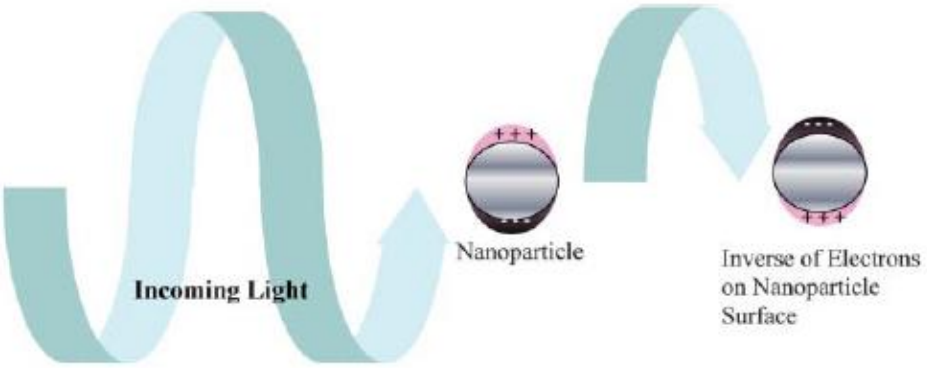

Figure 1.1 The origin of surface plasmon resonance due to coherent interaction of electrons with light. (Adapted from Ref.3)

Generally the relative permittivity of a material is a complex number with an imaginary component, which represents the dissipative processes the charge carriers suffer during their motion within the materials. When a metal NP's size is smaller than electron mean free path (~50 nm for gold and silver), we can ignore the dissipative effect and the electron scattering effect from the bulk. In this case, the frequency dependent relative permittivity of the metal can be expressed with the Drude model: [4]

$$\varepsilon_m(\omega) = 1 - \frac{\omega_p^2}{\omega^2} \tag{1.1}$$

$$\omega_p^2 = \frac{ne^2}{\varepsilon_0 m} \tag{1.2}$$

Where n is the number density of electrons, e the electron charge, m electron mass and ε_0 the relative permittivity of free space, ω_p is the plasmon frequency of the metal.

The displacement of the electron cloud from the nuclei gives rise to a dipole moment in the particle, and the Coulomb attraction between positive and negative charges results in restoring

forces. One can use electrostatics to derive a simple formula for the polarizability of a spherical particle: [5]

$$\alpha = 4\pi r^3 \frac{\varepsilon_m(\omega) - \varepsilon_d}{\varepsilon_m(\omega) + 2\varepsilon_d} \tag{1.3}$$

Where α is the polarizability, r the radius of the spherical particle, ε_d the relative permittivity of the surrounding dielectric. Mathematically the polarizability tends to a maximum when the denominator of equation (1.3) is zero, which corresponds to the strongest optical response of the particle (i.e. the maximum light extinction effect). This indicates that the particle has different optical response to incident monochromatic light of different wavelength.

For a typical glass its refractive index n =1.5 and $\varepsilon_d = n^2$ =2.25, if gold nanoparticles are embedded in a glass substrate, the surface plasmon resonance occurs where $\varepsilon_m(\omega)$ = -4.5 corresponding to the green part of spectrum at ca. 520 nm. That is why gold colloids normally present a ruby red color since they absorb the green visible light. Michael Faraday was the first to observe this spectacular phenomenon.[6] He prepared the first stable gold colloids suspension in 1857 and some of his original samples are still preserved at the Faraday Museum in London.[7] Actually 2000 years ago, Romans have used metal nanoparticles to make colorful glasses although they had no idea about the mechanism of coloration. The Lycurgus cup is a good example, it reflects green light and transmits ruby red light, which originates from the unique scattering and absorption characteristic of gold nanoparticles.

The surface plasmon resonance spectrum of a metal nanoparticle can be theoretically calculated by solving Maxwell's equations. The German Scientist Gustav Mie first accomplished the SPR spectra calculation for spherical particles in 1908.[8] Later on, Richard Gans improved on Mie's theory and made the calculation for spheroids possible in 1912. [9] So far, one can use Mie's method to simulate the SPR spectra of a spherical particle of any size. In order to simulate other geometries except spherical, concentric spherical shell, spheroids and infinite cylinder, a discrete

dipole approximation (DDA) has been developed. In principle, this numerical approach can be applied to particles of any arbitrary geometry.[10]

Based on the surface plasmon resonance theory, we can readily tune the SPR wavelength of metal NPs by varying the refractive index of dielectric medium surrounding particles, geometry, size of particles and so on. In the followed subsections, we will mainly introduce how size and geometry factors dictate the SPR wavelength of metal NPs.

1.1.2 Size Controlled SPR

Figure 1.2 shows the extinction spectra of gold nanoparticles with different size 22, 48 and 99 nm,[11] which were prepared by reducing gold ions with sodium citrate.[12] The molar extinction coefficient of gold colloids is estimated to be of the order of 10^9 M^{-1} cm^{-1}, which is three to four orders of magnitude higher than those of very strong absorbing organic dyes. It is notable that the SPR peak red shifts with the increase of the NPs size; meanwhile the bandwidth increases with the particles size. The above phenomenon can be well explained by the Mie theory.

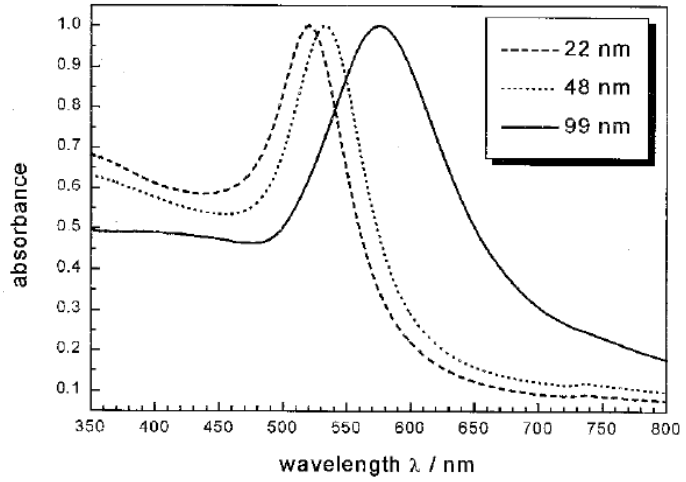

Figure 1.2 Optical absorption spectra of 22, 48 and 99 nm spherical gold nanoparticles. The broad absorption band corresponds to the SPR. (Adapted from Ref. 11)

When the NPs size is much smaller than the incident wavelength, only the dipole oscillation contributes to the extinction cross-section since the electrons vibrate coherently with light.[13] However, for larger nanoparticles the dipole approximation becomes invalid as the light cannot polarize the NPs homogeneously anymore. In this case, high-order modes such as quadrupole become responsible for the light extinction of the NPs. The larger the NPs, the more important are the high-order modes. Normally high-order modes have lower energies corresponding to plasmon resonance peak red shifts.[14]

With regard to plasmon bandwidth, this can be associated with dephasing of coherent electron oscillation.[15] Large bandwidth indicates a rapid loss of coherent electron motion. It is understandable that large NPs size will lead to inhomogeneous polarization, the electrons readily lose coherence. The dephasing time for 22, 44 and 99 nm gold nanoparticles is estimated to be 4.1, 3.9 and 2.6 fs by Link et al.[16] As a result, the plasmon bandwidth increases with the NPs size. However, for very small size NPs (< 20 nm) the size dependent absorption effect is more complicated; the boundary scattering induced electron coherence loss becomes prominent, and the plasmon bandwidth exhibits an inverse relation to the particle size.[17]

1.1.3 Shape Controlled SPR

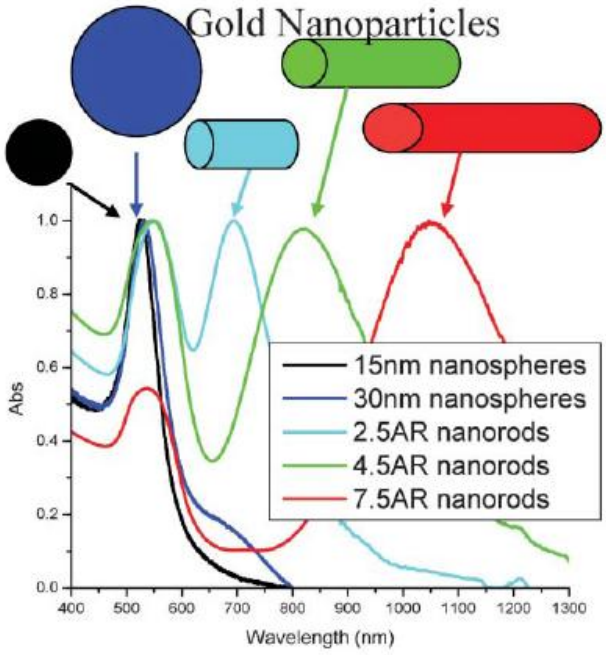

Figure 1.3 Absorption spectra of gold NPs of various sizes and shapes. (Adapted from Ref. 3)

Our discussion about surface plasmon resonance in section 1.1.2 is based on symmetrical spherical nanoparticles, which greatly simplifies SPR modes. Actually, the surface plasmon resonance sensitively depends on the shape of NPs. For instance, ellipsoids with three different axes have three different dipole modes. As the symmetry of a NP reduces, charge distribution on the surface can result in not only dipolar modes with different resonance frequencies but also higher order multilpolar modes. Figure 1.3 shows the absorption spectra of gold NPs with different shapes. When the spherical gold nanoparticles are enlarged, their surface plasmon resonance does not red shift significantly. However, when anisotropy such as a rod structure is applied to the NPs, their surface plasmon resonance peaks change dramatically. A new resonance peak appears in the gold nanorod SPR spectrum, which corresponds to high order resonance mode i.e. longitudinal plasmon resonance. It originates from oscillation of electrons along the

long axis. The intrinsic resonance peak around ca. 520 nm represents the transverse SPR, which corresponds to the electron oscillation perpendicular to the long axis. Normally, the transverse SPR mode is relatively insensitive to the length change of nanorod, and it coincides spectrally with the SPR of spherical nanoparticles. However, the longitudinal mode of gold nanorods red shifts significantly from red to infrared as the length increases. Thus the elongated gold NPs attract more interest for their fantastic optical properties.

Synthesis of metal nanorods could be accomplished in different manners. Electrochemical deposition of metals in a template with porous structure such as silicon or aluminum oxides has been reported.[18] Another method to prepare a nanorod structure is to reduce a metal salt in the presence of soft templates (micelles of surfactants).[19] The principle of soft templating includes diffusion-limited growth of NPs in nonspherical micelles as anisotropic nanoreactors. A more advanced soft-template method was developed by the Murphy group, which is the so-called seed-mediated growth method.[20] This approach allows to efficiently growing nanorod with well controlled geometric parameters. The underlying mechanism is as follows: as the seeding particles are added to solution, they are coved by surfactant molecules and then incorporate into micelles. The reduction of metal ions on the seed NPs results in the nanorod formation, the geometry of the nanorod is determined by the micelle anisotropy, which is associated with surfactant concentration and ionic strength.

1.1.4 The Application of Surface Plasmon Resonance

Surface Enhanced Raman Scattering

In 1974, for the first time the enhanced Raman signals of pyridine was observed on a rough silver electrode;[21] and in 1977, Van Duyne and Albrecht independently confirmed Fleischman's discovery and concluded that the enormously strong Raman signal indeed resulted from enhancement of the Raman scattering efficiency.[22-23] Interestingly, the enhanced surface enhanced Raman scattering (SERS) signal in an aqueous colloidal silver or gold solution can also

be observed. It indicates that enhanced SERS is not a surface effect but a nanostructure effect, which implies that plasmon resonance and electromagnetic field enhancement play an important role in SERS.[24] However, some other theories were also developed to explain the enhanced Raman signal. For instance, the so-called chemical effect emphasizes the importance of various potential electronic interactions between the molecule and the metal.[25]

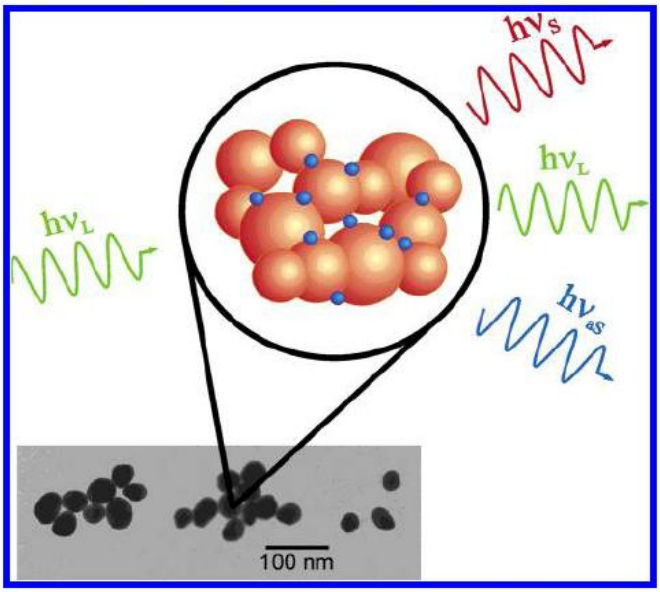

Figure 1.4 Surface-enhanced Raman Scattering. (Adapted from Ref. 26)

Figure 1.4 shows the schematic diagram of SERS, where blue dots represent the molecules and orange spheres are the metal NPs. The SERS Stokes signal P (ν_S) can be estimated as follows:[27]

$$P(\nu_S) = N\sigma \mid A(\nu_L) \mid^2 \mid A(\nu_S) \mid^2 I(\nu_L) \qquad (1.4)$$

where N is number of molecule involved in SERS process, σ is the Raman cross-section of the adsorbed molecules; $A(\nu_L)$ and $A(\nu_S)$ are the field enhancement factor of the laser and the Raman amplitudes, respectively.

This equation indicates the SERS enhances the signal by four orders of magnitude due to the field enhancement at the NPs surface. SERS enhancement factors were measured by

comparing the surface-enhanced Raman signal with the normal Raman scattering signal. Modest enhancement factors can reach 10^3-10^5 in initial experiments. Higher enhancement factor, 10^{10}-10^{11}, has also been observed for dye molecules.[28] So far SERS becomes a well-developed technology for Raman spectroscopic study.

Surface Plasmon Resonance Spectroscopy

In SPRS, plasmons are excited by light incident on a medium such as a glass prism under total internal reflection conditions, which penetrates into a metal film deposited on the surface of the medium. The evanescent electric field induces collective oscillation of electrons within the metal as we interpreted in subsection 1.1.1. At a particular angle, the incident light wavevector matches the plasmon wavevector fulfilling resonance conditions. In this case, energy is transferred from the photons to the plasmons, and a plasmon resonance can be observed as a sharp minimum of the reflectance plotted with the incident light angle, which is so-called SPR spectrum.

A typical SPRS apparatus is presented in Figure 1.5, and consists of four principal elements: 1) a p-polarized light source used to excite the plasmon; 2) a prism which couples light to the thin metal film; 3) a thin metallic film on the surface where plasmon can be excited; 4) a light detector. The configuration in Figure 1.5 is the so-called Kretschmann type SPRS, where the thin metal film is deposited directly on the coupling prism. In this SPRS geometry, the variation in the incident angle is accomplished by rotating the coupling prism.

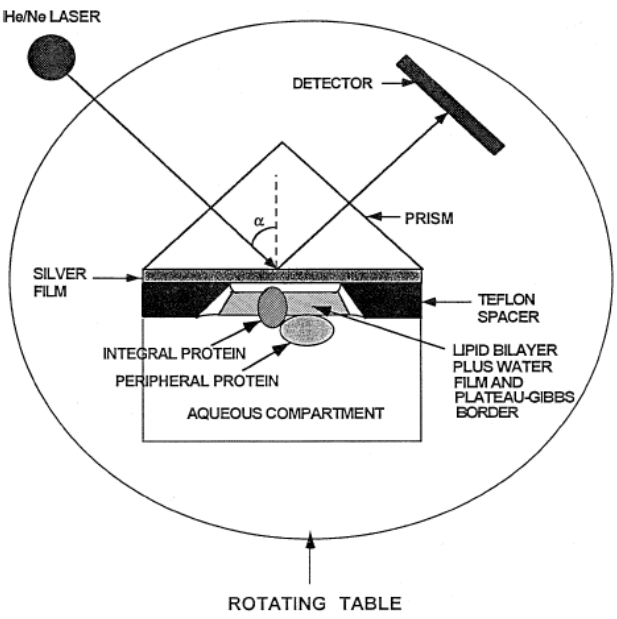

Figure 1.5 Top view of the experimental geometry of surface plasmon resonance spectroscopy. (Adapted from Ref. 29)

Surface plasmon resonance spectroscopy is used to detect molecular adsorption, such as polymers, DNA or proteins. Normally the angle of the reflection minimum is measured, and the mechanism of SPRS detection is based on that adsorbing molecules lead to a change in local refractive index, which in turn changes the resonance condition of the surface plasmon. Figure 1.6 shows the SPR spectrum change with the variation of refractive index and thickness of the dielectric medium adsorbed on the silver film, the SPR angle change takes on a linear relationship with both the dielectric medium refractive index increment and the adsorbed thickness increment, which makes SPRS a powerful tool to detect, for example, the molecular adsorption and to measure binding constants.[30]

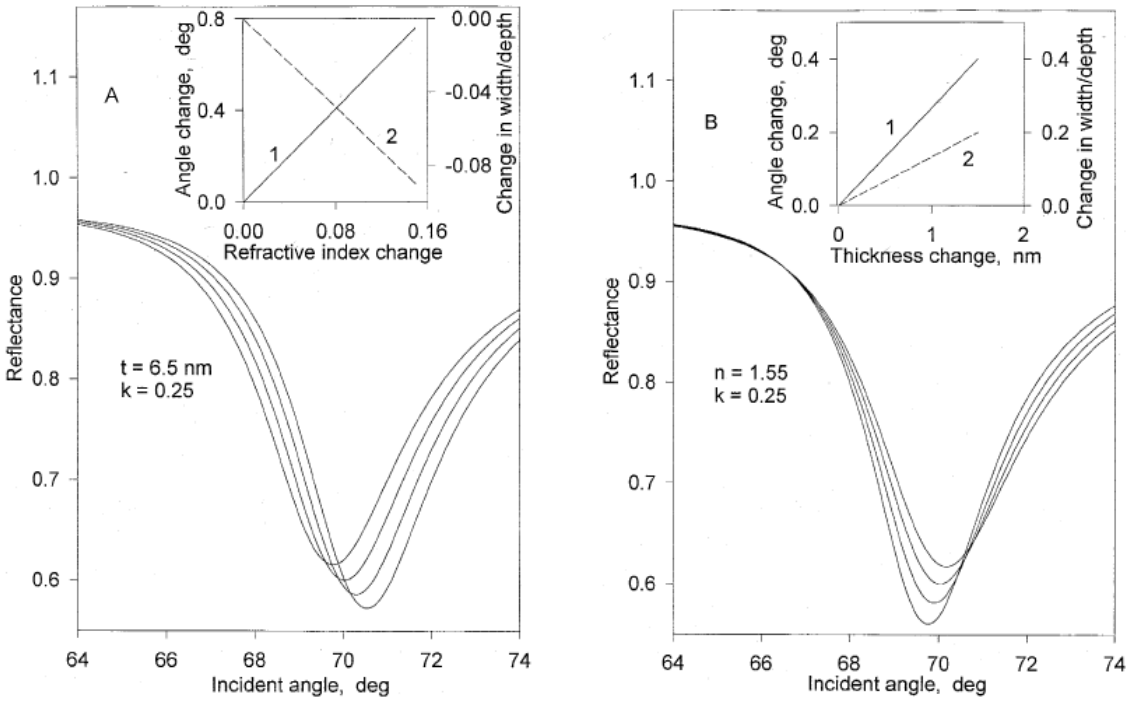

Figure 1.6 The changes in the SPR spectrum of a 61 nm silver film caused by alternating (A) the refractive index and (B) the thickness of a light absorbing dielectric layer deposited on the metallic film. (Adapted from Ref. 31)

1.2 Metal Enhanced Fluorescence

Among diverse applications of surface plasmon resonance in various research fields, metal enhanced fluorescence (MEF) phenomenon allows integrating the surface plasmon resonance into chromophore luminescence domain and thus attracts increasing interests. As early as 1970, Drexhage first pointed out that fluorescent emission intensity and lifetime of a chromophore depended on the distance between luminescent centers and a metallic mirror.[32] Later on, in the early 1980s, Glass et al. observed increased luminescence intensity of dye molecules adsorbed onto metal NP islands and films.[33] An enhanced emission from dye molecules adsorbed onto rough metallic islands was studied by Lakowicz et al. more recently in 2002.[34] Biteen et al. discovered an increased CdS quantum dots optical absorption due to gold nanospheres surface plasmon resonance effect.[35] With regard to application of MEF, it has gradually set foot in the fields of medical and biological imaging in the last decade. We will introduce the fundamental principles of MEF in this section.

1.2.1 Surface Plasmon Resonance Induced Local E-field

SRP induced local E-field enhancement is a crucial concept for the understanding of the metal enhanced fluorescence principle. This concept originates from SERS as introduced in chapter 1.1.4, where the 10^{10}-10^{11} Raman signal enhancement from local E-field enhancement effect. The SPR E-field of silver NPs with different geometries and alignment arrays will be introduced in this subsection.

Futamata et al. simulated the local E-field distribution of silver NPs under surface plasmon resonance condition using the Finite Difference Time Domain (FDTD) method, in which the numerical solutions of E-field can be obtained at given positions and time, provided the initial

electromagnetic field is given. Figure 1.7 shows their simulation results under different silver particles geometry and size.[36] The local E-field on isolated Ag circular cylinder surface shows the maximum enhancement factor 15-fold at 380 nm, while for right-angle triangular particles, it exhibits a vast E-field enhancement by 500-fold at 430 nm, which corresponds to its surface plasmon resonance wavelength. This giant enhancement effect, however, is confined to the edge of the triangular particle; the E-field enhancement decays drastically when the spatial location shifts away from the edge of the triangular or so-called "hot site". The E-field enhancement effect vanishes within a few nanometers range for the triangular particle, while this effective range can expand to a few tens of nanometers for the circular cylinder particle.

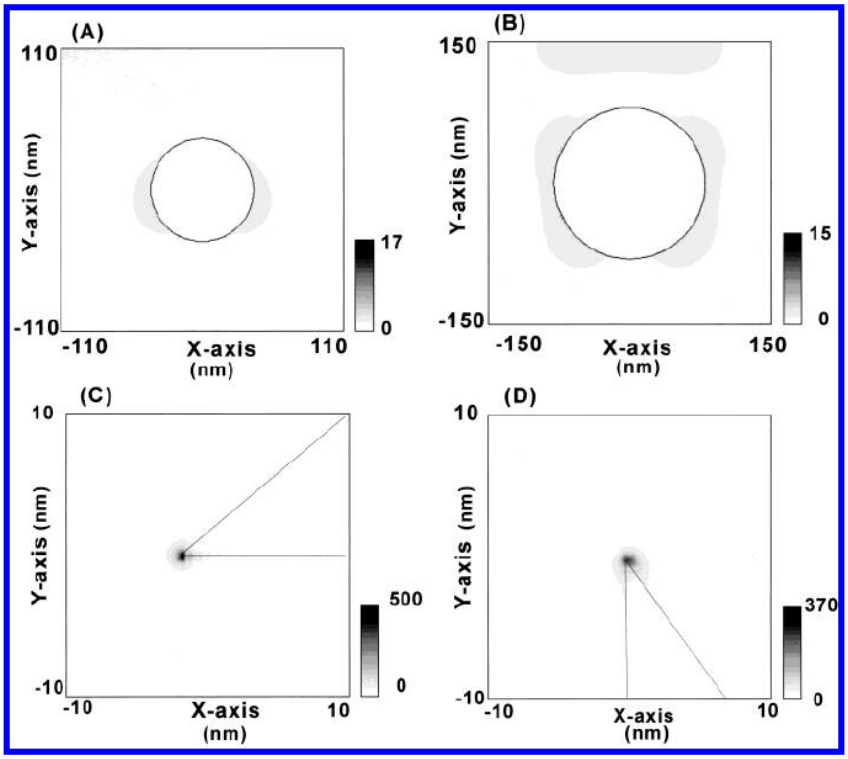

Figure 1.7 Spatial distribution of electric field on isolated silver particles at the peak wavelength: (a) circular cylinder (r=40 nm); (b) circular cylinder (r=80 nm); (c) symmetrical right-angle triangular (80 nm × 80 nm); (d) right-angle triangular particles (80 nm × 40 nm). Polarized light along x- and y- axes was used at 380 nm for circular cylinder geometry, and at 430 nm for triangular particles respectively. Electric field is shown as an amplitude enhancement relative to the incident field. (Adapted from Ref. 36)

Because we can rarely encounter an isolated single particle case in practical applications, a theoretical prediction on a more complicated aggregated particle system becomes important. Futamata et al. also made a simulation on two touching circular tube silver particles and investigated the relation between the E-field enhancement effect and the gap width as shown in Figure 1.8. Two touching particles present the maximum E-field enhancement by 370-fold, which results from localized surface plasmon coupling effect. As the space between the two particles increases, the enhancement effect decays remarkably due to the diminished local surface plasmon coupling effect. A huge enhancement factor can be still retained as long as the separation is less than 1 nm. However, only 5-fold local E-field enhancement factor can be achieved when the gap between the two particles is 20 nm.

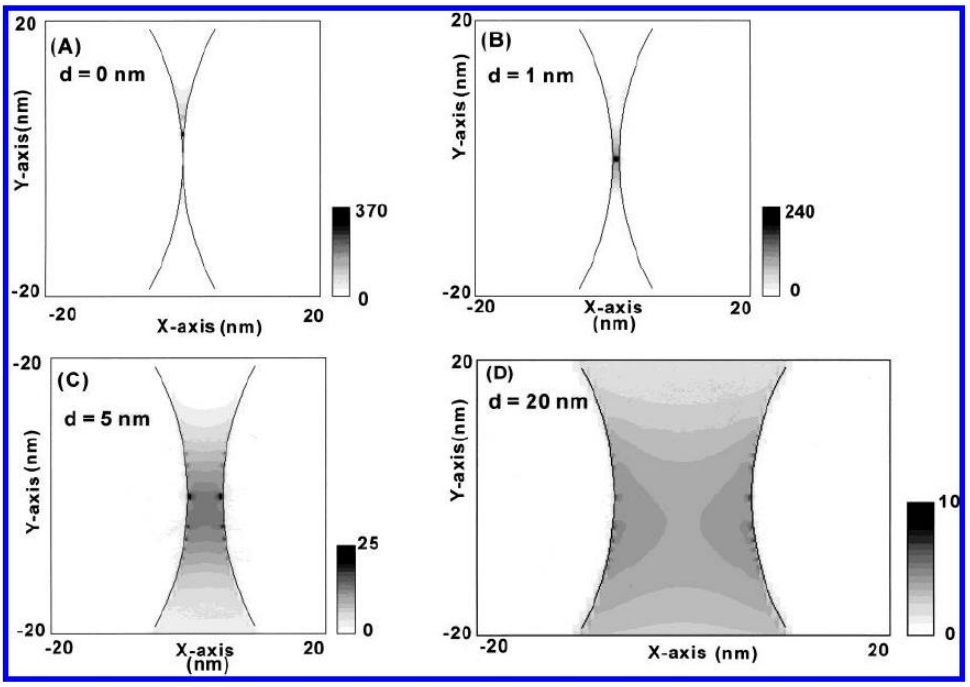

Figure 1.8 Electric field distribution for two touching silver circular tubes (r=40 nm) as a function of the spacing at 480 nm: (a) d= 0 nm, (b) d=1 nm; (c) d=5 nm; and (d) d=20 nm. (Adapted from Ref. 36)

Forrest et al. also simulated the local E-field distribution around a silver NP array via two-dimensional finite element solutions to solve Maxwell's equations.[37] Figure 1.9 shows the field distribution for a one dimensional array of Ag cylinders. The contours indicate the intensity enhancement of the E-field. 12-fold intensity enhancement was found in the gap between the cylinders. As a result, the absorbance of CuPc on the silver film (wavelength > 500 nm) is increased notably as shown in Figure 1.10. The 440 nm absorption peak corresponds to the intrinsic surface plasmon resonance of silver particles, which red shifts to 470 nm when CuPc is deposited due to the change of refractive index of the dielectric medium surrounding the silver NPs.

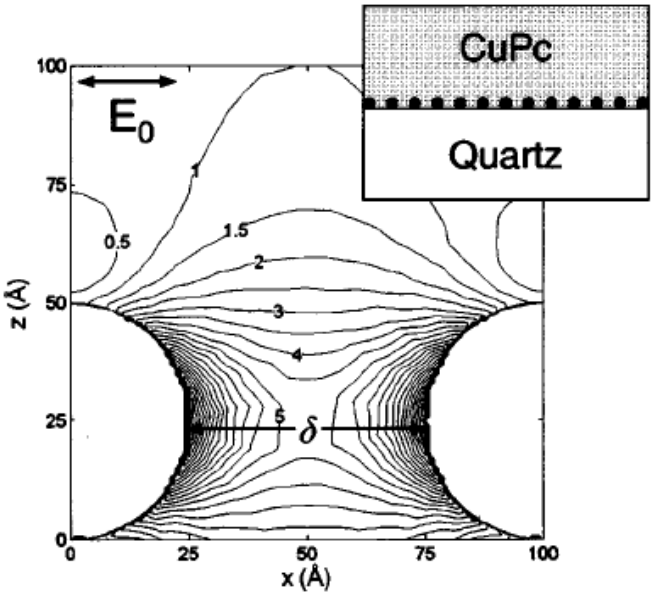

Figure 1.9 Contour map of the calculated intensity enhancement (I/I_0) of a silver particles chain. The diameter of Ag particle is 5 nm and center-to-center spacing d=10 nm, excitation wavelength is 690 nm. The particles lie on a quartz substrate (n=1.46, z=0) and are embedded in a dielectric medium (CuP_C). Contour labels represent the intensity enhancement and are spaced by 0.5. The polarization vector is indicated by the arrow and propagation is in the +z direction. Inset is the schematic diagram of the simulated geometry. (Adapted from Ref. 37)

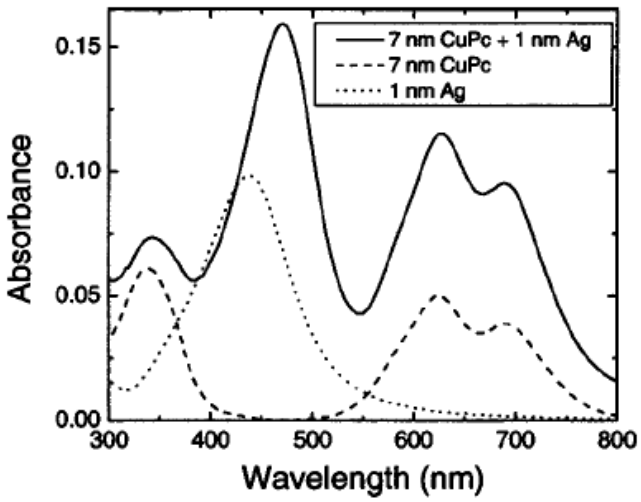

Figure 1.10 Measured absorption spectra of 1 nm Ag, 7 nm CuPc and 7 nm CuPc on 1 nm Ag. (Adapted from Ref. 37)

We have introduced the synthetic method of rod-like silver or gold NPs in section 1.1.3. In order to get vast local E-field enhancement, a triangular-like particle with a shape edge is highly desired. Herein we introduce a hard-template method to synthesize triangular shape NPs.

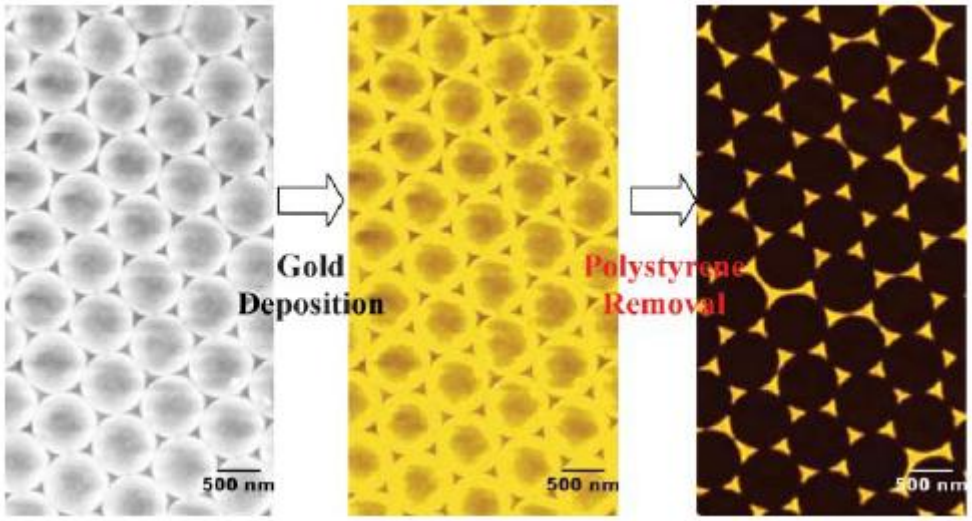

Figure 1.11 Deposition of polystyrene spheres on substrate, thermal evaporation of bulk gold and removal of polystyrene spheres to leave triangular gold NPs. (Adapted from Ref. 38)

El- Sayed et al. adopted a nanosphere lithography technique to fabricate triangular shape gold NPs as shown in Figure 1.11.[3] Firstly, a monolayer of closely packed monodisperse polystyrene spheres is deposited on a substrate, acting as a template for gold deposition. Normally the size of polystyrene spheres is about hundreds of micrometers in diameter. The metal gold is then evaporated into the voids of the polystyrene spheres. Finally the polystyrene spheres can be dissolved in organic solvents, leaving an array of triangular shaped gold NPs on the substrate. This method can produce monodisperse, uncapped metal NPs with a strict geometric shape alignment on a large scale.

1.2.2 Metal Enhanced Fluorescence Theory

Metal induced chromophore luminescence variation can be interpreted in terms of a Jablonski diagram shown in Figure 1.12.[39] E is excitation, Γ is radiative decay rate, and k_{nr} is non-radiative decay rate. Generally speaking, the metal-chromophore interaction can be divided into three parts: (1) Excitation enhancement; (2) Fluorescence quenching; and (3) Fluorescence enhancement.

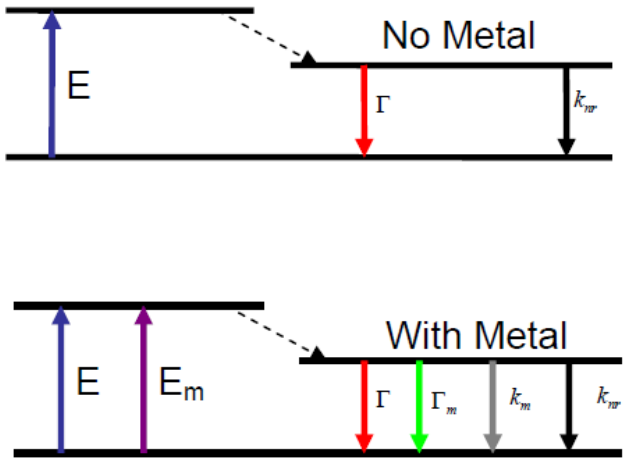

Figure 1.12 Jablonski diagram of chromophore without (top) and with (bottom) metal in the vicinity.

(1) Excitation enhancement. Metal SPR can result in vast enhanced local E-field as we described in section 1.2.1. If a fluorescent molecule is placed in this strong E-field region, its light absorption coefficient will increase according to the Fermi's golden rule: transition probability from one state to the other is proportional to the square of electric field strength the molecule experiences. Thus an additional term E_m is introduced to the molecule absorption, which results in the excitation enhancement.

With regard to the fluorescent emission, the presence of a metal NP can introduce two additional terms, Γ_m and k_m, which corresponds to the metal induced radiative decay rate and the nonradiative decay rate, respectively. The quantum efficiency of a fluorescent molecule Q_0 is then written as Q_m as follows:

$$Q_0 = \frac{\Gamma}{\Gamma + k_{nr}} = \Gamma \cdot \tau \tag{1.5}$$

$$Q_m = \frac{\Gamma + \Gamma_m}{\Gamma + \Gamma_m + k_m + k_{nr}} = \Gamma' \cdot \tau' \tag{1.6}$$

(2) Fluorescence quenching. If the metal-induced non-radiative decay rate k_m is dominant compared to the radiative decay rate terms Γ_m, i.e. $k_m >> \Gamma_m$, the quantum efficiency Q_m is less than Q_0, which is so-called fluorescence quenching effect, and it is the most common case occurring in metal-chromophore interaction.

(3) Fluorescence enhancement. If metal-induced radiative decay rate is much larger than the nonradiative decay rate, i.e. $k_m << \Gamma_m$, the quantum efficiency Q_m is increased compared to Q_0, which corresponds to fluorescence enhancement effect.

Indeed, these effects could coexist in the metal-chromophore interaction. The chromophore can exhibit enhanced or quenched fluorescence depending on the alignment of the chromophore and the metal nanoparticles. Herein the distance between the chromophore and the metal NPs plays a crucial role in controlling the fluorescence of the chromophore.

If a fluorescent molecule is in the vicinity of metal nanoparticles, the enhanced local E-field around NPs will facilitate the radiative decay of electrons in the excited state of the chromophore, thus it is easy to understand where the metal induced radiative decay term comes from and why fluorescence gets enhanced. However, provided the chromophore is very close to the metal NPs, its fluorescence is drastically quenched. As viewed from the enhanced local E-field theory, if a molecule gets closer to metal NPs, it tends to have higher quantum efficiency and fluorescence intensity. This apparently contradicts experimental observations.

Lakowicz developed a radiating plasmons (RP) concept to interpret the distance-dependant fluorescence.[40] According to the RP model, wavevector matching in the metal and dielectric medium interface is responsible for the light absorption or reflection. If the chromophore is very close to metal NPs, electron oscillations on metal surface induced by the chromophore dipole cannot radiate to the far-field and decay very rapidly into heat because wavevector matching is not possible. In such case the metal NPs dissipate the radiative energy from the chromophore and quench its fluorescence. However, to date detailed mechanism responsible for fluorescence quenching is still controversial. Jennings et al. investigated the fluorescence behavior of molecular dyes at a discrete distance away from 1.5 nm diameter gold NPs as a function of distance and energy. They claimed that the energy transfer to the metal surface, which is termed nanosurface energy transfer (NSET), was the dominant quenching mechanism.[41] Nevertheless, there is reasonable agreement that if the separation between metal NPs and chromophores is less than 7 nm, fluorescence quenching is normally observed; whereas metal enhanced fluorescence occurs when the chromophores are 10~30 nm away from the metallic structure, [39, 42] however some publications have reported an optimal distance as large as 60 nm.[43]

1.2.3 Spatial Separation and MEF

Metallic quenching effect on chromophore fluorescence is a common phenomenon. For instance, 5-nm thick silver surfaces were used in microscopy to quench emission from regions near the metal films.[44] In order to achieve MEF, it is important to immobilize a chromophore where it is in the concentrated E-field of the metal NPs and the fluorescent emission can be coupled to the far field. Generally speaking, two strategies exist in the present MEF literatures as illustrated in Figure 1.13.

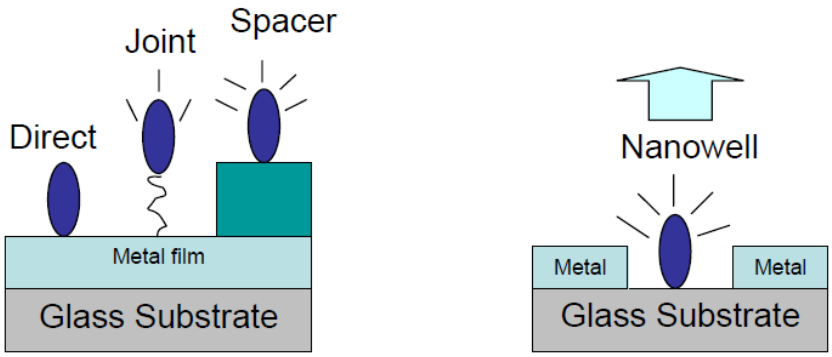

Figure 1.13 Illustration of methods to prevent fluorescence quenching: application of a spacer layer or a joint (left); application of a nanowell (right).

One strategy is the traditional method of securing vertical distance from the metal surface using a spacer. Several research groups succeeded in avoiding fluorescence quenching by using this method. Lakowicz et al. studied the distance-dependent fluorescence enhancement of Cy3 and Cy5 on a silver island film.[45] The distance to the surface was controlled by alternating layers of biotinylated bovine serum albumin (BSA) and avidin. The maximum fluorescence enhancement factor of 12-fold was reached for Cy3 when the first BSA-avidin layer was applied, and then the enhancement factor decreased to 2-fold for six layers of BSA-avidin spacer as shown in Figure 1.14. Similar enhancement happens on Cy5 fluorescence, which suggests that optimal

fluorescence enhancement is reached when the chromophores are 9 nm away from the silver island film surface.

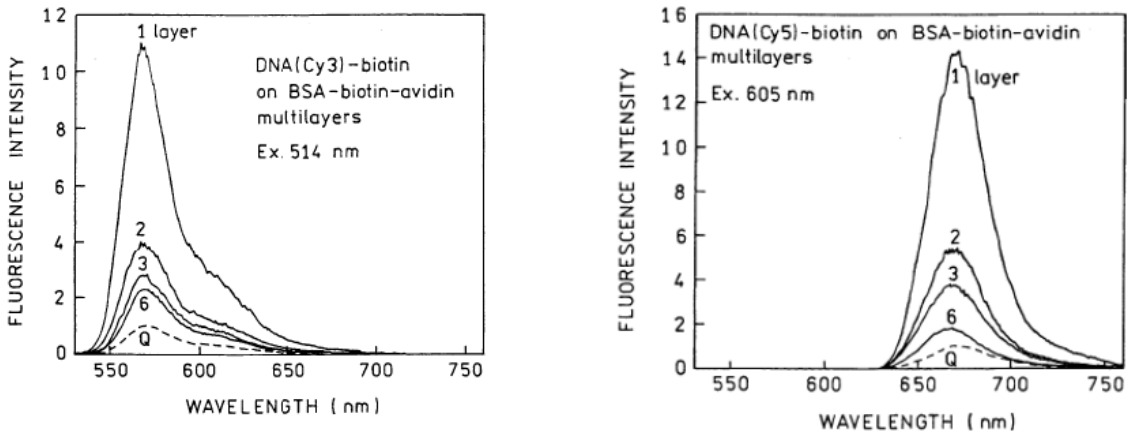

Figure 1.14 Emission spectra of Cy3 (left) and Cy5 (right) on silver island films with BSA-biotin-avidin layers spacer. (Adapted from Ref. 45)

Another strategy is that the horizontal distance is secured by using a nano-constructed metal film. Shalaev et al. reported the enhanced fluorescence in plasmonic nanoantennae as shown in Figure 1.15.[46] The nanowell pattern was written in a resist mark on a quartz substrate using electron beam lithography, followed by depositing gold with an electron beam evaporator, and finally rhodamine 800 was incorporated into nanoantennae system by sol-gel processing. Intensity measured from rhodamine 800 embedded around the nanoantenna structures shows significant enhancement compared with the signals away from the nanoantennae; the enhancement factor ranges from 20 to 100 fold as a function of the wavelength.

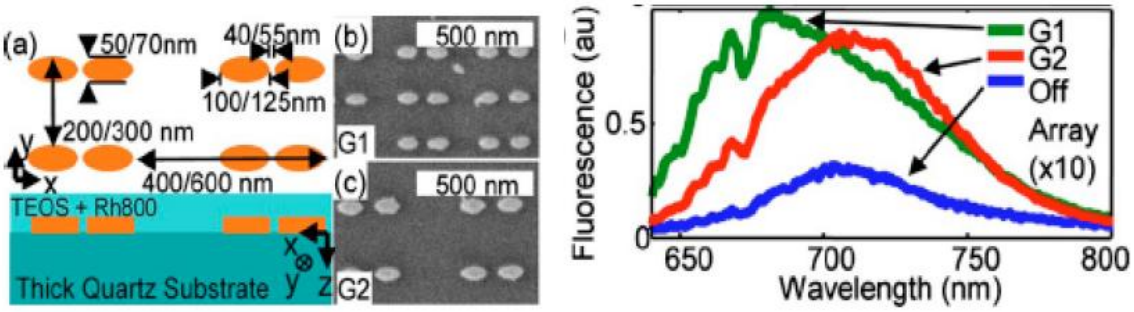

Figure 1.15 Rhodamine 800 coated nanoantenna array (left): (a) sketch of sample, (b) small dimensions geometry, (c) large dimensions geometry. Antenna enhanced fluorescence of rhodamine 800 compared with rhodamine 800 fluorescence away from the antennae (right). (Adapted from Ref. 46)

1.2.4 Spectral Overlap and MEF

Since the enhancement of local E-field around metal NPs depends on the wavelength of the incident light exciting surface plasmon, the fluorescence enhancement of a chromophore is expected to depend on the spectral overlap between the dye molecule and the metal NPs SPR. Falicia et al. investigated the fluorescence enhancement as a function of the spectral overlap. [47] The SPR wavelength of a gold nanoshell was adjusted by altering its inner (r1) and outer (r2) diameter denoted as [r1, r2], and ICG dye was attached to the gold nanoshell using HSA.

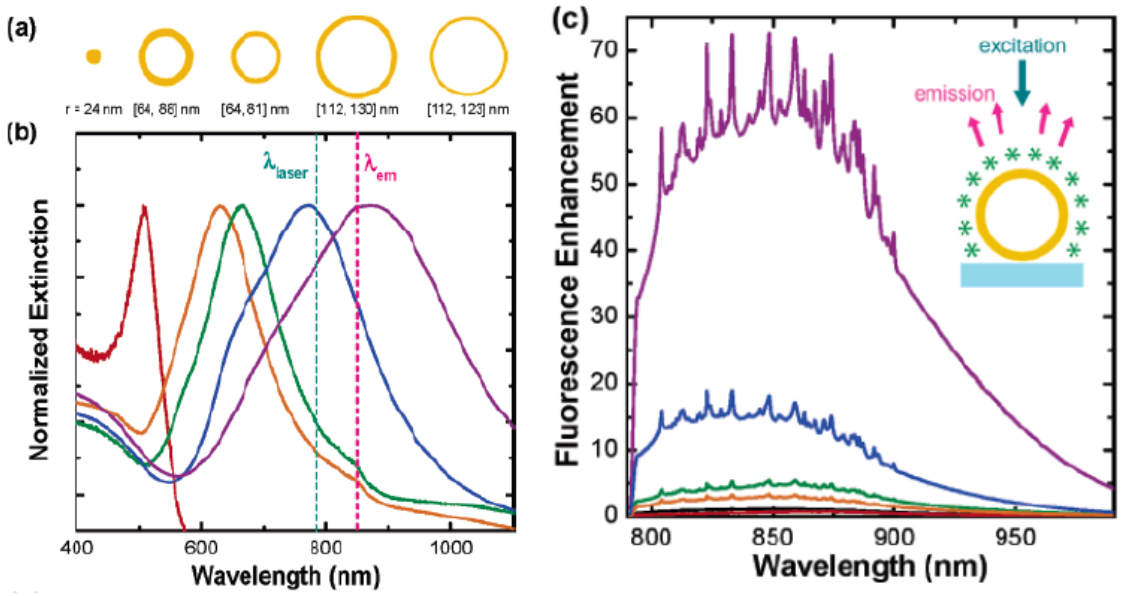

Figure 1.16 (a) gold colloid and nanoshells with different structures; (b) the normalized extinction spectra of above five nanostructures; (c) corresponding fluorescence emission from ICG conjugated to the nanostructures. (Adapted from Ref. 47)

A nanosphere with a diameter of 24 nm results in slight quenching of ICG fluorescence, [64, 81] and [64, 88] nanoshells exhibit modest enhancement. The SPR of [112, 130] nanoshell is

tuned to the ICG excitation wavelength, resulting in greatest near field enhancement 15-fold. The SPR of [112, 123] nanoshell shifts to the ICG emission maximum wavelength, which leads to maximum enhancement factor 50-fold. The above results suggest that optimal enhancement occurs when the metal NPs SPR has maximum overlap with the emission spectrum of the chromophore.

The SPR wavelengths of gold and silver are in the visible region, thus they are studied extensively in MEF phenomenon,[48-49] and they work well with the chromophores with absorption and emission in the visible range. However some widely used fluorophores absorb and emit in the UV region. In this regard, aluminum and zinc nanostructured substrates have been explored recently to enhance chromophores fluorescence particularly in the UV-blue region. Ray et al. reported a 9-fold fluorescence enhancement of 2-aminopurine on a 10 nm thick aluminum film.[50] Aslan et al. investigated the features of a textured zinc film, which presents a SPR peak in the UV region.[51] As a result, the zinc film induced up to 8-fold fluorescence enhancement of chromophores with emission wavelength in the blue range.

1.2.5 Shape and MEF

As we discussed in section 1.2.1, the geometry of metal NPs strongly influences the local E-field enhancement, a sharp edge can lead to a giant field enhancement. Thus the investigation of MEF under diverse particle geometries has been an active research field in the last decade.[52] Owing to increased sensitivity of resonance scattering compared to spheres, nonspherical NPs are promising for biomedical diagnosis application such as dark field microscopy.[6]

Geddes et al. reported a comparative experiment on ICG fluorescence enhancement by silver spheres and nanorods as shown in Figure 1.17. The silver nanorods adsorbed on a glass substrate exhibit two distinct SPR peaks, the peak at 440 nm corresponds to transverse resonance,

and the peak at 650 nm the longitudinal mode. Under a low loading of the nanorods on the surface (A_{650}=0.1), a 10-fold fluorescence enhancement was observed. However, as the loading density of nanorods increased to 0.48, a 50-fold ICG fluorescence intensity enhancement was achieved. The above results suggest a surface coated with low symmetry silver nanorods is more promising for MEF compared to a traditional silver island film.

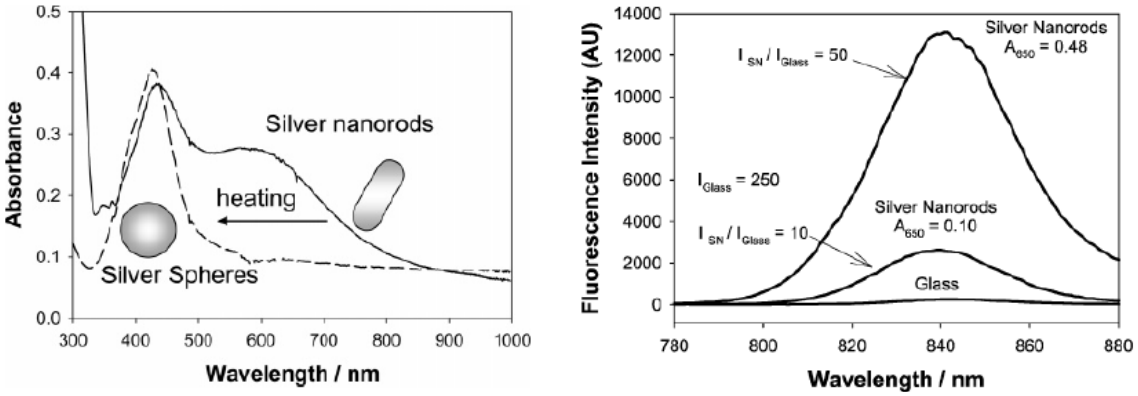

Figure 1.17 Absorption spectra of silver spheres and nanorods (left); metal enhanced ICG fluorescence by silver spheres and nanorods (right). (Adapted from Ref. 53)

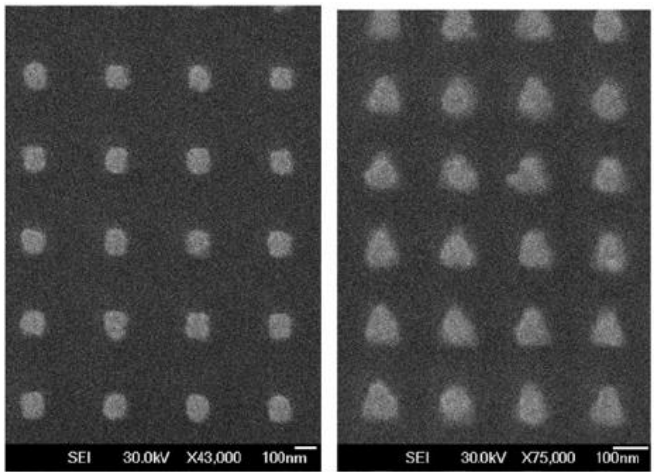

Figure 1.18 (left) A high magnification SEM image of square nanoparticles with 110 nm lateral size and 390 nm center-to-center interparticle spacing. (right) A high magnification SEM image of triangular nanoparticles with 110 lateral size and 210 nm center-to-center interparticle spacing. (Adapted from Ref. 54)

Corrigan et al. studied the enhanced fluorescence of various dyes including Cy3, Cy5 and Fluorescein using silver particle arrays with different cell geometries.[54] The silver particle arrays were fabricated by e-beam lithography together with e-beam evaporation techniques. Firstly, 25 nm Al_2O_3 was deposited on Si (001) substrates to increase adhesion and to avoid fluorescence quenching from the semiconducting substrates. PMMA was spin coated on the substrates and etched by e-beam lithography under different photomasks, and silver was deposited by an e-beam evaporator. Finally, the unwanted silver was removed by a lift-off procedure. The SEM images of the silver particle arrays are shown in Figure 1.18.

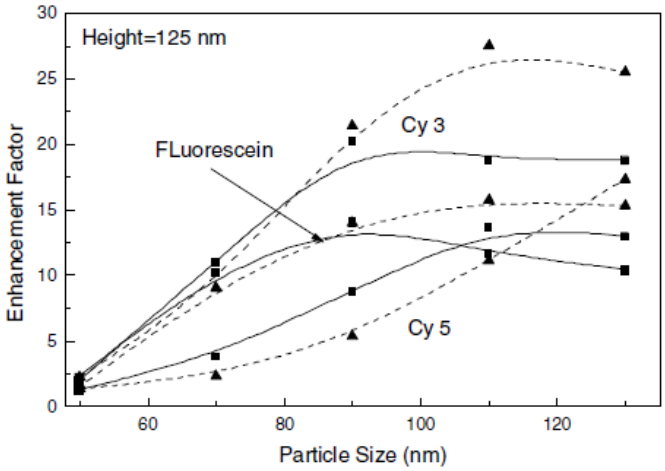

Figure 1.19 Comparison of fluorescence enhancements for Fluorescein, Cy3, and Cy5 using silver NP arrays of squared and triangular particle shape with thickness 125 nm. (Adapted from Ref. 54)

Figure 1.19 shows the comparison of fluorescence enhancement of dyes by silver arrays of different shapes. The triangular shape array shows a higher enhancement factor compared to the squared array on the whole, due to lower symmetry and thus larger enhanced field. Moreover, the fluorescence enhancement effect on Cy3 is notably higher than that on Cy5, and must result from the emission spectral difference of those two dyes. Cy3 is known to emit yellow light, but

Cy5 has emission in the near IR region. Although the authors did not report the extinction spectra of triangular and squared silver particle arrays, normally the SPR wavelength of silver NPs is in the visible region. Therefore it overlaps more with the emission spectrum of Cy3 causing higher fluorescence enhancement.

1.3 Organic Light Emitting Diode

Organic electroluminescence devices have been one of the most attractive research topics in materials science in the last two decades. The attraction and fascination of this field are mainly from the interdisciplinary nature of the OLEDs, which includes synthetic chemistry, physical chemistry, device physics, and electrical engineering. In this thesis, we only focus on the discussions about device physics, particularly about metal NPs incorporated OLEDs and surface plasmon enhanced electroluminescence.

1.3.1 Introduction to OLED

OLED is a leading technology for next generation full color flat panel displays.[55] It is a typical light-emitting diode with an organic film as emitting layer. Because the luminescence nature of an OLED is from the organic luminescent materials, OLED is thus a direct light source without needing a backlight and can display deep black level colors compared to liquid crystal display (LCD). More interestingly, it can be fabricated on a flexible substrate leading to flexible display which can be processed with roll-to-roll techniques.[56] Moreover, OLED has wider viewing angles, higher power efficiency and faster response time than LCD, which make it a promising display technology.

As early as 1963, an electroluminescence (EL) phenomenon was first observed in organic semiconductors by Pope et al.,[57] however its commercial potential was not discovered until 1987 when Tang et al. reported efficient EL under low voltage in an organic thin-film device at Kodak.[58] The concept of the organic EL was extended to polymers by Friend and coworkers in 1990.[59] Recent advances in materials and manufacturing techniques make OLEDs successfully applicable to small displays such as mobile phones, car stereos, digital cameras and so on.[55] So

far, the first commercially available OLED television named as XEL-1 was manufactured in 2007 by Sony as shown in Figure 1.20.

Figure 1.20 The first OLED TV in the world: Sony XEL-1.

A simplified OLED structure is shown in Figure 1.21, consisting of cathode, ETL, recombination layer/emission layer, hole transport layer (HTL) and anode. When a driving voltage ca. 5-10 V is applied across the two metallic electrodes, electrons are injected from the cathode, normally of low work function, into electron transport layer (ETL) where the electrons hop via the LUMOs of neighboring molecules towards the anode. Similarly, holes are injected from the anode and transport in HTL. In this way, electrons and holes can combine and form excitons in the recombination layer.

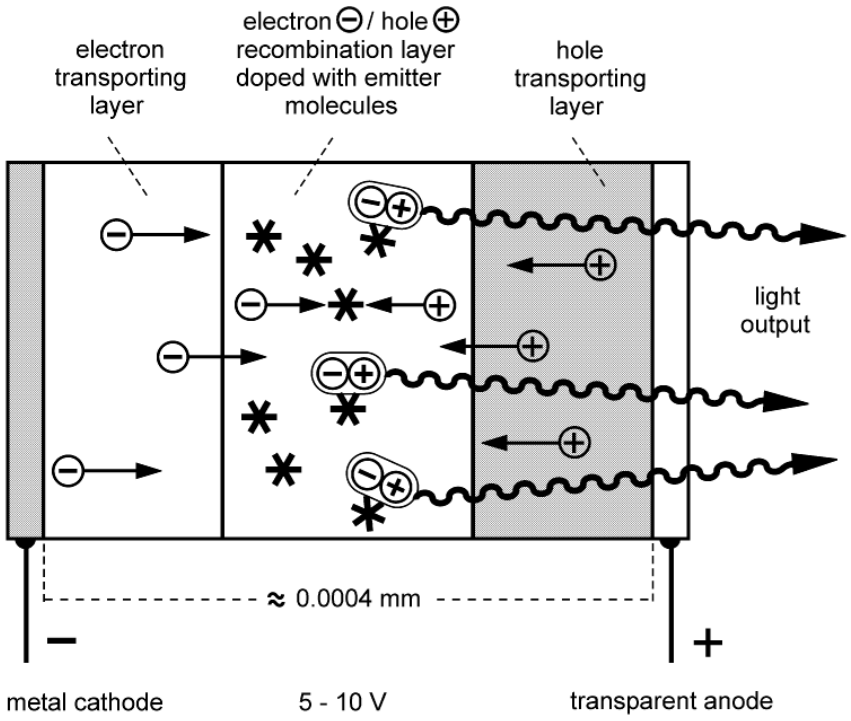

Figure 1.21 Schematic diagram describing an OLED structure and its working principles. (Adapted from Ref. 60)

Normally the anode of an OLED is a transparent metal oxide layer with good conductivity, which allows the light generated in the recombination layer to be emitted out. Indium tin oxide (ITO) is a widely used anode material in OLEDs, consisting of SnO_2 (10-20%) and In_2O_3 (90-80%). Different methods have been developed to deposit ITO on glass substrates such as thermal evaporation, sputter deposition, and so on.[61-62] ITO exhibits a relatively high work function, which is suitable for hole injection into the HOMO of the HTL material.

The electron and hole mobilities in organic materials are orders of magnitude smaller than those in crystalline inorganic semiconductors owing to the localized nature of the electronic states in amorphous organic materials. This offers enough time for electron/hole recombination, making a highly efficient EL possible under a low driving voltage.

A simple OLED structure is not able to achieve highly efficient EL. Independent from the quantum efficiency of the emitter molecules, device power efficiency losses can originate from many reasons, such as poor alignment of the electrodes work functions relative to the HOMO/LUMO of the adjacent layers, unbalanced electron and hole mobility, a low cross-section for electron-hole recombination, low light outcoupling efficiency and so on. OLED technology is far from being well developed at this stage and optimizations in materials and device structure design are still important.

An OLED can be fabricated in various ways depending on the material features. Generally speaking, vacuum thermal deposition and wet-coating are two main techniques for OLED processing. Thermal evaporation is applied to small molecules and metals which are sublimated by the joule effect and evaporated in a vacuum of ~ 10^{-6} torr or higher. One of the most prominent advantages of vacuum thermal deposition is that it enables the fabrication of multilayer devices in which the thickness of each layer can be controlled precisely. So far the vacuum thermal deposition techniques for OLEDs fabrication are successfully transplanted from the sophisticated semiconductor industry. Moreover, vacuum thermal deposition technique creates a relatively simple way to achieve multi-color display by using properly matched shadow masks for depositing RGB emitting materials. However, it has been reported that residual gases in the vacuum chamber may affect device performance. Brömas et al. found Ca deposited in a high vacuum system (~10^{-6} torr) led to much better OLED device performance than that deposited under a ultra-high vacuum (~10^{-10} torr), which is ascribed to the formation of a thin metal oxide buffer layer at organic material/metal interface.[63]

Since polymers generally crosslink or decompose under heating, they cannot be thermally evaporated in a vacuum chamber. Thus polymers are usually deposited in wet-coating ways, which enable efficient large-scale coating with low cost. However, this restricts the multi-layer deposition, in which the solvent used for the second layer deposition would not dissolve the first

deposited polymer layer. Gustaffson et al. fabricated flexible polymer light emitting diodes (PLEDs) by sequentially spin-coating an aqueous solution of conducting transparent polyaniline onto a layer of Poly[2-methoxy-5-(2'-ethylhexoxy)-1,4-phenylenevinylene] (MEH-PPV).[56] In addition, the wet-coating method cannot precisely control the thickness of films in-situ since the polymer concentration, the spinning rate, and the spin-coating temperature determine the final thickness of a film.

OLEDs can be sorted as small-molecule OLED, polymer OLED and hybrid OLED by material category, and we will expand our introduction to these three types of OLEDs in the following subsections.

1.3.2 Small-Molecule OLED

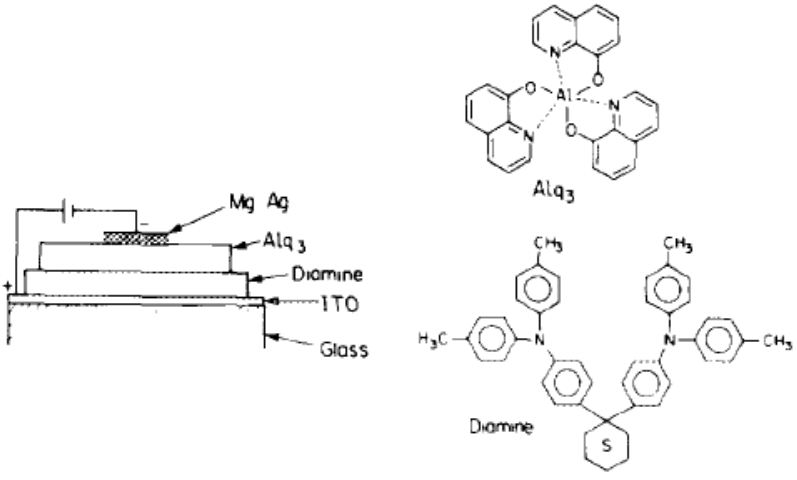

Figure 1.22 Configuration of Tang's OLED and molecular structures. (Adapted from Ref. 58)

Efficient OLEDs made of small molecules were first developed by Tang at Eastman Kodak;[58] the blue print of the first OLED is shown in Figure 1.22. In contrast to the mainstream OLED design in the 1980s in which a single layer of organic material was sandwiched between two injecting electrodes, Tang et al. adopted a double layer design, in which one layer was a luminescent layer Alq_3 and the other aromatic diamine layer was capable of only monopolar transport. The anode was typical ITO glass and the top electrode was a mixture of magnesium and silver with an atomic ratio of 10: 1. All the layers, including organic and metallic layers, were deposited using the vacuum thermal deposition method.

Measureable light emission can be only observed in forward bias, i.e. the ITO electrode was positively charged and the Mg-Ag electrode was negatively charged by an external voltage source, under a driving voltage as low as 2.5 V. It was a tremendous progress on EL since the EL of OLEDs before Tang's work needed a driving voltage on the order of 100 V. It is considered that the efficient charge carrier injection and recombination are responsible for the superior OLED performance.

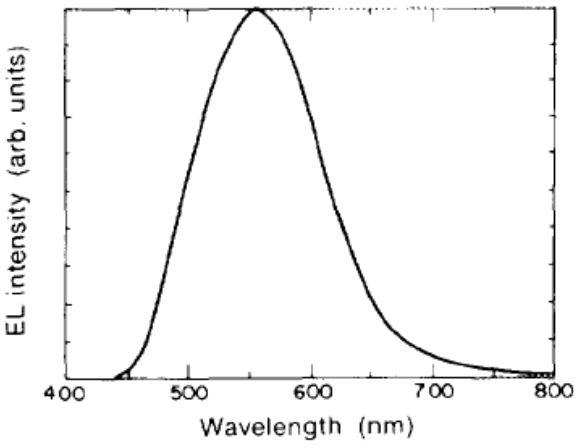

Figure 1.23 Electroluminescence Spectrum of Tang's OLED with a structure ITO/diamine/Alq_3/Mg: Ag. (Adapted from Ref.58)

The emission spectrum of the OLED is shown in Figure 1.23, the peak wavelength is ca. 550 nm and FWHM is about 100 nm, which is identical to the photoluminescence (PL) of an Alq_3 thin film. This indicates that the radiative recombination of the injected electrons and holes takes place in the Alq_3 layer. The diamine layer is known to transport holes only, blocking the electrons injected from the Mg: Ag electrode, thus the electron-hole pairs are trapped in the Alq_3 layer. More specifically, Tang reported that the recombination area was confined to a 30 nm-thick Alq_3 layer adjacent to the diamine layer.

The Mg: Ag alloy used in Tang's OLED has been extensively used in current OLEDs design due to its low work function. Mg is a low work function metal which is suited for electron injection into the LUMO of the organic materials. However, it is susceptible to oxidation in the atmosphere. The incorporation of Ag can retard the oxidation process of Mg; on the other hand, Ag can increase the sticking coefficient of Mg on organic films during thermal deposition.

Thanks to the bi-layer design and effective exciton blocking effect, Tang's OLED exhibited remarkably increased EL stability. The OLED could last 100 hours luminescence in argon ambient before its luminance efficiency decayed to half of the initial value. Although the lifespan of cutting-edge OLEDs is above 10,000 hours,[64] Tang's "stable" OLED luminescence was a huge leap in device stability in 1980s.

So far numerous small molecules have been used in OLEDs as hole transport materials, electron transport materials and red, green, and blue emitting materials. Hole transport materials play the roles of facilitating hole injection from the anode, accepting holes and transporting holes to the emitting layer. Meanwhile hole transport layer should also function as an electron-blocking layer, preventing electrons from escaping form the emitting layer. N,N'-Bis(3-methyl-phenyl)-N,N'-diphenyl-[1,1'-biphenyl]-4,4'-diamine (TPD) is a good hole transport material for OLEDs, [65] which was originally used as a charge-carrier transport material dispersed in a polymer binder in photoreceptors in electrophotography.[66] More recently, N,N'-di(1-naphtyl)-N,N'-diphenyl-

[1,1'-biphenyl]-4,4'-diamine (NPB) has been developed and used widely as a hole transport material. [67]

Analogous to the hole transport materials, electron transport materials generally play the roles of facilitating electron injection from the cathode, accepting and transporting electrons. Meanwhile, electron transport materials function as the hole-blocking layer which prevents the holes from escaping from the emitting layers. So far, Alq_3 has been widely used as an electron transport material, it is also a good green light emitting material. Other reported electron transport materials include oxadiazole derivatives, benzimidazole derivative such as 1,3-bis[5-(p-tert-butylphenyl)-1,3,4-oxadiazol-2-yl]benzene (OXD-7) and 2,2',2''-(1,3,5-benzenetriyl)tris-[1-phenyl-1H-benzimidazole] (TPBI). [68-69]

Emitting layer molecules have been broadly investigated and explored, so far a large material inventory has been established. Typically red emitting materials such as Rubrene and Pt(TPBP), green emitting molecules $Ir(ppy)_3$ and Alq_3, and blue materials Perylene and DPAVBi etc. have been well studied. [70,71,72] For small molecule OLEDs (SM-OLEDs), thermal deposition is an ideal choice for the devices fabrication, it enables the formation of well controlled, homogenous and multi-layer structural films. This high flexibility in layer design enables distinct function to each layer such as charge transport, charge blocking, and charge recombination etc. Those advances are responsible for the high luminance efficiency of the SM-OLEDs. However, the production process is expensive and of limited use for large-area devices.

1.3.3 Phosphorescent OLED

PHOLED is a type of OLEDs that takes advantage of emitting molecules phosphorescence to obtain higher internal efficiency than the fluorescent OLEDs. Due to its high-level energy efficiency potential, PHOLEDs have been attracting more interests, and so far they

still keep the highest efficiency record in the OLEDs field. Figure 1.24 explains the principle of triplet states harvesting in PHOLEDs.

According to spin-statistics, one can obtain 25% of excitons with a singlet character and 75% excitons with a triplet character. After exciton formation and relaxation, the lowest excited singlet and triplet states are populated. An organic fluorescent molecule exhibits an efficient radiative decay from $S_1 \rightarrow S_0$, which is so-called fluorescent emission. For an organic molecule intersystem crossing, $S_1 \rightarrow T_1$ and $T_1 \rightarrow S_0$, is forbidden according to selection rules, thus the intersystem crossing (ISC) transition probability is low and the decay of triplet population to ground state normally occurs in non-radiative ways at ambient temperature. In this way, 75% triplet excitons are lost in organic fluorescent molecules and their energy is converted to thermal energy.

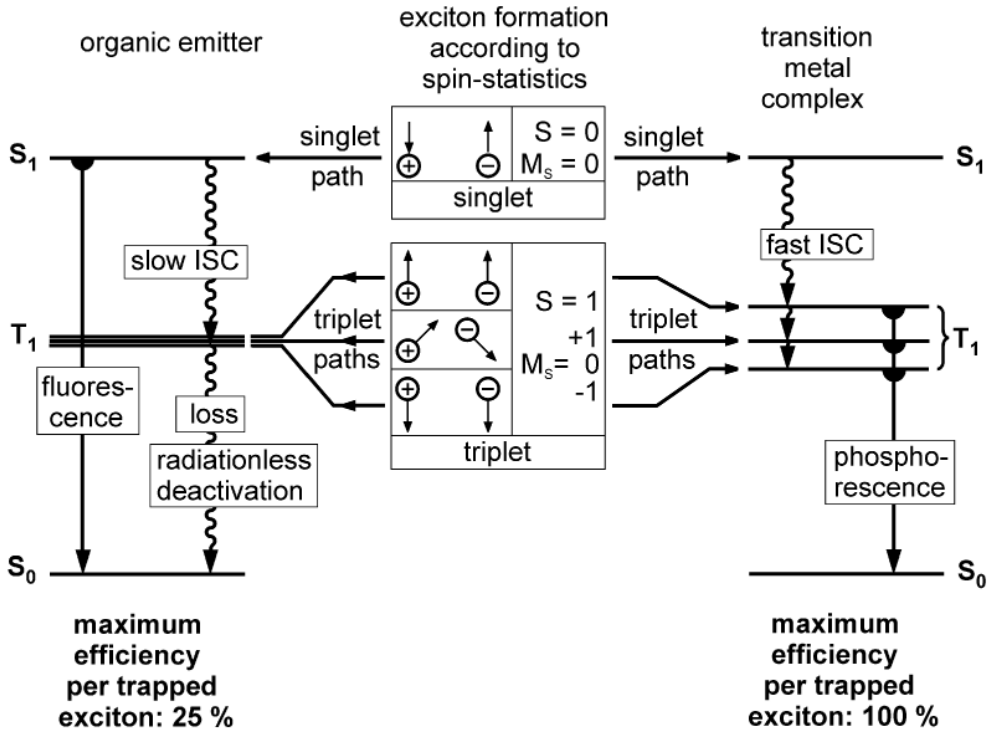

Figure 1.24 Schematic diagram explains the principle of triplet harvesting. (Adapted from Ref. 60)

The luminescence process in an organo-transition metal complex, however, is quite different from that in the pure organic molecules. Because the central metal ion in an organometallic complex carries significant spin-orbit coupling, the ISC transition $S_1 \rightarrow T_1$ becomes efficient and thus a singlet state emission $S_1 \rightarrow S_0$ is not observable. Moreover, the radiative $T_1 \rightarrow S_0$ rate can be sufficiently high so that efficient phosphorescence can emit at ambient temperature. As a result, all four possible spin orientations of the excitons can be harvested to create efficient luminescence. This triplet harvesting can in principle achieve four times higher EL efficiency for an organometallic complex emitter compared to a fluorescent emitter with only singlet emission.

Yang and Tsutsui first reported a phosphorescent OLED based on PVK: $Ir(ppy)_3$.[73] These devices contained a PVK: $Ir(ppy)_3$ layer as emitting layer and an electron transport layer, sandwiched between two electrodes. The external efficiency of the devices depended strongly on the choice of the electron transport layer. The highest efficiency 7.5%, was reported when OXD-7 was used as the ETL, but without a bathocuproine (BCP) blocking layer, as shown in Figure 1.25. Shortly afterwards, Lee et al. published a phosphorescent OLED with a similar device structure but with lower efficiency. Owing to the rather poor electron mobility in poly(9-vinylcarbazole) PVK, an additional small-molecule ETL was usually introduced into these devices by vacuum thermal deposition.[74]

Lamanski et al. first demonstrated an efficient single layer polymer electrophosphorescent device by adding PBD into the PVK host to increase electron transport.[75] As a result, the devices with 130 nm emitting layer consisting of PVK (67 wt.%), PBD (30 wt.%) and $Ir(ppy)_3$ (3 wt.%) sandwiched between the ITO and Mg:Ag electrodes, exhibited an EQE of 3.4% and 8 V turn-on voltage. Because none of the emission peaks from PVK or PBD was observed, the excitons were considered to form on the phosphorescent dopant exclusively. Vaeth

et al. further optimized Lamanski's device by incorporating a 5- nm hole blocking layer and a 30-nm Alq_3 ETL.[76] In the same year, Gong et al. increased the single-layer PHOLED efficiency to 10%, corresponding to 36 cd/A.[77] Two reasons are considered to be responsible for the efficiency increase. Firstly, a Ca electrode was used instead of the MgAg cathode, which favored the electron injection due to the lower work function of Ca; secondly, a green-emitter $Ir(DPF)_3$ was used, which is slightly more electron-rich than $Ir(ppy)_3$.

Interestingly the driving voltage of the PHOLEDs strongly depends on the phosphorescent dye concentration, which implies that the carriers (more likely the holes) are trapped deeply in the PVK matrix. For instance, the driving voltage of a 5% $Ir(DPF)_3$ doped PHOLED is as high as 37 V to reach 1 mA/cm^2 current density.

Optimization of PHOLEDs has been made from different point of views. Earlier works on devices with fluorescent and phosphorescent emitting layers have shown that a thin CsF layer in combination with a Ca, Al, and MgAg electrodes greatly increased electron injection.[78] Yang et al. used a CsF/Al cathode to replace the LiF/Al cathode,[79] the turn-on voltage (under which brightness = 0.1 cd/m^2) of the PHOLED was reduced to 3.5 V. The maximum luminance efficiency was 27 cd/A at a current density of 2.3 mA/cm^2 corresponding to an EQE=7.6%.

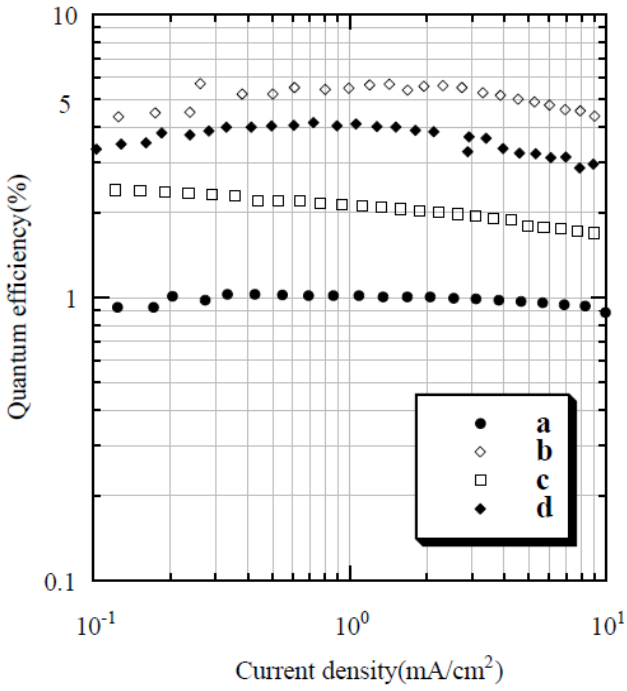

Figure 1.25 External quantum efficiency plotted versus current density for four devices. The ETL is (a) Alq_3, (b) OXD-7. The hole-blocking layer and ETL are (c) BCP/Alq_3, (d) BCP/OXD-7. (Adapted from Ref. 73)

On the other hand, one can also reduce the barrier height for hole injection to increase the power efficiency of PHOLEDs. Neher et al. demonstrated that TPD as a hole transport layer significantly increased device performance.[80] TPD is particularly suitable because the HOMO level of TPD 5.5 eV is similar to that of $Ir(ppy)_3$ 5.4 eV. Compared to a control device without TPD, the PHOLED with 6 wt.% $Ir(mppy)_3$ and 9 wt. % TPD showed higher luminance efficiency and PCE. The peak luminance efficiency of the TPD-doped device was 38 cd/A at a current density of 1.8 mA/cm^2, which corresponds to an EQE=10.7%.

1.3.4 Efficiency of OLED

A high power efficiency of OLEDs is highly desired not only for reducing the power consumption but also for prolonging the lifespan of the devices. A device working at a low input power at a given brightness can decrease ohmic heating and prevent the amorphous organic film from crystallization. External quantum efficiency is defined as a ratio of the number of photons emitted through the front face of the device to the number of injected electrons,[81] which can be written in a formula as follows:

$$\eta_{EL} = \xi\gamma r_{ST}\eta_{PL} \tag{1.7}$$

where (i) ξ is the out-coupling efficiency, (ii) γ is a ratio of the number of exciton-forming events to the number of electrons flowing in the external circuit, which represents the exciton formation probability. (iii) r_{ST} is the ratio of singlet exctions to total excitons formed from the recombining charge carriers, and (iv) η_{PL} is the PL quantum yield. We will expand our discussion on each factor contributing to the external quantum efficiency of OLEDs.

(i) If the emitting layer has a high refractive index n (n>>1), only part of the light, approximately $1/(2n^2)$ for a flat surface, can escape from the device, it corresponds to the factor ξ. A textured surface has been explored to increase the light out-coupling of OLEDs. Rocha et al. exploited a method to incorporate a grating in the active layer of an OLED.[82] An azo-dye polymer was spin-coated on a glass substrate and then irradiated by laser beams to yield a surface relief grating,[83] a 200 nm layer of ITO was sputtered over the azo layer followed by the evaporation of the active layer, and finally a 200 nm Al cathode was deposited. AFM verification was done to confirm that the surface modulation was transferred to each layer; the modulation amplitudes of the cathode on the top layer were even close to the amplitudes initially recorded on the azo-polymer. Unfortunately, the authors did not observe a significant difference in the emission intensity between the corrugated and the uncorrugated diodes. The modulations were considered

too small compared with the film thickness to induce considerable light out-coupling enhancement.

(ii) $\gamma \leq 1$, which is a measure of the balance between hole and electron injection, and of the probability that each of them will recombine with the other. It has been argued that in the relatively efficient OLEDs studied to date, γ could be close to 1. This factor can be optimized by changing the composition and the thicknesses of the HTLs and ETLs. Considerable efforts have been made to promote the injection of both electrons and holes from electrodes, and a balanced electron/hole ratio leads to a high OLED efficiency.

(iii) The ratio of singlet excitons formation r_{ST} is determined to be 25% based on spin-statistics as we interpreted in section 1.3.3. This factor indeed represents the ratio of excitons contributing to the EL. For a small organic molecule, only singlet excitons can result in fluorescence emission, i.e. r_{ST}=0.25. However, for an electrophosphorescent OLED, all the singlet and triplet excitons can engage in the EL, therefore in principle the r_{ST} factor in a PHOLED can approach unity.

(iv) η_{PL} of many dyes is close to 100% in solution. In most cases the quantum efficiency (QE) decreases as the dye concentration increases, which is known as concentration quenching effect due to the establishment of nonradiative decay paths in concentrated solutions or solids. Diverse nonradiative decay path ways would impair the exciton's contribution to EL. Thus a material with a high η_{PL} is highly demanded for OLEDs application.

In summary, according to equation (1.7), the upper limits of different terms appear to be ξ=0.2 (n≈1.54 for a glass substrate), γ=1, and r_{ST}=1. Hence a phosphorescent OLED could yield an external quantum efficiency η_{EL}=0.2 η_{PL}. The above discussions on external quantum efficiency of OLEDs give us an explicit guideline to optimize OLEDs performance, which builds up the foundation of our experimental works in the following chapters.

1.4 Organic Solar Cells

1.4.1 Introduction to Organic Solar Cell

The energy crisis is one of most serious problems our human beings need to solve in the 21st century. The development of green energies such as wind, solar and so on, is one of the solutions to change energy supply sources. Particularly, solar radiation is a clean renewable energy source with unlimited access. The photovoltaic effect is the direct conversion of incident light into electricity by a PN junction. Although the phenomenon is known for almost a century, a practical application was not accomplished until 1954, when Chapin et al. invented the first crystalline silicon solar cell with an efficiency of 6%. [84] It was rapidly realized that a solar cell was a convenient way to generate power in remote locations such as in space, and it was developed as the power supply for satellites and vehicles used in space industry. So far, the technology has now been developed for a wide range of applications such as the power supply for electric calculators and garden lights, the power supply in developing countries for water pumping, street lighting and so on. The power conversion efficiency of modern crystalline solar cells is over 20% and the PCE of tandem solar cells is over 40%.

As a new emerging technology, organic solar cells attract great attention from scientists due to their incomparable low production cost and flexibility. Among all photovoltaic cells, organic solar cells are unique since they can be fabricated by printing or wet-coating processes resulting in true low cost. We will focus our discussions on organic solar cells (OSC) in this section.

OSCs have a rapid development in the last decade, the efficiency of OSCs was evolving constantly, from 2.5% in 2001,[85] 5% in 2007, to 8.3% in 2011 achieved by Solamer Inc. 10%

power conversion efficiency is believed to be the benchmark for industrial scale launching, which requires intensified exchange of knowledge and experiences in a broad range of disciplines including material chemistry, material characterization, device physics, as well as device process and production technology. Although OSCs have much lower PCE compared to inorganic solar cells, the prospect of cheap production such as roll-to-roll process drives the development of OSCs further in a dynamic way. If a transparent and soft substrate is used for OSCs fabrication, a flexible OSC is approachable. Konarka Inc. has made that happen as shown in Figure 1.26. This paper-like OSC can be readily implemented into constructions, skyshades, and textiles to capture the sunlight. The two competitive production techniques used today are either wet solution processing or dry thermal evaporation of organic compounds, which benefit from the facile development of OLEDs using similar technologies.

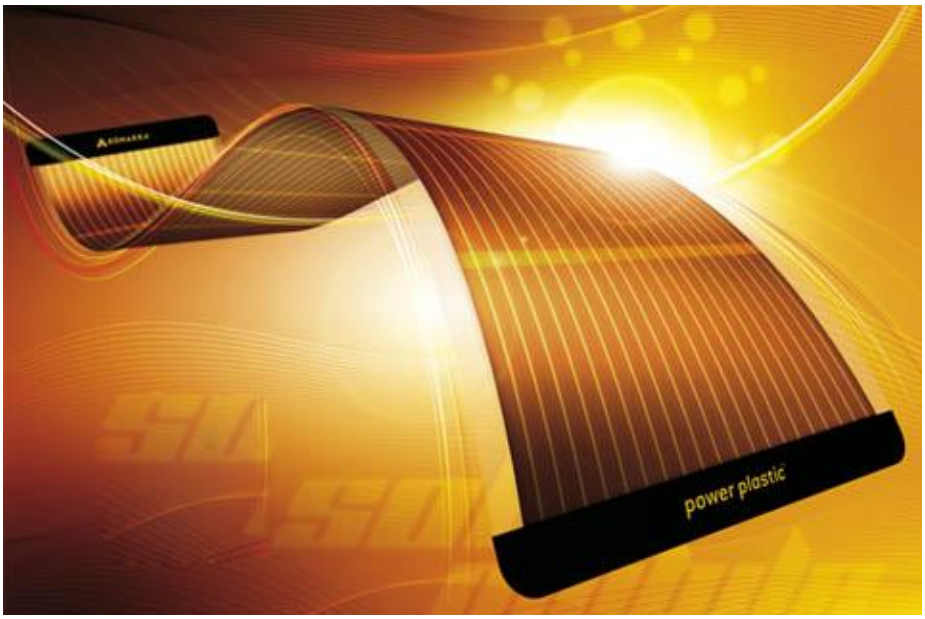

Figure 1.26 The flexible OSC product made by Konarka Inc.

The process of converting light into electric current in an organic solar cell is accomplished by four consecutive steps: (i) the absorption of photon leading to formation of an

exciton, (ii) exciton diffusion to a donor-acceptor (DA) interface, (iii) the charge separation occurs. (iv) the holes transport to anode and electrons transport to the cathode to supply a direct current for an external load.

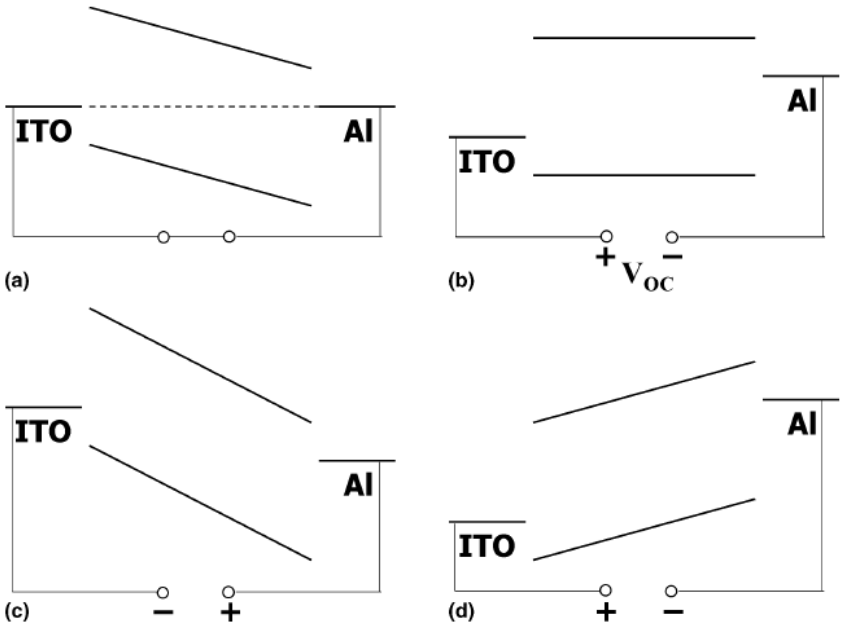

Figure 1.27 MIM picture of organic diode device. (a) short circuit; (b) open circuit; (c) reversed bias; (d) forward bias. ($V>V_{OC}$) (Adapted from Ref. 86)

To understand how an intrinsic semiconductor device works, a metal-insulator-metal (MIM) model is used as shown in Figure 1.27.[87] A semiconductor sandwiched between two metal electrodes with different work functions is depicted in several different situations. (a) When no voltage is applied across the device (i.e. short circuit condition), the built-in electric field results from the difference of two metals' work functions. Under illumination, separated charge carriers can drift to the respective electrodes: the electrons go towards the lower work function metal and the holes move to the higher work function metal. In this case, the device works as a solar cell. (b) When the applied voltage equals to the difference between two metals' work functions, it is known as the "flat band condition", the voltage is called flat band voltage $V_{FB.}$ As there is no

internal electric field, the drift current is zero, but the diffusion current produced by the accumulation of charge carriers at the DA interface still remains. When the applied voltage is further increased to a value at which the backward drift current induced by the reversed internal electric field can just compensate the forward diffusion current, no net current flows through the diode,[88] this is so called "open circuit condition". The applied voltage is called open circuit voltage V_{OC}. For a good solar cell in which holes and eletrons can be extracted efficiently from the DA interface, the V_{FB} is close to the V_{OC}. (c) When a reverse bias is applied on the device, the generated charge carriers drift under a strong electric field to the respective electrodes and the diode works as a photodetector. (d) When a forward bias larger than V_{OC} is applied on the device, the metal electrodes can efficiently inject charges into the semiconductor. If these excitons can recombine radiatively, then the device works as a LED and turns on under this condition.

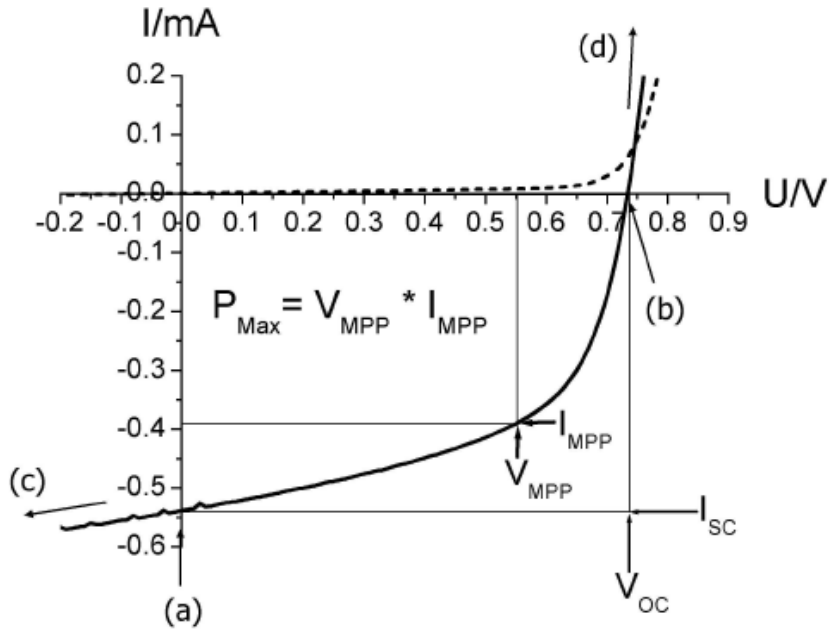

Figure 1.28 Current-Voltage (IV) curves of an organic solar cell under dark and illuminated conditions. (Adapted from Ref. 86)

The I-V curves of a typical organic solar cell are shown in Figure 1.28. In the dark, no current flows across the device until the metal electrodes start injecting charge carriers efficiently into the device at a forward bias larger than V_{OC}. Under illumination, the current flows in the opposite direction compared to the injected current. In the fourth quadrant, the maximum generated photocurrent occurs under short-circuit condition; and the photocurrent reduces to zero under open circuit condition. At a certain point, denoted as the maximum power point (MPP), the product of current and voltage reaches maximum. Then the fill factor (FF) is determined as follows:

$$FF = \frac{V_{MPP} \times I_{MPP}}{V_{OC} \times I_{SC}} \tag{1.8}$$

It represents the part of the product of V_{OC} and I_{SC} that can be used. The power conversion efficiency (PCE) of a solar cell is then determined by comparing the solar cell's peak power to the sunlight power which is 100 mW/cm^2 under 1.5 AM condition.

$$PCE = \frac{P_{OUT}}{P_{IN}} = \frac{I_{MPP} \times V_{MPP}}{P_{IN}} = \frac{FF \times I_{SC} \times V_{OC}}{P_{IN}} \tag{1.9}$$

1.4.2 Small-Molecule Solar Cell

The first OSC was based on a single organic molecular layer sandwiched between two metal electrodes of different work functions fabricated by thermal evaporation technique. Because the exciton diffusion length for most organic materials is below 20 nm,[89] only excitons generated in a small region (less than 20 nm) from the metal contacts can contribute to the photocurrent. This type of single layer solar cell exhibited poor FF, high series resistance and low efficiency due to exciton diffusion limit.

Later on, a bilayer heterojunction device was developed,[90] in which a donor and an acceptor were stacked together with a planar interface. The bilayer is sandwiched between two metal electrodes. The donor HOMO and the acceptor LUMO matching the work functions of anode and cathode is crucial to achieve high power conversion efficiency.

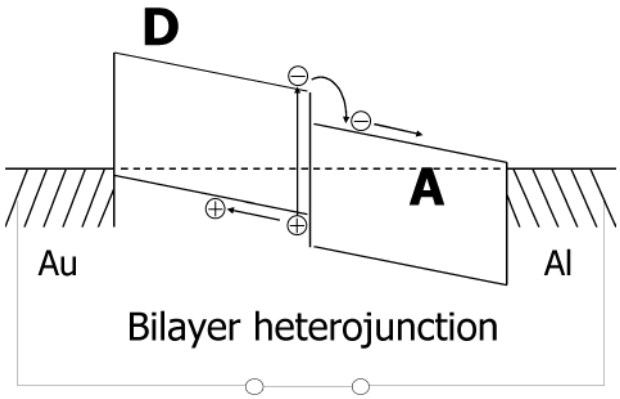

Figure 1.29 Schematic diagram of a bilayer heterojuntion device. D represents the donor, and A for acceptor. (Adapted from Ref. 86)

As shown in Figure 1.29, an electron is excited from the HOMO to the LUMO ($S_0 \rightarrow S_1$) when the donor D absorbs a photon. Provided an acceptor molecule is in close proximity, the electron could transfer to the LUMO of A in an energetically favored way. The success of the DA concept relies on the condition that the recombination rate between the holes in D and the electrons in A is several orders of magnitude smaller than the forward charge transfer rate. [91]

Another advantage of a bilayer heterojunction device over a single layer device is that electrons transport within n-type acceptor and holes move within p-type donor after excitons dissociation at the DA interface. Thus the electrons and holes are effectively separated from each other and charge recombination is greatly reduced. As a result, the photocurrent could linearly depend on the irradiation intensity provided the charge trap effect is too small to be neglected.[92]

Bilayer devices can be fabricated in various ways including thermal deposition, solution spin-coating or combination of those two.[93] The PCE of a bilayer heterojunction device consisting of copper phthalocyanine (CuPc) and C_{60} is reported as high as 4.2% by Forrest and co-workers.[94]

The DA interface where the exciton dissociates is the core to further increase the efficiency of OSCs. Reducing the mean distance between donor and acceptor molecules is one approach to increase the J_{SC}. To accomplish this goal without reducing the overall thickness of the active layers, a blend of donor and acceptor molecules has been used to form an interpenetrating DA network. That is so-called bulk heterojunction (BHJ) devices.

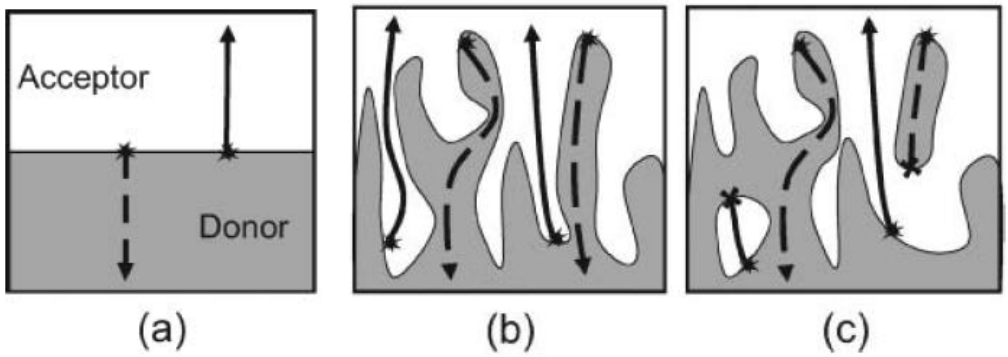

Figure 1.30 Representation of donor/acceptor interface architecture: (a) a planar heterojunction, (b) optimal bulk heterojunction, where there is complete phase separation; (c) a non-ideal bulk heterojunction, isolated regions of donor and /or acceptor phases prevent the collection of photogenerated charges. (Adapted from Ref. 95)

Differing from a planar heterojunction structure introduced by Tang, in which homogeneous donor and acceptor layers stack together as shown in Figure 1.30 (a), a BHJ structure expands the photocurrent generation region,[101] enabling excitons a higher probability to reach a nearby DA interface and dissociate. In an optimal arrangement as shown in Figure 1.30 (b), [96] the width of the phases in the interdigitated structure should be on the order of twice of the

exciton diffusion length, it ensures that excitons generated in the center of the donor and/or acceptor phases have a good chance to dissociate.

However, it is difficult to achieve an optimal phase separation structure realistically. Although co-deposited mixture of donor and acceptor small molecules has been demonstrated to reach a high PCE of 3.5 % under 1 sun (AM 1.5) illumination,[97] the performance of a BHJ solar cell relies critically on the microstructure of the mixture. For instance, co-evaporation does not lead to an ideal structure but results in a microstructure where isolated phase regions exist, it prevents effective charge collection since there is no path way for electron/hole to reach the contact electrodes in the isolated phase regions as shown in Figure 1.30 (c).

Generally speaking, a BHJ solar cell can be fabricated via co-deposition of donor and acceptor molecules, or solution casting of a donor-acceptor blend. So far, one of the most efficient BHJ solar cells is based on solution spin-coated poly(3-hexyl-thiophene) (P3HT) and [6,6]-phenyl C_{61} butyric acid methyl ester (PCBM) blend, it presents higher than 4% PCE under 1 sun irradiation. [98] We will expand our introduction on P3HT-PCBM solar cell in the following subsection.

1.4.3 Polymer Solar Cell

Figure 1.31 presents four common chemicals used in OSCs. CuPc is normally deposited by thermal evaporation, the rest of the other three contain side chains which enable them to be soluble in common organic solvents. This allows these polymers to be cast from solutions using wet-processing techniques such as spin coating, dip coating, ink jet printing, screen printing and so on. This attracts great interest from industry since it permits large-area OSCs production at ambient temperature and pressure together with little material loss.

Another advantage of polymers as active layer is that many conjugated polymers have high peak optical absorption coefficient. Crystalline silicon solar cells must be made ca. 100 μm thick to efficiently absorb sunlight. However, organic polymer solar cells only need 100 ~ 500 nm polymer layer to absorb most of the light in their absorption range.

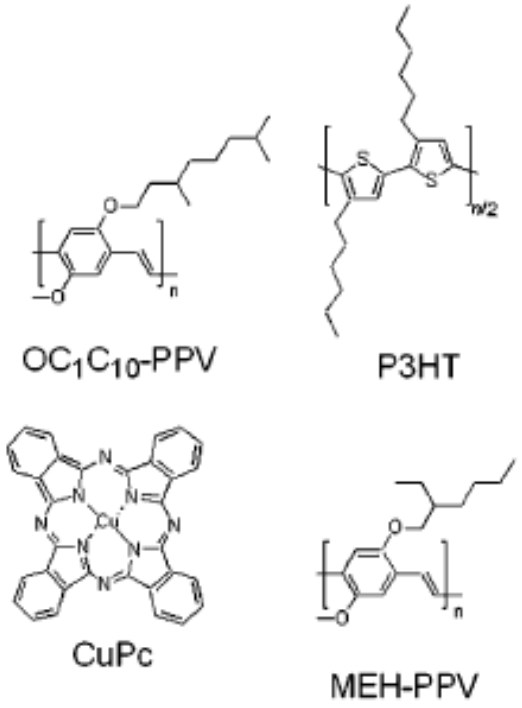

Figure 1.31 Chemical structures of four common organic semiconductors used in OSCs. (Adapted from Ref. 99)

The polymer solar cells also underwent a device structure evolution from single layer solar cells, bilayer solar cells to bulk heterojunction solar cells. Therefore, the polymer solar cells have been showing inferior PCE until the emergence of the BHJ structure. Heeger et al. and Friend et al. in 1995 independently blended two conjugated polymers with offset energy levels.[100-101] A PL quenching was observed, implying that the excitons generated in a donor polymer could reach the DA interface and then dissociate before recombination. The resulting solar cells initially delivered only ~6% external quantum efficiency under low light intensity,

however that was increased to 29% corresponding to a PCE of 1.9 % under 1 sun radiation by optimizing the device structure.[102]

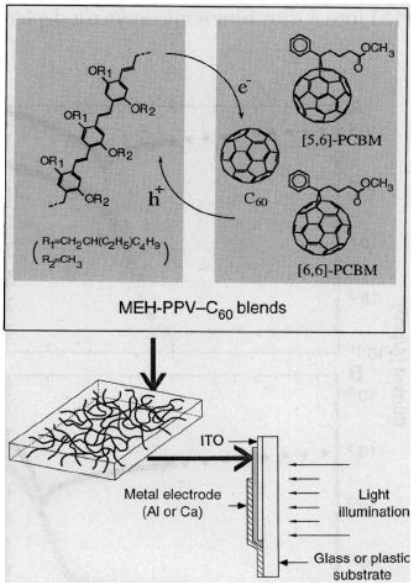

Figure 1.32 The schematic diagram of the photoinduced charge transfer process in MEH-PPV: C_{60} DA blends. (Adapted from Ref. 103)

A drastic efficiency increase on polymer solar cells began from the introduction of [6,6]-phenyl C_{61} butyric acid methyl ester (PCBM) into polymers blend by Heeger's group in 1995,[103] they found both luminescence quenching of the polymer and much better carrier transport could be achieved. Figure 1.32 shows the charge transfer process in the MEH-PPV: PCBM polymer BHJ solar cell. Due to the built-in potential at DA interface, ultrafast charge transfer and charge separation occurred with a quantum efficiency approaching unity, leaving holes in the MEH-PPV phase and electrons in the PCBM phase. As a result the device exhibited 2.9% PCE, it was two orders of magnitude higher than that of a device made with pure MEH-PPV.

The conjugated polymer-PCBM BHJ solar cells are the most studied polymer solar cells currently. Diverse methods have been developed to optimize device performance, such as

controlling morphology, employing charge collection layers, and inverting device layout. One significant improvement was made by Shaheen et al.,[104] who found that the morphology of a blend could be optimized by casting the polymer and PCBM in a solvent that prevents a long-range phase separation. As shown in Figure 1.33, a thin film cast from toluene exhibits a phase separation on the order of 500 nm, however a film cast from chlorobenzene solution presents much finer phase separation (< 100 nm) due to increased mutual solubility for the two components. As we previously discussed, the exciton diffusion length in organic materials is less than 20 nm, thus smaller phase separation domain can help more excitons diffuse to the interface, contributing more photocurrent to the solar cell. That was confirmed by the J-V curves shown in Figure 1.33 (c). As a result, a device with more than doubled external quantum efficiency (EQE) was achieved, and corresponding PCE raised to 2.5 % under AM 1.5 illumination condition.

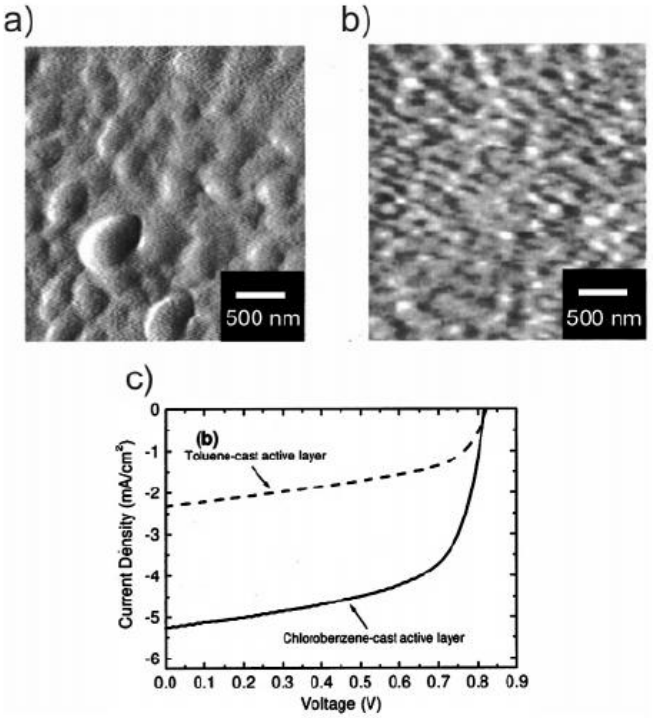

Figure 1.33 AFM images of the top surface of 100 nm films of DMO-PPV-PCBM blends after spin coating from (a) toluene and (b) chlorobenzene. (c) J-V curves of OSC cells made from these solvents under 1.5 AM illumination. (Adapted from Ref. 104)

Another important improvement of solar cells came from the renovation of the conjugated polymers. Padinger et al. found that P3HT had higher hole mobility compared to other PPV derivatives,[105] which resulted in an EQE above 70% at the absorption maximum and 3.5 % PCE under white light illumination. Shortly after the discovery of P3HT application in the solar cells, thermal treatment was developed to further increase the hole mobility and thus PCE due to increased crystallinity of the polymer.[106] Later on, it was found that a high-boiling-point solvent with long solvent-soaking time could optimize the morphology through self-assembly.[107] Recent advance of the P3HT: PCBM polymer solar cell yields over 4% PCE.

A number of new PCE records of polymer solar cells have been achieved since 2007, which can be ascribed to improved synthetic design of donors or acceptors. Generally speaking, there are three mainstreams in current advanced material design for polymer solar cell application. Firstly, the J_{SC} could be increased by lowering the E_g of the donor polymer and maintaining the polymer HOMO-fullerene LUMO gap. Secondly, the V_{OC} could be increased by maintaining the E_g of the donor polymer but shifting both the HOMO and LUMO level of the polymer down in energy, [108] since the V_{OC} of a polymer solar cell relies on the energy difference between the LUMO of the acceptor and the HOMO of the donor.[109] Last but not least, the V_{OC} could be increased by maintaining the E_g of the donor polymer but raising the LUMO level of the fullerene. A polymer solar cell could approach 10% PCE provided those three techniques could be well combined. In the past few years, a series of new co-polymer donors have been synthesized using alternating electron-rich and electron-poor monomers, these so-called push-pull polymers have smaller E_g than the homopolymers.[110] As a result, 8.3% PCE has been announced by Solarmer Inc. as the new world record for a polymer solar cell.

1.4.4 Inverted Solar Cell

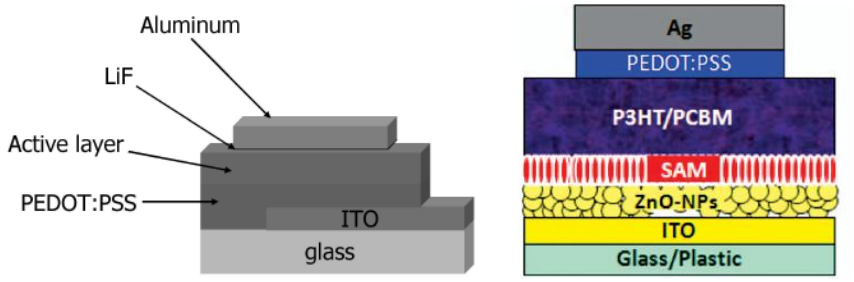

Figure 1.34 Solar Cell architectures: (left) conventional structure;[86] (right) inverted structure. (Adapted from Ref. 111)

The structure of polymer solar cells can be divided mainly into two categories as shown in Figure 1.34. The majority of polymer solar cells were fabricated in the conventional architecture, in which poly(3,4-ethylenedioxythiophene): poly(styrenesulfonate) (PEDOT: PSS) is used as a HTL coated on ITO and low work function metal electrode Al or Ca is evaporated on top as the electron collecting electrode. However there are a few notable drawbacks in this type of cell architecture. ITO could be corrupted over time by acidic PEDOT:PSS. [112] On the other hand, top electrodes Al and Ca with low work functions are susceptible to oxygen in the environment; formation of an insulating oxide layer at the interface could lead to significant performance decrease.[113] Moreover, the conventional structure requires the top metal electrode deposited under high vacuum which is not compatible with roll-to-roll process. Therefore, an inverted solar cell structure is developed, showing great prospect not only for increased device stability but also for compatibility with industrial roll-to-roll technique.

In an inverted architecture, the polarity of charge collection is opposite to that of the conventional architecture. Transparent electrode ITO is used as the cathode in a typical inverted solar cell structure, and high work function metals such as Au, Ag are used as top anode for hole collection; those air-stable top electrodes can resist to oxidation even under exposure to the

atmosphere. Moreover, the usage of high work function metals enables non-vacuum coating techniques to deposit the top electrode, reducing fabrication complexity and cost.

Nunzi et al. first proposed the concept of the inverted solar cell.[113] In their polymer solar cells, BCP or perylene buffer layer was used to modify the work function of ITO making it function as the cathode. Moreover, the BCP or perylene layer over ITO could prevent the diffusion of indium into the polymer. As a result, longer lifespan from solar cells with an inverted architecture was observed, PCE of the inverted solar cells decreased to 70% of the initial value after two-week exposure to air. Later on, better n-type metal oxide layers such as ZnO and TiO_2 were developed to modify the ITO surface and selectively collect electrons in inverted solar cells owing to their high optical transparency in the visible and near IR region, high charge carrier mobility and solution processibility. [114-115]

White et al. demonstrated an efficient inverted solar cell based on a high temperature processed sol-gel ZnO on top of ITO and an Ag electrode as the top contact.[115] The ZnO sol-gel was annealed in air at 300 ºC for 5 minutes to crystallize the ZnO and increase its electron mobility. As a result, 2.97% PCE was achieved. It was reported that devices stored under nitrogen with periodic exposure to air maintained efficiency 2.32% after seven-day storage. Yang et al. found a nano-ridge structure of ZnO prepared from sol-gel method resulted in better device performance than a planar ZnO structure. [116] A planar ZnO underlayer film is usually prepared by directly annealing ZnO gel at 275 ºC for 5 minutes, the nano-ridge film can be prepared by annealing ZnO gel with a temperature rising ramp from room temperature to 275 ºC at a ramping rate 50 ºC/min. The nano-ridge ZnO plays similar role as a nanorod-like ZnO, creating a much larger interfacial area for charge separation compared to a planar ZnO. As a consequence, the PCE of the inverted solar cell was increased from 3.2% to 4.0%.

On the other hand, p-type transition metal oxides were also developed to selectively collect holes from the active layer and prevent the diffusion of top contact metal atoms towards polymers. NiO, V_2O_5 and MoO_3 are reported to be good HTL materials modifying the interface

between an active layer and a top metal electrode.[117,118,119] An inverted solar cell with 2.57% efficiency was demonstrated using vacuum deposited MoO_3/Ag as the top metal anode and high temperature annealed TiO_2 on the ITO as the cathode.[120] Inverted cells with efficiency of 3.55 % were achieved by using MoO_3 as the top buffer layer and Ca as the electron collecting layer over ITO.[121] Semi-transparent inverted cells were demonstrated by using MoO_3/sputtered ITO as the top electrode, the MoO_3 buffer layer can prevent damage to the active layer during the sputtering process of ITO coating, leading to 1.9% efficiency. [122]

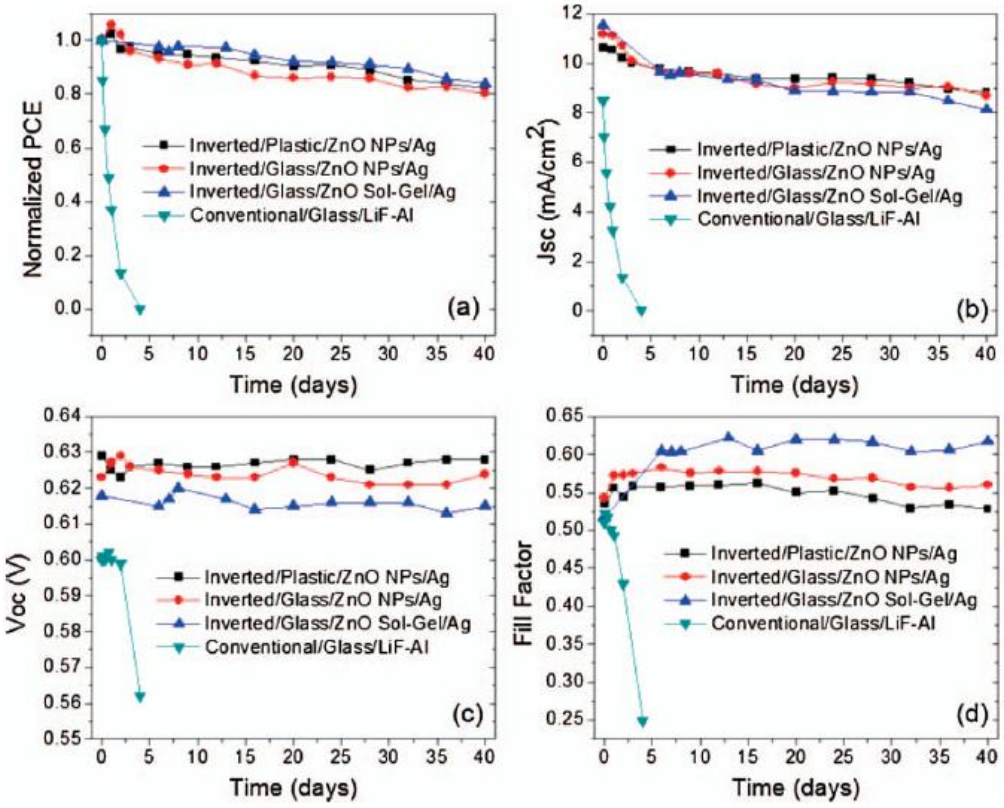

Figure 1.35 Device performance of un-encapsulated conventional and inverted solar cells stored 40 days in air under ambient conditions. (a) Normalized PCE, (b) J_{SC}, (c) V_{OC}, (d) FF. (Adapted from Ref. 123)

High air-stability is one important merit of an inverted cell over a conventional cell. To quantitatively study the stability of devices under ambient air exposure, unencapsulated inverted solar cells and conventional solar cells were fabricated, periodically tested and stored in air for 40 days by Hau et al. shown in Figure 1.35. The conventional device with LiF/Al as top electrode was extremely unstable in air, its PCE decreased drastically in air, and more than half of the initial PCE got lost after 1 day storage. The device totally degraded after 4-day storage in air. The J-V curves of the conventional solar cell presented in Figure 1.36 (a) show a drastic decrease in photocurrent in the first couple of days, and only negligible photocurrent remained after 4-day exposure. The inverted solar cell, however, shows superior air stability. The V_{OC} and FF almost remained constant over the period of 40-day exposure, whereas the J_{SC} decreased gradually leading to 20% PCE loss after 40 days.

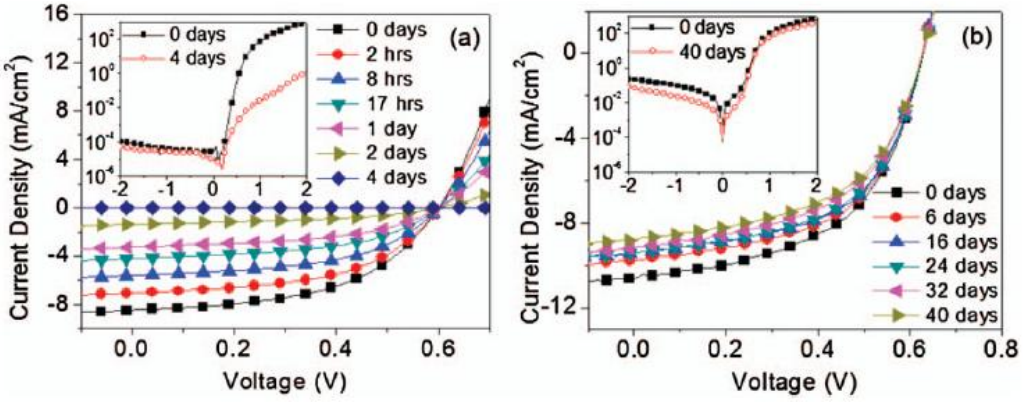

Figure 1.36 (a) J-V curves of un-encapsulated conventional BHJ solar cell over a period of 4 days in air. (b) J-V curves of un-encapsulated inverted BHJ solar cell over a period of 40 days in air. (Adapted from Ref. 123)

Improvement in device air-stability is attributed to both the PEDOT:PSS layer and the silver electrode. The PEDOT:PSS can effectively retard oxygen diffusion towards the active layer. In addition, the silver electrode can form a layer of silver oxide in air thereby increasing its effective work function to 5.0 eV, which results in good match with the PEDOT: PSS work

function 5.2 eV and increases electrical potential coherence at the interface. [124] Provided a solar cell is of good air stability, the encapsulation process can be performed under ambient conditions, which substantially reduces the fabrication complexity.

1.4.5 Tandem Solar Cell

Another way to increase OSCs efficiency is using a tandem cell architecture, which has a multilayer structure equivalent to two solar cells in series. A tandem solar cell offers a number of advantages. Firstly, two subcells are in series connection, the V_{OC} of a tandem cell in principle equals to the sum of two subcells' V_{OC}. Secondly, the active layers of the two subcells could have different bandgaps thus covering a broader spectral range. Moreover, since the mobility of charge carriers in organic materials is low, the increase in active layer thickness causes the increase of series resistance of the device, reducing both the V_{OC} and FF. A tandem solar cell can have thicker active layer in total but does not lead to increase of series resistance. Therefore, the tandem cell architecture can increase light harvesting for OSCs.

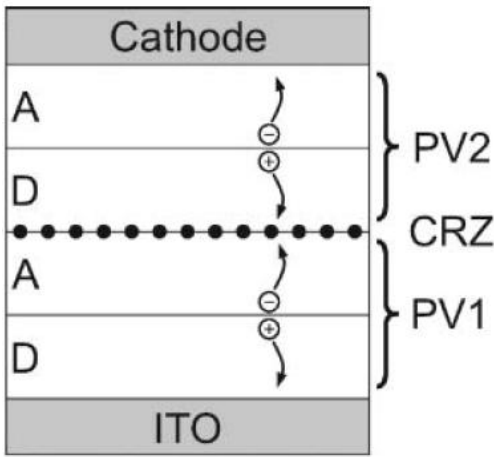

Figure 1.37 Schematic diagram of a tandem OSC. D is the donor and A acceptor, the interface between PV cell 1 and PV cell 2 is labeled as charge recombination zone (CRZ). (Adapted from Ref. 125)

Hiramoto et al. first developed a tandem solar cell in 1990;[126] the concept of a tandem structure in OSCs was implemented from the inorganic tandem solar cells. Figure 1.37 shows a tandem solar cell prototype consisting of two individual DA junctions with a charge recombination zone. The PV1 front cell normally has a wide bandgap donor material and PV2 back cell has a narrow bandgap donor material, PV1 and PV2 are separated by a charge recombination zone. Light absorption in two subcells generates excitons in PV1 and PV2, the excitons dissociate at the DA interface in each subcell. The holes in PV1 and the electrons in PV2 are collected at the adjacent electrodes. To avoid built-up charge within the cells, the electrons in PV1 and the holes in PV2 diffuse to the charge recombination zone where they meet and recombine.

The main challenge to realize tandem cells is balancing the photocurrent from each subcell as the current in a series-connected device is limited by the subcell current whichever is smaller (assume the subcells are ideal solar cells with infinite shunt resistances). This can be accomplished by varying the active layer thickness or selecting proper group of active layer materials. Forest et al. reported a tandem solar cell consisting of multiple CuPc/ PTCBI DA junctions separated by a thin silver film as the charge recombination zone (CRZ).[127] Here silver and gold nanoclusters are commonly used CRZ materials. As a result, the PCE of the tandem solar cell was 2.5% which was even more than the double of a single subcell PCE 1.1%. It was considered that the optical field enhancement due to surface plasmon of metal clusters in the CRZ was responsible for the extraordinary high efficiency.

Another alternative way to design tandem solar cell is using p-i-n architecture as shown in Figure 1.38. The active layer is sandwiched between p- and n-type charge transport layers, which are normally wide bandgap materials and do not absorb the visible light. The i layer, which is the active layer, generates the photocurrent. Leo et al. reported a p-i-n structure tandem solar with 3.8% PCE, whereas the single cell PCE was around 2.1%. In fact, it is universal to observe

that the PCE of a tandem cell is less than the double of the single subcell PCE. Normally the V_{OC} could be readily doubled by a tandem cell structure; however, the J_{SC} of a tandem cell is lower than that of the single subcell cell. Because two subcells have identical absorption, the back subcell would absorb fewer incident photons after the light passes through the front subcell. Therefore the back cell should be the limiting cell causing a lower J_{SC} in the tandem cell.

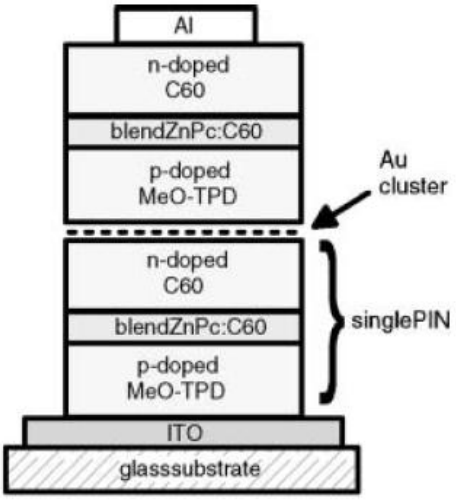

Figure 1.38 Concept of a stacked p-i-n organic solar cell with active layers sandwiched between p-and n-type wide bandgap charge transport layers. (Adapted from Ref. 128)

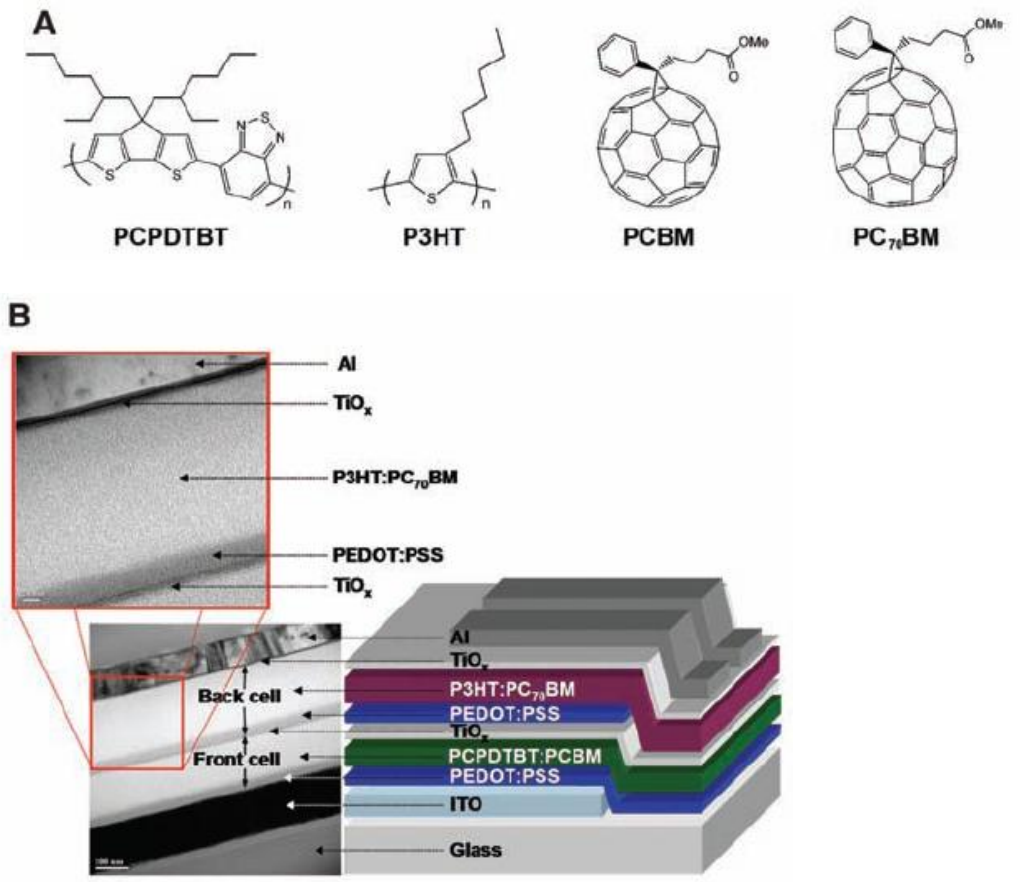

Figure 1.39 (a) molecular structure of active layer materials. (b) schematic diagram of polymer tandem solar cell with TEM cross-section image of the cell. (Adapted from Ref. 129)

So far tandem solar cells have been investigated with diverse structures such as small-molecule BHJ, polymer BHJ, and hybrid structure in which a conjugated polymer subcell and a small molecule subcell are used. Heeger et al. reported an all-solution processing tandem polymer solar cell exceeding 6% PCE.[129] Figure 1.39 shows the tandem solar cell structure, in which TiO_x fabricated in a sol-gel method with low temperature annealing (80° C) reduces the complexity of device processing, since normally a semi-transparent CRZ intermediate layer is evaporated by vacuum thermal deposition. Here TiO_x is considered with a few separate functions. Firstly, the TiO_x layer separates the PEDOT:PSS from the PCPDTBT: PCBM active layer.

Secondly, the TiO_x collects the electrons from the bottom cell. Thirdly, the TiO_x functions as a hole blocking layer. Finally, the TiO_x on the top of the P3HT: PCBM layer separates the Al electrode from the active layer preventing the diffusion of metal atoms towards the polymer. Moreover it also functions as an optical spacer to redistribute the light field and optimize the efficiency of the top cell. [130]

The fabricated conjugated polymer tandem solar cells by Heeger et al. exhibit superior cell characteristics shown in Figure 1.40. The PCPDTBT: PCBM single cell yields J_{SC}=9.2 mA/cm^2, V_{OC}=0.66 V, FF=0.50, and PCE=3.0%; and the P3HT: PCBM single cell yields J_{SC}=10.8 mA/cm^2, and V_{OC}=0.63 V, FF=0.69, and PCE=4.7%. When they are connected in series, the tandem cell shows J_{SC}=7.8 mA/cm2, V_{OC}=1.24 V, FF=0.67 and PCE=6.5%. Although the J_{SC} of the tandem cells is lower than that of any single subcell, the tandem cells still maintain excellent fill factor and high PCE. All in all, a tandem architecture could be an effective approach to increase solar cell efficiency.

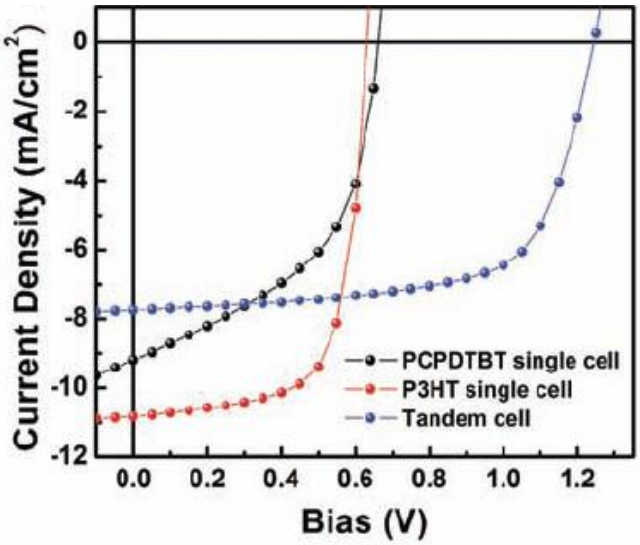

Figure 1.40 J-V characteristics of single cells and tandem cell with PCPDTBT: PCBM and P3HT: PCBM composites under AM 1.5 illumination. (Adapted from Ref. 129)

1.5 Research Motivation and Outline

With a clear picture of the surface plasmon properties and background knowledge of organic optoelectronic devices including OLEDs and OSCs, I started my PhD program research projects with fundamental studies on surface plasmon enhanced fluorescence, in which we explored the methods for metal NPs synthesis; investigated the fluorescence variation with distance between a chromophore and metal NPs as well as fluorescence decay lifetime. The details of experimental works on MEF will be discussed in Chapter 2.

After we gained a comprehensive understanding of metal NPs surface plasmon and metal enhanced photoluminescence phenomenon, we extended our research focus from metal-enhanced photoluminescence scope to electroluminescence, which was a proposed but was not a well-studied field with great prospect. Here we developed various methods to incorporate metal NPs into diverse OLEDs, including SM-OLEDs, PHOLEDs, and hybrid OLEDs. An encouraging metal enhanced EL was not observed until good understanding of OLEDs device physics and proper integration of surface plasmon into OLEDs were realized. The surface plasmon of metal NPs is discovered to promote charge carrier injection, favor exciton formation and facilitate the exciplex formation at the interface on the positive side; it also induces unwanted light extinction and luminescence quenching on the other hand. Study of surface plasmons in OLEDs provides valuable insight on surface plasmon properties. Details on metal NPs applications in OLEDs will be discussed in Chapter 3.

Optoelectronic devices OLEDs and solar cells have a great similarity in nature, indeed they work in a reversed electron-to-photon / photon-to-electron process. With accumulated knowledge on surface plasmon enhanced OLEDs luminescence, we set our feet into the organic solar cell field, which has been a hot research topic since 2000. Various strategies were employed in optimization of OSCs towards higher device efficiency including material innovation,

processing technique improvement, device structural reform and so on. Here we broke a new path to optimize OSCs via the surface plasmon of metal NPs. We incorporated metal NPs into OSCs mainly through vacuum thermal deposition method, and investigated the coexisting optical and electrical functions of metal NPs in OSCs including polymer solar cells and hybrid tandem solar cells. The new insight of surface plasmon in OSCs provides explicit guideline for OSCs optimization. Details of surface plasmon in organic solar cells will be discussed in Chapter 4.

However, we still have many promising proposals unfinished, particularly in OSC scope due to limited PhD program time span. Therefore we will list some feasible proposals in the last Chapter to evoke the attention of readers.

References

[1] Ritchie, R. H. Phys. Rev. **1957**, 106, 874.

[2] a) Baik, J. M.; Lee, S. J.; Moskovits, M. Nano Lett **2009**, 9, 672. b) Cle, C.; Gunning, A. P.; Syson, K.; Bowater, L.; Field, R. A.; Bornemann, S. J. Am. Chem. Soc. **2008**, 130, 15234.

[3] Eustis. S.; El-Sayed, M. A. Chem. Soc. Rev. **2006**, 35, 209.

[4] a) Kreibig. U., Vollmer, M. Optical Properties of Metal Clusters. Springer, Berlin **1995**. b) Murray, W. A.; Barnes, W. L. Adv. Mater. **2007**, 19, 3771.

[5] Bohren, C. F.; Huffman, D. R. Absorption and Scattering of Light by Small Particles, Wiley, New York 1983.

[6] Hu, M.; Chen, J.; Li, Z. Y.; Au, L.; Hartland, G. V.; Li, X.; Marquez, M.; Xia, Y. Chem. Soc. Rev. **2006**, 35, 1084.

[7] Faraday, M. Philos. Trans. R. Soc. London, **1857**, 147, 145.

[8] Mie, G. Ann. Phys. **1908**, 25, 377.

[9] Gans, R. Ann. Phys. **1912**, 37, 881.

[10] Kelly, K. L.; Coronado, E.; Zhao, L. L.; Schatz, G. C. J. Phys. Chem. B **2003**, 107, 668.

[11] Link, S.; El-Sayed, M. A.; Int. Rev. Phys. Chem. **2000**, 19, 409.

[12] Turkevich, J. Colloidal gold. Gold Bull. (Geneva) **1985**, 18, 86.

[13] Mulvaney, P. Langmuir **1996**, 12, 788.

[14] Papavassiliou, G. C. Prog. Solid St. Chem. **1980**, 12, 185.

[15] a)Lamprecht, B.; Leitner, A., Aussenegg, F. R. Appl. Phys. B **1997**, 64, 269.b) Lamprechet, B.; Krenn, J. R.; Leitner, A.; Aussenegg, F. R. Appl. Phys. B **1999**, 69, 223.

[16] Link, S.; El-Sayed, M. A. J. Phys. Chem. B **1999**, 103, 4212.

[17] Yu, Y.; Chang, S.; Lee, C., Wang, C. R. C. J. Phys. Chem. B **1997**, 101, 6661.

[18] a) Chen, W.; Cai, W.; Zhang, L. J. Colloid Interface Sci. **2001**, 238, 291. b) Pan, S. L.; Chen, M.; Li, H. L. Colloids Surf. A **2001**, 180, 55.

[19] a) Jana, N. R.; Gearheart, L.; Murphy, C. J. J. Phys. Chem. **2001**, 105, 4065. b) Nikoobakht, B.; El-Sayed, M. A. Chem. Mater. **2003**, 15, 1957.

[20] Jana, N. R.; Gearheart, L.; Murphy, C. J. Adv. Mater. **2001**, 13, 1389.

[21] Fleischman, M.; Hendra, P. J.; McQuillan, A. J. Chem. Phys. Lett. **1974**, 26, 163.

[22] Jeanmaire, D. L.; Duyne, R. P. V. J. Electroanal. Chem. **1977**, 84, 1.

[23] Albrecht, M. G.; Creighton, J. A. J. Am. Chem. Soc. **1977**, 99, 5215.

[24] Moskovits, M. J. Chem. Phys. **1978**, 69, 1459.

[25] Persson, B. N. J. Chem. Phys. Lett. **1981**, 82, 561.

[26] Kneipp, K.; Kneipp, H.; Kneipp, J. Acc. Chem. Res. **2006**, 39, 443.

[27] Kneipp, K.; Kneipp, H; Itzkan, I.; Dasari, R. R.; Feld, M. S. Chem. Rev. **1999**, 99, 2957.

[28] a) Hildebrandt, P.; Stockburger, M. J. Phys. Chem. **1984**, 88, 5935. b) Pettinger, B.; Krischer, K. J. Electron Spectrosc. Relat. Phenom. **1987**, 45, 133. c) Kneipp, K. Exp. Tech. Phys. **1988**, 36, 161.

[29] Salamon, Z.; Macleod, H. A.; Tollin, G. Biochimica et Biophysica Acta **1997**, 1331, 131.

[30] a) Soulages, J. L.; Salamon, Z.; Wells, M.; Tollin, G. Natl. Acad. Sci. USA **1995**, 92, 5650. b) Salamon, Z.; Wang, Y.; Soulages, J. L.; Brown, M. F.; Tollin, G. Biophys. J. **1996**, 71, 283. c) Salamon, Z.; Tollin, G. Biophys. J. **1996**, 71, 848. d) Salamon, Z.; Tollin, G. Biophys. J. **1996**, 71, 858.

[31] Salamon, Z.; Macleod, H. A.; Tollin, G. Biochimica et Biophysica Acta **1997**, 1331, 117.

[32] Drexhage, K. H. Proc. Int. Conf. Lumin. **1970**, 693.

[33] Glass, A. M.; Liao, P. F.; Bergman, J. G. Opt. Lett. **1980**, 5, 368.

[34] Lakowicz, J. R.; Shen, Y.; Auria, S. D.; Malicka, J.; Fang, J.; Gryczynski, Z.; Gryczynski, I. Anal. Biochem.**2002**, 301, 261.

[35] Biteen, J. S.; Pacifici, D.; Lewis, N. S.; Atwater, H. A. Nano Lett. **2005**, 5, 1768.

[36] Futamata, M.; Maruyama, Y.; Ishikawa, M. J. Phys. Chem. B **2003**, 107, 7607.

[37] Rand, B. P.; Peumans, P.; Forrest, S. R. J. Appl. Phys. **2004**, 96, 7519.

[38] Hang, W.; Qian, W.; El-Sayed,M. A. Proc. SPIE Int. Soc. Opt. Eng. **2005**, 5927, 592701.

[39] Lakowicz, J. R. Principles of Fluorescence Spectroscopy. 3rd edition, Springer Science, New York.

[40] Lakowicz, J. R. Anal. Biochem.**2005**, 337, 171.

[41] Jennings, T. L.; Singh, M. P. Strouse, G. F. J. Am. Chem. Soc. **2006**, 128, 5462.

[42] Ray, K.; Badugu, R.; Lakowicz, J. R. Langmuir, **2006**, 22, 8374.

[43] Sokolov, K.; Chumanov, G.; Cotton, T. M. Anal. Chem. **1998**, 70, 3898.

[44] Cooper, M. Nature Rev. **2002**, 1, 515.

[45] Ray, K.; Badugu, R.; Lakowicz, J. R. Langmuir **2006**, 22, 8374.

[46] Bakker, R. M.; Yuan, H.; Liu, Z.; Drachev, V. P.; Kildishev, A. V.; Shalaev, V. M.; Pederen, R. H.; Gresillon, S.; Boltasseva, A. Appl. Phys. Lett. **2008**, 92, 043101.

[47] Falicia, T.; Glenn, P. G.; Bruce, R. J.; Naomi, J. H. Nano Lett. **2007**, 7, 496.

[48] Chen, Y.; Munechika, K.; Ginger, D. S. Nano Lett. **2007**, 7, 690.

[49] Kuhn, S.; Hakanson, U.; Rogobete, L.; Sandoghdar, V. Phys. Rev. Lett. **2006**, 97, 017402.

[50] Ray, K.; Chowdhury, M. H.; Lakowicz, J. R. Anal. Chem. **2007**, 79, 6480.

[51] Aslan, K.; Previte, M. J.; Zhang, Y.; Geddes, C. D. J. Phys. Chem. C **2008**, 112, 18368.

[52] Noguez, C. J. Phys. Chem. C **2007**, 111, 3806.

[53] Aslan, K.; Leonenko, Z.; Lakowicz, J. R.; Geddes, C. D. J. Phys. Chem. B **2005**, 109, 3157.

[54] Corrigan, T. D.; Guo, S.; Phaneuf, R. J. Szmacinski, H. J. Fluoresc. **2005**, 15, 777.

[55] Borchardt, J. K. Mater. Today **2004**, 7, 42.

[56] Gustafsson, G.; Cao, Y.; Treacy, G. M.; Klavetter, F.; Colaneri, N.; Heeger, A. J. Nature, **1992**, 357, 477.

[57] Pope, M.; Kallmann, H. P.; Magnate, P. J. Chem. Phys. **1963**, 38, 2042.

[58] Tang, C. W.; VanSlyke, S. A. Appl. Phys. Lett. **1987**, 51, 913.

[59] Burroughes, J. H.; Bradley, D. D. C.; Brown, A. R.; Marks, R. N.; Mackay, K.; Friend, R. H.; Burns, P. L.; Holmes, A. B. Nature, **1990**, 347, 539.

[60] Yersin, H. Top Curr. Chem. **2004**, 241, 1.

[61] Salehi, A. Thin Solid Films **1998**, 324, 214.

[62] (a) Ichihara, K.; Inoue, N.; Okubo, M. Thin Solid Films **1994**, 245, 152. (b) Davis, L. Thin Solid Films **1993**, 236, 1. (c) Lee, W. K.; Machino, T.; Sugihara, T. Thin Solid Films **1993**, 224, 105.

[63] Brömas, P.; Birgersson, J.; Johansson, N.; Lögdlund, M.; Salaneck, W. R. Synth. Met. **1995**, 74, 179.

[64] Meyer, J.; Schneidenbach, D.; Winkler, T.; Hamwi, S.; Weimann, T.; Hinze, P.; Ammermann, S.; Johannes, H. H.; Riedl, T.; Kowalsky, W. Appl. Phys. Lett. **2009**, 94, 233305.

[65] Adachi, C.; Tsutsui, T.; Saito, S. Appl. Phys. Lett. **1989**, 55, 1489.

[66] Stolka, M.; Yanus, J. F.; Pai, D. M. J. Phys. Chem. **1984**, 88, 4707.

[67] Van Slyke, S. A.; Chen, C. H.; Tang, C. W. Appl. Phys. Lett. **1996**, 69, 2160.

[68] O'Brien, D.; Bleyer, A.; Lidzey, D. G. Bradley, D. D. C. J. Appl. Phys. **1997**, 82, 2662.

[69] Gao, Z.; Lee, C. S.; Bello, I.; Lee, S. T.; Chen, R. M.; Luh, T. Y.; Shi, J.; Tang, C. W. Appl. Phys. Lett. **1999**, 74, 865.

[70] Xu, D.; Li, X.; Wang, X.; Zhao, C.; Zhao, J.; Deng, Z.; Lu, Z.; Chen, Z. Spectrosc. Spect. Anal. **2011**, 31, 340.

[71] Colle, M.; Tsutsui, T. Synth. Met. **2000**, 111, 95.

[72] Baek, H. I.; Lee, C. H. J. Phys. D **2008**, 41, 105101.

[73] Yang, J. M.; Tsutsui, T. Jpn. J. Appl. Phys. Part 2-Lett. **2000**, 39, L828.

[74] Gill, W. D.; Kanazawa, K. K. J. Appl. Phys. **1972**, 43, 529.

[75] Lamansky, S.; Djurovich, P. I.; Abdel-Razzaq, F.; Garon, S.; Murphy, D. L.; Thompson, M. E. J. Appl. Phys. **2002**, 92, 1570.

[76] Vaeth, K. M.; Tang, C. W. J. Appl. Phys. **2002**, 92, 3447.

[77] Gong, X.; Robinson, M. R.; Ostrowski, J. C.; Moses, D.; Bazan, G. C.; Heeger, A. J. Adv. Mater. **2002**, 14, 581.

[78] Yang, X.H.; Mo, Y. Q.; Yang, W.; Yu, G.; Cao, Y. Appl. Phys. Lett. **2001**, 79, 563.

[79] Yang, X. H.; Neher, D.; Hertel, D.; Daubler, T. K. Adv. Mater. **2004**, 16, 161.

[80] Yang, X. H.; Neher, D. Appl. Phys. Lett. **2004**, 84, 2476.

[81] Kim, J. S.; Ho, P. K. H.; Greenham, N. C.; Friend, R. H. J. Appl. Phys. **2000**, 88, 1073.

[82] Rocha, L.; Dumarcher, V.; Malcor, E.; Fiorini, C.; Denis, C.; Raimond, P.; Geffroy, B.; Nunzi, J.-M. Synth. Met. **2002**, 127, 75.

[83] Fiorini, C.; Prudhomme, N.; de Veyrac, G.; Maurin, I.; Raimond, P.; Nunzi, J.-M. Synth. Met. **2000**, 115, 121.

[84] Chapin, D. M.; Fuller, C. S.; Pearson, G. L. J. Appl. Phys. **1954**, 25, 676.

[85] Shaheen, S.E.; Brabec, C. J.; Sariciftci, N. S.; Padinger, F.; Fromherz, T.; Hummelen, J. C. Appl. Phys. Lett. **2001**, 78, 841.

[86] Hoppe, H.; Sariciftci, N. S. J. Mater. Res. **2004**, 19, 1924.

[87] Sze, S. M. Physics of Semiconductor Devices, John Wiley & Sons, New York, **1981**.

[88] Moliton, A.; Nunzi, J-M. Polym. Int. **2006**, 55, 583.

[89] (a)Theander, M.; Yartsev, A.; Zigmantas, D.; Sundstrom, V.; Mammo, W.; Andersson, M. R.; Inganas, O. Phys. Rev. B **2000**, 61, 12957. (b) Haugeneder, A.; Neges, M.; Kallinger, C.; Spirkl, W.; Lemmer, U.; Feldmann, J.; Scherf, U.; Harth, E.; Gugel, A.; Mullen, K. Phys. Rev. B **1999**, 59, 15346. (c) Stubinger, T.; Brutting, W. J. Appl. Phys. **2001**, 90, 3632. (d) Savenije, T. J.; Warman, J. M.; Goossens, A. Chem. Phys. Lett. **1998**, 287, 148. (e) Schlebusch, C.; Kessler, B.; Cramn, S.; Eberhardt, W. Synth. Met. **1996**, 77, 151.

[90] Tang, C. W. Appl. Phys. Lett. **1986**, 48, 183.

[91] Nogueira, A. F.; Montari, I.; Nelson, J.; Durrant, J. R.; Winder, C.; Sariciftci, N. S.; Brabec, C. J. Phys. Chem. B **2003**, 107, 1567.

[92] Rostalski, J.; Meissner, D. Sol. Energ. Mat. Sol. C. **2000**, 63, 37.

[93] (a) Halls, J. J. M.; Pichler, K.; Friend, R. H.; Moratti, S. C.; Holmes, A. B. Appl. Phys. Lett. **1996**, 68, 3120. (b) Halls, J. J. M.; Friend, R. H. Synth. Met. **1997**, 85, 1307.

[94] (a) Peumans, P.; Forrest, S. R. Appl. Phys. Lett. **2001**, 79, 126. (b) Xue, J.; Uchida, S.; Rand, B. P.; Forrest, S. R. Appl. Phys. Lett. **2004**, 84, 3013.

[95] Rand, B. P.; Genoe, J.; Heremans, P.; Poortmans, J. Prog. Photovolt: Res. Appl. **2007**, 15, 659.

[96] Hiramoto, M.; Yamaga, T.; Danno, M.; Suemori, K.; Matsumura, Y.; Yokoyama, M. Appl. Phys. Lett. **2006**, 88, 213105.

[97] Uchida, S.; Xue, J.; Rand, B. P.; Forrest, S. R. Appl. Phys. Lett. **2004**, 84, 4218.

[98] Sekine, N.; Chou, C. H.; Kwan, W. L.; Yang, Y. Org. Electron. **2009**, 10, 1473.

[99] Coakley, K. M.; McGehee, M. D. Chem. Mater. **2004**, 16, 4533.

[100] Yu, G.; Heeger, A. J. J. Appl. Phys. **1995**, 78, 4510.

[101] Hall, J. J. M.; Walsh, C. A.; Greenham, N. C.; Marseglia, E. A.; Friend, R. H.; Moratti, S. C.; Holmes, A. B. Nature **1995**, 376, 498.

[102] Granstrom, M.; Petritsch, K.; Arias, A. C.; Lux, A.; Andersson, M. R.; Friend, R. H. Nature **1998**, 395, 257.

[103] Yu, G.; Gao, J.; Hummelen, J. C.; Wudl, F.; Heeger, A. J. Science **1995**, 270, 1789.

[104] Shaheen, S. E.; Brabec, C. J.; Sariciftci, N. S.; Padinger, F.; Fromherz, T.; Hummelen, J. C. Appl. Phys. Lett. **2001**, 78, 841.

[105] Padinger, F.; Rittberger, R. S.; Sariciftci, N. S. Adv. Funct. Mater. **2003**, 13, 85.

[106] Ma, W.; Yang, C.; Gong, X.; Lee, K.; Heeger, A. J. Adv. Funct. Mater. **2005**, 15, 1617.

[107] Li, G.; Yao, Y.; Yang, H.; Shrotriya, V.; Yang, G.; Yang, Y. Adv. Funct. Mater. 2007, 17, 1636.

[108] Kooistra, F. B.; Knol, J.; Kastenberg, F.; Popescu, L. M.; Verhees, W. J. H.; Kroon, J. M. Org. Lett. **2007**, 9, 551.

[109] Brabec, C. J.; Cravino, A.; Meissner, D.; Sariciftci, N. S.; Fromherz, T.; Rispens, M. T.; Sanchez, L.; Hummelen, J. C. Adv. Funct. Mater. **2001**, 11, 374.

[110] Kroon, R.; Lenes, M.; Hummelen, J. C.; Blom, P. W. M.; De Boer, B. Polym Rev. 2008, 48, 531.

[111] Hau, S. K.; Yip, H.-L.; Jen, A. K. Y. Polym Rev. **2010**, 50, 474.

[112] de Jong, M. P.; van IJzendoorn, L. J.; de Voigt, M. J. A. Appl. Phys. Lett. **2000**, 77, 2255.

[113] Sahin, Y.; Alem, S.; de Bettignies, R.; Nunzi, J. M. Thin Solid Films **2005**, 476, 340.

[114] Waldauf, C.; Morana, M.; Denk, P.; Schilinsky, P.; Coakley, K.; Choulis, S.A. Appl. Phys. Lett. **2006**, 89, 233517.

[115] White, M. S.; Olson, D. C.; Shaheen, S. E.; Kopidakis, N.; Ginley, D. S. Appl. Phys. Lett. **2006**, 89, 143517.

[116] Sekine, N.; Chou, C. H.; Kwan, W. L.; Yang, Y. Org. Electron. **2009**, 10, 1473.

[117] Irwin, M. D.; Buchholz, B.; Hains, A. W.; Chang, R. P. H.; Mark, T. J. Proc. Natl. Acad. Sci. USA **2008**, 105, 2783.

[118] Liao, H. H.; Chen, L. M.; Xu, Z.; Li, G.; Yang, Y. Appl. Phys. Lett. **2008**, 92, 173303.

[119] Sun, X. W.; Zhao, D. W.; Ke, L.; Kyaw, A. K. K.; Lo, G. Q.; Kwong, D. L. Appl. Phys. Lett. **2010**, 97, 053303.

[120] Tao, C.; Ruan, S. P.; Zhang, X. D.; Xie, G. H.; Shen, L.; Kong, X. Z.; Dong, W.; Liu, C. X.; Chen, W. Y. Appl. Phys. Lett. **2008**, 93, 193307.

[121] Zhao, D. W.; Liu. P.; Sun, X. W.; Tan, S. T.; Ke, L.; Kyaw, A. K. K. Appl. Phys. Lett. **2009**, 95, 153304.

[122] Schmidt, H.; Flugge, H.; Winkler, T.; Bulow, T.; Riedl, T.; Kowalsky, W. Appl. Phys.Lett. **2009**, 94, 243302.

[123] Hau, S. K.; Yip, H. L.; Bake, N. S.; Zou, J.; O'Malley, K.; Jen, A. K. Y. Appl. Phys. Lett. **2008**, 92, 253301.

[124] Kim, J. B.; Kim, C. S.; Kim, Y. S.; Loo, Y. L. Appl. Phys. Lett. **2009**, 95, 183301.

[125] Xue, J.; Uchida, S.; Rand, B. P.; Forrest, S. R. Appl. Phys. Lett. **2004**, 85, 5757

[126] Hiramoto, M.; Suezaki, M.; Yokoyama, M. Chem. Lett. **1990**, 3, 327.

[127] Yakimov, A.; Forrest, S. R. Appl. Phys. Lett. **2002**, 80, 1667.

[128] Drechsel, J.; Maennig, B.; Kozlowski, F.; Pfeiffer, M.; Leo, K.; Hoppe, H. Appl. Phys. Lett. **2005**, 86, 244102.

[129] Kim, J. Y.; Lee, K.; Coates, N. E.; Moses, D.; Nguyen, T. Q.; Dante, M.; Heeger, A. J. Science **2007**, 317, 222.

[130] Kim, J. Y.; Kim, S. H.; Lee, H. H.; Lee, K.; Ma, W.; Gong, X.; Heeger, A. J. Adv. Mater. **2006**, 18, 572.

Chapter 2

Surface Plasmon Enhanced Luminescence

We will focus on the application of surface plasmon in photoluminescence in this chapter. The role of the surface plasmon in metal NPs-dye interaction will be discussed, the importance of an optical spacer will be addressed, and the potential application of metal NPs surface plasmon in optical microscopy will be referred.

2.1 Silver Enhanced $Eu(fod)_3$ Luminescence

2.1.1 Background

As we mentioned in the first chapter about metal enhanced luminescence, it is well understood that metals readily quench the luminescence of chromophores in their near vicinity. [1] Therefore, an optical spacer is required to reduce the quenching effect and eventually increase the luminescence intensity, and great attention has been devoted to protein or DNA layers as spacers for the biology application.[2-3] In this work, silver NPs were chosen as the surface plasmon resonance source, fluorophores were not covalently coupled to the silver NPs by using a polymer thin film as the spacer, which renders the freedom to control the fluorophores-to-metal separation.

On the other hand, although metal enhanced fluorescence phenomenon has been widely studied, little research was dedicated to metal enhanced rare-earth (RE) ion luminescence.[4-5] Investigation of plasmon coupled RE ion luminescence is of great scientific significance for several reasons: RE ions have complex energy levels, which permit tunable emission with narrow band width, thus are good candidates for efficient and stable luminescence. So far, RE

ions have been successfully used as continuous wave laser media and erbium-doped fiber amplifiers (EDFA). [6-7]

In this research, we investigated the plasmon coupled photoluminescence of $Eu(fod)_3$, which was used as light emitting RE material in OLEDs.[8] A PVA film was used as the spacer to separate the silver NPs from the RE complex, the distance dependent enhancement effect was investigated. To our understanding, this method is potentially adoptable by OLEDs fabrication and optimization.

2.1.2 Experimental

All the materials: silver nitrate (99.99%), sodium hydroxide (98%), ammonium hydroxide, D-glucose (99%), poly(methyl methacrylate) (PMMA, $M_w \approx 15000$), polyvinyl alcohol (PVA, M_w=9000-10,000) were purchased from Sigma and used as received without further purification. $Eu(fod)_3$ was purchased from Strem Chemicals.

The silver NPs film, denoted as silver island film (SIF) in this study, was prepared in the way reported by Lakowicz et al. [9] 0.22 g silver nitrate was dissolved in 26 mL distilled water and eight drops of 5% NaOH were added under stirring. The resulting dark-brownish precipitate was dissolved by adding less than 1 mL of ammonium hydroxide. The clear solution was then cooled down in ice bath, followed by soaking the pre-cleaned glass slides in the solution. A fresh solution of D-glucose (0.35 g in 4 mL of water) was then added and stirred for 2 minutes at low temperature and then the mixture was allowed to warm up to room temperature. When the glass slides changed color, they were removed from growth solution and washed out with distilled water. The coated slides were stored in water prior to the experiment. Only half of the glass slides were coated with SIF, the other half being used as reference. PVA aqueous solutions with different concentrations (0%, 0.1%, 0.2%, 0.5% and 1.0% in weight) were spin coated at 1000

rpm speed for 30s, as a spacer on SIF. 1mM $Eu(fod)_3$ was dissolved in a 0.1% (w/w) PMMA toluene solution. The blend was then spin coated onto dried PVA films. Please note here toluene does not dissolve PVA. Although $Eu(fod)_3$ has a quite low QE (ca. 5%),[10] it is suitable for us to study the metal enhanced luminescence phenomenon because the amplification would be remarkable.

The absorption spectra were taken with a Lambda 20 UV-Vis spectrometer (PerkinElmer). Fluorescence in the $^5D_0 \rightarrow ^7F_1$ transition region was measured with the sample geometry shown in Figure 2.1. Sample slides were excited with an incidence angle of 45º at 308 nm using a UV-lamp coupled to a monochromator (SID-101 Photon Technology International). Fluorescence was measured from the SIF side using a USB2000-Ocean Optics spectrometer. For low temperature measurements, the samples were immersed in liquid nitrogen for 30 seconds and quickly transferred to the sample holder. A cold slide may cause the condensation of water from the atmosphere on its surface, resulting in light scattering and thus inaccurate fluorescence absolute value measurement. However, we intend to just compare the fluorescence intensity on glass and SIF substrates, the condensation problem would not affect our relative variation measurement. Atomic force microscope (AFM) images were captured with a Veeco multimode microscope. Luminescence decay lifetime was recorded at room temperature on a Photon Technologies International QuantaMaster Model C-60 spectrometer. Film thickness was measured with a Dektak 8 (Veeco) Stylus Profilometer. Fluorescence emission images were captured with an Axio Observer (Carl Zeiss) microscope.

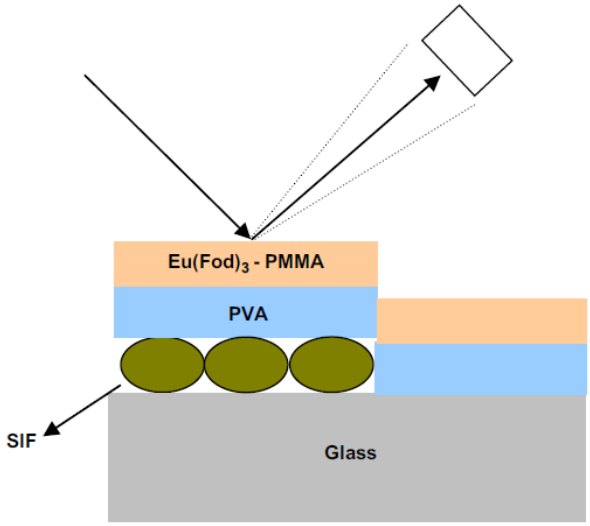

Figure 2.1 Schematic geometry of sample and PL measurement configuration.[11]

2.1.3 Results and discussion

Microstructure of the freshly prepared SIF is characterized by AFM as shown in Figure 2.2. The size of the silver NPs ranges from 50 nm to 100 nm in radius. The extinction spectrum of the SIF is shown in Figure 2.3; the broad absorption peak with maximum at 480 nm is attributed to the plasmon resonance of the silver NPs. With regard to metallic NPs, an extinction spectrum is used thoroughly in this thesis instead of an absorption spectrum because not only absorption but also scattering contributes to the light extinction for metal NPs.

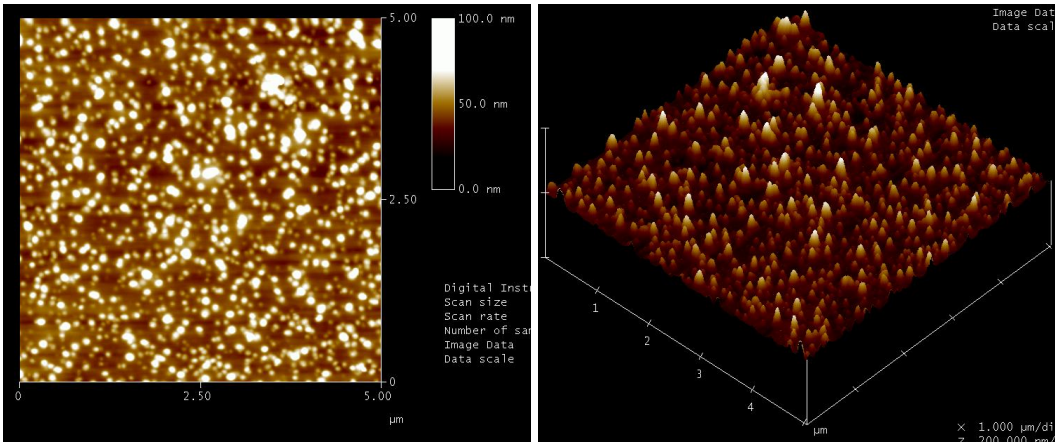

Figure 2.2 Two-dimensional (left) and three-dimensional (right) images of AFM scan of silver island film before PVA coating.

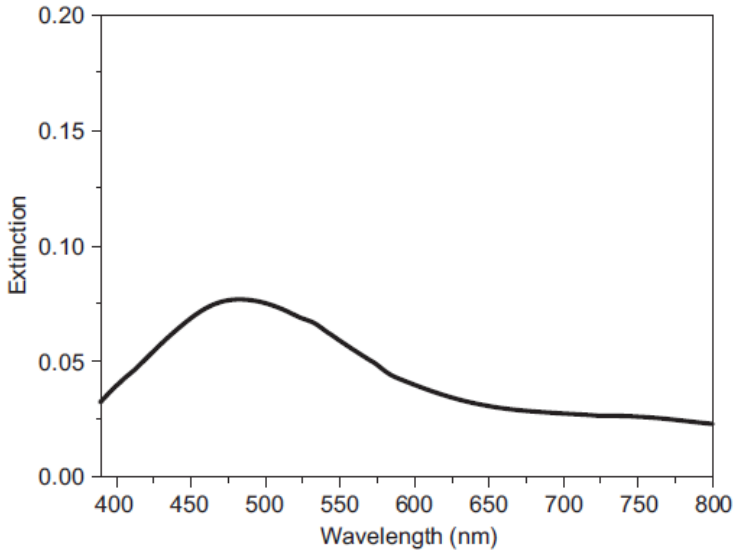

Figure 2.3 Extinction spectrum of the silver island film.[11]

With the film containing $Eu(fod)_3$ coated directly on top of the SIF, the PL almost keeps the same as that from the film spin coated on top of the blank glass slide. We attribute luminescence on top of the SIF to Eu ions that are partly isolated from the metal by the PMMA matrix. As shown in Figure 2.4, Eu/PMMA films on top of the PVA spacer have significant red emission at 610 nm, which is identical to that in toluene solution. We did not notice a significant

PL intensity difference when the $Eu(fod)_3$ complex was previously washed three time by deuterated water, although water is expected to quench Eu(III) luminescence. The sample coated with 0.1% PVA spacer layer exhibits a four-fold fluorescence intensity enhancement. It must result from the metal plasmon-chromophore interaction. Moreover, this result demonstrates that PVA film serves efficiently as spacer between the emission layer and the SIF. We also measured the PL spectrum at liquid nitrogen temperature (insert of Figure 2.4), the fluorescence intensity enhancement factor is further increased to 5-fold, which can be ascribed to reduced non-radiative decay at lower temperature.

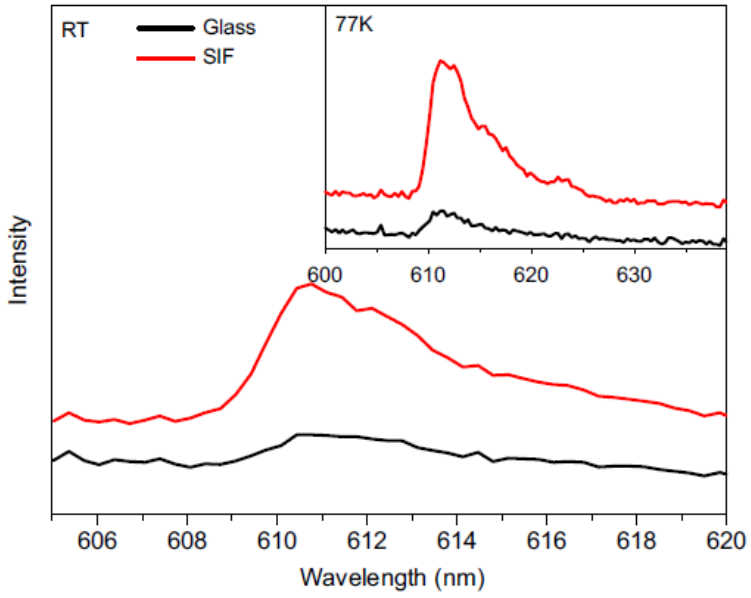

Figure 2.4 The PL of $Eu(fod)_3$ on SIF (red) and glass (black) by applying 0.1% PVA as spacer at room temperature and liquid nitrogen temperature.[11]

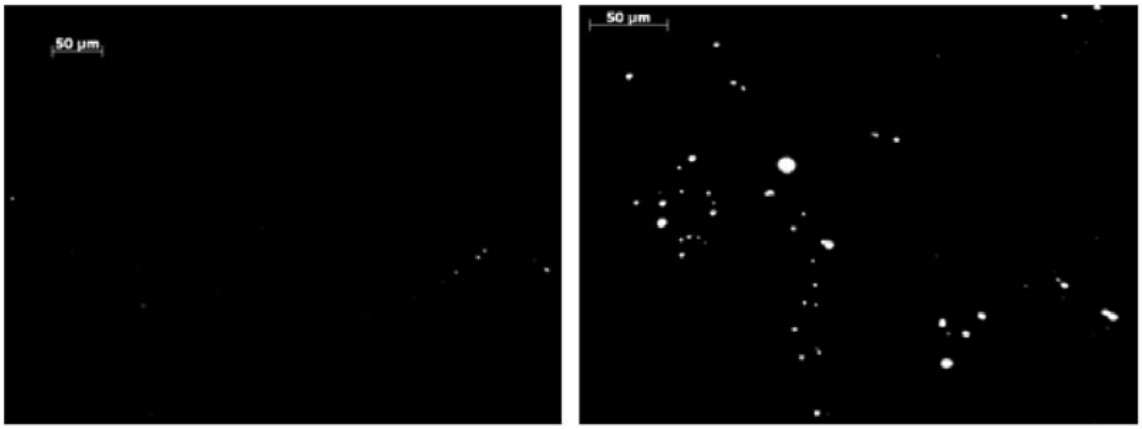

Figure 2.5 Representative fluorescence emission microscopy images of $Eu(fod)_3$ on 0.1% PVA coated glass substrate (left) and SIF (right). [11]

We also studied the fluorescence of $Eu(fod)_3$ under optical microscope, Figure 2.5 shows the fluorescent microscope images of $Eu(fod)_3$ luminescence with 0.1% PVA spacer. The emission spots over the SIF are clearly brighter than that on top of the glass part of the slide, which further confirms the SIF enhanced $Eu(fod)_3$ luminescence phenomenon and suggests the potential application of surface plasmon in microscopic imaging.

The radiative decay rates of the Eu complex on top of the SIF and glass were also investigated respectively. One can derive the quantum efficiency as follows: [12]

$$Q_0 = \frac{\Gamma}{\Gamma + \kappa} = \Gamma \cdot \tau \tag{2.1}$$

where Γ is the radiative decay rate and κ is the sum of all non-radiative decay rates, τ the excited state decay lifetime. Based on equation (2.1), either the decrease of the non-radiative decay rate or the increase of the radiative rate will contribute to an increase in the quantum efficiency. Comparison of the Eu complex radiative decay rate with (Γ_S) and without (Γ_0) SIF is then simplified as follows:

$$\frac{\Gamma_S}{\Gamma_0} = \frac{Q_S}{Q_0} \cdot \frac{\tau_0}{\tau_S} \tag{2.2}$$

Replacing the quantum efficiency ratio by emission intensity ratio measured under the same excitation and absorption conditions on both SIF and glass yields:

$$\frac{\Gamma_S}{\Gamma_0} = \frac{I_S}{I_0} \cdot \frac{\tau_0}{\tau_S} \tag{2.3}$$

Where I_S and I_0 are the PL emission intensity of the Eu complex on SIF and glass respectively, which are estimated from the integral area under the emission spectra profiles. It becomes clear that lifetime is an important parameter to estimate the radiative decay rate variation induced by silver surface plasmon.

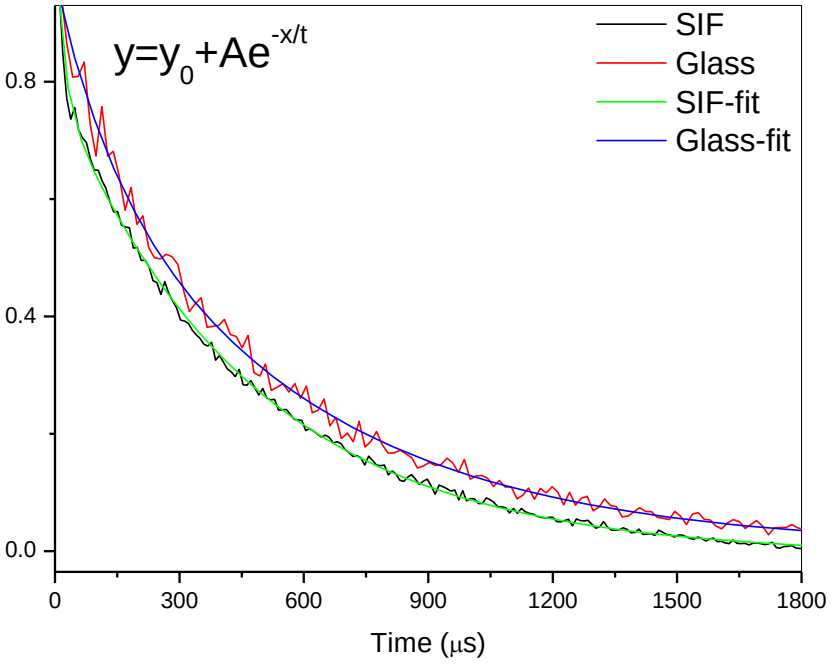

Figure 2.6 Time resolved luminescence decay of the Eu complex with 0.1% PVA on the SIF and glass at room temperature. [11]

Thus we measured the lifetimes of the $Eu(fod)_3$ with 0.1% PVA spacer on both SIF and glass substrate as shown in Figure 2.6. They can be fitted by monoexponential decay yielding mean lifetimes 499 μs on glass and 367 μs on SIF. Replacing the τ_S and τ_0 with the measured lifetime values, we get a five-fold increase of the radiative decay rate of the Eu complex due to

metal enhanced luminescence effect. Moreover, we can calculate the ratio between non-radiative and radiative decay rates of the Eu complex on glass, which yields the radiative rate on glass Γ_0= 1.8× 10^{-4} s^{-1} and on SIF Γ_m= 9×10^{-4} s^{-1}. The moderate enhancement factor compared to other chromophores used as biological labels may be ascribed to the smaller overlapping between $Eu(fod)_3$ emission spectrum and silver plasmon resonance wavelength. [13,14,15,16]

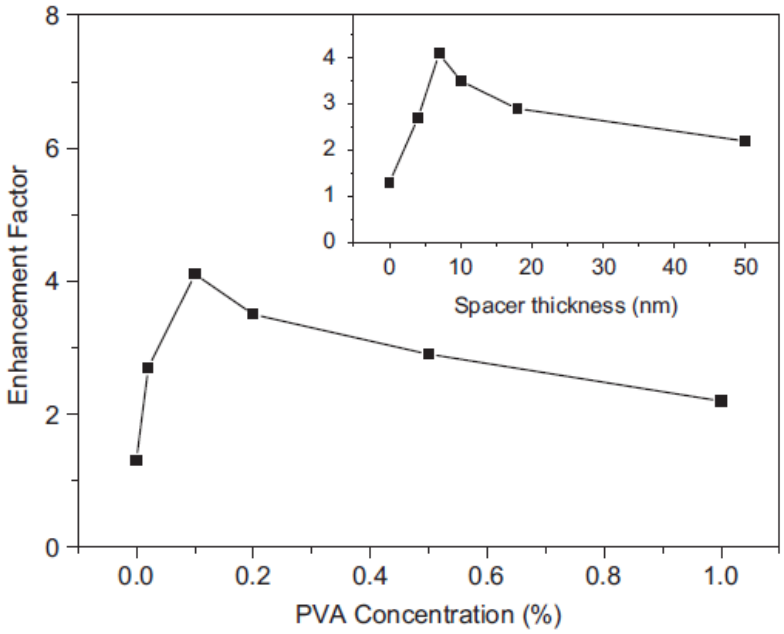

Figure 2.7 Enhancement factor Vs. PVA concentration (w/v) and spacer thickness (inset) at room temperature. [11]

In order to investigate the spacer effect on MEF, we measure the PL intensity enhancement under various PVA film thicknesses as shown in Figure 2.7.The thickness of the PVA film spacer was controlled by changing its concentration in solution. Notably, a thin PVA layer contributes to considerable PL enhancement of the Eu complex compared to the non-coated sample. The enhancement factor rises with the increase of the PVA concentration and reaches a maximum at 0.1% concentration, and then enhancement effect weakens and is expected to vanish with further increase of the PVA concentration. Results of the distance dependent MEF are presented in the inset of Figure 2.7. The optimal separation between silver NPs film and the Eu

complex layer is found around 7 nm, which is consistent with the result reported by Lakowicz et al. using a protein layer as the spacer. [17] The above results show that there are three main regions away from the silver film: the quenching zone, the enhancement (MEF) zone and the immune zone. In the near proximity of the SIF, luminescence is significantly quenched; enhancement is the dominant effect with an increased separation; the chromophore escapes from plasmon interaction for larger distances. The optimal distance is normally believed as 10 nm away from the silver NPs surface,[18] although some publications have reported an optimal distance as large as 60 nm.[19]

2.1.4 Conclusion

Luminescence intensity of the rare-earth complex $Eu(fod)_3$ is enhanced by surface plasmon of the silver NPs with PVA film spacer; meanwhile its fluorescence decay lifetime is shortened, resulting in a five-fold increase on Eu(III) radiative decay rate. Luminescence enhancement strongly relies on the separation between Eu complex and silver NPs film. Optimal separation is found ca. 7 nm. We hereby demonstrated a potential method by which rare-earth ion based OLED luminescence efficiency can be optimized.

2.2 Silver NPs Enhanced Rhodamine Luminescence

2.2.1 Background

Based on the understanding of the luminescence from Eu complex, we get a clear clue to achieve enhanced fluorescence by using an optical spacer. So far, more attention on MEF study is dedicated to the QE improvement of the chromophores used as fluorescent labels such as Indocyanine Green (ICG), Fluorescein isothiocyanate (FITC), and so on, which are of relatively low QE; [20,21] therefore surface plasmon significantly increases the sensitivity of imaging. However, when the study scale reduces to single molecule level, the investigation of MEF on high QE chromophore becomes significant since the signal noise ratio will decrease dramatically. Therefore the investigation of a surface plasmon coupled high QE dye luminescence will help us approach single molecule fluorescence study. However, to date only little research has been dedicated to metal enhanced high QE dye luminescence. [22]

In this research, we attached a high QE dye rhodamine B onto silver NPs. In order to avoid the significant fluorescence quenching, we chose Human Serum Albumin (HSA) protein as a spacer considering it has suitable size and non-luminescent characteristic. HSA is the most abundant protein in blood plasma with a diameter around 8 nm. [23] It consists of 585 amino acids and contains a free thiol that can adhere to the surface of noble metal NPs.[24]These ascendant properties make it suitable for attaching the dye to metal and meanwhile serving as an optical spacer to minimize fluorescence quenching.

Here we labeled the HSA with rhodamine B, and attached it to silver NPs. The fluorescent spectra together with decay lifetime were investigated, the photostability of the hybrid system was studied, and silver enhanced rhodamine luminescence mechanism was discussed.

2.2.2 Experimental

Rhodamine B (RB, 95%), Human Serum Albumin (HAS, 96-99%) were purchased from Aldrich; N-hydroxysuccinidmide (NHS, 97%) and dicyclohexylcarbodiimide (DCC, 99.0%) were obtained from Fluka.

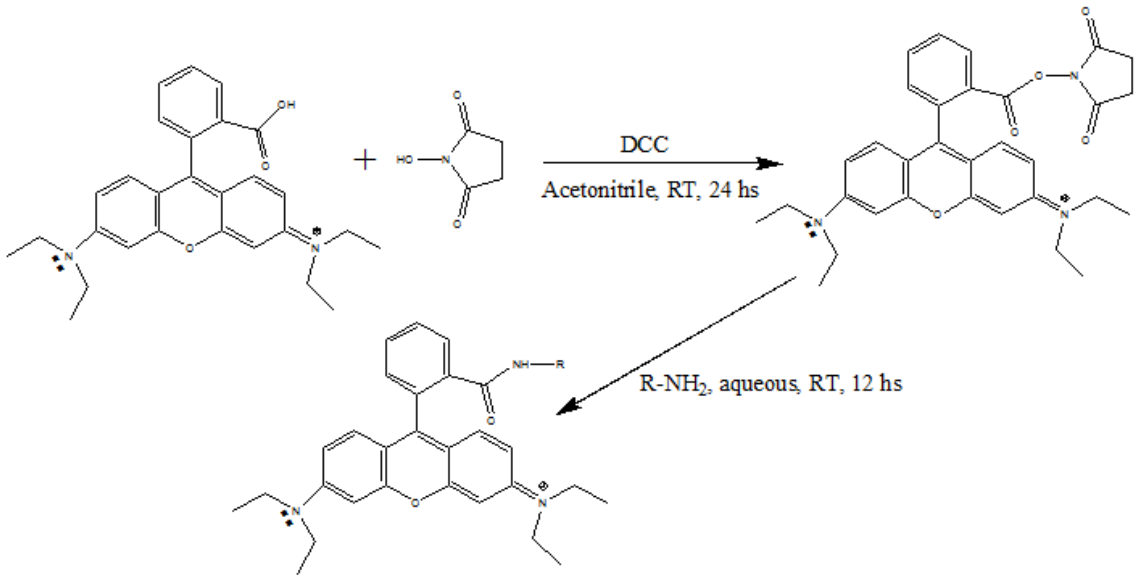

Figure 2.8 Schematic diagram for producing RB-NHS ester and labeling the HSA protein (Here the primary amine represents the protein) [25]

Rhodamine NHS ester is synthesized in the way described in literature,[26] 0.6 g RB and 0.15 g NHS were dissolved in 25 mL acetonitrile, and then a solution of 0.3 g DCC in 12 mL acetonitrile was added under dried condition to the blend slowly, and kept on stirring at room temperature for 24 hours as shown in Figure 2.8. The white precipitate was removed from the mixture by filtration. After evaporating the solvent of the filtrate, the crude product was purified by column chromatography using CH_2Cl_2: EtOH (3:1) as eluent to afford RB-NHS ester (yield=37%).**^{1}H-NMR** (400 MHz, $CDCl_3$, δ): 8.32 (1H, d), 7.85 (1H, t), 7.77 (1H, t), 7.34 (1H, d), 7.10 (2H, d), 6.85(4H, q), 3.67(8H, q), 2.65 (4H, s), 1.34(12H, t).**^{13}C-NMR** (100 MHz, $CDCl_3$, δ): 172.7, 168.9, 164.9, 158.6, 157.5, 155.4, 133.3, 132.9, 131.1, 130.8, 130.1, 129.8,

114.2, 113.3, 96.1, , 46.0, 25.2, 12.5. **MS (ESI, m/z)**: [M-Cl]+ calcd for $C_{32}H_{34}N_3O_5$, 540.3; found, 540.0. These data are consistent with the literature report which provides further evidence for the identity of the RB-NHS ester. [26]

The SIF was fabricated in the same way as described in section 2.1.2. Labeling protein was accomplished as follows: fresh prepared 4 mL RB-NHS ester ethanol solution (1 mg/mL) was added into 10 mL HSA phosphate buffered saline (PBS PH=7.4) solution (2.5 mg/mL). The mixture was incubated at room temperature overnight. The as prepared SIF slide and blank glass were soaked into the blend solution overnight, and washed extensively with distilled water followed by ethanol to remove excess RB-NHS ester. Finally the SIF slides were dried by nitrogen flow. Herein a blank glass slide is taken as reference, since albumin protein is known to spontaneously adhere to glass forming an essentially complete monolayer. [27]

Proton and ^{13}C NMR spectra were recorded on a Bruker 400 MHz spectrometer, Electrospray ionization mass spectrometry [ESI-MS] experiments were performed on a Qstar XL MS/MS (Applied Biosystems) system. An absorption spectrum was taken with a Lambda 20 UV/Vis spectrometer (PerkinElmer). Fluorescent signals were collected by USB2000-Ocean Optics spectrometer at a 60º angle away from normal when sample slides were excited vertically by Nd^{3+}-YAG laser (Centennia, Intra-cavity Doubled CW Laser at 532 nm), the same setup was used to study photostability in which fluorescence intensity decrease was monitored under exposure to laser irradiation (200 mW). The Nd^{3+}-YAG laser we used is a continuous wave (CW) laser instead of a pulsed laser, thus the photoablation effect on the organic dye as well as on the protein is not that significant under such power intensity. The time-resolved fluorescence lifetime was measured by a home-made setup by Sunny Rao. It consists of a pulsed laser (PiLAS) at 405 nm of FWHM 45 ps, a Single Photon Avalanche Detector (SPAD), Constant Fraction Discriminators (CFDs), and Time Correlated Single Photon Counting (TCSPC) module (SensL).

The TCSPC keeps track of arrival time of the photon at the detector with respect to the laser pulse shot at the sample giving the histogram of all the fluorescent photons.

2.2.3 Results and Discussion

The extinction spectrum of the rhodamine B attached SIF is shown in Figure 2.9. The absorption peak at 410 nm is ascribed to the plasmon resonance of silver. Although there is no detectable absorption peak assigned to rhodamine B due to its relatively low concentration, considerable fluorescence emission signal with peak wavelength at 580 nm confirms the successful attachment of rhodamine B to silver NPs. Figure 2.10 presents the PL spectra of rhodamine B on glass substrate and SIF. The fluorescence intensity on SIF is found to be twice of that on blank glass. The increased PL from SIF demonstrates that silver NPs can enhance the fluorescence of RB with HSA as spacer. The PL enhancement is moderate; [13, 14] nevertheless it is reasonable since RB is a high QE dye.

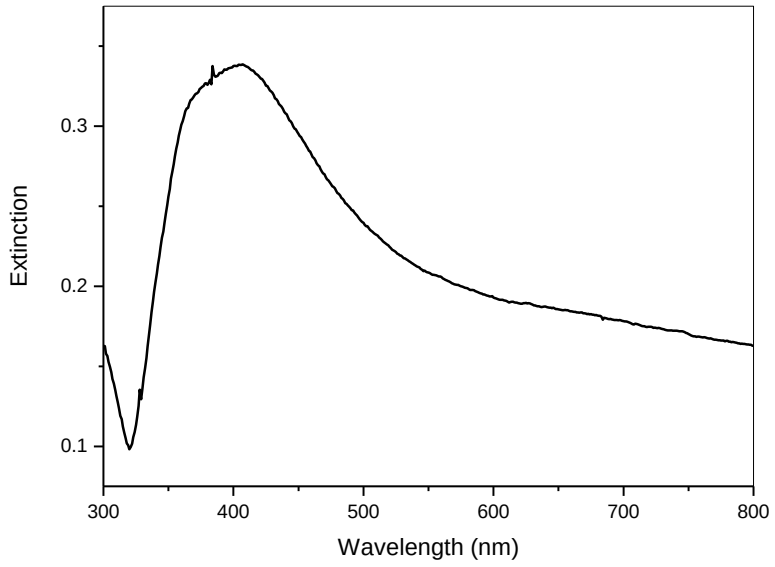

Figure 2.9 The extinction spectrum of RB-HSA attached SIF.[25]

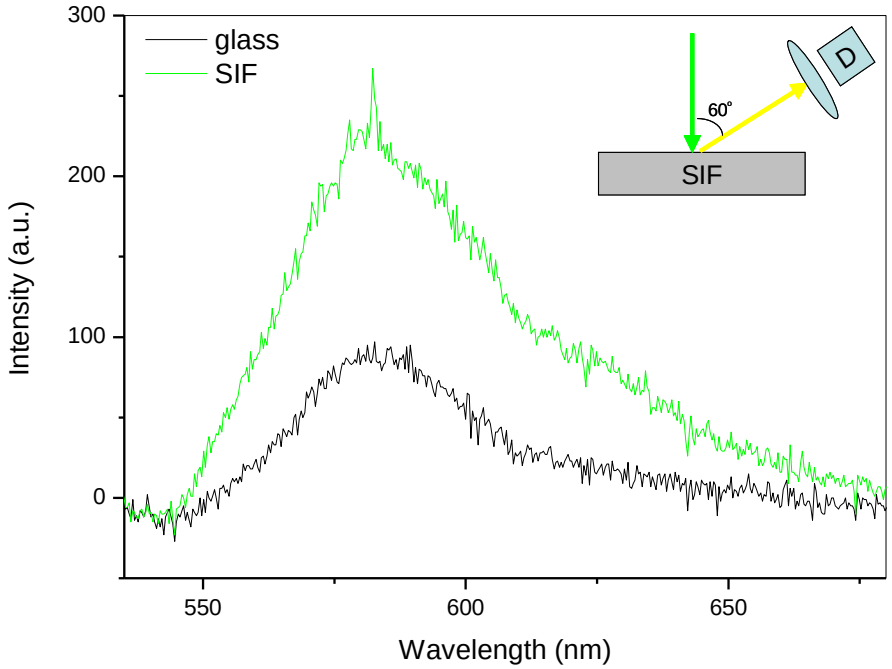

Figure 2.10 Emission spectra of RB on SIF and blank glass with HSA spacer.[25]

Figure 2.11 shows the fluorescence decay lifetime of RB on glass and SIF. The decay curve of RB on glass substrate could be fitted well by monoexponential function yielding a lifetime 3.0 ns, whereas the decay curve of RB on SIF needs to be fitted by bi-exponential function giving a mean lifetime 0.68 ns, which consists of a longer lifetime component 2.1 ns (weight 18%) and a shorter lifetime component 0.37 ns (weight 82%). Recalling the SIF sample fabrication and surface morphology, we observed that silver NPs were well separated and the NPs coverage is far less than unity. Reasonably dye molecules are expected to adhere on vacancy position between two isolated NPs on the glass substrate. The longer lifetime component 2.1 ns, which is closer to that of pure dye molecules 3.0 ns, is more likely due to those partial dye molecules adhering in the vacancy between silver islands. They experience less interaction with silver NPs. The much shorter lifetime component 0.37 ns must be attributed to the dye molecules attached directly on

silver NPs retaining intense interaction with silver NP surface plasmon. Moreover, we can estimate that the presence of the silver NPs reduces the lifetime of RB by about eight-fold.

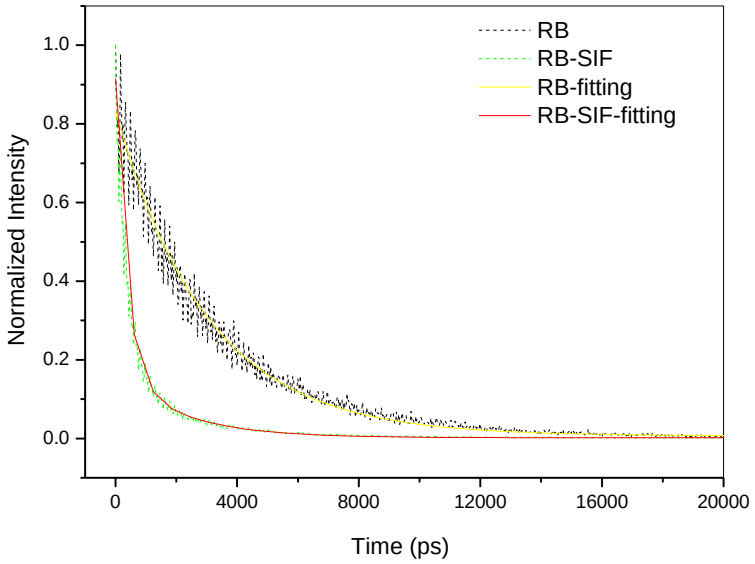

Figure 2.11 Fluorescence lifetime decay of RB on glass (black) and SIF (green).[25]

The photobleaching effect is an inextricable problem coming along with the single molecule detection which makes a stable fluorescent signal difficult to capture. Photobleaching is known as a nonreversible photochemical reaction of a chromophore with oxygen in the environment destroying the chemical structure of the dye molecule permanently. Normally chromophore molecules tend to undergo bleaching in triplet state which has much longer lifetime than the singlet state, thus any reduction of lifetime would relieve the photobleaching effect and promote the durability of the dye molecule, since the molecule would have less time to stay in singlet or triplet excited states. Therefore, we performed a comparative experiment to study the photobleaching of RB on SIF and glass substrate. The temporal evolution of the fluorescence intensity was recorded as shown in Figure 2.12. It is notable that the dye molecules on the blank glass substrate bleach much faster than those on SIF. The fluorescence intensity of RB on blank glass decays to half of its initial value after 60 seconds. However, it takes more than 300 seconds

to decay to the same extent for RB on SIF, this greatly stable photoluminescence of dye molecules on SIF would facilitate the single molecule study in atmosphere.

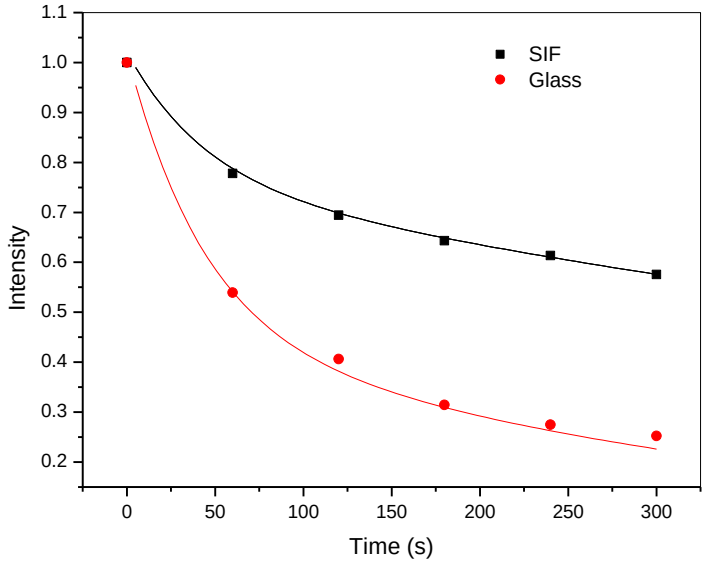

Figure 2.12 Temporal evolution of normalized fluorescence intensity of RB on SIF and glass substrate.[25]

We exposed a half-coated-SIF glass substrate with RB-HSA on top to UV light (925 μW), the RB molecules near the border of the SIF and blank glass were irradiated to ensure the RB molecules on both sides were exposed to an even radiation field, and the fluorescence image snapshots of those molecules were shown in Figure 2.13. It is notable that dye molecules on blank glass substrate bleach much faster than those on SIF. On average, the dye molecules bleach within 30 minutes on glass substrate. However, they can survive as long as 240 minutes over SIF indicating that SIF can suppress the photobleaching of RB effectively.

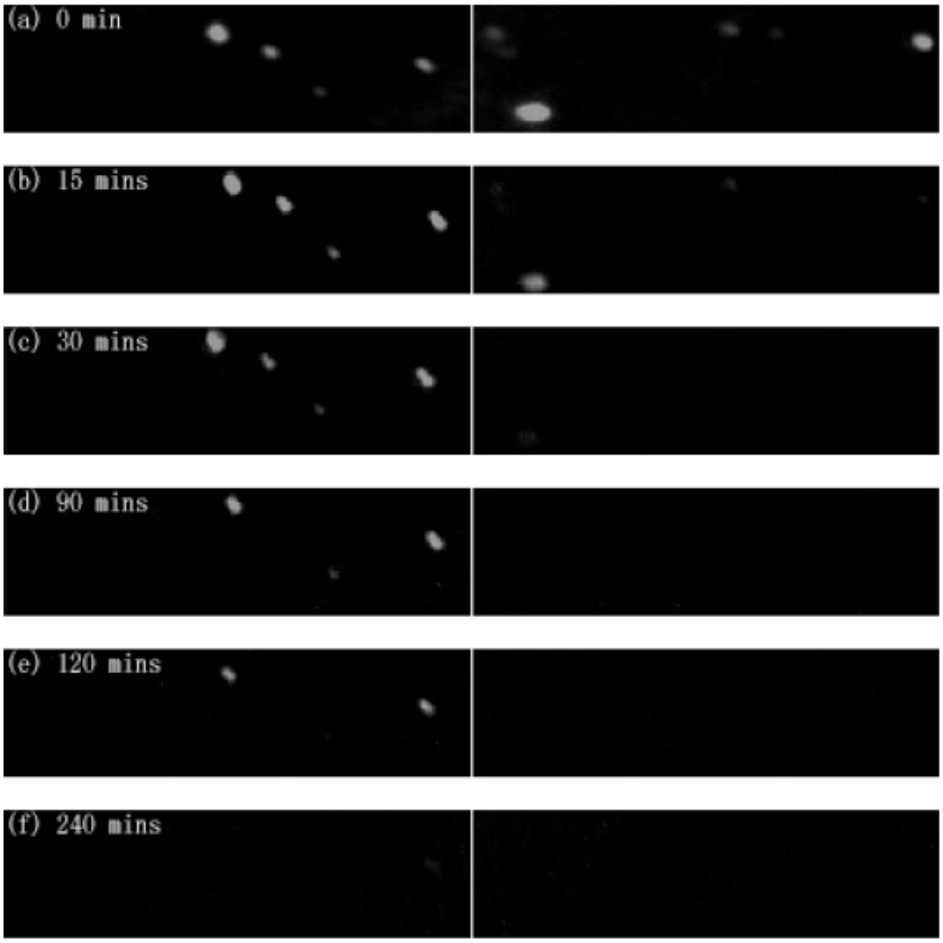

Figure 2.13 The fluorescence images evolution of RB-HSA on SIF (left) and glass (right) under the exposure to UV light. (from top to bottom are 0, 15, 30, 90, 120, 240 minutes exposure respectively)[25]

2.2.4 Conclusion

We have shown that Rhodamine B dye is successfully attached to SIF via Human Serum Albumin protein which serves as a spacer to separate the dye from silver NPs, avoiding fluorescence quenching. Metal enhanced fluorescence effect is observed in the present hybridized system, and the lifetime of RB is reduced by 8-fold with the presence of the silver NPs. Notable photostability improvement on dye molecules would greatly facilitate single molecule study.

References

[1] Jennings, T. L.; Singh, M. P.; Strouse, G. F. J. Am. Chem. Soc. **2006**, 128, 5462.

[2] Kruszewski, S.; Wybranowski, T.; Cyrankiewicz, M.; Ziomkowska, B. Pawlaczyk, A. Acta Phys. Pol. A **2008**, 113, 1599.

[3] Mackowski, S.; Wormke, S.; Maier, A. J.; Brotosudarmo, T. H.P; Harutyunyan, H.; Hartschuh, A.; Govorov, A. O.; Scheer, H.; Brauchle, C. Nano Lett. **2008**, 62, 3653.

[4] Wang, Y.; Zhou, X.; Wang, Y.; Zhou, J. Mater. Lett. **2008**, 62, 3582.

[5] Kalkman, J.; Kuipers, L.; Polman, A.; Gersen, H. Appl. Phys. Lett. **2005**, 86, 041113.

[6] Lupei, V.; Pavel, N.; Taira, T. Appl. Phys. Lett. **2003**, 83, 3653.

[7] Dubinskii, M.; Zhang, J.; Kudryashov, I. Appl. Phys. Lett. **2008**, 93, 031111.

[8] Iwanaga, H.; Amano, A.; Aiga, F.; Harada, K.; Oguchi, M. J. Alloys Compd. **2006**, 408-412, 921.

[9] Lakowicz, J. R.; Shen, Y.; D'Auria, S.; Malicka, J.; Fang, J.; Gryczynski, Z.; Gryczynski, I. Anal. Biochem. **2002**, 301, 261.

[10] Kazakov, V. P.; Voloshin, A. I.; Shavaleev, N. M. Mendeleev Communications **1998**, 3, 83.

[11] Liu, F.; Aldea, G.; Nunzi, J-M. J. Lumin. **2010**, 130, 56.

[12] Zhang, Y.; Aslan, K.; Malyn, S. N.; Geddes, C. D. Chem. Phys. Lett. **2006**, 427, 432.

[13] Malicka, J.; Gryczynski, I.; Geddes, C. D.; Lakowicz, J. R. J. Biomed. Opt. **2003**, 8, 472.

[14] Stranik, O.; Nooney, R.; McDonagh, C.; MacCraith, B. D. Plasmonics **2007**, 2, 15.

[15] Tam, F.; Goodrich, G. P.; Johnson, B. R.; Halas, N. J. Nano Lett. **2007**, 7, 496.

[16] Aisaka, T.; Fujii, M.; Hayashi, S. Appl. Phys. Lett. **2008**, 92, 132105.

[17] Malicka, J.; Gryczynski, I.; Gryczynski, Z.; Lakowicz, J. R. Anal. Biochem. **2003**, 315, 57.

[18] Ray, K.; Badugu, R.; Lakowicz, J. R. Langmuir, **2006**, 22, 8374.

[19] Sokolov, K.; Chumanov, G.; Cotton, T. M. Anal. Chem. **1998**, 70, 3898.

[20] Falicia, T.; Glenn, P. G.; Bruce, R. J.; Naomi, J. H. Nano Lett. **2007**, 7, 496.

[21] Kruszewski, S.; Wybranowski, T.; Cyrankiewicz, M.; Ziomkowska, B.; Pawlaczyk, A. Acta Physica Polonica A **2008**, 113, 1599.

[22] Liu, F.; Nunzi, J-M. Appl. Phys. Lett. **2011**, 99, 123302.

[23] Sugio, S.; Kashima, A.; Mochizuki, S.; Koda, N.; Kobayashi, N. K. Protein, Eng. **1999**, 12, 439.

[24] Anfinsen, C. B.; Edsall, J. T.; Richards, F. M.; Eisenberg, D. S. Adv. Protein Chem. **1999**, 45, 153.

[25] Liu, F.; Rao, B. S.; Aldea, G.; Nunzi, J-M. Proc. SPIE **2011**, 8113, 81130C.

[26] Meng, Q.; Yu, M.; Zhang, H.; Ren, J.; Huang, D. Dyes Pigments **2007**, 73, 254.

[27] Doron, A.; Katz, E.; Willner, I. Langmuir **1995**, 11, 1313.

Chapter 3

OLEDs Performance Enhanced by Silver Nanoparticles

In this chapter, we will focus on the application of silver NPs surface plasmons in improving the performance of diverse OLEDs including small molecule OLEDs, phosphorescent OLEDs and hybrid OLEDs. The roles of silver NPs in each type of OLED will be discussed and interpreted. Improved device performance cannot be achieved unless a tailored nanostructure is properly incorporated into the OLEDs.

3.1 Electroluminescence Measurement

3.1.1 Principles

In addition to the transmittance and absorbance, light is described by flux, intensity, illuminance, and luminance (brightness). Flux is the total luminous power (measured in lumens); intensity is the angular concentration of flux (candelas); illuminance is the surface density of incident flux (lumen/m^2) and luminance or brightness is the intensity emitted per unit area (candelas/m^2).[1]

Since OLEDs are used for display purposes, the response of the human eye described by the photopic luminosity function or luminous efficiency function must be taken into account, [2] which is shown in Figure 3.1. Luminous intensity can be determined by measuring flux in any given solid angle, Ω, which is defined as the size of the aperture divided by the square of the distance between the light source and the detector.

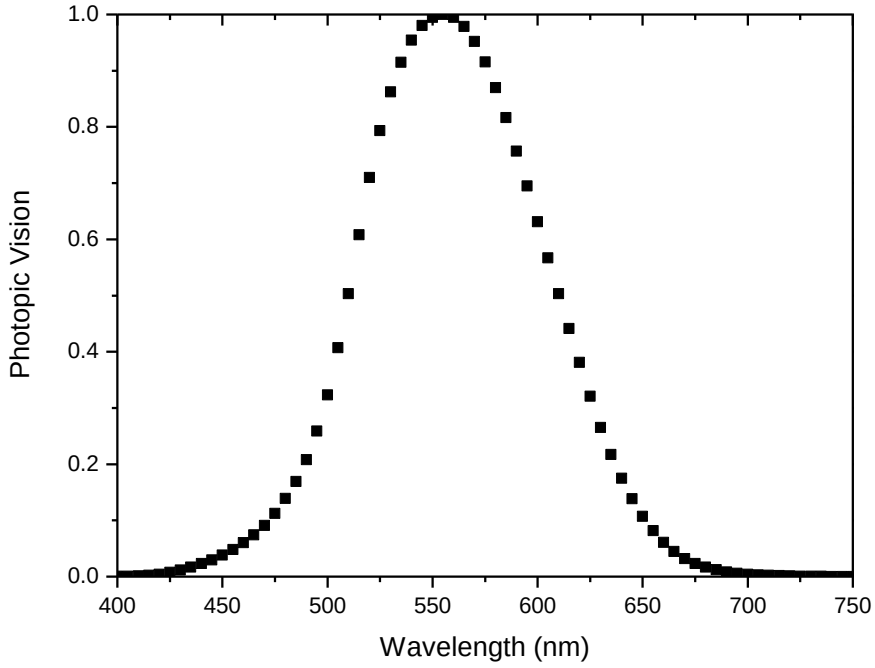

Figure 3.1 The photopic luminosity function. (Adapted from Ref. 2)

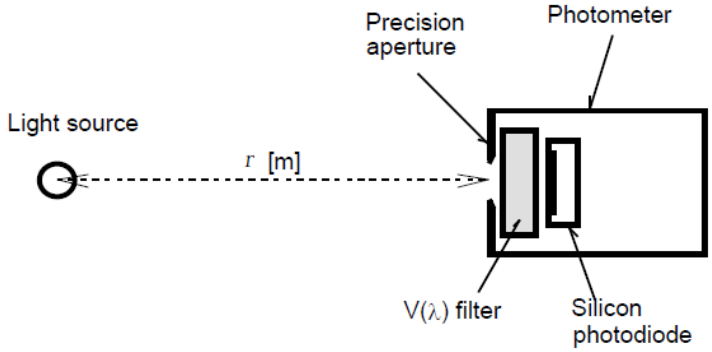

Figure 3.2 Configuration for measuring OLED luminous intensity. (Adapted from Ref. 3)

To measure luminous intensity one must first choose a reference direction for the measurement, and one must then determine the solid angle to be used in the measurement. For display applications, the reference direction should be chosen as the forward viewing direction

(along the direction perpendicular to the surface of OLEDs). Luminous intensity is defined as the emission in unit of cd/m^2 from the emitting surface.

As shown in Figure 3.2, a photometer consists of a silicon photo diode, a V(λ) filter and a precision aperture. The responsivity R_{vf} of the photometer for luminous flux (lm) is given by

$$R_{vf} = \frac{\int_{\lambda} P(\lambda)s(\lambda)d\lambda}{K_m \int_{\lambda} P(\lambda)V(\lambda)d\lambda} \qquad (A/lm) \tag{3.1}$$

where P(λ) is the spectral power distribution of the light to be measured, V(λ) is the spectral luminous efficiency function, s(λ) is the absolute spectral responsivity (A/W) of the photodiode, and K_m is the maximum spectral efficacy 683 lm/W. If the area S (m^2) of the aperture is known and the responsivity R_{vf} is uniform within the aperture opening (i.e. a small solid angle), the responsivity R_{vi} of the photometer for illuminance is given by

$$R_{vi} = S \cdot R_{vf} \quad (A/(lm/m^2)) \tag{3.2}$$

When a calibrated photometer is used to measure the illuminance from a point source, the luminous intensity I_v of the source is given by

$$I_v = r^2 \cdot I / R_{vi} \quad (cd) \tag{3.3}$$

where r is the distance (m) between the light source and the aperture of the photometer and I is the output current (A) from the photometer.

Based on the definition of solid angle, equation (3.3) can be reformulated as:

$$I_v = \frac{r^2 \cdot I}{S \cdot R_{vf}} = \frac{I}{\Omega \cdot R_{vf}} \quad \text{(cd)} \tag{3.4}$$

Once the luminance L (cd/m^2) is accurately measured, then the luminous efficiency LE(cd/A), luminous power efficiency PE(lm/W) and external quantum efficiency η_{ext} (the ratio of

the number of photons emitted by the OLED into the viewing direction to the number of electrons injected) can be calculated by the following equations: [4, 5]

$$LE(cd/A) = \frac{L}{j} \tag{3.5}$$

$$PE(lm/W) = \frac{\pi \cdot L}{jV} \tag{3.6}$$

$$\eta_{ext}(\%) = \frac{5 \times 10^{-3}}{(h\nu)\phi(\lambda)} LE \tag{3.7}$$

where j is the current density, V is the driving voltage, hν is the emitted photon energy in eV, and $\Phi(\lambda)$ is the luminous efficiency function.

Another approach to measure luminance intensity is to use an integrating sphere containing a calibrated detector, which measures all the emitted photons from the light source and thus the total output of the device. Once the external quantum efficiency is measured, L, LE, and PE can be calculated by using the above equations. [6]

3.1.2 Experimental Setup for Electroluminescence Measurement

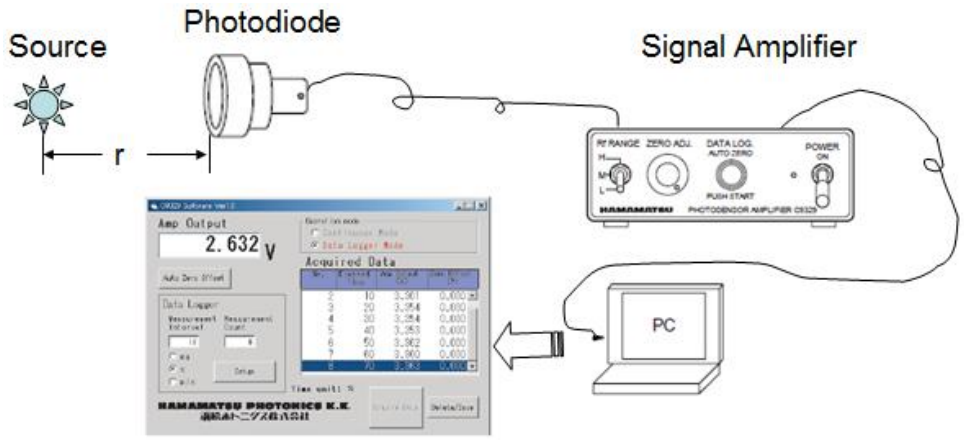

Figure 3.3 Schematic diagram of homemade setup for luminance measurement.

Our homemade luminance measurement setup is shown in Figure 3.3, which consists of a silicon photodiode (S2281 series, Hamamatsu Photonics K.K), a photosensor amplifier (C9329, Hamamatsu Photonics K.K) and a PC with C9329 software Ver 1.0. The distance r between our OLEDs and the silicon photodiode is fixed at 12 cm, and the detector active area S= 1 cm^2. Thus the steradian in our setup can be determined as $\Omega=S/r^2= 1/12^2=0.00694$ sr, which fulfills the test condition recommended by CIE ($\Omega\leq$ 0.01 Sr**)**. The absolute spectral responsivity of the silicon photodiode s(λ) can be obtained from the supplier as shown in Figure 3.4. Provided we are investigating a Alq_3 based OLED, the spectral power distribution P(λ) can be measured by the spectrometer (USB2000-Ocean Optics) as shown in Figure 3.5. The spectral luminous efficiency function V(λ) is given by CIE as shown in Figure 3.1. Therefore we can calculate the responsivity of the photometer R_{vf} value as follows:

$$R_{vf} = \frac{\int_{\lambda} P(\lambda)s(\lambda)d\lambda}{K_m \int_{\lambda} P(\lambda)V(\lambda)d\lambda} = 6.16\times10^{-4}\,(\mathrm{A/lm})$$

If the output reading from the software is 1 V under 10^9 V/A conversion impedance, the current from the photodiode is then determined as 1 nanoAmpere. Based on equation (3.4) the luminance intensity of the source is calculated as:

$$I_v = \frac{I}{\Omega \cdot R_{vf}} = \frac{10^{-9}}{0.00694 \times 6.16 \times 10^{-4}} = 2.34 \times 10^{-4} \text{ (cd)}$$

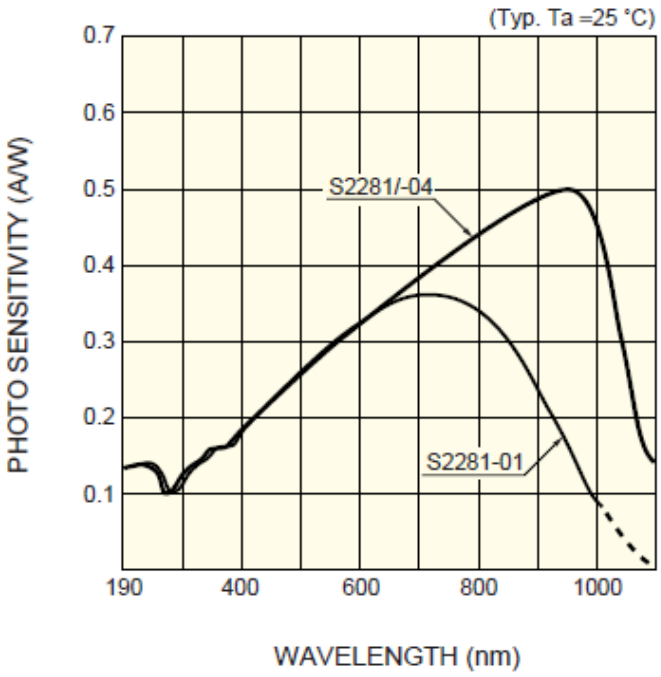

Figure 3.4 Spectral response of S2281 series silicon photodiode (Hamamatsu Photonics K.K)

As the active area of our OLEDs is 0.2 cm^2, the brightness or luminance of OLED can then be obtained as follows:

$$L = I_v / S_{OLED} = \frac{2.34 \times 10^{-4} cd}{0.2 \times 10^{-4} m^2} = 11.69 \text{ cd/m}^2$$

The photosensor amplifier has three conversion ranges 10^9, 10^7 and 10^5 V/A respectively, that enables it to detect various brightness. The resolution of the photosensor amplifier is 0.001 V, thus the lower limit for brightness detection is ca. 0.01 cd/m^2.

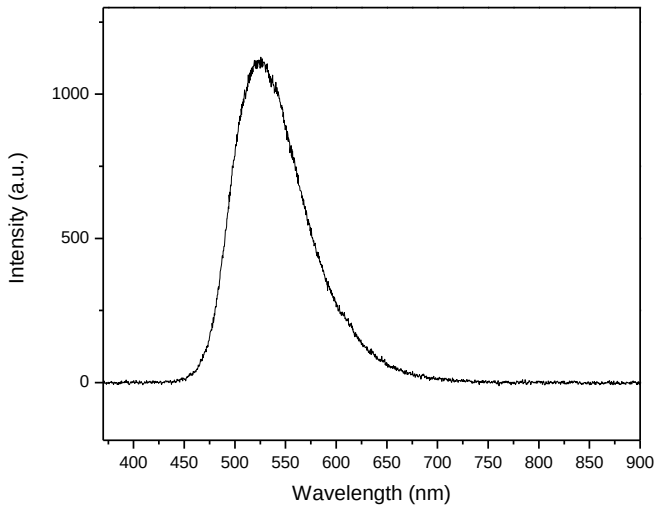

Figure 3.5 Electroluminescence spectrum of Alq_3 measured by spectrophotometer.

3.2 Silver NPs Increased SM-OLED Luminescence

3.2.1 Background

Recently surface plasmon enhanced luminescence (fluorescence and phosphorescence) has been attracting great interest due to its potential application in biological imaging and single molecule detection.[7,8] So far most of the research has been limited to surface plasmon enhanced PL in which the surface plasmon of noble metals such as gold and silver NPs could increase the PL intensity of chromophores up to two orders of magnitude.[9] However little attention has been paid to plasmon enhanced EL which also shows great potential in improving the EL efficiency of OLEDs. [10,11] Although Li et al. recently reported that the silver NPs increased the PL efficiency of Alq_3 more than three times,[12] their OLED trial device with silver NPs failed due to a deep charge trapping effect, the deteriorated performance discourages the extension of surface plasmon enhanced PL towards EL.

An OLED using the fluorescent small molecule Alq_3 as emitting layer is a well studied SM-OLED. To date various methods have been developed to increase its performance. Two of the most popular strategies are balancing the hole/electron ratio and reducing the carrier injection barrier. [13] The former method mainly relies on doping HTL to reduce hole mobility or inserting a buffer layer between HTL and the anode to impede the hole injection. However, it inevitably elevates the turn-on voltage, and there exists a tradeoff between low driving voltage and high efficiency. [14,15] The latter method requires the development of new materials that match the work functions of anodes and cathodes.

Therefore, we explored a method to increase SM-OLED EL efficiency without elevating driving voltage by metal surface plasmon. In this research we incorporated noble metal NPs into OLEDs building various layout structures, the influence of metal NPs on device EL efficiency

was investigated, distance (between metal NPs and emission centers) dependent EL enhancement effect was studied; and surface plasmon increased EL mechanism was discussed.

3.2.2 Experimental

Alq_3 (99.995%) was purchased from Aldrich, NPB (sublimation grade) was purchased from Lumtec and BCP (>97%) was obtained from Fluka. All the materials were used as received without further purification. Our OLEDs were fabricated on transparent ITO slides with sheet resistance 15 Ω/□ as shown in Figure 3.6. The ITO slide with dimension 2.5 cm by 2.0 cm was etched by 2 M HCl to create a cross shape insulated area. In that way a slide is divided into two individual parts which yields two diodes on one ITO glass substrate. The etched ITO slides were cleaned with toluene, ethanol, detergent (Decon) and distilled water, the wet slides were dried out by N_2 flow.

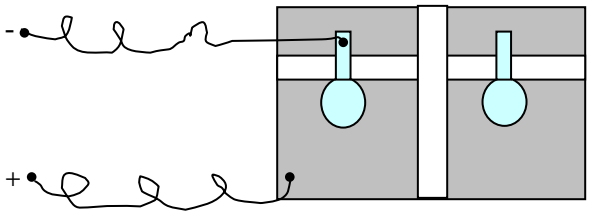

Figure 3.6 Schematic diagram of etched ITO slide geometry.

The organic materials and metal were deposited by vacuum thermal evaporation (Kurt. J. Lesker) as shown in Figure 3.7. A roughing pump and a turbo pump supply a low vacuum for the deposition chamber (< 10^{-6} mbar). Both metals and organic materials are heated by joule effect; the deposition processes are precisely controlled by the Sigma software. The film thickness is monitored by quartz crystal microbalance (QCM), and a shadow mask is used to create a pattern

for metal electrode deposition as shown in Figure 3.6. OLEDs with structure ITO/ NPB (50 nm)/Alq_3 (x nm)/ BCP (6 nm) /aluminum (200 nm) were fabricated by depositing each layer in order onto pre-clean ITO slide under 10^{-6} mbar vacuum. The UV-Vis spectrum was recorded on a Lambda 20 spectrometer (PerkinElmer), the PL intensity was measured by USB2000-Ocean Optics spectrometer, atomic force microscopy (AFM) image was captured with a Veeco multimode microscope. The current-voltage curves were measured on Keithley (4200-SCS), the EL luminance intensity was measured with our homemade setup as introduced in Section 3.1.

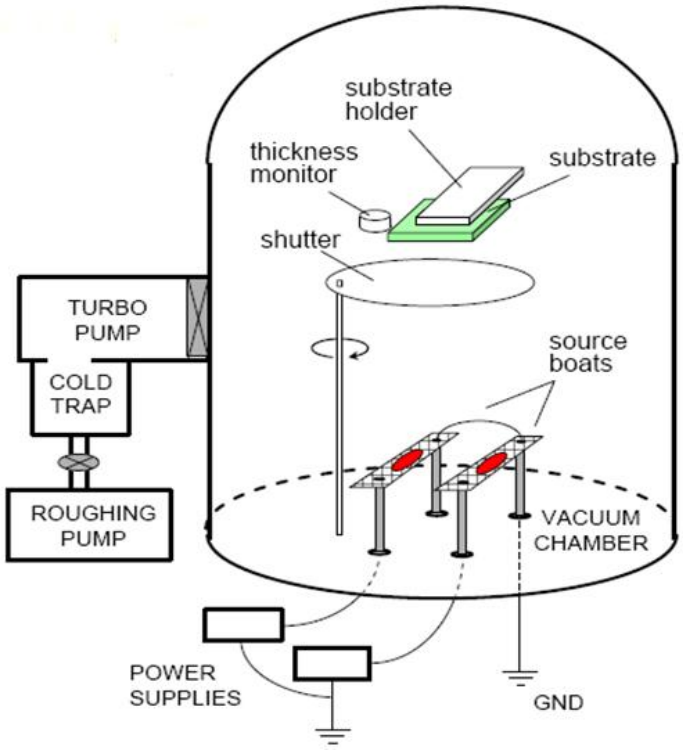

Figure 3.7 Schematic diagram of Kurt J. Lesker vacuum thermal deposition setup.

3.2.3 Results and Discussion

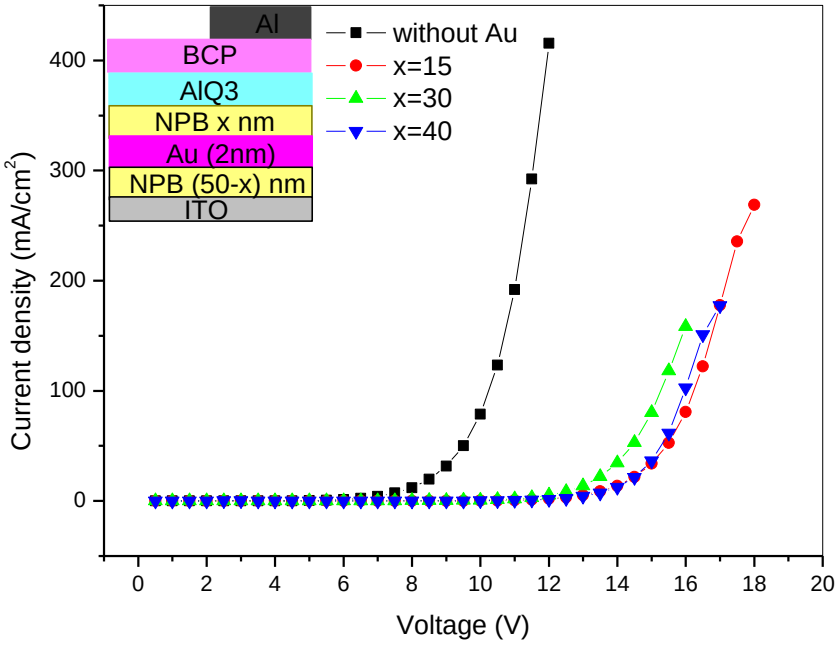

Figure 3.8 J-V curves of OLEDs incorporated with gold NPs in NPB layer with different distance away from NPB/Alq_3 interface, the devices have structure of ITO/ (50-x) nm NPB/ 2 nm Au/ x nm NPB/ 60 nm Alq_3/ 8 nm BCP/ 200 nm Al.

The emitting layer of present diodes is a thin layer (ca. 10 nm) of Alq_3 adjacent to the NPB layer. [16] In order to study surface plasmon controlled EL of OLEDs, we buried 2 nm gold NPs into NPB hole transport layer in different depth creating different separation from the NPB/Alq_3 interface. The diode structure is presented in the inset of Figure 3.8. It is notable that the diode without Au NPs exhibits a good rectification characteristic with lower turn-on voltage. However, with incorporation of Au NPs into NPB, regardless of the doping position, the diode exhibits a higher turn-on voltage, which indicates that Au NPs retard the transport of the holes due to trapping effect and thus increase the hole injection barrier. [17,18]

Subsequently we investigated the EL of the diodes with Au NPs as shown in Figure 3.9. Although the J-V curves do not show considerable difference for OLEDs of different Au NPs

doping position, their luminous efficiency curves exhibit quite different characters. With the increase of upper layer NPB thickness, namely the separation between gold NPs and Alq_3 emission layer, the luminous efficiency increases gradually. This provides the evidence of surface plasmon coupling EL since the charge transport properties remain the same for these OLEDs and distance dependent luminescence is a typical property of surface plasmon coupling luminescence. But unfortunately, none of above structures exhibit increased device performance on either the driving voltage or luminous efficiency. Therefore, the device configuration needs to be modified.

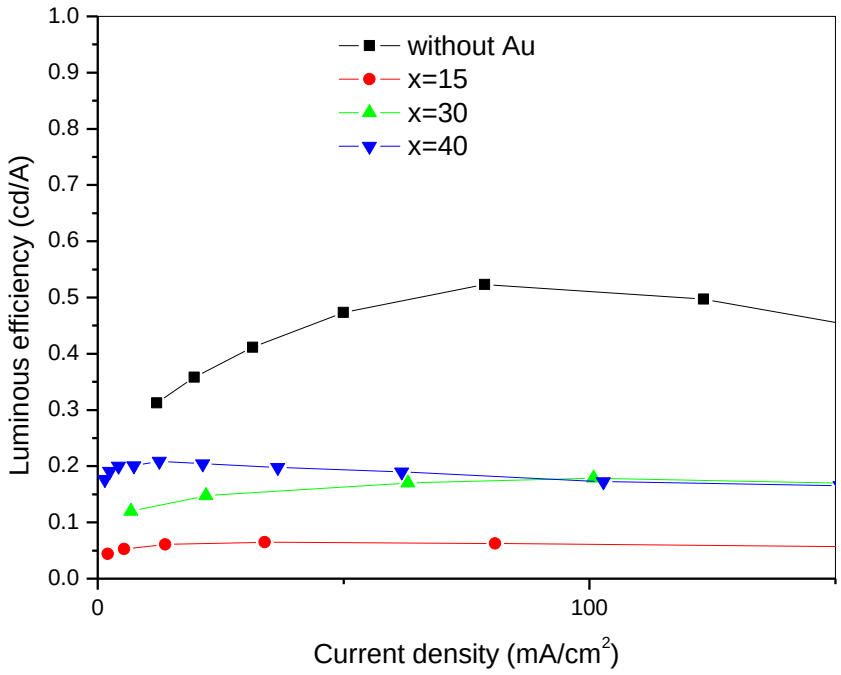

Figure 3.9 The luminous efficiency varies with the current density of pristine OLED and Au NPs doped OLEDs.

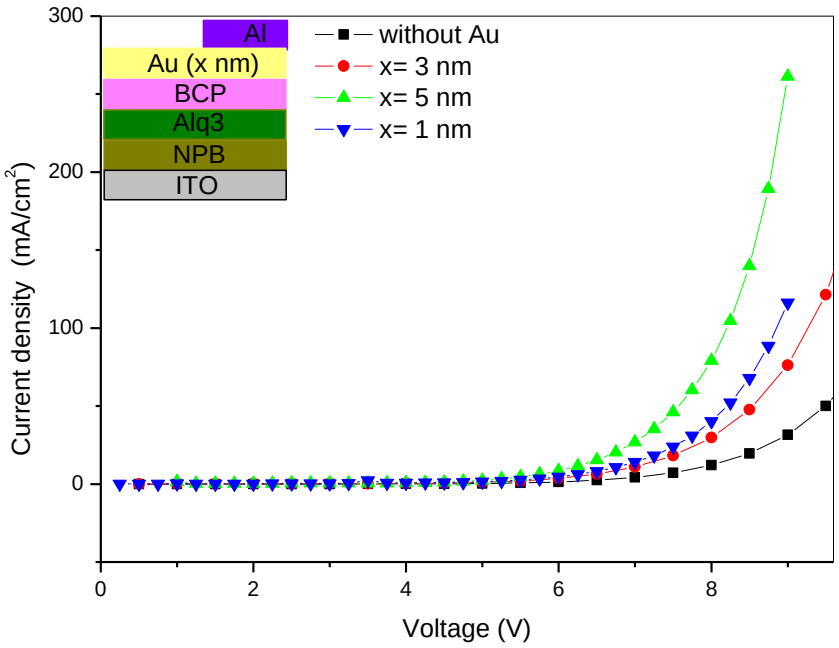

Figure 3.10 J-V curves of OLEDs with Au NPs underneath the cathode Al, inset is the configuration of modified OLED: ITO/ 50 nm NPB/ 60 nm Alq_3/ 8 nm BCP/ x nm Au / 200 nm Al

As the OLEDs with Au NPs doped in NPB layers result in higher turn-on voltage and lower luminous efficiency, the incorporation strategy needs to be reevaluated. As an alternative way to incorporate NPs in OLED, we evaporated a thin layer of gold NPs underneath the Al cathode as shown in the inset of Figure 3.10. The thickness of Alq_3 layer is 60 nm and the luminescence layer thickness is around 10 nm. Thus the non-luminescent Alq_3 layer together with BCP layers could serve as spacer under this device configuration. The J-V curves of the OLEDs show dramatically increased current density when gold NPs were incorporated, which could result from increased electron injection from cathode due to amplified electric field near gold NPs surface known as lightning rod effect.[19]

We notice that the current density decreases when the Au NPs thickness is increased from 1 nm to 3 nm, it results from the fact that a thicker gold film contains larger size Au NPs which have smaller curvature radius and thus weaken the E-field amplification. However, when the

thickness of the gold film is further increased to 5 nm, the current density is elevated surprisingly compared to both 1-nm and 3-nm gold film incorporated diodes. As it is well known, the increase of the Au NPs layer thickness can lead to the formation of a continuous Au film, indeed 5 nm is very close to the threshold film thickness (ca. 6 nm) of a continuous film for gold deposition.[20] A continuous gold film can effectively modify the BCP/Al interface by eliminating the Al_xO_y layer, this oxide layer is known to exist when directly evaporating Al on an organic layer under 10^{-6} mbar vaccum because the residual oxygen and water in an evaporation chamber can oxidize the Al.[21] Besides our diodes testing was performed in atmosphere without encapsulation, the organic/Al interface has higher chance to be oxidized. In our device structure BCP is an insulator layer behaving similarly as LiF for tunneling electron injection, and 6 nm is an optimal thickness for electron injection according to literature report.[22] Therefore an additional insulator layer Al_xO_y forming at BCP/Al interface will increase the electron tunneling distance and make the electron injection less efficient. Actually Scholz et al. also reported that the electron injection decreased in an OLED with structure ITO/Alq_3/Al when the oxygen concentration in the vacuum chamber was increased corresponding to a thicker insulator layer at the Alq_3/Al interface. [21] Because inert metal gold resists oxidation very well, no oxide layer forms at the BCP/Au interface. This must contribute to the current density improvement for the 5-nm gold film incorporated diode.

The work function of the bulk gold is larger than that of Al, causing higher potential barrier for electrons injection according to the flat band diagram as shown in Figure 3.13, however the electrons injection is entirely a tunneling behavior through triangle potential barrier, the work function difference between Au and Al would not affect the electron injection significantly. Actually this was confirmed by Sun et al. using Au as the cathode in an OLED with structure ITO/NPB/Alq_3/LiF/Au.[23] Their OLEDs with LiF/Au cathode had comparable efficiency to OLEDs with the LiF/Al cathode.

The voltage-luminance curves of the diodes are shown in Figure 3.11. Notably the luminance intensity of the diodes is increased significantly by Au NPs under the same driving

voltage. Incorporation of the Au NPs into the OLEDs lowers the device turn-on voltage, which benefits from the improvement of electron injection.

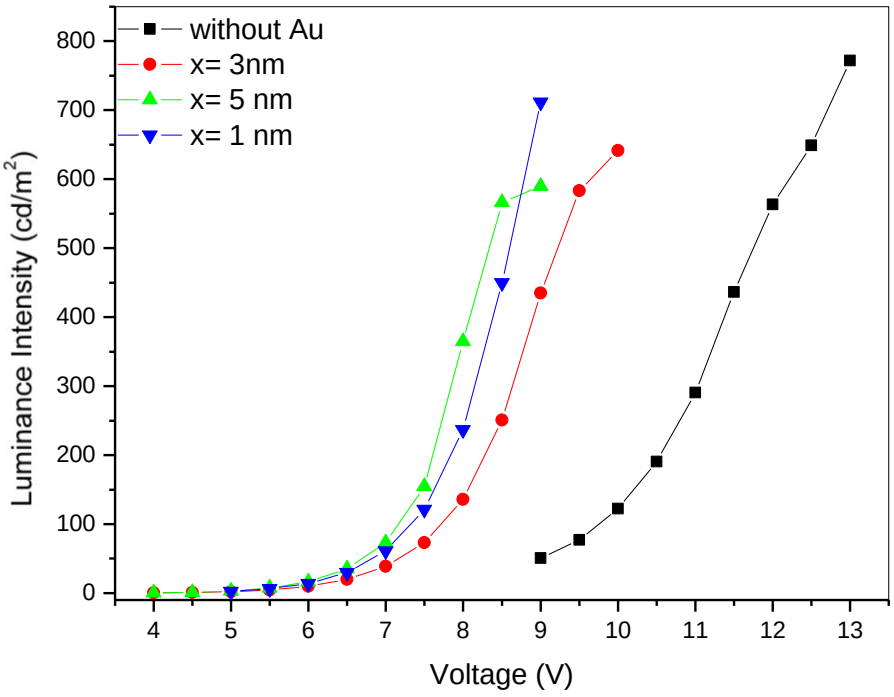

Figure 3.11 Luminance vs. driving voltage curves of pristine OLED and Au doped OLEDs

Moreover we investigated the luminous efficiency of the diodes as presented in Figure 3.12. For 1 nm gold NPs doped OLEDs, the maximum luminous efficiency is increased by 15% compared to pristine OLED. The above results indicate the insertion of gold NPs between exciton blocking layer and cathode is a much advanced method to optimize the performance of OLEDs. It not only lowers the driving voltage but also increases the luminous efficiency, although the increment is moderate. Owing to the absence of plasmon enhanced Alq_3 luminescence effect in the OLED incorporating a 5-nm continuous gold film, the OLED exhibits lowest efficiency among those three Au-modified OLEDs. It also implies that a discrete distribution of metal NPs is more favorable for OLEDs efficiency enhancement.

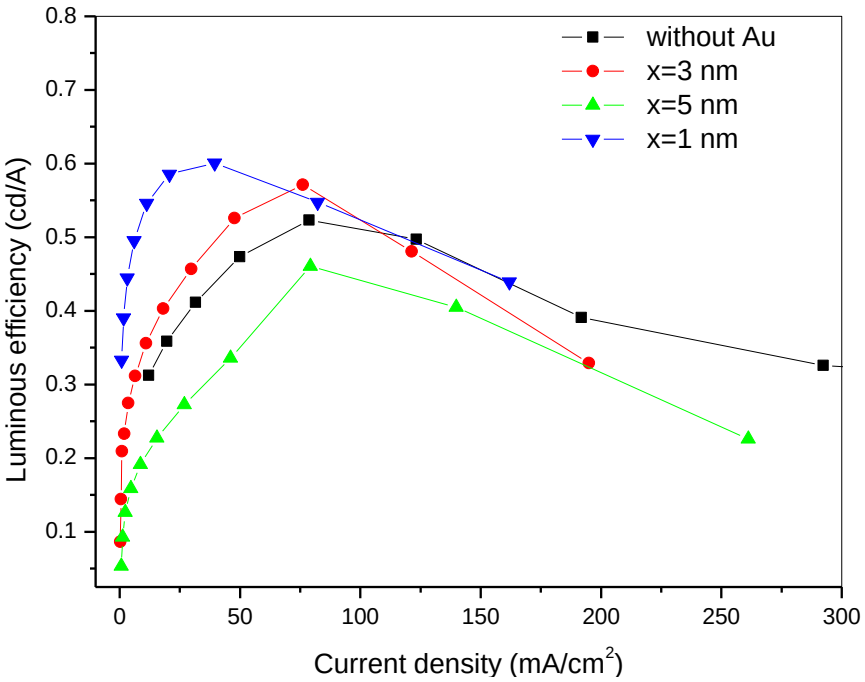

Figure 3.12 Luminous efficiency of pristine OLED and Au NPs doped OLEDs varies with current density.

In order to further optimize the OLEDs performance, we also tried to bury gold NPs layer inside Alq_3 emitting layer to form Alq_3(x nm)/ Au (1 nm)/ Alq_3 (60-x nm) sandwich structure (x varies from 10 to 60), however the performance of the OLEDs degrades and all the Au NPs incorporated devices exhibit deteriorated performance, with luminous efficiency decreasing up to three orders of magnitude. This could be due to charge recombination in the Alq_3 at locations where luminescence is quenched by the Au NPs. A drastic drop of luminous efficiency is thus reasonable.

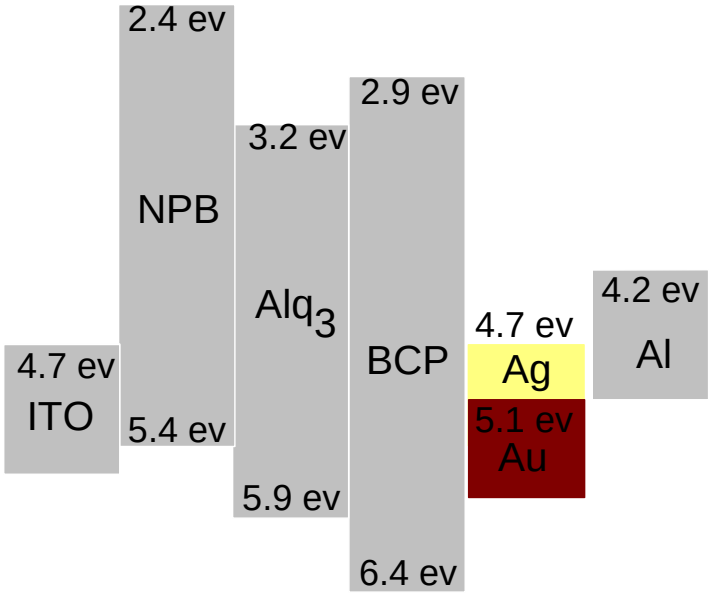

Figure 3.13 Energy level alignment of each material used in OLEDs

Similar to gold NPs, NPs of noble metal silver also have the surface plasmon resonance in the visible range. Therefore we replaced 1 nm Au NPs with 1 nm Ag NPs, and incorporated them underneath the Al cathode to investigate how silver NPs affect the SM-OLEDs performance.

The AFM image of 1 nm silver NPs layer deposited by thermal evaporation is shown in Figure 3.14. The nonspherical silver NPs are of an average size around 40 nm, which spread discretely in the form of islands, this morphology favors considerable metal enhanced fluorescence effect. [24,25]

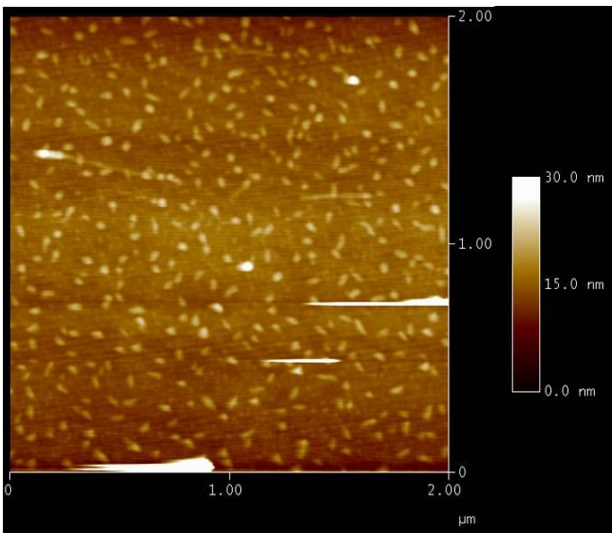

Figure 3.14 Two-dimensional AFM image of 1 nm (mass thickness) silver NPs layer fabricated by thermal evaporation on blank glass substrate.

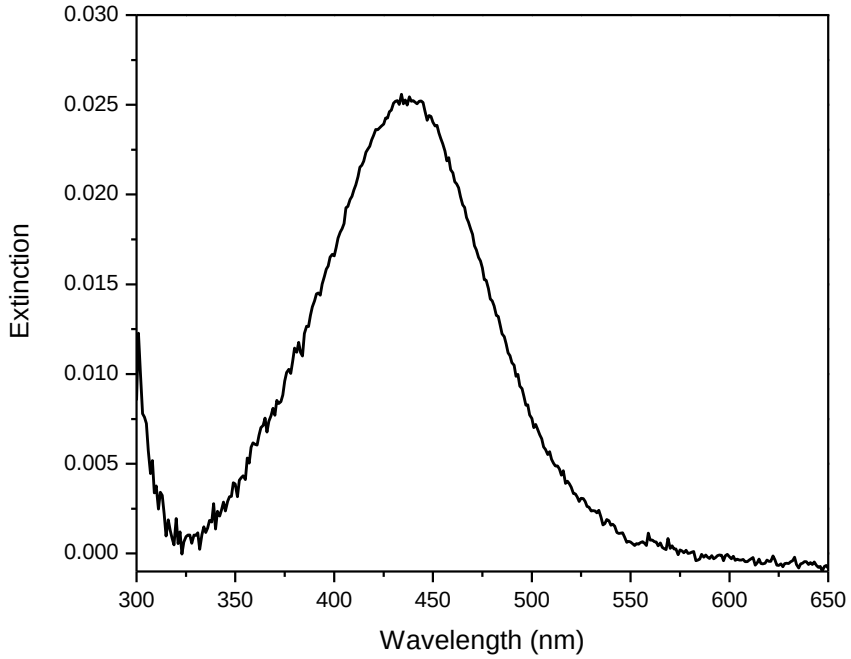

Figure 3.15 Extinction spectrum of 1 nm silver NPs deposited by thermal evaporation.

The extinction spectrum of the silver NPs is shown in Figure 3.15; the peak wavelength around 440 nm represents typical surface plasmon resonance of metallic silver, and the absorption

cross-section of the silver NPs is estimated to be 5.75 $\times 10^{-12}$ cm^2. Figure 3.16 shows a picture of a working SM-OLED under forward bias, the bright green emission from the SM-OLED corresponds to the intrinsic EL emission of Alq_3.

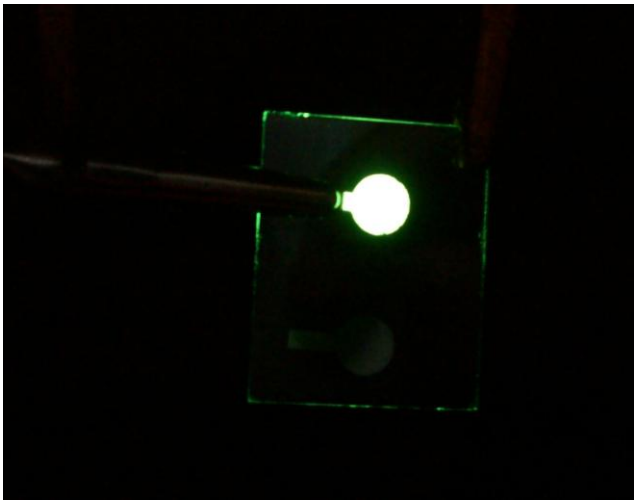

Figure 3.16 A picture of Alq_3 based SM-OLED under forward bias.

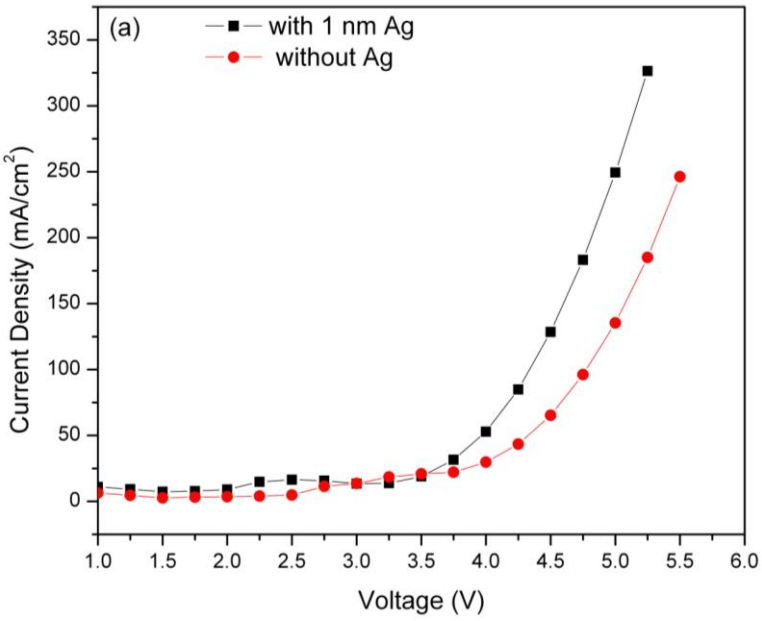

Figure 3.17 J-V curves of OLEDs with and without 1 nm silver NPs, Alq_3 thickness is 30 nm.

Figure 3.17 shows the J-V curves comparison between pristine OLED and 1 nm silver NPs doped OLED. It is notable that the current density is higher in the high voltage range. According to the Fowler-Nordheim tunneling theory, [26] the electron injection energy barrier is estimated to decrease from 0.11 eV to 0.1 eV with the presence of the silver NPs, which must result from E-field aided electron tunneling. The Fowler-Nordheim tunneling theory was valid and extensively used in single carrier injection scenario.[45] The current density in our diodes is mainly determined by electrons injection, since the holes have two orders of magnitude higher mobility in NPB than that of electrons in Alq_3 and will accumulate at NPB/Alq_3 interface,[16] screening the hole injection from the anode. Therefore, it is rational to fit the J-V curves in our diodes using the Fowler-Nordheim tunneling theory. Because the E-field strength at a rough surface with large curvature is much higher compared to a planar surface,[27] the enhanced E-field can reasonably impulse electron tunnelling through the triangle energy barrier. As a result the current density is increased.

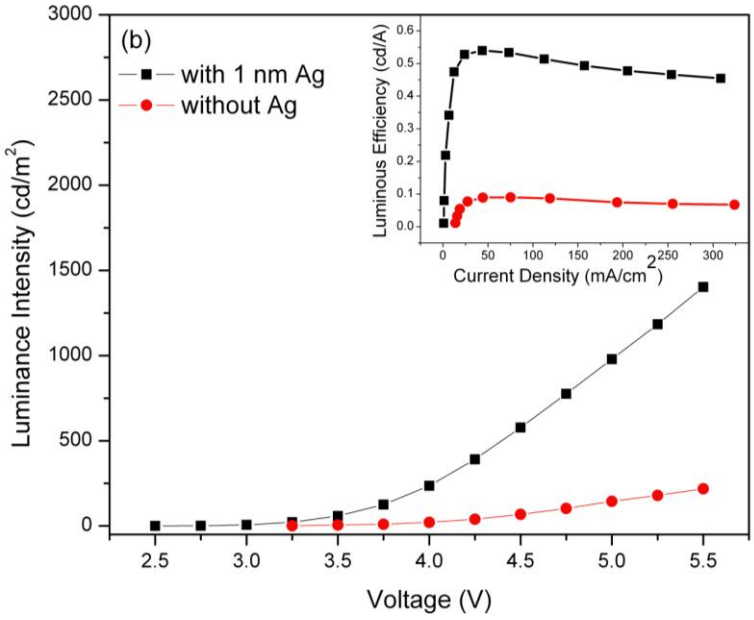

Figure 3.18 Luminance vs. voltage curves of pristine OLED and Ag NPs doped OLED, the Alq_3 layer thickness is 30 nm, the inset is the luminous efficiency-current density curves of diodes.

Figure 3.18 shows the OLED luminance plotted versus driving voltage, the turn-on voltage (at which brightness = 1 cd/m^2) is estimated to decrease by 0.5 V in the presence of the silver NPs, meanwhile the luminance is increased drastically in high driving voltage range. The luminous efficiency of the OLEDs is presented in the inset of Figure 3.18, notably the maximum device efficiency is increased by 6-fold in the presence of 1 nm silver NPs with Alq_3 thickness of 30 nm. On the one hand this can benefit from the well balanced hole/electron ratio due to increased injection of minority charge carrier electrons;[28] on the other hand it can also be attributed to surface plasmon enhanced PL efficiency. [29] As is known the magnitude of the electric field resulting from surface plasmon decreases with the increase of distance away from metal NPs surface, thus the influence of silver NPs on device efficiency should be susceptible to the distance variation between emitting centers and NPs if surface plasmon enhanced Alq_3 QE does exist. In order to validate this hypothesis, we designed a series of comparative experiments to investigate the enhancement effect under various separations between Ag NPs and the emitting centers, by changing the Alq_3 layer thickness.

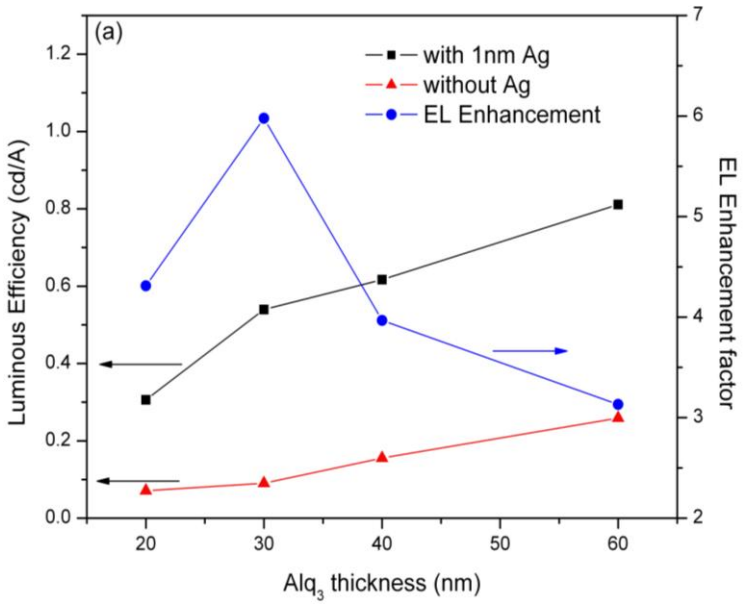

Figure 3.19 Luminous efficiency and EL enhancement factor vs. Alq_3 thickness curves of OLEDs with and without Ag NPs.

As presented in Figure 3.19 the luminous efficiency of both pristine OLED and Ag modified OLEDs decreases with reduction of Alq_3 thickness, which should result from metal electrode quenching effect.[16] With the decrease of Alq_3 thickness from 60 nm to 20 nm, the emission region becomes closer and closer to the 200 nm-thick aluminum cathode. As a result the energy dissipating effect of excitons into the cathode via nonradiative energy transfer becomes more and more prominent, greatly impairing the luminous efficiency of the device. However, the Ag NPs induced luminous efficiency enhancement factor keeps on increasing with the decrease of Alq_3 thickness from 60 nm to 30 nm, which provides evidence that Ag NPs indeed engage in surface plasmon enhanced PL efficiency. Along with the emitting centers getting closer to the Ag NPs layer, the reduced distance will result in remarkable increase of the electric field strength surrounding emitting centers; as a consequence, the radiative decay rate of excitons will be increased, and thus Alq_3 PL efficiency is enhanced. However, with further decrease of Alq_3 thickness to 20 nm, the enhancement factor decreases somewhat which suggests that emitting centers start shifting away from optimal enhancement site.[30] It is worth mentioning that all devices incorporated with 1 nm Ag NPs layer exhibit increased current density, regardless of Alq_3 deposition thickness, which further confirms our surface plasmon impelled electron injection interpretation.

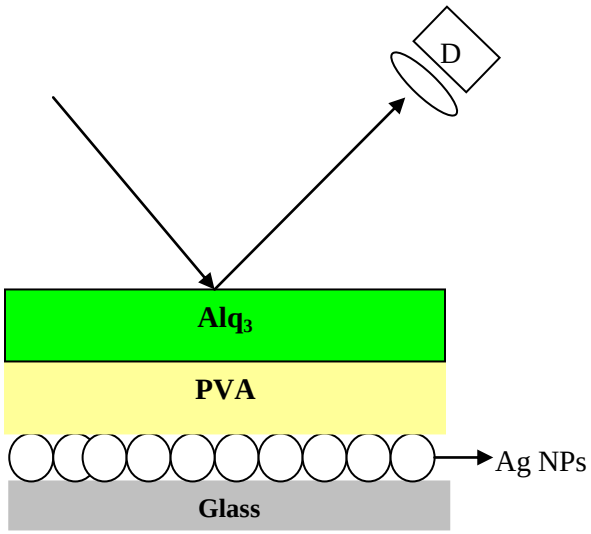

Figure 3.20 The geometry for measuring Ag surface plasmon enhanced Alq_3 photoluminescence.

In order to further support our plasmon increased Alq_3 PL QE argument, we investigated surface plasmon controlled Alq_3 PL by applying a polyvinyl alcohol (PVA) spacer as reported in our previous work,[30] and the Ag NPs density was kept the same with that in the diodes we studied. The glass slides with configuration Ag NPs/PVA (7~60 nm)/Alq_3 (30 nm) were excited with 365 nm monochromatic light and the PL signal is collected by fluorometer as shown in Figure 3.20. Distance dependent PL enhancement results are presented in Figure 3.21. Obviously the secure distance for PL enhancement is over 11 nm, and there is barely interaction between Ag NPs and Alq_3 molecules when the separation is above 50 nm. Since the PL enhancement is still observed when Alq_3 thickness is 20 nm according to Figure 3.19, this implies that the real recombination region of Alq_3 is less than 15 nm adjacent to NPB, and the rest of Alq_3 (> 5nm) and 6 nm BCP serve as spacers, it is consistent with the result reported in literature that the recombination zone of a bilayer diode could be less than 10 nm.[16] Therefore, we can solely attribute the EL enhancement (3.1-fold) to the increase of electron injection when the Alq_3

thickness is 60 nm since the separation between Ag NPs and Alq_3 emitting region is over 50 nm. Based on this estimate, we can conclude that the maximum PL enhancement factor 1.9-fold occurs on 30 nm-Alq_3 diode. However, the maximum PL enhancement factor is only 1.4 based on distance dependent PL enhancement trials, this deviation can result from the permittivity difference between Alq_3-BCP spacer and PVA spacer.

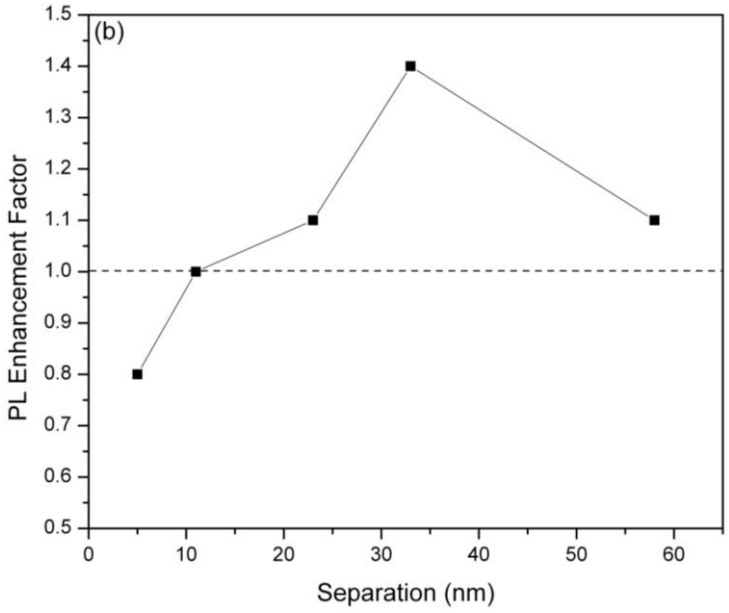

Figure 3.21 Distance dependent Alq_3 PL enhancement, PVA layer with various thicknesses is applied as spacer.

3.2.4 Conclusion

In this work we have incorporated metal NPs (silver and gold) into Alq_3 based SM-OLED. Burying NPs in either HTL NPB layer or ETL Alq_3 layer results in deteriorated device performance due to charge carriers trapping effect. However, the incorporation of metal NPs beneath the cathode Al helps electron injection and thus increases the luminous efficiency of the OLEDs. Silver is a better candidate than gold to optimize SM-OLEDs, probably due to its

different wetting ability on BCP to yield a discrete NP islands morphology. Here we need more microstructure study on BCP/Ag and BCP/Au to validate this hypothesis.

Ag NPs play dual role in improving SM-OLED EL efficiency. By increasing electron injection and promoting the radiative decay rate of excitons due to surface plasmon enhanced local electric field, silver NPs serve well as a surface plasmon resonance source and increase the OLED luminous efficiency up to 6-fold. Under the circumstance that an alkali metal was used to dope ETL to form an ohmic contact with the cathode regardless the cathode materials, silver was reported to be a better cathode than Al to increase OLED efficiency due to its lower absorption and higher reflectivity in the visible range.[31] However, that mechanism is entirely different from ours for OLED performance enhancement, since we employed nanostructured Ag as sharp tips instead of bulk Ag. It is the lightning rod effect together with plasmonic effect that contributes to the performance enhancement in our OLEDs.

3.3 Silver-Silicon Hybrid NPs Enhanced PHOLED Luminescence

3.3.1 Recent Advance on PHOLED

For the purpose of large-area display or illumination, solution processes utilizing polymeric materials, such as spin-coating or inkjet printing are feasible. However, a relatively low device efficiency of fluorescent polymer emitters unfortunately retards their practical application in polymer OLEDs. It is widely recognized that a phosphorescent emitter layer will provide a significant breakthrough in obtaining both large active area and high device efficiency, since in principle it could approach 100% internal quantum efficiency. In this regard, much effort has been devoted to demonstrate highly efficient electrophosphorescence from Ir or Pt complex.[32]

The application of OLEDs in the display industry strongly depends on three elemental colors: blue, green and red. So far, blue luminescence is still the bottleneck of OLEDs in both luminance intensity and lifetime. Most studied red phosphorescent molecules include $Btp_2Ir(acac)$, which has emission wavelength ca. 620 nm with HOMO at 5.1 eV and LUMO at 2.4 eV, platinum-based complex $Pt(thpy)_2$, europium and ruthenium complex.[33,34,35] Xia et al. reported a ruthenium-complex with rather high red emitting efficiency,[35] their OLED consists of an ITO anode, a PVK layer doped with 5 wt. % dye, a PBD hole-blocking layer, an Alq_3 ETL and a LiF/Al cathode. The maximum luminous efficiency was 8.6 cd/A at a brightness of 4 cd/m^2, which dropped notably to 2.6 cd/A at higher brightness 100 cd/m^2. Moreover, a high driving voltage of 21 V for a brightness 100 cd/m^2 compromises the high luminous efficiency of their diodes. Chen et al. reported a $btp_2Ir(acac)$ based red OLED, [36] which consists of ITO: PEDOT: PSS anode, a PVK: PBD (1:1) matrix doped with 4 wt. % dye, and Ca/Al cathode. The diode emits pure red light with maximum at 614 nm and peak EQE was 3.3 %, corresponding to 2.6

cd/A luminous efficiency at a brightness of 147 cd/m^2. Nakamura et al. reported a $btp_2Ir(acac)$ based OLED with higher efficiency by replacing 2-(4-Biphenylyl)-5-phenyl-1,3,4-oxadiazole (PBD), Ca with 1,3-bis[5-(p-tert-butylphenyl)-1,3,4-oxadiazol-2-yl]benzene (OXD-7) and Cs respectively,[37] the maximum luminance efficiency reached 4.3 cd/A corresponding to 5.5 % EQE.

For green phosphorescent emitters, Gong et al. demonstrated a single-layer device with EQE close to 10% corresponding to 36 cd/A luminous efficiency and 2.5 lm/W PCE.[38] Ca-electrode was used instead of the Mg-Ag cathode in their device fabrication, and a Tris[9,9-dihexyl-2-(pyridinyl-2')fluorine]iridium ($Ir(DPF)_3$) green emitter was used instead of $Ir(ppy)_3$. However their OLEDs required a high driving voltage of ca. 45 V. Tsutsui et al. reported a multilayer OLED with 6.5 wt.% $Ir(ppy)_3$ doped in a 4,4'-N,N'-dicarbazol-biphenyl (CBP) host,[39] which exhibited EQE 13.7% and PCE 38.3 lm/W at the brightness 105 cd/m^2. Surprisingly the driving voltage required for maximum efficiency was only 4.0 V and corresponding current density was 0.215 mA/cm^2.

With regard to blue emission, unfortunately only few phosphorescent dyes emit blue light. A widely studied blue-emitting Ir complex is Bis(2-(4,6-difluorophenyl)pyridyl-N,$C^{2'}$)iridiumpicolinate (FIrpic) with emission maximum at ca. 470 nm. Kawamura first reported FIrpic doped poly(9-vinylcarbazole) (PVK) PHOLED with highest efficiency 1.3% corresponding to 2.9 cd/A luminous efficiency at a dye concentration of 10 wt. %.[40] Interestingly, the device performance changed slightly when the dye concentration in PVK was increased from 2.5 wt. % to 10 wt. %. Provided charge injection barriers were decreased and electron transport molecules were added, the performance of FIrpic based blue PHOLED could be significantly increased. A superior blue OLED with structure ITO/PEDOT:PSS/PVK: OXD-7: FIrpic (12 wt. %)/ Ca/Al was developed by Tanaka et al.[41] The maximum EQE was reported to be 5.9% corresponding to luminous efficiency 12 cd/A.

So far, PHOLED represents the state of the art OLED. Thus any development and optimization of PHOLEDs would be of great scientific and economical significance. In this research, we aimed to increase PHOLED luminescence via metal NPs surface plasmon. Hybrid nanostructure consisting of a metal core and an insulator shell was synthesized and incorporated into PHOLED, here an insulator shell is coated on the Ag NPs intentionally to avoid exciton quenching and this will be interpreted in detail in the following discussion section. Surface plasmon enhanced PHOELD luminous efficiency was observed and the underlying mechanisms were disentangled.

3.3.2 Experimental

Silver NPs were obtained in traditional sodium citrate reducing method.[42] 90 mg $AgNO_3$ was dissolved in 500 mL of distilled water and the solution was heated to boil. 1% sodium citrate aqueous solution (10 mL) was added and the blend was kept boiling under stirring for 1 hour, the color change of the blend from milk white to greenish yellow indicates the formation of silver NPs. The large particles were removed by centrifugation at 500 rpm for 1 hour.

Silver NPs with different silica shell thickness were prepared as follows: 50 mL silver NPs aqueous solution was dissolved in 200 mL ethanol, the pH of the solution was adjusted to 10 by adding 6.5 mL 30 wt.% ammonia. Subsequently, 1 mL tetraethylorthosilicate (TEOS) ethanol solution (10 mM) was added into silver NPs solution every 30 minutes, in total X mL (X=2, 5, 10 and 30) TEOS ethanol solution were added to obtain different silica layer thickness. The Ag-SiO_2 core-shell NPs and pure silver NPs obtained from 50 mL initial silver NPs aqueous solution were finally dispersed into 8 mL chlorobenzene.

PHOLEDs were fabricated with a structure shown in Figure 3.22. PEDOT: PSS was spin coated on pre-cleaned ITO glass at the speed of 4000 rpm, and baked in vacuum oven at 110 ºC

for 30 min. Subsequently, the emitting layer consisting of PVK (68.4 wt. %), PBD (29.4 wt. %), $Ir(ppy)_3$ (2.2 wt. %) in chlorobenzene was spin coated on top of PEDOT: PSS layer at the speed of 3000 rpm. Here PBD is employed to facilitate the electron transport in polymer matrix. Subsequently 6 nm BCP as an exciton blocking layer and 30 nm Alq_3 as an electron injection/transport layer were evaporated followed by 200-nm aluminum under 10^{-6} mbar vacuum. Bare Ag NPs or silica coated Ag NPs were incorporated into OLED devices by dispersing them into chlorobenzene solution and mixing with emitting layer solution, the blend was spin coated on top of PEDOT layer after 10-minute treatment in sonication bath. A protocol is listed as follows: 400 μL Ag-SiO_2 NPs or bare Ag NPs chlorobenzene solution is added into 400 μL emitting layer solution to make the PVK concentration in chlorobenzene 20 mg/mL.

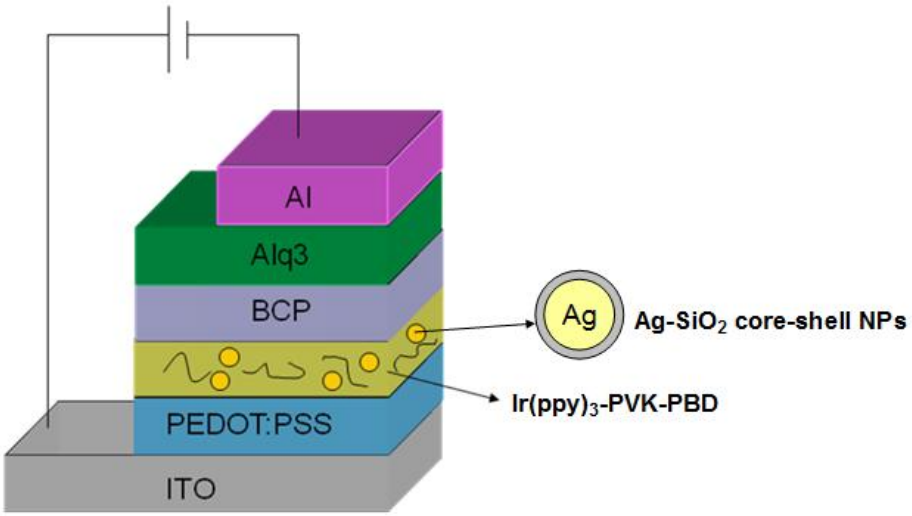

Figure 3.22 Configuration of PHOLED doped with silver-silica core-shell NPs.

Polyvinylcarbazole (PVK), 2-(4-biphenylyl)-5-(4-tert-butylphenyl)-1,3,4–oxadiazole (PBD, 99%), silver nitrate, and tris(2-phenylpyridine)iridium ($(Ir(ppy)_3$, 99%) were purchased

from Aldrich, Poly (3, 4-ethylenedioxythiophene) poly (styrenesulfonate) (PEDOT: PSS, PH1000) was obtained from Clevios.

The UV-Vis spectra were recorded on a Lambda 20 spectrometer (PerkinElmer). Transmission electron microscopy (TEM) images were taken on a Hitachi-7000 Instruments operated at 75 kV. The EL spectrum was measured by USB2000-Ocean Optics spectrometer. The current-voltage curves were measured on Keithley (4200-SCS), and the EL brightness was measured using our homemade setup.

3.3.3 Results and Discussion

To investigate the microstructure of the silver colloids and meanwhile verify if the silica layer wraps on Ag colloids surface successfully, we took the dark field TEM images of the Ag NPs growing in solution with different TEOS concentrations as shown in Figure 3.23. There are clearly two different contrasts in all the TEM images, the bright white one is assigned to the Ag NPs core due to its heavy elemental mass, and the dim halo is assigned to the SiO_2 shell which scatters electrons moderately. Moreover, it shows that shell thickness can be readily tuned by adjusting the amount of TEOS for polycondensation. The more TEOS added for shell growth, the thicker the SiO_2 shell. As a result, we successfully obtained silica shell thickness 7 nm, 13 nm, 27 nm and 60 nm respectively.

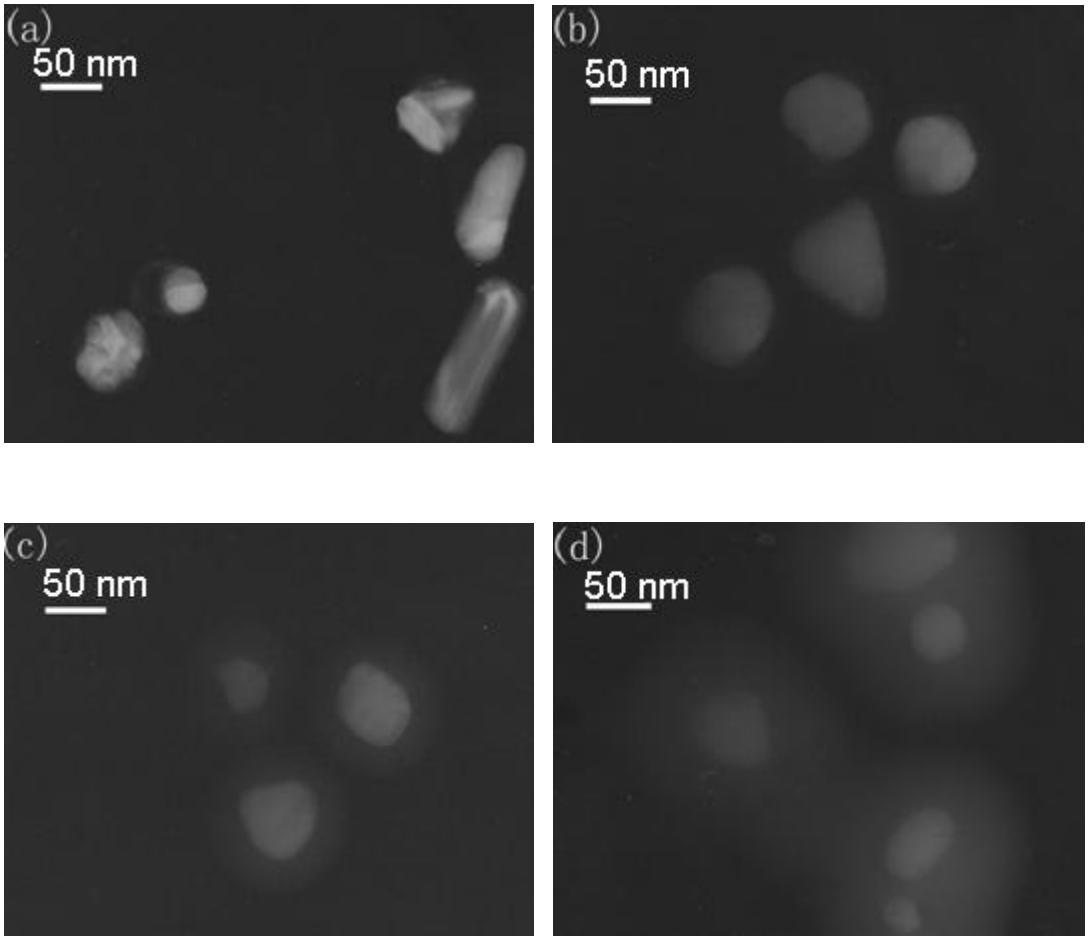

Figure 3.23 TEM images of Ag-SiO_2 core shell NPs with different shell thickness, (a) 2 mL, (b) 5 mL, (c) 10 mL, and (d) 30 mL TEOS (10 mM) is added for shell growth. [43]

The UV-Vis spectra presented in Figure 3.24 exhibit the evolution of silver surface plasmon resonance with coating and growth of SiO_2 on the surface of the colloidal silver. The peak wavelength at 445 nm of the bare silver colloids represents the typical surface plasmon resonance. With the increase of the shell thickness, the surface plasmon resonance peak shifts to longer wavelength; this red-shift results from the local environment, namely, refractive index change on metal surface according to surface plasmon theory.[44] It further confirms the formation of Ag-SiO_2 hybrid nanostructure. Recalling the equations (1.1), (1.2), (1.3) in Chapter 1, one can

derive the following equation relating the surface plasmon resonance frequency with dielectric constant of the surrounding medium:

$$\omega^2 = \frac{\omega_p^{\ 2}}{2\varepsilon_d + 1} \tag{3.8}$$

With the coating of a silica layer, the refractive index n of the surrounding medium increases. If one takes $\varepsilon_d = n^2$, the surface plasmon resonance frequency should decrease with silica coating corresponding to a red shift of the resonance wavelength. The EL spectrum of PHOLEDs as shown in Figure 3.25 exhibits the electroluminescence feature from $Ir(ppy)_3$ exclusively, it implies a very efficient energy transfer from the host PVK to the dopant $Ir(ppy)_3$. [45]

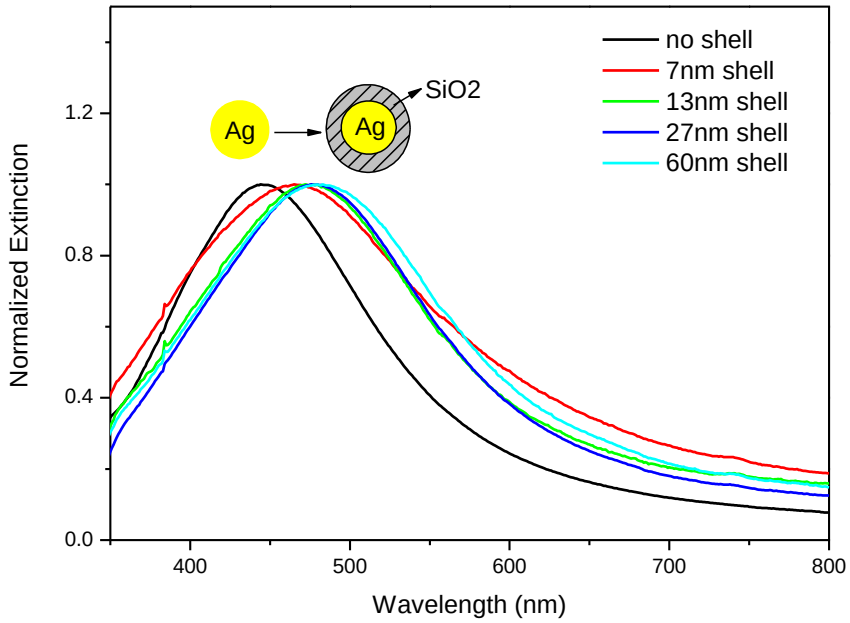

Figure 3.24 Extinction spectra of Ag-SiO_2 NPs with different shell thickness dispersed in ethanol.

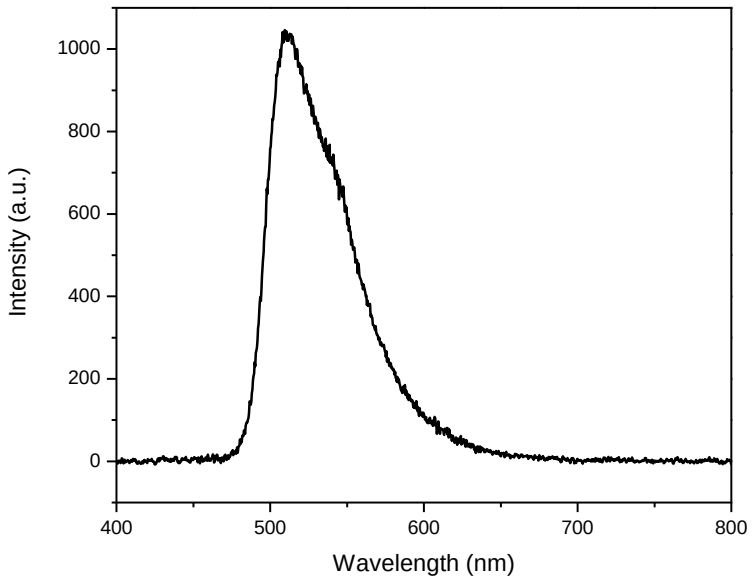

Figure 3.25 EL spectrum of fabricated PHOLEDs

We measured the current density-voltage curves of PHOLEDs incorporated with Ag-SiO_2 NPs and bare Ag NPs respectively as presented in Figure 3.26. Interestingly, the current density of the PHOLED with bare silver NPs dopant in emitting layer increases remarkably, which indicates that doping silver NPs increases the charge carriers mobility in the emitting layer. In the present PHOLED configuration holes were reported to be trapped by $Ir(ppy)_3$ and exciton recombination takes place on phosphorescent dye.[45] A slow electron transport process is believed to be the limiting step for effective exciton formation and recombination, which is thus responsible for high driving voltage for this PVK-$Ir(ppy)_3$ phosphorescent OLED. Therefore, electron transport molecules such as PBD, OXD-7 are normally added into the emitting layer to increase the electron mobility and thus device performance. In our case, it is more likely that silver NPs increase the electron mobility in the emitting layer due to the establishment of additional conductive pathway from the silver islands bridge. In theory this should increase device efficiency due to more balanced hole/electron ratio.

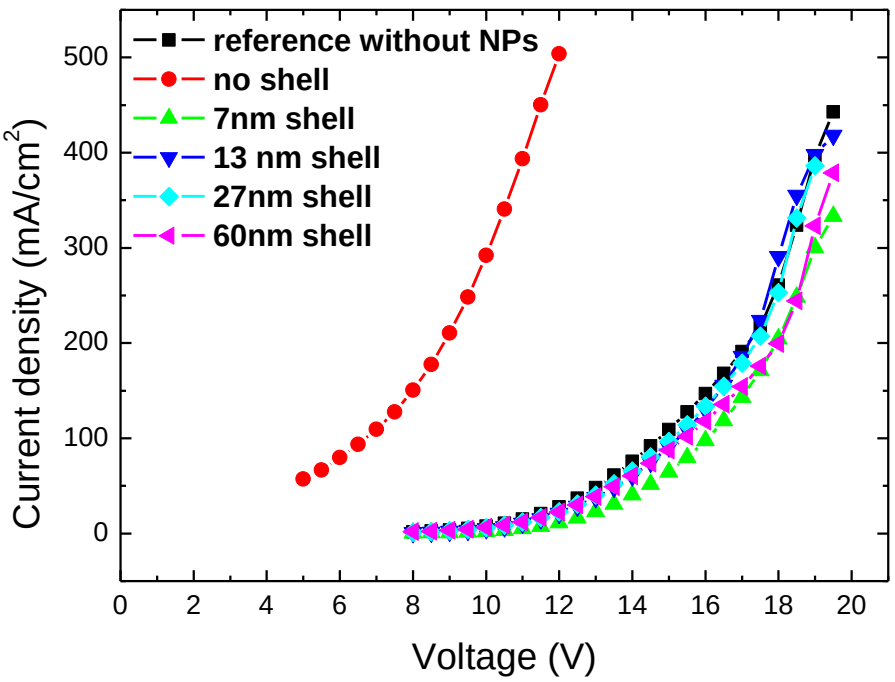

Figure 3.26 J-V curves of PHOLEDs doped with Ag-SiO_2 NPs of different silica shell thickness but same particle concentration. [43]

The luminous efficiency-current density curves of the PHOLEDs doped with silver NPs of different silica shell thickness are presented in Figure 3.27. Surprisingly, the luminous efficiency of the PHOLED doped with bare silver NPs is depressed greatly compared to the reference OLED. This contradicting result indicates that other competitive mechanisms cannot be ruled out. It is reported that bare silver NPs can cause charge carrier recombination on its surface,[46] which could lead to exciton quenching and thus reduce the device performance. Moreover, bare Ag NPs could also quench the luminescence of $Ir(ppy)_3$ if the phosphorescent dye molecules are in the vicinity of Ag NPs according to the radiative plasmon model.[24] As a consequence, the quenching effect from bare Ag NPs is dominant and results in the reduction of luminous efficiency, although bare NPs can effectively lower the driving voltage of the present PHOLED.

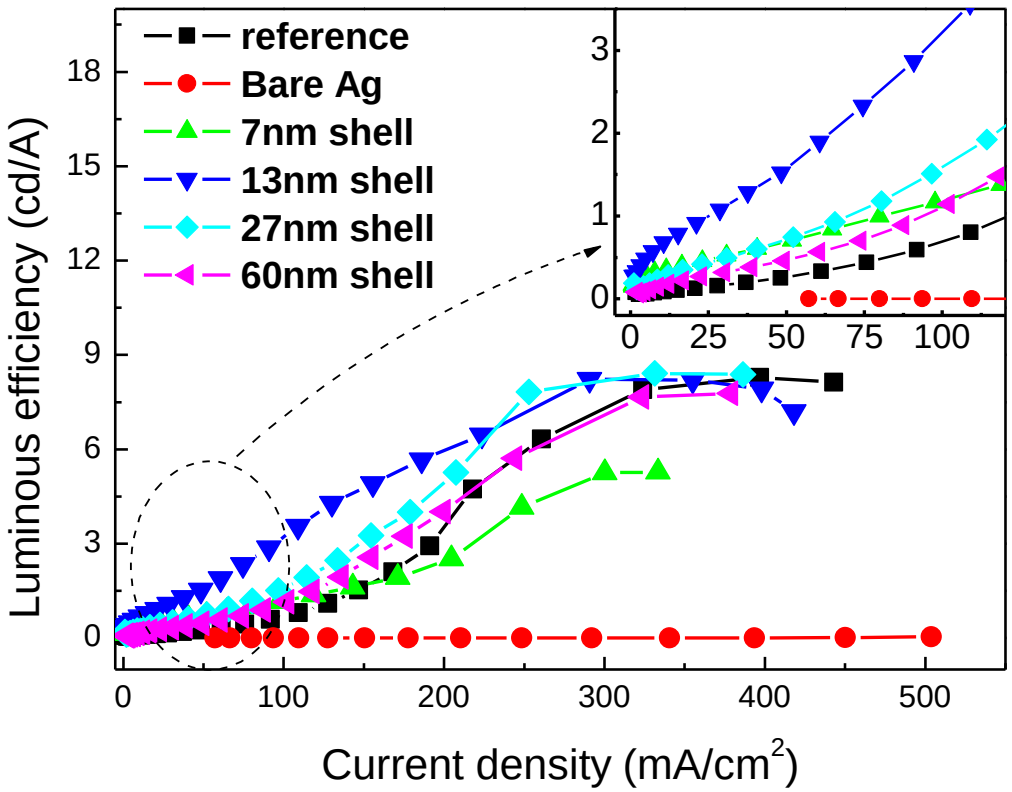

Figure 3.27 Luminous efficiency Vs. current density curves of PHOLEDs doped with Ag-SiO_2 NPs of different silica shell thickness but identical particle concentration.[43]

Therefore we coated a silica spacer on the Ag NPs surface. Our motivation is to avoid the luminescence quenching after blending Ag NPs with phosphorescent dye molecules. As shown in Figure 3.26, the current densities of the PHOLEDs incorporated with Ag-SiO_2 NPs do not show obvious differences from that of the reference. This can be ascribed to the insulating nature of the silica shell, which cannot offer electrons a shortcut to pass through the emitting layer and thus does not favor the charge mobility increase.

Although doping Ag-SiO_2 in the emitting layer cannot lower the driving voltage of the devices, the luminous efficiency of the PHOLEDs with Ag-SiO_2 NPs shows remarkable increase in the low current density region as shown in Figure 3.27. In the high current density region the maximum luminous efficiency of all the PHOLEDs tends to be identical except the one doped

with Ag-SiO_2 NPs of 7 nm shell. Since the quantum efficiency of $Ir(ppy)_3$ is close to 100%,[47] the limited effect of Ag-SiO_2 NPs on improving the maximum luminous efficiency of $Ir(ppy)_3$ is not a surprise. The reduced maximum luminous efficiency by doping Ag-SiO_2 NPs of 7 nm shell thickness suggests that the surface plasmon quenched dye luminescence is still present, and indicates that a 7 nm silica shell is an insufficient spacer to avoid luminescence quenching.[24] As the shell thickness is increased to 13 nm or above, no suppression on maximum luminous efficiency is observed, which implies that a 13 nm silica spacer is necessary to eliminate metal induced luminescence quenching on phosphorescent dye.

The luminous efficiency enhancement effect in the low current density region (i.e. low voltage region), is attributed to increased exciton formation probability by surface plasmon as shown in Figure 3.28. In the low field case, the holes are trapped by the dye molecules; the electron density is low and so is the recombination probability which is proportional to the product of electron and hole densities. However, local electric field at Ag NPs may enhance the cross section for electron-hole capture and in consequence the recombination probability. It is notable that Ag-SiO_2 NPs with 13 nm shell contribute maximum enhancement to PHOLED luminous efficiency, which corresponds to an optimized tradeoff between charge recombination and exciton quenching. Whereas under the high E-field (i.e. high current density region), the exciton formation probability saturates due to high electron number density in emitting layer even in the absence of surface plasmon, in this high field case, surface plasmon induced E-field cannot increase PHOLED luminous efficiency anymore.

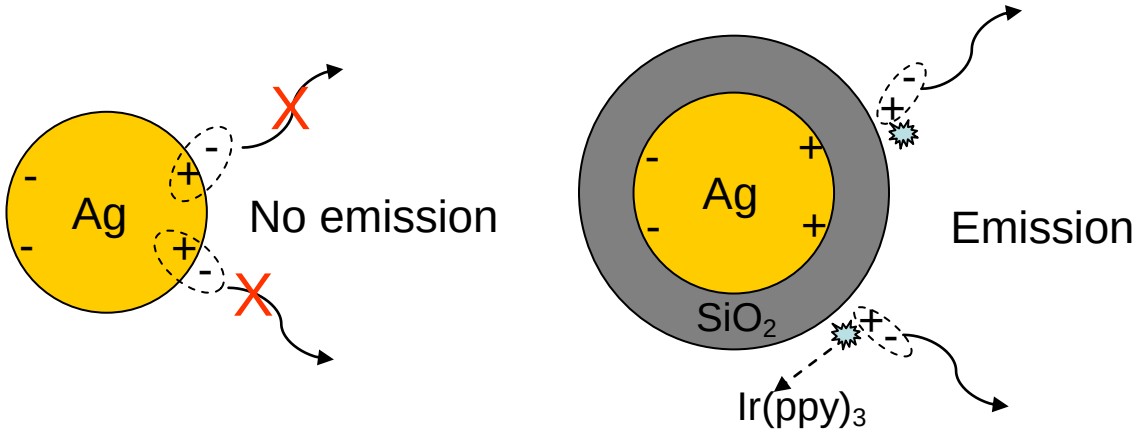

Figure 3.28 Schematic diagram interpreting surface plasmon enhanced $Ir(ppy)_3$ electroluminescence.

Figure 3.29 presents the variation of the PHOLED luminance efficiency with brightness. Although the PHOLED efficiency is not enhanced at high brightness > 30, 000 cd/m^2, we can clearly observe that the PHOLED luminance efficiency is increased by a factor of 3 at a moderate brightness 200 cd/m^2 (display industry standard brightness) via doping Ag-SiO_2 NPs, which is important for practical display application. The joule heat generated inside OLED is one of the device degradation factors due to facilitated crystallization of amorphous organic materials. Therefore the increase of PHOLED luminous efficiency by incorporating Ag-SiO_2 NPs will not only cut down power consumption but also reduce unwanted joule heat in the device, prolonging the device working lifespan.

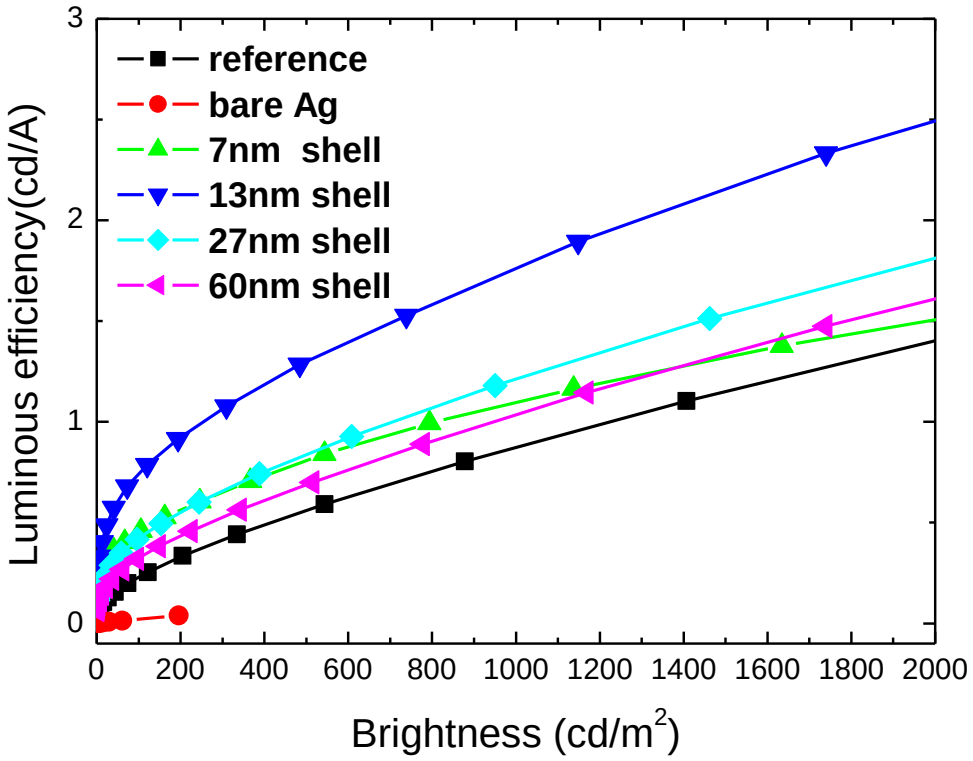

Figure 3.29 Luminous efficiency vs. brightness curves of PHOLEDs doped with Ag-SiO_2 NPs of different silica shell thickness but same particle concentration.[43]

3.3.4 Conclusion

Silica coated Ag hybrid NPs were synthesized and used into PHOLEDs successfully. Doping bare silver NPs into PHOLED reduces device performance due to unwanted exciton recombination on NPs as well as metal induced luminescence quenching. Ag-SiO_2 core-shell structure, however, can increase the luminous efficiency of the PHOLEDs. The silica shell serves as a spacer to avoid luminescence quenching and an insulator to avoid charge recombination in the close vicinity of the Ag NPs surface. A 13 nm or above shell thickness is needed to avoid luminescence quenching. The surface plasmon of silver NPs can notably increase the PHOLED luminous efficiency under low current density by favoring exciton formation; however that is no longer valid under high current density since exciton formation probability becomes saturated.

3.4 Hybrid OLED Based on Dye Functionalized Ag-SiO_2 Nanoparticles

3.4.1 Background

To date various methods have been developed to optimize OLEDs' efficiency. The replacement of fluorescent emitters by phosphorescent emitters increases the internal quantum efficiency by taking advantage of triplet state recombination;[16] doping HTL to reduce hole mobility and balance hole/electron ratio renders much higher external efficiency to the diodes;[48] designing surface texture to reduce the light trapping is another way to increase diode efficiency.[49] Moreover, surface plasmon of noble metal NPs is also an effective way to optimize OLED performance by favoring charge injection and exciton formation etc. as demonstrated by our group.

In view of the enhancement effect of surface plasmon on chromophore luminescence and photostability,[30] the development and investigation of metal NPs-chromophore hybrid structures in OLED luminescence application becomes promising. It may potentially increase diode luminous efficiency and also prolong the working lifespan of a diode. Only little research however has been dedicated to this scope so far.

Wu et al. reported a green polymeric OLED based on poly(9,9-dioctylfluorene-alt-thiophene) (PDOFT) polymer linked gold NPs.[50] The root-mean-square roughness of the PDOFT-Au film is nearly ten times higher than that of PDOFT film, resulting in an increased interfacial contact area between the emitting layer and the deposited cathode. The increased interfacial area together with the photo-oxidation-suppressing and hole-blocking characteristics of the Au NPs yield a superior performance of this polymer OLED. Increased electron injection, lowered

threshold voltage together with increased brightness and luminous efficiency were observed in gold NPs modified device, particularly the luminous efficiency gains one order of magnitude increase, it shows great prospect to investigate the application of metal NPs functionalized luminescent molecules in OLEDs.

Riedel et al. reported increased polymer OLED luminescence by doping SiO_2/TiO_2 clusters. [51] They found that incorporation of pure SiO_2 led to the most efficient diode performance with increased luminous efficiency up to 4-fold at 60 mA/cm^2. The scattering effect of nanocluster can be ruled out for the enhancement effect. The underlying mechanism was ascribed to a randomly nanopatterned cathode layer created by the SiO_2 NPs which in turn increases the electric field at the organic-cathode interface and favors electron injection. The concept of rough surface facilitating charge injection is also valid in our proposed diode design.

In this research, we fabricated novel rhodamine dye functionalized silver-silica core-shell nanostructures. The silica shell is particularly designed to avoid fluorescence quenching, which is rigid and robust compared to the protein spacer used in Chapter 2. Moreover we studied the photostability of hybrid NPs and surface plasmon enhanced PL; exciplex induced EL spectral broadening was proposed; time resolved EL was measured and the charge transport process in the OLEDs was disentangled.

3.4.2 Experimental

Silanized rhodamine B was synthesized in the way described by Nedelcev:[52] 0.96 g rhodamine B was dissolved into 30 mL chloroform. The solution was heated to boil under vigorous stirring. 0.002 mol (0.465 mL) APTES was added to the RB solution dropwise. The water formed during the condensation reaction was distilled out. 30 minutes later, the reaction was stopped and the chloroform was removed by rotovap. A red product of silanized rhodamine

B was obtained (100% yield). **^{1}H-NMR** (400 MHz, $CDCl_3$, δ): 8.00 (1H, d), 7.60 (2H, dt), 7.20 (1H, d), 6.60 (2H, d), 6.46 (2H, d), 6.36 (2H, dd), 3.81 (6H, q), 3.37 (8H, q), 2.94(2H, s), 1.85 (2H, s), 1.15-1.25 (21H, m), 0.69 (2H, s). The proton NMR spectrum of our product is consistent with the literature report which provides further evidence for the identity of silanized rhodamine B.

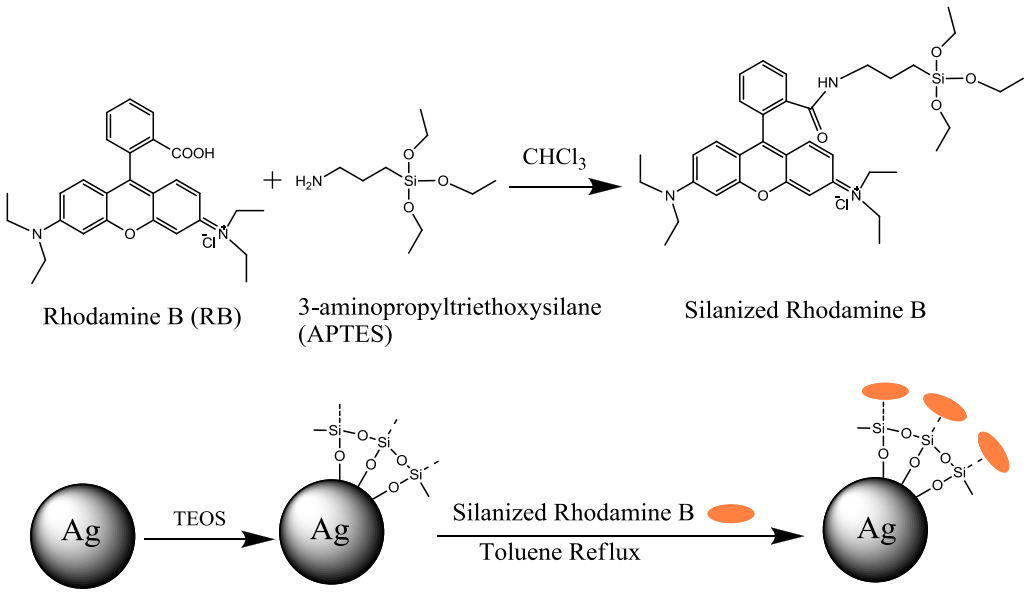

Figure 3.30 Schematic diagram for silanized Rhodamine B synthesis and Ag-SiO_2-RB hybrid NPs fabrication.

The synthesis of silica coated silver NPs was achieved using the same recipe described in section 3.3.2. The link of silanized rhodamine B with Ag-SiO_2 NPs was accomplished as follows: Ag-SiO_2 NPs obtained from the initial 100 mL silver NPs aqueous solution was then dispersed into 50 mL anhydrous toluene, and the silanized rhodamine B obtained from the above batch together with 314 µL (1 mmol) triethoxy(octyl)silane were added into the NPs solution, the obtained mixture was refluxed at 110ºC for 12 hours under dry nitrogen atmosphere. Here the triethoxy(octyl)silane is used to increase the solubility of the hybrid NPs in organic solvents. The functionalized NPs were separated from solution by centrifugation, washed with toluene three

times and dried in a vacuum oven overnight. The dark reddish powder implies RB was successfully linked to Ag-SiO_2 NPs via covalent bond. This type of hybrid NPs does not have appreciable solubility in organic solvents probably due to the formation of cluster aggregation, and chloroform is determined as the best solvent for it.

The obtained hybrid NPs were used as the emitting layer of OLEDs as shown in Figure 3.31. A hole injection layer PEDOT:PSS was spin coated on pre-cleaned ITO glass at a speed of 4000 rpm for 40 seconds. The spin coating method was attempted for hybrid NPs deposition, but only small amount of the NPs could be deposited on the slide due to the low viscosity leading to the short circuit of the device. The addition of a polymer matrix could increase the viscosity of the solution yielding a thicker film, but it would result in the drop of the conductance in the emitting layer for the non-conjugated polymer, and unwanted fluorescence for the conjugated polymer. Thus we designed a homemade setup for hybrid NPs deposition in a spray method which can avoid the usage of a polymer matrix.

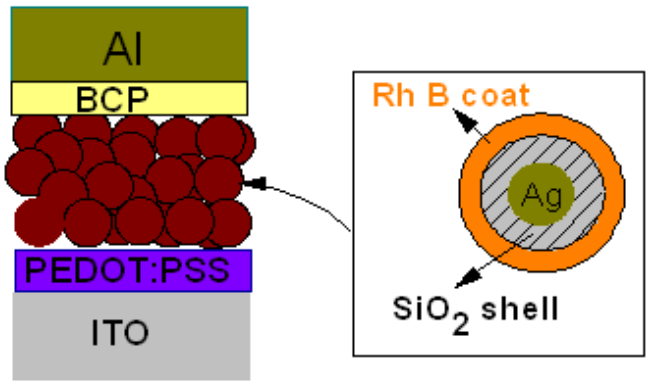

Figure 3.31 Schematic diagram of our hybrid NPs based OLED. [53]

Our homemade setup for NPs spray deposition is shown in Figure 3.32. It consists of a capillary tube inside a well sealed external pipe with a tiny aperture at the bottom which only allows the capillary tube passing through it. A solution of the dispersed hybrid NPs in chloroform

goes through the capillary tube and drips to the aperture of the external tube. A N_2 flow is blown from the side arm of the external tube at the speed of 3.5 L/minute, causing the pressure to build up drastically at the aperture of the external tube, which atomizes the droplet. Our PEDOT coated ITO substrate is placed 5 cm underneath the aperture; a uniform and thick enough NPs film can be obtained in such a way. A protocol is listed as follows: 5 mg hybrid NPs are dissolved in to 3 mL chloroform and dispersed with sonication bath for 10 minutes before spray. 1 mL suspension yields an emitting layer of one diode.

After the deposition of the hybrid NPs, the substrate was transferred into the vacuum chamber, and a 6 nm BCP hole blocking layer was deposited by thermal evaporation, finally 200 nm Al was deposited as cathode.

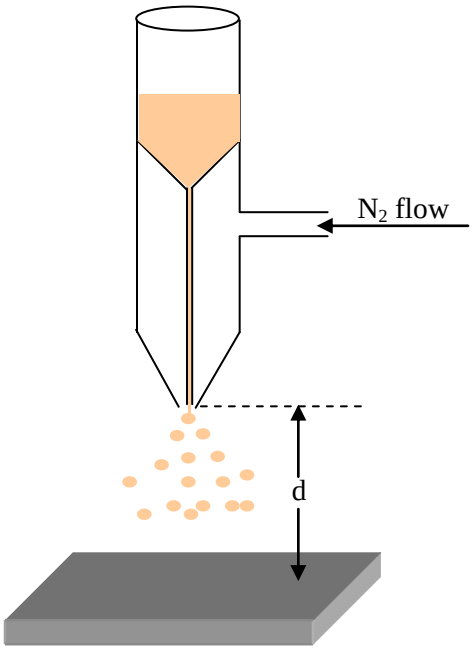

Figure 3.32 Homemade setup for NPs spray deposition.

The UV-Vis spectra were recorded on a Lambda 20 spectrophotometer (PerkinElmer). AFM images were taken on the Ambios multifunction microscope running in AFM mode. The EL spectra were measured by USB2000-Ocean Optics spectrometer. The current-voltage curves were measured on Keithley (4200-SCS), and the EL brightness was measured with our homemade setup.

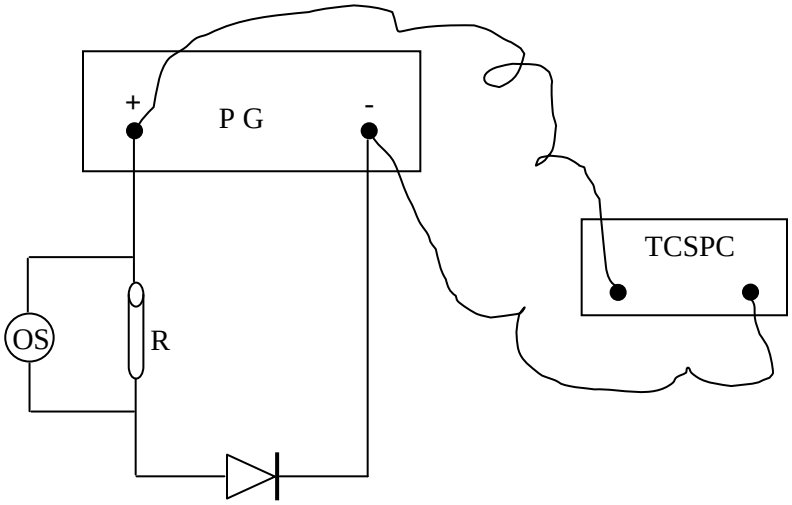

Figure 3.33 Schematic diagram of our time resolved electroluminescence measurement. PG refers to a pulse generator, OS refers to oscilloscope used to measure the voltage drop across the resistance R. TCSPC is the counting module connected to single photon avalanche detectors.

Time resolved EL luminescence was tested in the configuration shown in Figure 3.33, using the Keithley (4200-SCS) as pulse generator. A square voltage pulse with amplitude 15 V was applied in the circuit. The duty cycle was 50%, and both rise and fall time was set to minimum 1 μs, and the pulse width was 100 μs. The Keithley (4200-SCS) was also used as an oscilloscope to measure the voltage drop on a resistance (100 Ω) which was connected in series with the OLED, so that the current passing through the OLED could be obtained by calculating the current from the resistance. A synchronous pulse signal from the Keithley (4200-SCS) was

also sent to the Time Correlated Single Photon Counting (TCSPC) Module (SensL), which links to Single Photon Avalanche Detectors (SPAD). In general, the counting module keeps track of arrival time of the OLED photon at the detector with respect to the electric pulse generated from Keithley giving the histogram of all the luminescence photons.

3.4.3 Results and Discussion

Figure 3.34 shows the UV-Vis spectra measured at each functionalization step, from the bare silver NPs, silica coated Ag NPs to Ag-SiO_2-RB hybrid NPs. The pure silver NPs dispersed in ethanol shows an absorption peak at 440 nm, which represents the typical resonance peak of metallic silver. When the silver NPs are coated by silica, the absorption peak red shifts to 480 nm, this can be attributed to the refractive index increase as we interpreted in section 3.3.3. With the binding of RB onto silver-silica NPs, the extinction spectrum evolves into a broad hump with absorption maximum around 550 nm which is identical to that of pure RB. It should result from the superposition between silver NPs surface plasmon and RB absorption. In addition, the absorption broadening could be ascribed to longitudinal resonance modes from elongated Ag NPs clusters. [54]

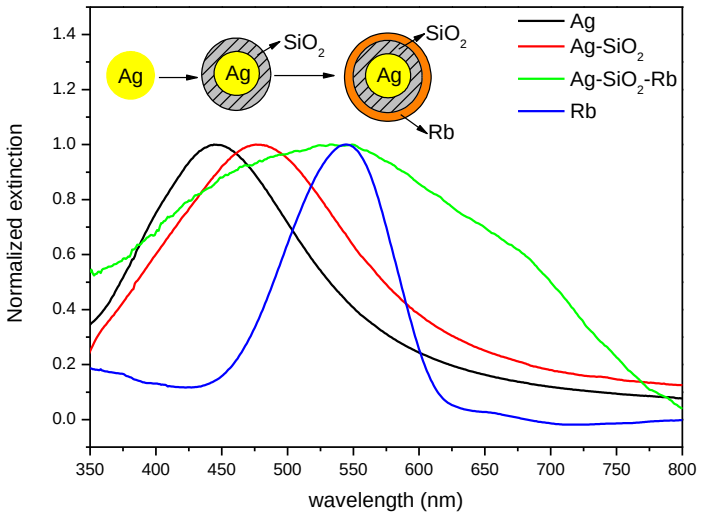

Figure 3.34 Evolution of the extinction spectrum from Ag NPs to Ag-SiO_2 core-shell NPs till Ag-SiO_2-RB hybrid NPs. [53]

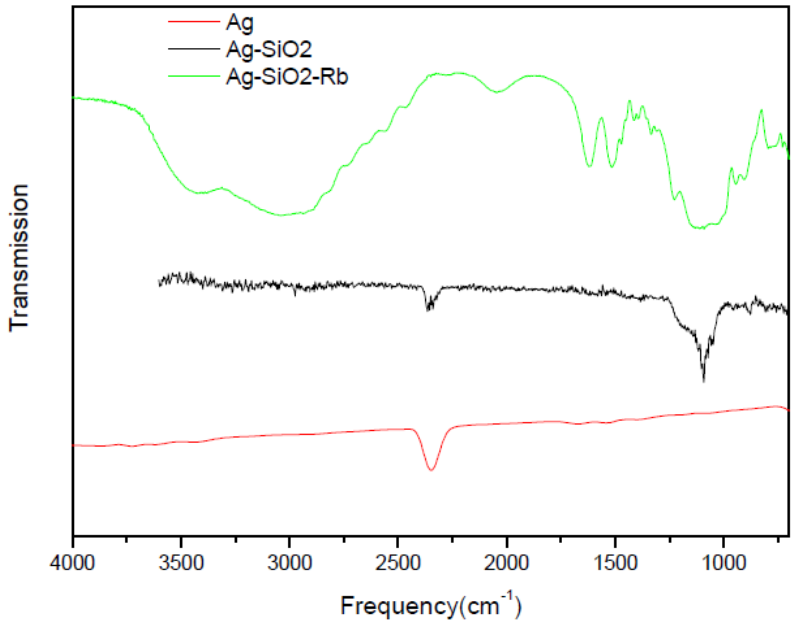

Figure 3.35 Infrared spectra comparison of bare Ag, Ag-SiO_2 and Ag-SiO_2-RB nanostructure.

In addition, we also investigated the FTIR spectra of the NPs before and after functionalization as shown in Figure 3.35. Bare silver NPs have no IR peak except the one around 2200 cm^{-1}, which is assigned to the CO_2 from the atmosphere. The silica coated silver NPs have a notable peak around 1100 cm^{-1}, which is a typical Si-O stretch peak, this confirms that silica was coated on Ag NPs surface successfully. For Ag-SiO_2-RB NPs, there are numerous peaks emerging in its IR spectrum. The peak at 1620 cm^{-1} is a typical stretching vibration peak of an amide, the peaks at 2800~2900 cm^{-1} can be assigned to methyl group vibration, and a broad peak at 3000~3500 cm^{-1} can be ascribed to the vibration of a secondary amine N-H bond, this further confirms that RB is attached to the surface of the silver-silica core-shell NPs.

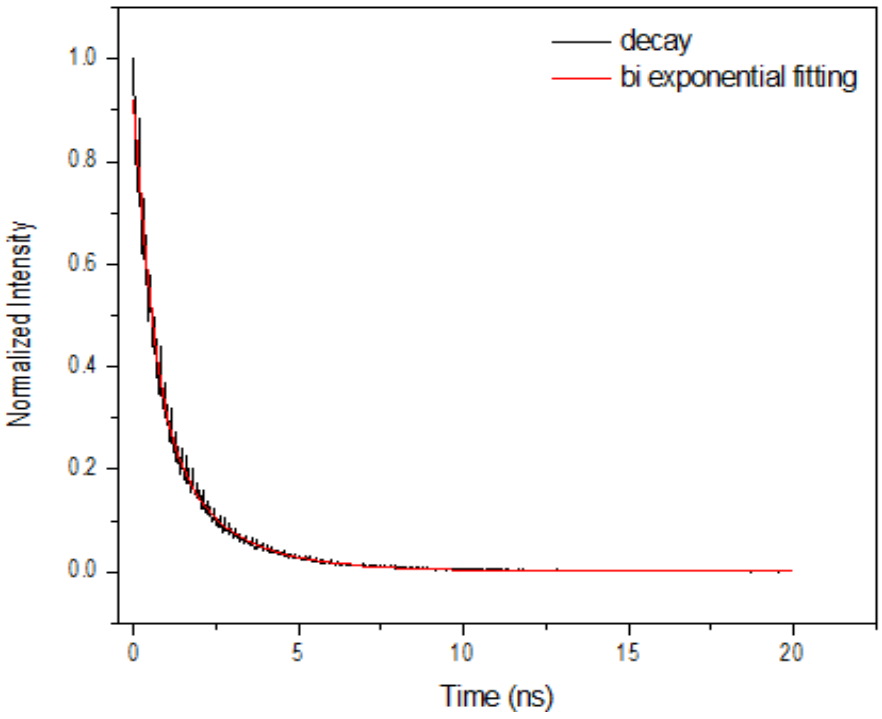

Figure 3.36 Time resolved PL decay of Ag-SiO_2-RB hybrid NPs. [53]

We measured the luminescence lifetime of the hybrid NPs; the time-correlated single photon counting PL intensity decay curve shown in Figure 3.36 can be fitted with biexponential decay. As a result, two lifetime components 0.58 ns and 1.96 ns are obtained. However the lifetime of RB in solution is reported as long as 7 ns. [55] The much shorter lifetime component from hybrid NPs can be attributed to metal enhanced radiative decay rate of the exciton, which means that the electrons in the excited state have greater probability to relax back to the ground state via photoluminescence channel instead of phonon relaxation which is a nonradiative decay. As a result, the photoluminescence quantum efficiency is increased and consequently the fluorescent lifetime is shortened. We attribute the longer lifetime component to the part of the RB molecules which are oriented away from the silver NPs, they thus experience lower enhancement effect. The 1.07 ns average lifetime implies that hybrid NPs may have better photostability than pure RB molecules for which degradation channels have larger probability.

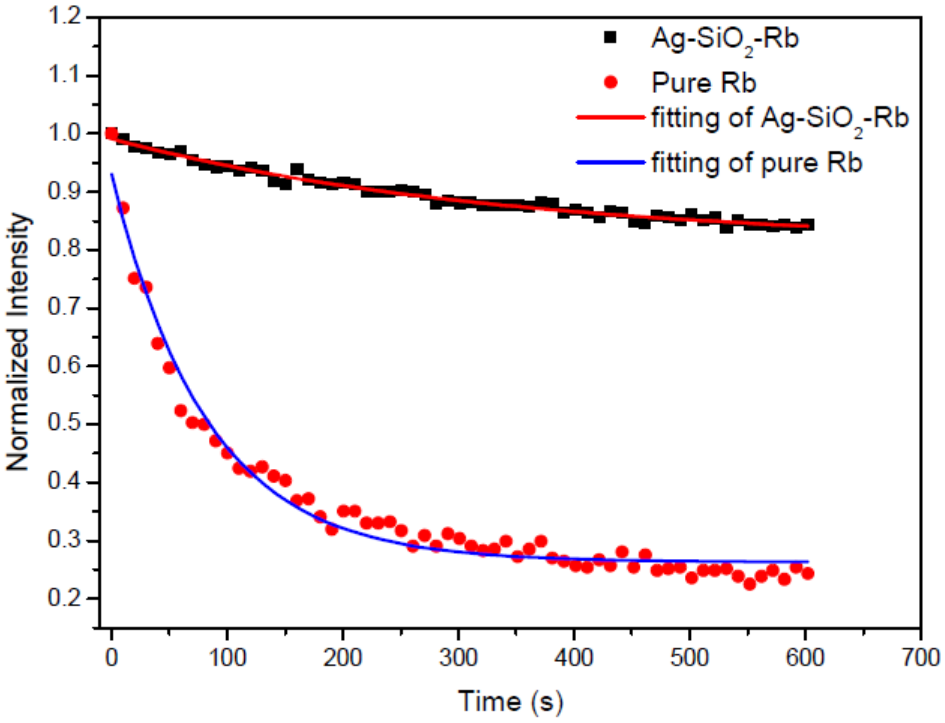

Figure 3.37 Photobleaching of pure RB and Ag-SiO_2-RB hybrid NPs on glass substrate, samples were irradiated by 200 mW/cm^2 Nd-YAG (532 nm) laser. [53]

We investigated the photostability of hybrid NPs by recording the PL intensity evolution under irradiation of 532 nm laser light (Nd^{3+}-YAG, 200 mW/cm^2). As shown in Figure 3.37 the PL intensity of the hybrid NPs degrades to 85% of their original intensity after 600 seconds exposure; while it only takes 10 seconds for pure RB to reach the same intensity decay. This remarkable increase of photostability indicates that the hybrid NP is a highly stable light source which might find potential application in single photon emitting devices.

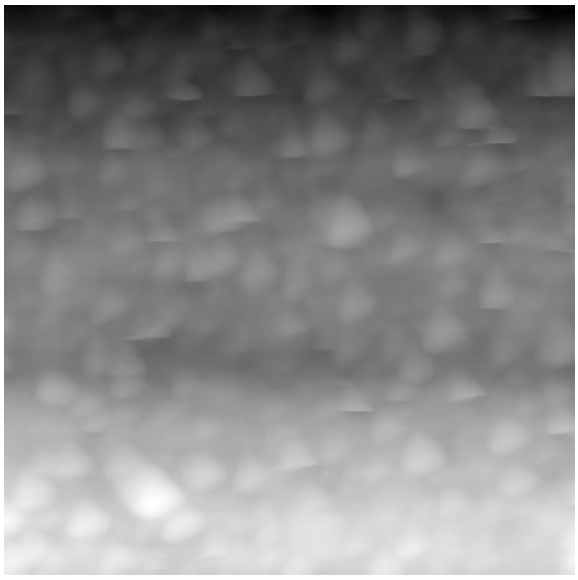

Figure 3.38 AFM image (1×1 μm^2) of sprayed Ag-SiO_2-RB hybrid NPs. [53]

The AFM profile of the spray deposited hybrid NPs on the substrate is shown in Figure 3.38. The hybrid NPs have quite even distribution, and it is clearly observed that the emitting layer consists of a NPs multilayer, this stacked NPs structure ensures enough thickness for the emitting layer and thus prevents the device from current leakage and short circuit.

We have investigated the performance of OLEDs with hybrid NPs and pure RB as emitting layers. The J-V curves are shown in Figure 3.39. Both diodes present very good rectification characteristic. However, the hybrid NPs diode has higher turn-on voltage compared with the pure RB diode, which can be attributed to deep charge trapping in the hybrid NPs layer. The luminance–current density curves of both diodes are shown in Figure 3.40. Notably, the hybrid NPs diode presents much higher luminance intensity compared to pure rhodamine B diode under the same current density, the maximum luminous efficiency of the hybrid NPs diode is estimated to be 6.8 fold higher than that of the RB diode. This benefits from the surface plasmon enhanced luminescence.

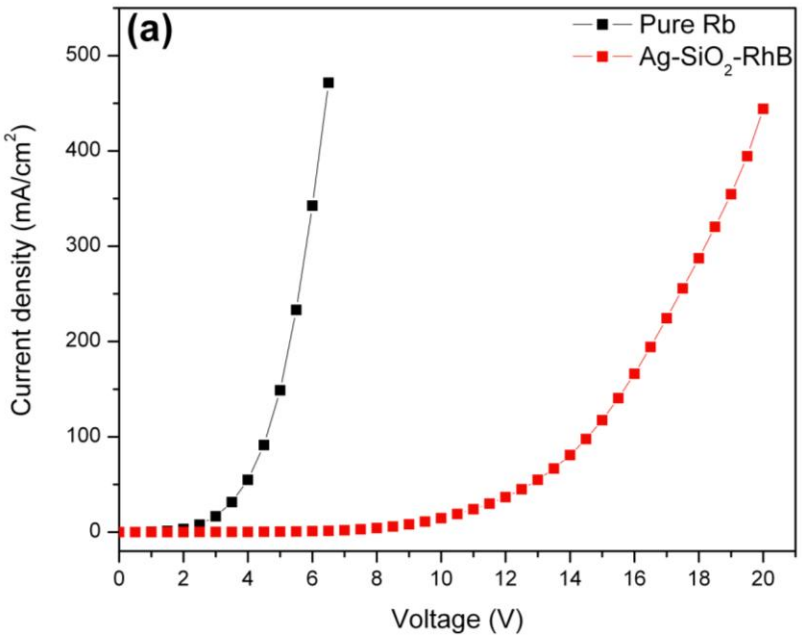

Figure 3.39 J-V curves of OLEDs with pure rhodamine B and hybrid NPs as emitting layers. [53]

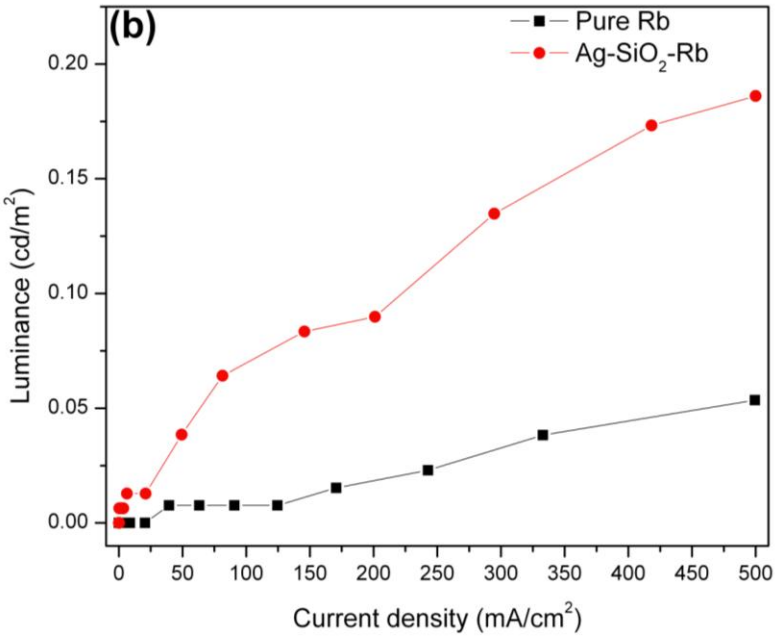

Figure 3.40 Luminance-current density curves of OLEDs with pure rhodamine B and hybrid NPs as emitting layers. [53]

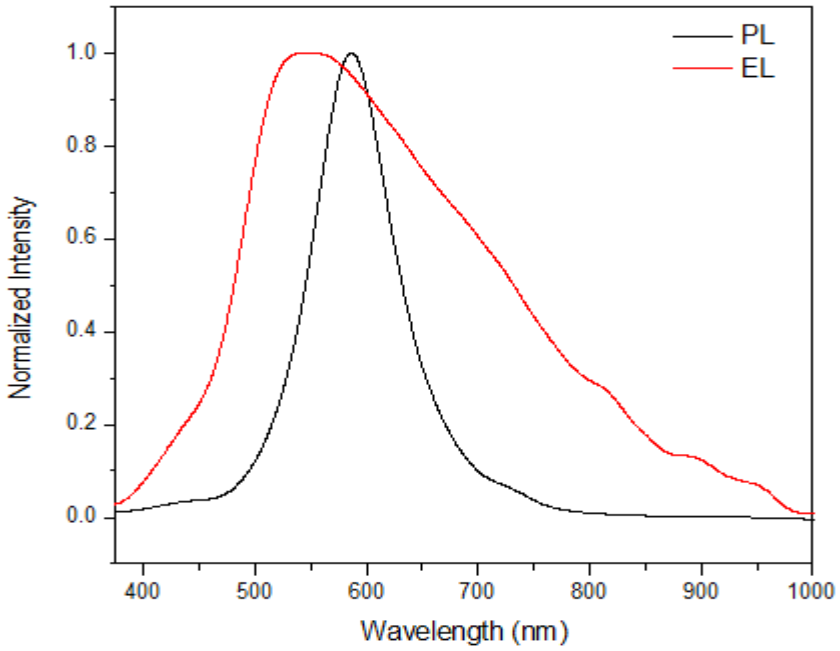

Figure 3.41 Photoluminescence and electroluminescence spectra of OLED with Ag-SiO_2-RB hybrid NPs as emitting layer. [53]

The PL and EL spectra of the hybrid NPs OLED are presented in Figure 3.41. The EL spectrum shows remarkable broadening compared with its PL spectrum. Because the spectral broadening only occurs in the EL experiment, this rules out dimer formation induced spectral broadening that should also be observed in the PL. It is more likely that the spectral broadening originates from charge recombination at an interface. It is known that excitation by an external light source on a bulk material will not induce charge accumulation at an interface since the exciton decay occurs on a nanosecond time scale. However, charge carriers tend to gather at an interface in the EL process due to massive charge injection from electrodes and low mobility in hybrid materials, which offers considerable probability to form exciplexes.[56] In order to validate that hypothesis, we fabricated another OLED with the same structure except that the hybrid NPs were replaced by concentrated RB dye, but we failed to observe the spectral broadening feature, the EL spectrum of this diode was identical to its PL spectrum. This indicates that the surface

plasmon of the silver NPs plays an important role in facilitating exciplex recombination at the interface. Indeed, surface plasmons induce an enhanced evanescent electric field, which in turn favors exciplex recombination. Direct exciplex luminescence from the LUMO level of RB at -3.5 eV to the depleted HOMO level of PEDOT at -5.1 eV is thus tentatively assigned to the broad emission spectrum as shown in Figure 3.42. Exciplex emission was observed at the interface between ETL and HTL. [57] However, the exciplex emission from hole injection layer /ETL interface was barely reported. We need more supplementary experiments to validate the exciplex hypothesis. For instance, inserting a HTL such as NPB between PEDOT and the Ag-RB NPs layer should be done to confirm the EL spectral broadening phenomenon.

Another possible mechanism responsible for spectral broadening is the inhomogeneity of recombination regions such as rough surface and aggregated nanostructure which would broaden the electroluminescence emission spectra.

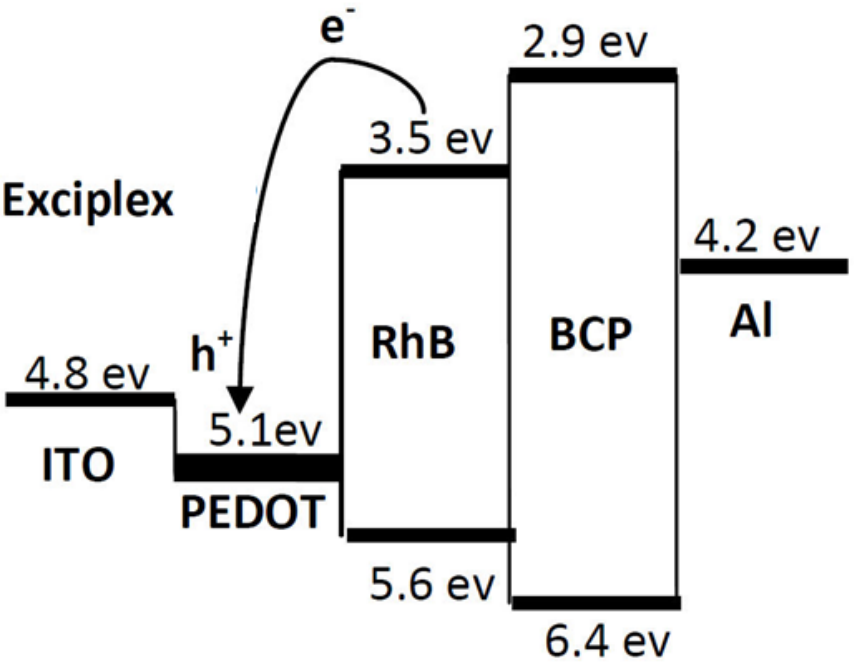

Figure 3.42 Schematic diagram interpreting the potential pathway for exciplex formation.

In order to investigate charge transport behaviour in our OLEDs, we measured time resolved EL as shown in Figure 3.43. Electric pulse width was set as 100 μs and both the rise and fall time 1 μs. There is no obvious delay time t_d observed in the present OLED, which usually corresponds to the charge carrier (holes and electrons) transport time in a diode with thicker organic films. In the present diode structure, holes should reach the NPs layer within a very short time interval since PEDOT is considered as a conductor, meanwhile electrons are injected into the NPs by means of tunnelling through the BCP, which is also a fast process. Thus it is understandable that we do not observe any delay time.

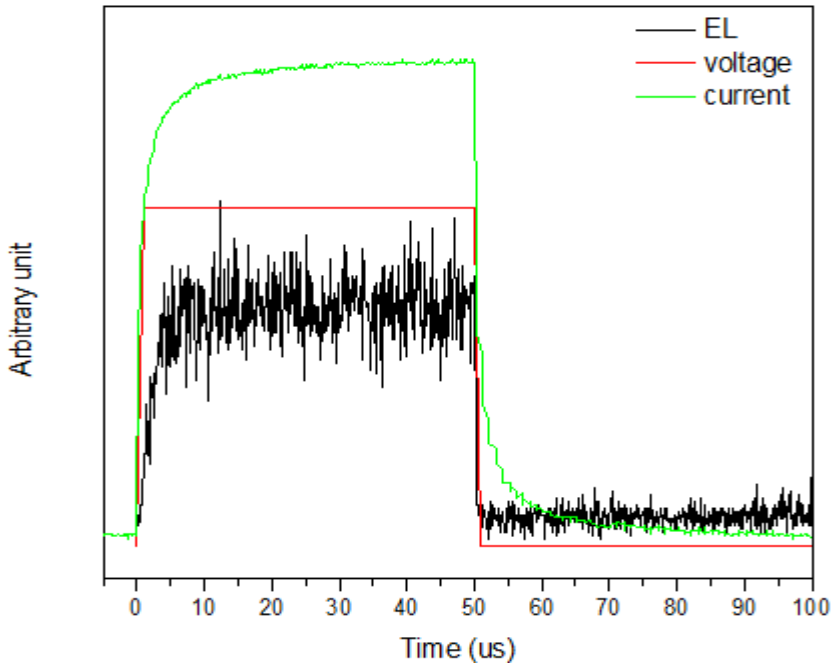

Figure 3.43 Time resolved electroluminescence of OLED with hybrid NPs as emitting layer.[53]

However, we clearly observe that EL signal takes about 5-6 μs to reach saturation, which is limited by charge carrier dynamics. With the increase of the EL signal, the current density also increases. That cannot be explained by the classic capacitor model, in which the current density

should decrease along with the accumulation of charges at the interface of organic layers. We interpret our charge transport process as follows: the holes can pass through the PEDOT layer easily and accumulate in the NPs layer due to the BCP hole blocking layer. A space charge induced electric field builds up, expediting electron tunnelling from the aluminum cathode into the NPs layer. As a result, both the current and EL intensity increase. When charge distribution comes to equilibrium, i.e. the minimum hole concentration is established in the hybrid NPs layer, both the current and EL intensity saturate. Finally when the bias voltage is turned off, we can still observe a current decay due to the relaxation of the trapped charges inside the diode. [58] However, we do not observe a corresponding EL decay, because the bias voltage falls below the threshold (turn-on) voltage, and no EL can be generated although current flows through the diode.

3.4.4 Conclusion

A novel rhodamine dye functionalized Ag-SiO_2 core-shell NP was synthesized and applied into OLED as an emitting layer. The EL of the hybrid NPs shows much broader spectrum than its PL spectrum. The presence of surface plasmon enhanced electric field favors the spectral broadening. This will inspire us to tune OLED electroluminescence, to design and optimize white light OLEDs from a novel point of view. In addition, greatly stable luminescence benefiting from surface plasmon also makes the hybrid NP a good light source for the study of single photon emission.

References

[1] Holmes, J. G. Proc. SPIE **1978**, 126, 2.

[2] Mullen, K.; Scherf, U. Organic Light-Emitting Devices 1st Edition **2006**, Wiley-Vch

[3] Ohno, Y.; Cromer, C. L.; Hardis, J. E.; Eppeldauer, G. Journal of Illuminating Engineering Society **1994**, 23-1, 88.

[4] Keitz, H. A. E. Light Calculations and Measurements, 2nd editon, Macmillan and Co Ltd, **1971**.

[5] Gong, X.; Robinson, M. R.; Ostrowski, J. C.; Moses, D.; Bazan, G. C.; Heeger, A. J. Adv. Mater. **2002**, 14, 581.

[6] Greenham, N. C.; Friend, R. H.; Bradley, D. D. C. Adv. Mater. **1994**, 6, 491.

[7] Fu, Y.; Lakowicz, J. R. Plasmonics **2007**, 2, 1.

[8] Malicka, J.; Gryczynski, I.; Geddes, C. D.; Lakowicz, J. R. J. Biomed. Opt. **2003**, 8, 472.

[9] Aisaka, T.; Fujii, M.; Hayashi, S. Appl. Phys. Lett. **2008**, 92, 132105.

[10] Koller, D. M.; Hohenau, A.; Ditlbacher, H.; Galler, N.; Aussenegg, F. R.; Leitner, A.; Krenn, J. R.; Eder, S.; Sax, S.; List, E. J. W. Appl. Phys. Lett. **2008**, 92, 103304.

[11] Yates, C. J.; Samuel, I. D. W.; Burn, P. L.; Wedge, S.; Barnes, W. L. Appl. Phys. Lett. **2006**, 88, 161105.

[12] Li, W.; Pan, S.; Rothberg, L. J. Proc. SPIE **2008**, 7032, 703224.

[13] Aziz, H.; Popovic, Z. D.; Hu, N.; Hor, A.; Xu, G. Science **1999**, 283, 1900.

[14] Wang, G.; Tao, X.; Wang, R. Compos. Sci. Technol. **2008**, 68, 2837.

[15] Liu, Z.; Zou, J.; Chen, J.; Huang, L.; Peng, J.; Cao, Y. Polymer **2008**, 49, 1604.

[16] Shinar, J. Organic Light-emitting Devices **2004**, (Springer Press, New York).

[17] Park, J. H.; Lim, Y. T.; Park, O. O.; Kim, J. K.; Yu, J. W.; Kim, Y. C. Chem. Mater. **2004**, 16, 688.

[18] Wang, F.; Chen, Z. J.; Gong, Q. H.; Wu, K. W.; Wang, X. S.; Zhang, B. W.; Tang, F. Q. Appl. Phys. Lett. **1999**, 75, 3243.

[19] Liu, D.; Fina, M.; Ren, L.; Mao, S. S. Appl. Phys. Lett. A. **2009**, 96, 353.

[20] Echlin, P. Handbook of Sample Preparation for Scanning Electron Microscopy and X-Ray Microanalysis **2009,** (Springer Press, New York).

[21] Scholz, S.; Huang, Q.; Thomschke, M.; Olthof, S.; Sebastian, P. J. Appl. Phys. **2008**, 104, 104502.

[22] Kim, W-J.; Choi, H-M.; Kim, J-S.; Kim, T-W.; Hong, J-W. **2009**, DOI: 10.1109/ICPADM. 2009. 5252293.

[23] Sun, Z.; Ding, B.; Wu, B.; You, Y.; Ding, X.; Hou, X. J. Phys. Chem. C **2011** DOI: 10. 1021/jp205871a.

[24] Lakowicz, J. R.; Shen, Y.; D'Auria, S.; Malicka, J.; Fang, J.; Gryczynski, Z.; Gryczynski, I. Anal. Biochem. **2002**, 301, 261.

[25] Cheng, P.; Li, D.; Yuan, Z.; Chen, P.; Yang, D. Appl. Phys. Lett. **2008**, 92, 041119.

[26] Flower, R. H.; Nordheim, L. Proc. R. Soc. Lond. Ser. A **1928**, 119, 173.

[27] Hohertz, D.; Gao, J. Adv. Mater. **2008**, 20, 3298.

[28] Aziz, H.; Popovic, Z. D.; Hu, N.; Hor, A.; Xu, G. Science **1999**, 283, 1900.

[29] Lakowicz, J. R. Anal. Biochem. **2005**, 337, 171.

[30] Liu, F.; Aldea, G.; Nunzi, J. M. J. Lumin. **2010**, 130, 56.

[31] Wu, M-H.; Lee, J-H.; Leung, M-K.; Hsu, Y-N. Proc. SPIE **2005**, 5632, 178.

[32] You, Y.; Park, S. Y. Dalton Trans. **2009**, 1267.

[33] Lamansky, S.; Kwong, R. C.; Nugent, M.; Djurovich, P. I.; Thompson, M. E. Org. Electron. **2001**, 2, 53.

[34] Robinson, M. R.; Ostrowski, J. C.; Bazan, G.C.; McGehee, M. D. Adv. Mater. **2003**, 15, 1547.

[35] Xia, H.; Zhang, C. B.; Qiu, S.; Lu, P.; Zhang, J. Y.; Ma, Y. G. Appl. Phys. Lett. **2004**, 84, 290.

[36] Chen, F. C.; Yang, Y.; Thompson, M. E.; Kido, J. Appl. Phys. Lett. **2002**, 80, 2308.

[37] Nakamura, A.; Tada, T.; Mizukami, M.; Yagyu, S. Appl. Phys. Lett. **2004**, 84, 130.

[38] Gong, X.; Robinson, M. R.; Ostrowski, J. C.; Moses, D.; Bazan, G. C.; Heeger, A. J. Adv. Mater. **2002**, 14, 581.

[39] Tsutsui, T.; Yang, M.-J.; Yahiro, M.; Nakamura, K.; Watanabe, T.; Tsuji, T.; Fukuda, Y.; Wakimoto, T.; Miyaguchi, S. Jpn. J. Appl. Phys. **1999**, 38, L1502.

[40] Kawamura, Y.; Yanagida, S.; Forrest, S. R. J. Appl. Phys. **2002**, 92, 87.

[41] Tanaka, I.; Suzuki, M.; Tokito, S. Jpn. J. Appl. Phys. **2003**, 42, 2737.

[42] Lee, P. C.; Meisel, D. J. Phys. Chem. **1982**, 86, 3391.

[43] Liu, F.; Nunzi, J-M. Appl. Phys. Lett. **2011**, 99, 123302.

[44] Murray, W. A.; Barnes, W. L. Adv. Mater. **2007**, 19, 3771.

[45] Müllen, K.; Scherf, U. Organic Light-Emitting Devices **2006** (WILEY-VCH, Weinheim)

[46] Pan, S.; Rothberg, L. J. Proc. SPIE **2007**, 6641, 664109.

[47] Goushi, K.; Kawamura, Y.; Sasabe, H.; Adachi, C. Jpn. J. Appl. Phys. **2004**, 43, L937.

[48] Gautier-Thianche, E.; Sentein, C.; Lorin, A.; Denis, C.; Raimond, P.; Nunzi, J. M. J. Appl. Phys. **1998**, 83, 4236.

[49] Reineke, S.; Lindner, F.; Schwartz, G.; Seidler, N.; Walzer, K.; Lüssem, B.; Leo, K. Nature **2009**, 459, 234.

[50] Wu, S.-H.; Huang, H-M.; Chen, K-C.; Hu, C-W.; Hsu, C-C.; Tsiang, R. C-C. Adv. Funct. Mater. **2006**, 16, 1959.

[51] Riedel, B.; Hauss, J.; Aichholz, M.; Gall, A.; Lemmer, U.; Gerken, M. Org. Electron. **2010**, 11, 1172.

[52] Nedelcev, T.; Racko, D.; Krupa, I. Dyes Pigments **2008**, 76, 550.

[53] Liu, F.; Rao, B. S.; Nunzi, J-M. Org. Electron. **2011**, 12, 1279.

[54] Chuntonov, L.; Haran, G. Nano Lett. **2011**, 11, 2440.

[55] Nhuang, T. H.; Canva, M.; Chaput, F.; Goudket, H.; Roger, G.; Brun, A.; Manh, D. D.; Huang, N. D.; Boilot, J.-P. Opt. Commun. **2004**, 232, 343.

[56] (a) Singh, S. P.; Mohapatra, Y. N.; Qureshi, M.; Manoharan, S. S. Appl. Phys. Lett. **2005**, 86, 113505. (b) Ng, A. M. C.; Djurisic, A. B.; Chan, W. K.; Nunzi, J. M. Chem. Phys. Lett. **2009**, 474, 141.

[57] (a) Liu, FL.; Ruden, P. P.; Campbell, I. H.; Smith, D. L. Appl. Phys. Lett. **2011**, 99, 123301. (b) Gebler, D. D.; Wang, Y. Z.; Blatchford, J. W.; Jessen, S. W.; Fu, D.K.; Swager, T. M.; MacDiarmid, A. G.; Epstein, A. J. Appl. Phys. Lett. **1997**, 70, 1644. (c) Jenekhe, S. A.; Osaheni, J. A. Science **1994**, 265, 765. (d) Osaheni, J. A.; Jenekhe, S. A. Macromolecules **1994**, 27, 739.

[58] Barth, S.; Müller, P.; Riel, H.; Seidler, P. F.; Rieβ, W. J. Appl. Phys. **2001**, 89, 3711.

Chapter 4
Metal Nanoparticles in Organic Solar Cells

We have demonstrated successful applications of silver NPs, functional silver NPs and hybrid NPs in OLEDs in Chapter 3. Here we focus on the organic solar cell, which was a very active research area in the last decade, and aim to explore and develop the application of metal NPs surface plasmon in organic solar cells. In this chapter, we will discuss three types of organic solar cells: small molecule solar cell, polymer solar cell, and tandem solar cell. We will demonstrate the strategies to optimize CuPc based SM-OSC; moreover the incorporation of silver NPs into polymer OSC will be introduced and the roles that Ag NPs play in enhancing OSC PCE will be interpreted; the essential factors leading to successful tandem solar cell will be addressed, particularly gold NPs enhanced device performance will be highlighted.

4.1 Silver NPs Increased Polymer Organic Solar Cells Performance

4.1.1 Background

Owing to its low cost for large scale production, OSC has been attracting great interests in last decade. However, the power conversion efficiency (PCE) of present OSCs is still too low, thus the optimization of OSCs is a very hot research topic currently. To date diverse ways have been developed to optimize the OSC efficiency. The synthesis of new low band-gap polymers is the mainstream leading to the improvement of OSCs PCE.[1] Besides the development of charge transport layer materials for better charge carrier extraction,[2] and the primary solvent together with cosolvent system for better donor-accepter phase separation,[3] could also effectively increase device efficiency. Moreover, the development of light trapping techniques inside the solar cell is another approach.

For wafer-based solar cells inverted pyramids of a size around 10 μm can be used for light trapping; however this surface texture is not applicable for the thin film solar cell since it normally has a thickness 1~2 μm. In this case, metal NPs could be a good substitute to enhance light trapping. So far, Pillai et al. reported 7-fold enhancement of the absorption for a wafer-based cell at λ =1200 nm, and up to 16-fold enhancement at λ=1050 nm for 1.25 μm thin film silicon solar cell by using silver NPs.[4] The underlying mechanism is believed to the increased optical path length in silicon thin film due to the large scattering cross section of the metal NPs as shown in Figure 4.1. Therefore this light trapping process can effectively enhance silicon solar cell efficiency.

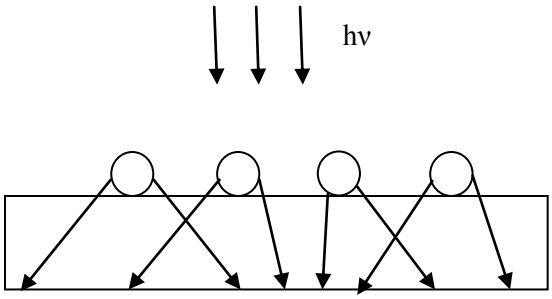

Figure 4.1 Schematic diagram of light trapping process in silicon solar cell.

The incorporation of metal NPs in organic solar cells, however, is not as successful as that in the silicon solar cells. Yoon et al. reported plasmon enhanced optical absorption in organic bulk heterojunction (BHJ) photovoltaic devices using a self-assembled layer of silver NPs, which were deposited between the HTL and polymer layer.[5] Although the solar cell containing silver NPs presents slightly greater short circuit current I_{sc}, it suffers from significant decrease of both fill factor and V_{oc}, which results in lower PCE. The reduced cell efficiency is attributed to charge recombination on the surface of the silver NPs and retarded charge extraction. Another factor which does not favor this type of cell structure is that the silver NPs may scatter part of the incident light back to glass substrate, blocking the transmission of the incident light into the polymer layer. Temple et al. found that silver NPs did not enhance silicon solar cell efficiency due to back scattering and absorption effects from silver NPs which impair the incident light passing through cell.[6]

So far, most of the research work devoted to nanoparticle incorporated organic solar cells cannot really isolate the optical function of a nanoparticle from its electronic function due to the multiple roles it plays in solar cell.[7,8] Thus we designed the BHJ solar cell with a configuration as shown in Figure 4.2, which enables us to investigate the optical function of metal NPs in solar

cell solely. In this research, we incorporated Ag NPs into P3HT based polymer solar cell; surface plasmon controlled solar cell performance was investigated. The Ag NPs induced light scattering effect was interpreted explicitly.

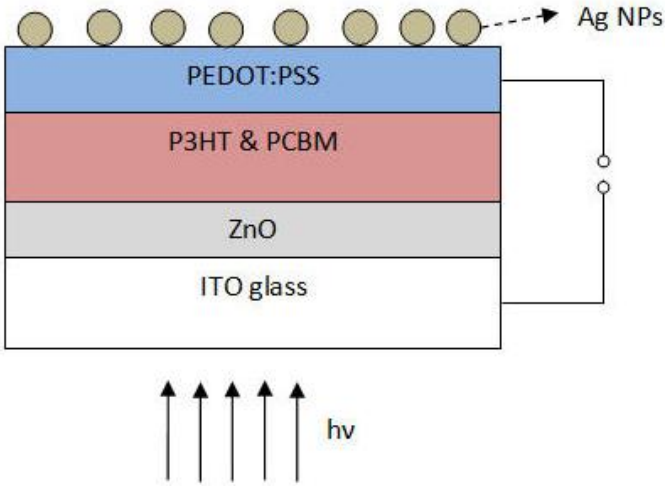

Figure 4.2 Schematic diagram of inverted solar cell containing silver NPs.

4.1.2 Experimental

Poly(3-hexylthiophene) and zinc acetate dihydrate were purchased from Aldrich; [6,6]-phenyl C61 butyric acid methyl ester (PCBM, 99%) was obtained from SES Research, Poly (3, 4-ethylenedioxythiophene) poly (styrenesulfonate) (PEDOT: PSS, PH1000) was obtained from Clevios.

We adopted an inverted solar cell structure with a high work function metal as the top electrode, which requires the transparent conductive electrode ITO to serve as cathode. The inverted structure is expected to result in higher device stability. Here we used a sol-gel method to fabricate a ZnO layer on top of the ITO to selectively collect electrons. Since ZnO is well known as an n-type semiconductor, it only transports the electron making ITO electrode a cathode. The ZnO film was fabricated in the same way reported by Sekine et al.[9]: ZnO precursor

solution containing 0.75 M zinc acetate dihydrate and 0.75 M monoethanolamine in 2-methoxyethanol was stirred overnight and aged another 12 hours before using. The precursor solution was spin coated on pre-cleaned ITO glass substrate at 2000 rpm for 40 seconds, and then baked on a hotplate at 275 ºC for 5 minutes. The transparent ZnO film was then washed with distilled water, acetone and isopropanol to remove any residual organic materials from the surface, and finally the ZnO layer was dried under N_2 flow. The active layer was obtained by spin coating the P3HT and PCBM blend mixture (20 mg/mL P3HT in 1,2-dichlorobenzene, P3HT: PCBM=1: 1 in weight ratio). The spin speed and time were set as 600 rpm and 1 minute. The pristine film was annealed in a glove box at 110 ºC for 10 minutes to crystallize the P3HT film. Subsequently, PEDOT: PSS was spin coated over P3HT: PCBM active layer. Since PEDOT: PSS is a hydrophilic layer whereas P3HT is a hydrophobic layer, PEDOT cannot wet P3HT well, leading to poor film configuration. Here we added 5% DMSO (v/v) into the PEDOT solution to increase the PEDOT conductivity and 1 wt. % Triton 100 to increase the PEDOT layer adhesive force on P3HT layer. The modified PEDOT solution exhibits a much better wetting ability on P3HT layer, yielding a uniform layer over P3HT after spin coating. Under the device configuration shown in Figure 4.2, the PEDOT layer was employed as the anode. Silver NPs were deposited on top of the PEDOT layer via vacuum thermal deposition. All the devices were further annealed at 120 ºC for 10 minutes after PEDOT deposition to remove water under N_2 atmosphere, and annealed at 150 ºC for 10 minutes to ripen the Ag NPs after NPs deposition.

The UV-Vis spectra and transmission spectra were recorded on a Lambda 20 spectrometer (PerkinElmer), atomic force microscopy (AFM) images were captured with an Ambios multimode microscope. The current-voltage curves were measured on Keithley (4200-SCS). BHJ solar cells were irradiated using a halogen lamp, and all the data were calibrated afterwards with a standard AM 1.5 100 mW/cm^2 solar simulator. All measurements were carried out in air at ambient temperature.

4.1.3 Results and Discussion

Prior to incorporate silver NPs into BHJ solar cells, it is important to understand how silver NPs affect light transmission into solar cells. Therefore we deposited 14 nm silver films (mass thickness) on a glass substrate via thermal deposition and tested their transmission spectra. As shown in Figure 4.3 the pristine silver film attenuates incident light transmission in the whole UV-vis region via absorption and scattering. The lowest transmission rate at 550 nm corresponds to the silver surface plasmon resonance, at which up to 70% of the incident light is lost after passing through the silver film.

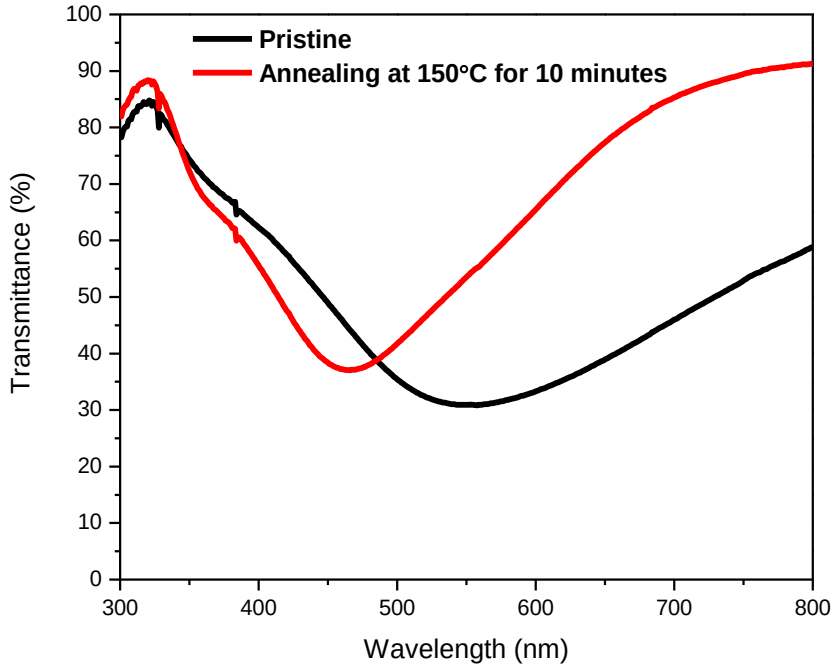

Figure 4.3 Transmission spectra of 14 nm silver film on glass substrate before and after annealing.

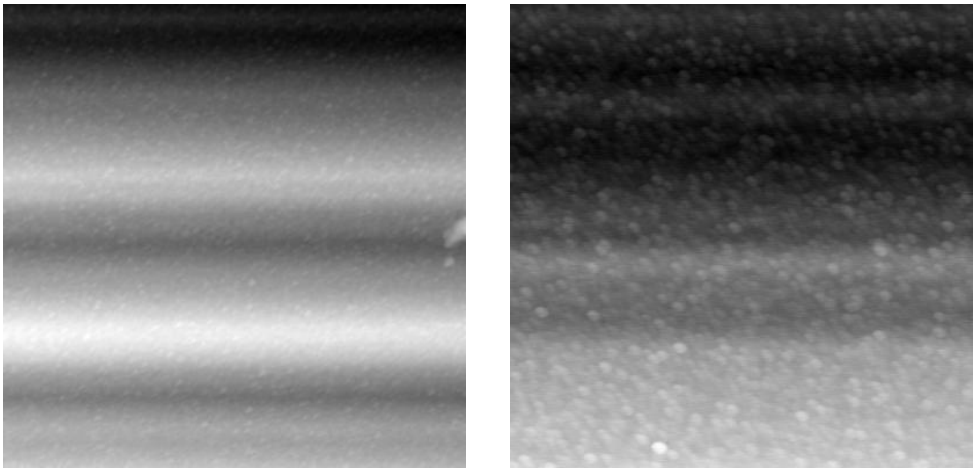

Figure 4.4 AFM images (5 µm × 5 µm) of 14 nm silver film on glass substrate before (left) and after (right) annealing at 150 ºC for 10 minutes.

After annealing the silver film in a glove box at 150 ˚C for 10 minutes, the film efficiently allows the near-IR light to pass. However, the annealed Ag NPs still attenuate the visible light from 400 nm to 600 nm which covers the absorption region of P3HT polymer. With regard to the blue shift of the surface plasmon resonance wavelength from 550 nm to 460 nm, that results from size and shape change of the silver NPs, which is confirmed by the following AFM study as shown in Figure 4.4. Indeed similar result was also observed by Temple et al.[6] According to the AFM images, pristine silver NPs have mean size around 40 nm in diameter, while after 10 minutes heat treatment the particle size increases to around 150 nm benefiting the light scattering instead of the light absorption. Recalling our BHJ solar cell design together with transmission spectra, we would definitely encounter substantial light loss provided the silver NPs were placed underneath the P3HT polymer, which actually is a widely investigated device structure by researchers who attempted to incorporate metal NPs into solar cells.[10] Thus the transmission spectra guide us to incorporate silver NPs above the P3HT layer.

As we have to deposit the Ag NPs above the P3HT layer, here we face two configuration choices: one is above PEDOT layer, and the other is sandwiched between P3HT and PEDOT layers. In order to investigate which configuration is better for surface plasmon enhanced solar

cell performance, we prepared two types of solar cells with silver NPs film deposited directly over the PEDOT or sandwiched between P3HT and PEDOT. Absorption spectra of the prepared solar cells are shown Figure 4.5.

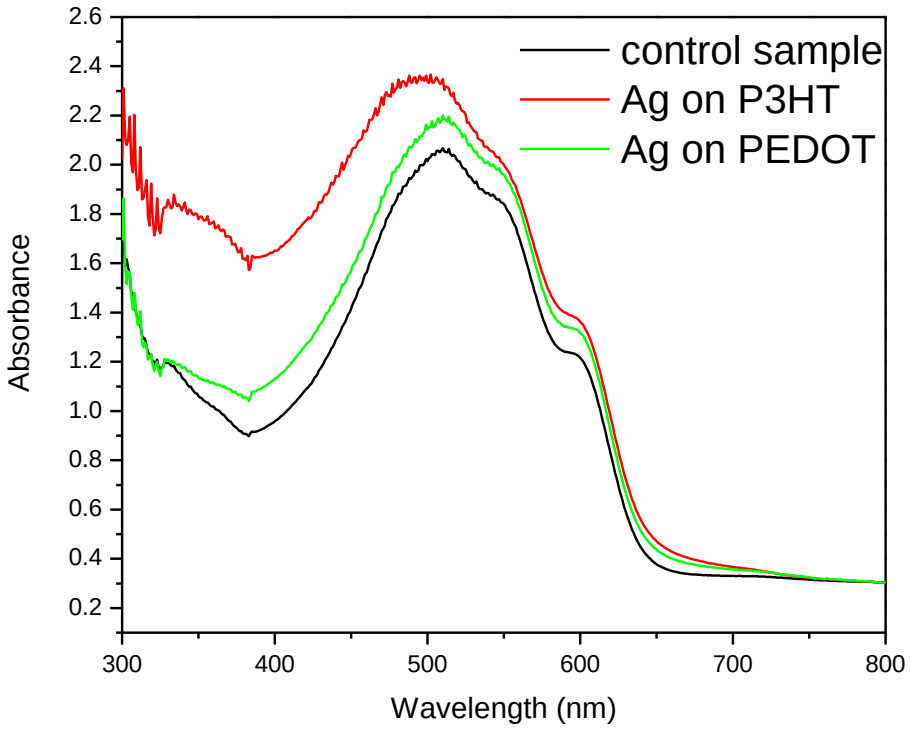

Figure 4.5 Absorption spectra of BHJ solar cells with different silver NPs deposition configuration.

The control cell exhibits a broad absorption peak ranging from 300 nm to 650 nm, as a typical absorption spectrum of a P3HT and PCBM blend. The peak at 300 ~ 400 nm belongs to PCBM absorption, while the spectral region from 450 nm to 650 nm is assigned to π-π* transition of the P3HT backbone, the shoulder peak around 600 nm corresponds to a higher crystallization or ordering of intra-chain interactions in the P3HT polymer.[11] We can clearly observe an increase in absorbance over the whole absorption range for the solar cell incorporated with silver NPs over the PEDOT layer. According to Mie theory,[12] when the size of the silver NPs is above 60 nm, its

scattering effect rather than the absorption effect becomes the dominant contribution to light extinction. Thus the polymer absorbance enhancement may result from back scattering of the incident light by silver NPs so that the absorption optical path length increases in the polymer layer. On the other hand, surface plasmons of the silver NPs can also result in the elevation of the polymer extinction coefficient. Similar to the SERS principle, a metal nanostructure can increase the absorption of a molecule by enhanced E-field effect. If the polymer molecules are in the vicinity of the silver NPs, the ground state to excited state transition probability can be increased. In other words, the extinction coefficient is increased by silver NPs and so is the absorbance of the polymer.

We also notice that the solar cell with silver NPs sandwiched between P3HT and PEDOT has larger absorbance enhancement, it must benefit from shorter distance between the polymer and silver NPs layer so that more polymer molecules settle in the enhanced E-field region.

Table 1 Performance of the inverted solar cells with different configurations.

	Anode	J_{sc} (mA/cm^2)	V_{oc}(V)	FF (%)	PCE (%)
Control sample	PODOT:PSS	0.39	0.45	24	0.041
P3HT/Ag NPs/PEDOT	PODOT:PSS	0.44	0.39	25	0.042
P3HT/PEDOT/Ag NPs	PODOT:PSS	0.88	0.35	26	0.078
Control sample	Metal	9.76	0.43	33	1.40
P3HT/PEDOT/Ag NPs	Metal	12.16	0.44	31	1.66

Table 1 shows the influence of the silver NPs on solar cells performance. The control sample shows moderate PCE 0.041%, which is much lower than reported inverted solar cell PCE 3.2%.[9] It can be ascribed to the replacement of the metal anode silver (~100 nm) by the conductive PEDOT layer. Apparently the conductivity of PEDOT is not as good as that of silver, inferior performance is thus not a surprise. When silver NPs are deposited on top of PEDOT

layer, the J_{sc} of the cell is increased notably from 0.39 to 0.88 mA/cm^2. On the one hand, this enhancement must benefit from increased polymer absorbance, which in turn generates more excitons and larger photocurrent. On the other hand, the coupling between surface plasmon and organic excitons is also reported to result in more efficient charge transport in the BHJ blend,[10] that might also contribute to the J_{sc} increase. As a result, the PCE of the solar cell is increased by a factor of 1.9. We notice that a film of 14 nm silver NPs is not conductive, which rules out the possibility that silver NPs enhance cell PCE by improving anode conductivity.

We expect more gain on J_{sc} and PCE for solar cell with silver NPs sandwiched between P3HT and PEDOT based on our absorption spectra measurement. However, the solar cell only shows similar performance with the control sample as presented in Table 1. This may result from the direct contact of the silver NPs with P3HT. Silver NPs are reported to provide direct charge recombination sites in organic solar cell,[5,13] in such way Ag NPs could lower the effective charge output from solar cell. The quenching effect from silver NPs offsets the enhancement effect, J_{sc} slightly increases to 0.44 mA/cm^2, and PCE remains the same as that of the control sample. We also fabricated a cell with silver NPs film sandwiched between ZnO and P3HT layer for comparison. The PCE of the prepared solar cell is two orders of magnitude lower than that of the control sample due to strong back-scattering and absorption effects from silver NPs. This result is indeed expected.

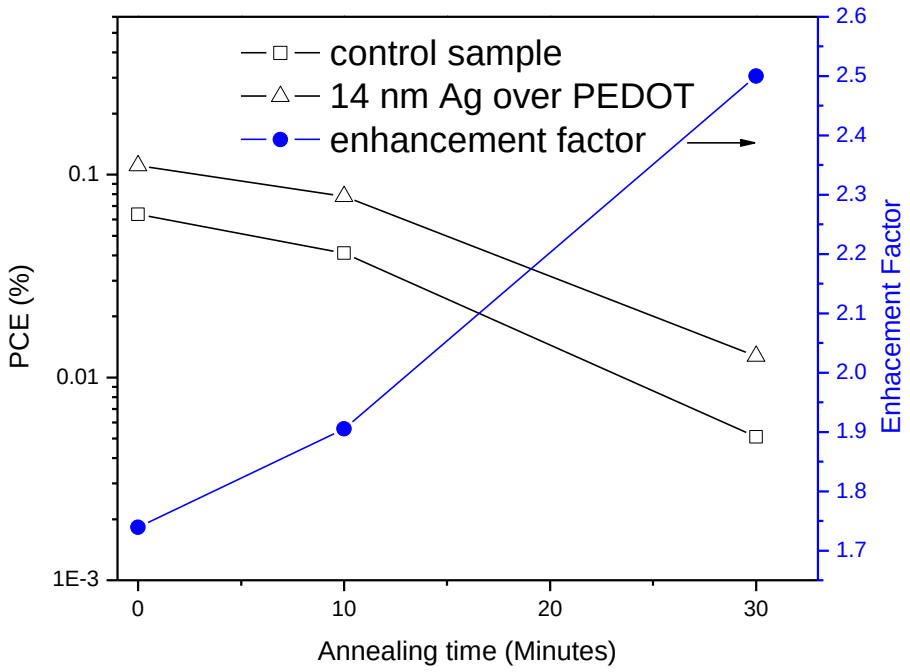

Figure 4.6 Annealing time dependent PCE of solar cells with and without Ag NPs.

In order to investigate how the size of silver NPs affects solar cell performance, we compared the PCE of the solar cells with and without silver NPs under different thermal treatment time as presented in Figure 4.6. It is notable that 10-minute anneal at 150 ºC causes 35% PCE drop on control sample, which implies that the polymer blend structure changes within 10-minutes annealing period. Indeed that is due to the formation of large-scale PCBM aggregation as reported by Huang and co-workers.[14] The disrupted bi-continuous phase retards the charge transport. As the annealing time increases to 30 minutes, the control cell suffers from efficiency drop as high as 92%, indicating that longer annealing process causes larger scale aggregation. However, it is notable that Ag NPs induced PCE enhancement factor increases along with the prolongation of the annealing time. It is well known that the thermal treatment drives small NPs to form larger particles and meanwhile reduces the surface coverage.[15] On the one hand, larger silver NPs (less than incident light wavelength) results in stronger scattering effect according to Mie theory; on the other hand, less compact surface coverage facilitates surface plasmon coupling

with polymer molecules.[16] As a result, the growth of the silver NPs favors the PCE increase of solar cells compared to the control cells although the polymer blend structure is disrupted. A more advanced way to deposit silver NPs by lithography with a shadow mask could be developed to take better control of the silver NPs size and distribution. It cuts out the annealing process and thus does not disturb the polymer layer microstructure. More prominent enhancement effect and higher PCE could be achieved in this way.

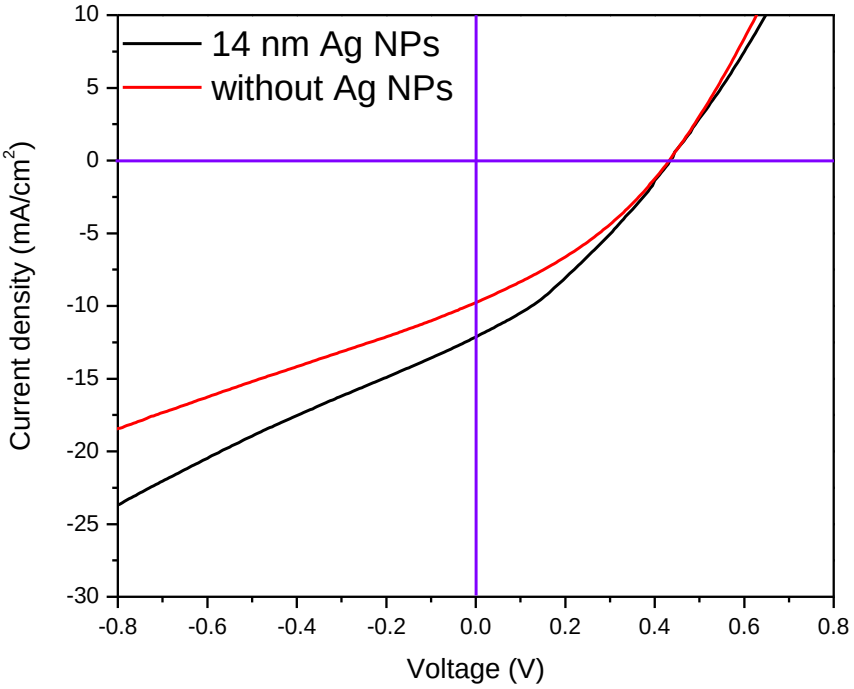

Figure 4.7 J-V curves of solar cells with and without silver NPs, a metal anode is employed on both cells.

Considering that the inverted solar cells with PEDOT:PSS as anode have low efficiency, we deposited 100 nm silver film over the PEDOT as metal electrode. Note here the deposition of an additional 100 nm silver film over the annealed silver NPs would result in a rough metal/organic interface instead of planar one, the Ag NPs induced effects will still exist instead of vanishing completely. The cell performance increases drastically due to the improvement of

charge extraction ability. The current density-voltage curves of the solar cells with metal anode are shown in Figure 4.7. The J_{sc} of the control sample is 9.76 mA/cm^2, and it is further increased to 12.16 mA/cm^2 by silver NPs deposited over PEDOT. The V_{oc} undergoes a neglectable change from 0.43 V to 0.44 V. As a result the PCE is increased from 1.4% to 1.66%; the mirror reflection effect from the top metal electrode weakens the nanoparticle enhancement effect on PCE, and this should be responsible for the moderate PCE enhancement factor (1.2 fold) which is less than the enhancement factor 1.9 fold in the case that PEDOT is employed as anode.

4.1.4 Conclusion

In inverted P3HT BHJ solar cell, silver NPs increase polymer absorbance by means of increasing absorption optical path length and improving polymer extinction coefficient via Ag NPs scattering effect and surface plasmon enhanced local E- field. As a result, the J_{sc} of the solar cell is increased significantly. Besides, the growth of silver NPs by thermal treatment can further optimize the PCE enhancement; however, large aggregation of PCBM forms greatly deteriorating cell performance. Because silver NPs can offer charge carrier recombination sites, direct contact of silver NPs with polymer layer does not increase solar cell efficiency. Thermal evaporation is a feasible way to incorporate metal NPs into solar cell, and could be developed as an effective way to increase BHJ solar cell efficiency.

4.2 Optimization of Small Molecule OSC

4.2.1 Background

As we aim to investigate tandem solar cell performance and we have studied the P3HT polymer solar cell, a solar cell of complementary absorption range with regard to P3HT polymer would be an ideal choice. Copper phthalocyanine (CuPc) is a widely studied small molecule solar cell which has an absorption peak in the near IR region, thus we have chosen CuPc solar cell as the research objective and aim to optimize its efficiency by all means before we start designing the tandem solar cell.

The Forrest research group devoted tremendous works on CuPc solar cell, and so far they still keep the highest record for CuPc solar cell efficiency. In 2001 Forrest et al. reported a bi-layer heterojunction solar cell based on CuPc and C_{60}.[17] In their devices, an exciton blocking layer was applied to transport electrons and meanwhile block exciton in the acceptor layer. A device with structure ITO/PEDOT: PSS/ CuPc (20nm)/C_{60} (40 nm)/ BCP (8 nm) / Al was reported with PCE 3.6% under AM 1.5 150 mW/cm^2 illumination.

Later on in 2004, the Forrest group reported a bi-layer solar cell based on CuPc and C_{60} with higher efficiency 4.2%,[18] which is still considered as the best CuPc solar cell to date. They adopted a similar cell design with their previous report: ITO/ CuPc (20 nm)/ C_{60} (40 nm)/ BCP (10 nm)/ Ag (100 nm), the obtained solar cell presented a surprising low series resistance 0.1 Ω cm^2 and a high fill factor 60%. However, this 4.2% efficiency was measured under 4-12 suns illumination intensity, and the PCE increased with the incident optical power density, the PCE of the solar cell dropped to ca. 3.3 % under moderate illumination (1 sun).

Moreover, in 2007 Forrest et al. developed a multi-layer structure CuPc/C_{60} solar cell,[19] in which alternating CuPc and C_{60} layers were stacked on each other. The obtained solar cell had the structure: ITO/CuPc (14.5 nm) /[C_{60} (3.2 nm)/CuPc (3.2 nm)]$_n$/ C_{60} (40 nm)/ BCP (10 nm)/ Ag. Here n is the repeat unit number, ranging from 0 to 12. Along with the increase of factor n from 2 to 6, the J_{sc} significantly increased by a factor of 3, and then dropped as n further increased due to increased series resistance. As a result, the highest PCE, 4.4 %, was achieved with 6 alternant layers. This novel multilayer cell structure design enables the excitons to dissociate effectively at CuPc/C_{60} interface.

Although the Forrest group published outstanding results on CuPc small molecule OSC, however, their results could be hardly repeated by others. Concern about the material impurity is evoked. In the Forrest group, all the organic materials were obtained commercially and then purified using thermal gradient sublimation, this definitely yields higher purity and might be responsible for their extraordinary high solar cell efficiency. Zhang et al. reported an inverted CuPc-C_{60} bi-layer solar cell with the structure ITO/ Ca (1 nm) / C_{60} (40 nm)/ CuPc (25 nm)/ MoO_3 (10 nm)/Ag, [20] here Ca was used to modify the work function of ITO enabling it to work as cathode, and MoO_3 is a p-type semiconductor selectively transporting holes. Although various optimization methods were attempted such as changing MoO_3 thickness, CuPc thickness etc., the best PCE obtained on their solar cells design was 0.64%, which is much lower compared to the PCE reported by Forrest et al.

It is not uncommon to gain PCE less than 1% for CuPc based solar cell. Shan et al. reported an inverted solar cell based on CuPc: C_{60} bulk heterojunction solar cell with structure: ITO/ TiO_2 (130 nm) / CuPc: C_{60} (6: 1, 20 nm) / CuPc (20 nm)/ PEDOT: PSS (50 nm)/ Au (30 nm).[21] Their optimization processes were focused on the CuPc: C_{60} ratio as well as the TiO_2 morphology, it turns out that the CuPc: C_{60} blend layer with ratio 6: 1 was critical to increase cell efficiency; moreover a porous TiO_2 structure can also favor the exciton dissociation due to large

interface area. Nevertheless, their best PCE was only 0.36%, which suggests that a moderate efficiency of a CuPc solar cell is reasonable provided no further purification on organic materials is employed.

4.2.2 Experimental

CuPc (sublimation grade), MoO_3 (99.99%) and zinc acetate dihydrate (99.0%) were obtained from Aldrich; C_{60} (99.9%) was purchased from SES Research. All the organic materials were used without further purification.

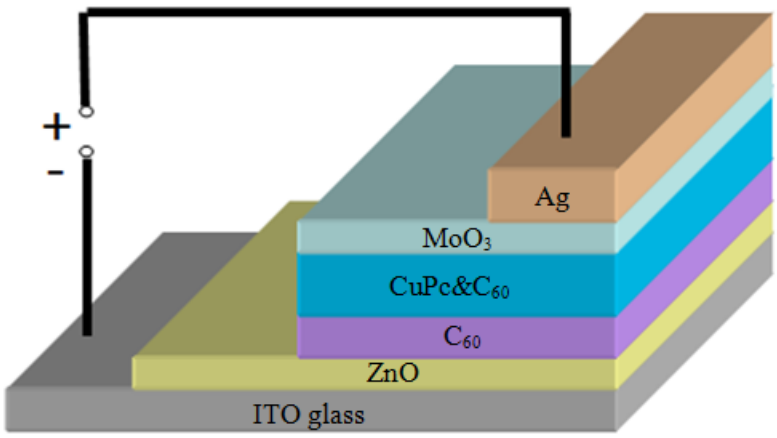

Figure 4.8 Schematic diagram of inverted CuPc solar cell.

The device structure is shown in Figure 4.8. ZnO layer was coated on ITO in the way introduced in section 4.1.2, which selectively collects the electrons. The C_{60} layer was deposited by vacuum thermal deposition, the sublimating temperature was around 390~400 ºC. The CuPc and C_{60} blend was fabricated by vacuum thermal co-deposition. The Kurt J. Lesker vacuum evaporator is capable of depositing two organic sources simultaneously. The evaporation rates of these two sources can be precisely monitored by two individual sensors so that we can control the CuPc and C_{60} ratio readily. MoO_3 was evaporated under vacuum as well and finally 100 nm Ag film was thermally deposited as anode.

The current-voltage curves were measured on Keithley (4200-SCS). Solar cells were irradiated by using a halogen lamp, and all the data were calibrated afterwards with a standard AM 1.5 100 mW/cm^2 solar simulator. All the measurements were carried out in air at ambient temperature.

4.2.3 Results and Discussion

We have fabricated inverted solar cells with different structure as shown in Figure 4.9. The bi-layer cell with structure ITO/ZnO/C_{60} (30 nm) /CuPc (20 nm) /BCP/Ag shows inferior performance with V_{oc} only 0.23 V and efficiency 0.06%. Thus we switched to BHJ structure, in which donor and acceptor are mixed together so that more effective exciton dissociation process is expected. The BHJ solar cell with structure ITO/ZnO/C_{60} (10 nm) /CuPc-C_{60} (51 nm, 1: 0.7)/CuPc (10 nm) /Ag does exhibit higher V_{oc} and larger J_{sc} than those of the bi-layer cell. The CuPc layer is employed as HTL, which also separates the metal electrode from the active blend layer to avoid exciton quenching. However, the fill factor is poor as indicated in Table 2.

Table 2 Parameters of solar cells with different structures

Samples	J_{sc} (mA/cm^2)	V_{oc}(V)	FF (%)	PCE (%)
(1)	0.73	0.23	37.8	0.06
(2)	1.98	0.35	20.0	0.14
(3)	1.86	0.39	20.4	0.15
(4)	2.07	0.22	30.7	0.14

The BHJ solar cell performance strongly depends on the phase separation of donors and acceptors. If large donor or acceptor domain emerges in the blend, partial excitons will be trapped, lowering the device efficiency. Therefore we deposited the organic compounds at higher substrate temperature 80 ºC, whereupon the fill factor is increased notably; moreover the current

density is also enhanced, the underlying mechanism being that the organic molecules tend to self-organize under higher temperature resulting in ordered microstructure.[22] However V_{oc} decreases leading to an unchanged PCE compared to the control cell, which is still not clearly understood.

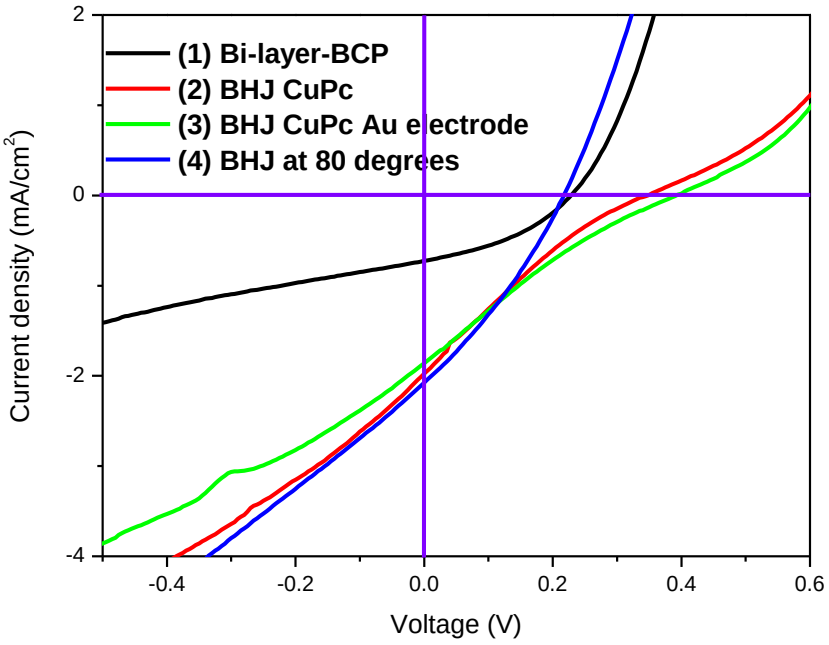

Figure 4.9 J-V curves of CuPc solar cells with different configurations: (1) bi-layer structure, ITO/ZnO/C_{60} (30 nm) /CuPc (20 nm) /BCP/Ag; (2) ITO/ZnO/C_{60} (10 nm) /CuPc-C_{60} (51 nm, 1: 0.7)/CuPc (10 nm) /Ag; (3) ITO/ZnO/C_{60}(10 nm)/CuPc-C_{60} (51 nm)/CuPc (10 nm)/ Au; (4) is (2) deposited with substrate temperature set as 80 °C.

According to the energy level alignment shown in Figure 4.10, there is a quite large energy level mismatch between Ag work function and the HOMO of CuPc molecule. We reduced the energy gap by replacing Ag with higher work function metal Au (5.1-5.4 eV), however the resulting solar cell with structure ITO/ZnO/C_{60}(10 nm)/CuPc-C_{60} (51 nm)/CuPc (10 nm)/ Au only presents minor efficiency increase. Although we got improvement on solar cell efficiency compared to the bi-layer solar cell, the above solar cell structures still yield efficiency much lower than the literature reports. [20, 21]

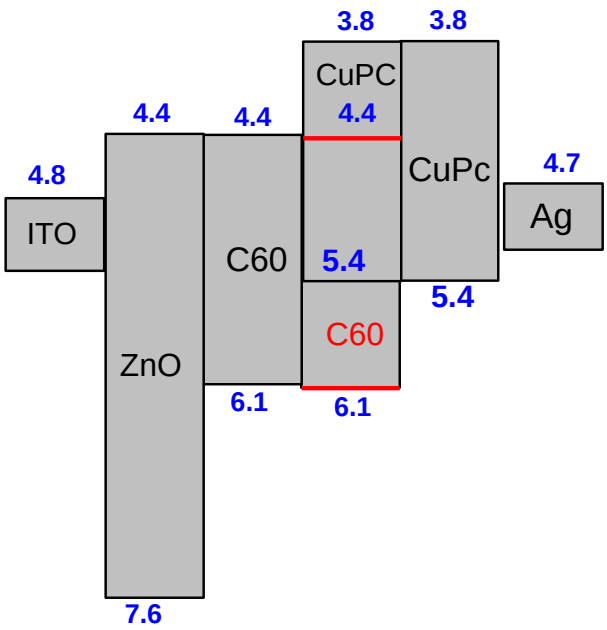

Figure 4.10 Energy level alignment of CuPc BHJ solar cell

Owing to the poor fill factor of the CuPc BHJ cells, we replaced CuPc with MoO_3 which has a HOMO level at -5.3 eV and LUMO at -2.3 eV.[23] MoO_3 as a good p-type semiconductor was being considered as substitute of PEDOT as hole transport material. It has lower LUMO energy compared to CuPc, which can effectively block the electron transport towards metal electrode. Figure 4.11 shows the J-V curves of solar cells with MoO_3 as HTL. All the cells have decent fill factor as shown in Table 3. For BHJ solar cell with structure ITO/ ZnO/ C_{60}(10 nm)/ CuPc-C_{60} (51 nm)/ MoO_3 (3 nm)/ Ag , the replacement of CuPc with MoO_3 increases device efficiency with a factor of 3.4, the J_{sc} increases from 1.98 mA/cm^2 to 2.86 mA/cm^2, the V_{oc} increases from 0.35 V to 0.40 V, and most significantly the fill factor is increased from 20% to 40.9%, it should benefit from the electron blocking effect and excellent hole transport feature of MoO_3. Moreover, we also observed 2.5-fold enhancement on PCE for bi-layer cell when CuPc HTL is replaced by MoO_3 layer, which mainly results from the increase of J_{sc} and V_{oc}. Above results indicate that MoO_3 is an excellent HTL material for CuPc solar cell design.

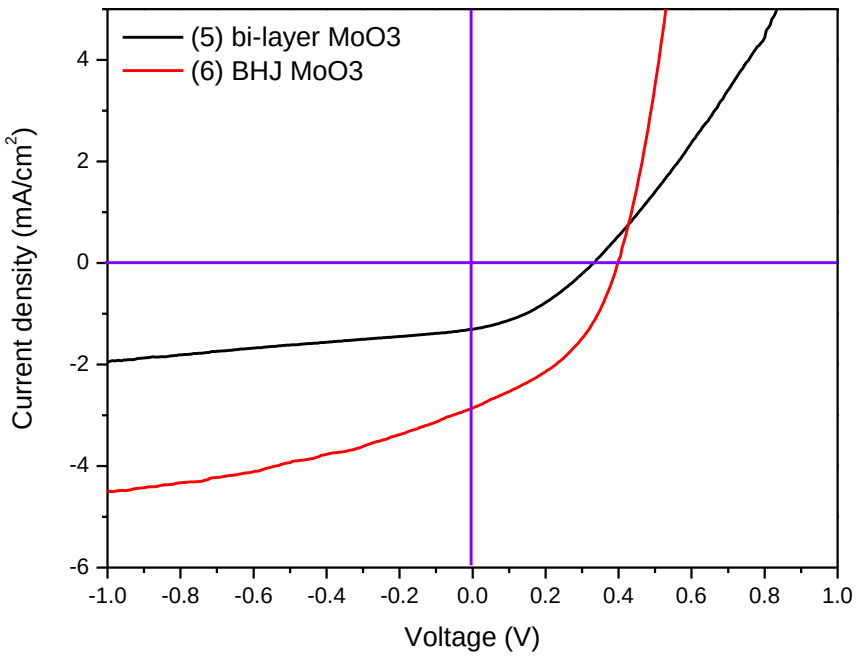

Figure 4.11 J-V curves of solar cells with MoO_3 as hole transport layer: (5) ITO /ZnO / C_{60} (40 nm) / CuPc (25 nm)/ MoO_3 (3 nm)/ Ag; (6) ITO/ ZnO/ C_{60}(10 nm)/ CuPc-C_{60} (51 nm)/ MoO_3 (3 nm)/ Ag

Table 3 Parameters of solar cells with MoO_3 as HTL

Samples	J_{sc} (mA/cm^2)	V_{oc}(V)	FF (%)	PCE (%)
(5)	1.30	0.33	36.4	0.16
(6)	2.86	0.40	40.9	0.47

According to the device architecture shown in Figure 4.8, the C_{60} layer and MoO_3 are employed as ETL and HTL respectively. Normally an organic semiconductor has lower conductivity than inorganic materials owing to the localized nature of the electronic states in amorphous organic materials. [24] Thus an unbalanced hole and electron extraction is expected, and it is more likely that part of electrons get trapped in C_{60} layer reducing device efficiency. In order to optimize the device performance, we adopted a co-evaporation technique to introduce

rhodamine B into C_{60} layer, which is known as a good cationic N-dopant dye. [25] The Rhodamine B molecule is believed to form a neutral radical in situ when it sublimes, then electron transfers from the reduced rhodamine B to C_{60} matrix leading to N-type doping.[25] The electron conductivity of a material could be formulated as $\sigma = N\mu e$ where N is the electron number density, μ is the electron mobility in the material, and e is the electron charge. Doping RB would introduce extra electrons into C_{60} improving electron number density and thus C_{60} conductivity.

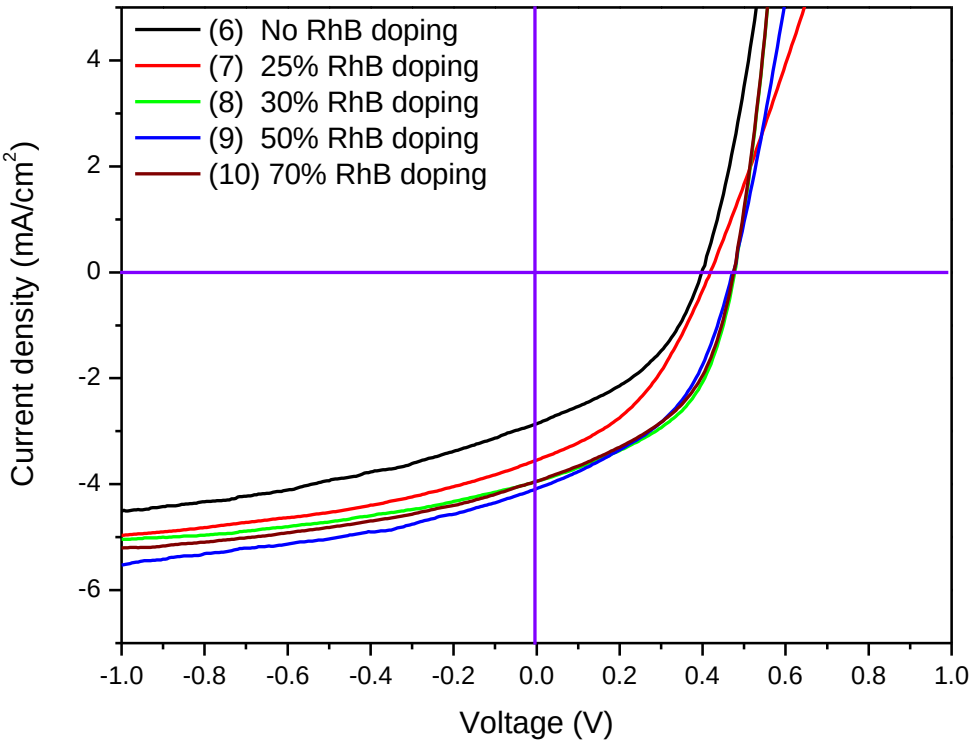

Figure 4.12 J-V curves of CuPc BHJ solar cells doped with different RB concentration in C_{60} layer.

The performance comparison between CuPc BHJ cells doped with different RB concentration is presented in Figure 4.12 and Table 4. Notably, doping RB significantly increases the device performance. For 25% RB doped cells, the J_{sc} increases from 2.86 mA/cm^2 to 3.55 mA/cm^2, and the V_{oc} increases from 0.40 V to 0.42 V. With further increase of RB dopant

concentration to 30% or above, the V_{oc} further increases and then remains as a constant 0.47 V. The J_{sc} also tends constant, which suggests 30% RB doping is enough to optimize present inverted CuPc cell. The obtained highest PCE, 0.91%, is almost the double of an undoped cell's PCE. Comparatively speaking, our optimized cells also exhibit much higher PCE than inverted CuPc solar cells reported very recently.[20, 21] The superior performance indicates that our inverted CuPc BHJ solar cells are properly designed and rhodamine B is indeed a good N-dopant for organic semiconductors.

Table 4 Performance of CuPc BHJ solar cells doped with different RB concentration in C_{60}.

Samples	J_{sc} (mA/cm^2)	V_{oc}(V)	FF (%)	PCE (%)
(6)	2.86	0.40	40.9	0.47
(7)	3.55	0.42	39.9	0.59
(8)	3.95	0.47	48.8	0.91
(9)	4.08	0.47	44.3	0.85
(10)	3.94	0.47	46.6	0.86

4.2.4 Conclusion

In order to fabricate and optimize an inverted CuPc organic solar cell, we tried different cell structures and materials. A BHJ structure is more efficient than traditional bi-layer structure due to increased exciton dissociation probability. Replacement of CuPc hole transport material by p-type MoO_3 greatly increases the device performance due to better electron blocking property and higher hole mobility. More importantly, incorporation of N-dopant molecule rhodamine B into C_{60} ETL essentially increases the device performance by improving C_{60} conductivity, leading to more balanced hole/electron extraction. The optimized inverted CuPc cells exhibit much higher PCE compared to reported values in literature recently.

4.3 Air Stable Hybrid Inverted Tandem Solar Cell Design

4.3.1 Background

The Organic solar cell (OSC) is an active research area in the last decade due to its incomparable low production cost in high volume together with flexibility. However, the OSC bears low PCE and low stability compared to inorganic solar cells such as silicon solar cell,[26,27] which greatly restricts its practical application.

In order to increase the efficiency of OSCs, tandem solar cells were developed which consist of multijunctions of BHJ or bilayer solar cells. A tandem solar cell has a number of advantages compared to a single cell: first of all, it has higher V_{oc} which ideally equals the sum of the subcells V_{oc} since they are connected in series; in addition, tandem solar cell can be made of several subcells with different bandgaps, which have complementary absorption and potentially cover the whole solar spectrum region. So far diverse types of tandem solar cells have been investigated, including small-molecule solar cell, polymer solar cell, and hybrid solar cell which consists of a polymer subcell together with a small-molecule subcell.[28, 29,30]The hybrid tandem solar cell combines the merits of spin-coating and vacuum thermal deposition techniques and meanwhile has a large selectivity among various small molecules and polymers, thus it has attracted increasing interest in the past few years. [31,32]

OSC has low stability and short lifespan since organic materials and metals such as aluminum in OSC are susceptible to water and oxygen. Therefore, OSC with regular structure (ITO as anode and aluminum as cathode) normally presents low air stability provided it is not encapsulated by other techniques. Sahin et al. developed an inverted solar cell with a high-work function metal gold as anode and ITO as cathode via work function adjustment by BCP or perylene.[33] Because aluminum electrode tends to form an insulating oxide layer at the interface

whereas gold is more stable in oxygen environment, the obtained inverted device exhibited increased air stability compared to aluminum on top devices. Later on, more effective electron collection layers such as ZnO, TiO_2 were explored to optimize inverted solar cell design,[34,35]thus inverted solar cell efficiency and stability got further increase.

Although tandem solar cell and inverted solar cell have been investigated respectively, only little research was dedicated to develop an inverted tandem solar cell which would have potentially higher efficiency and stability.[36,37] Moreover existing inverted tandem cells were mainly fabricated based on identical polymer subcell, which did not expand the absorption range of the tandem solar cell; on the other hand, the top polymer cell can swallow the bottom polymer cell potentially through spin coating method unless tight interfacial layer was employed, but the interfacial layer might block the light transmission or slow the charge transport down. Thus that inspires us to develop a hybrid inverted tandem solar cell in which a small-molecule top cell fabricated via vacuum thermal deposition would not disturb the polymer bottom cell and two subcells can have complementary absorption. In addition, it will increase the diversity of the inverted tandem solar cells.

In this research, we developed a hybrid inverted tandem solar cell based on P3HT polymer and CuPc small-molecule subcells which have been studied and optimized as discussed previously in section 4.1 and 4.2, these two subcells have complementary absorption as shown in Figure 4.14. We doped C_{60} ETL and built a symmetrical n-i-p/Au/n-i-p tandem cell structure, which led to significant V_{oc} increase on tandem solar cell. In addition, we further increased the tandem solar cell V_{oc} together with fill factor (FF) by incorporating gold NPs, and realized an ideal tandem solar cell performance.

4.3.2 Experimental

Poly (3-hexylthiophene) (P3HT), molybdenum oxide (MoO_3, 99.99%), zinc acetate dihydrate (99.0%), copper phthalocyanine (CuPc, sublimation grade) and Rhodamine B (RB) were purchased from Aldrich; [6,6]-phenyl C_{61} butyric acid methyl ester (PCBM, 99%), C_{60} (99.9%) and C_{70} (99.0%) were obtained from SES Research. All the materials were used as received without further purification. ZnO thin film was coated on pre-cleaned ITO glass substrate with sheet resistance 15 Ω/□ in the way described in section 4.1.2. Then 250 nm active layer consisting of P3HT and PCBM blend (20 mg/mL P3HT in 1,2-dichlorobenzeene, P3HT: PCBM= 1:1 by weight) was deposited on top of the ZnO. The obtained film was annealed in a glove box for 10 minutes at 110˚C, and transferred into a vacuum chamber for further deposition under 10^{-6} mbar vacuum. 3 nm MoO_3, X (x=0.5, 1, 3, 5) nm gold, 10 nm C_{60}, 51 nm CuPc/C_{60} (1: 0.7 weight ratio, co-deposition) and another 3 nm MoO_3 were deposited in order, and finally 100 nm Ag was deposited as anode. The obtained tandem cell has a configuration shown in Figure 4.13.

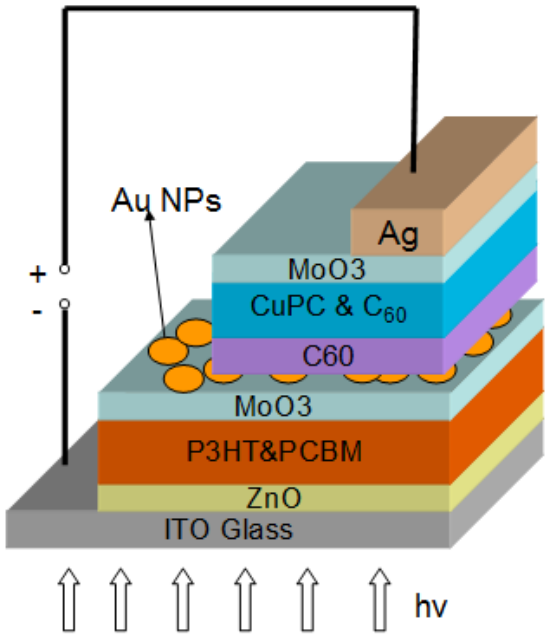

Figure 4.13 Schematic diagram of hybrid inverted tandem solar cell.

We also fabricated single polymer cell with structure ITO/ZnO/P3HT: PCBM/MoO_3/Ag and small-molecule single cell with structure ITO/ZnO/ C_{60}/CuPc: C_{60}/MoO_3/Ag as references. The current-voltage curves were measured on Keithley (4200-SCS). Solar cells were irradiated using a halogen lamp, and all the data were calibrated afterwards with a standard AM 1.5 100 mW/cm^2 solar simulator. All measurements were carried out in air at ambient temperature.

4.3.3 Results and discussion

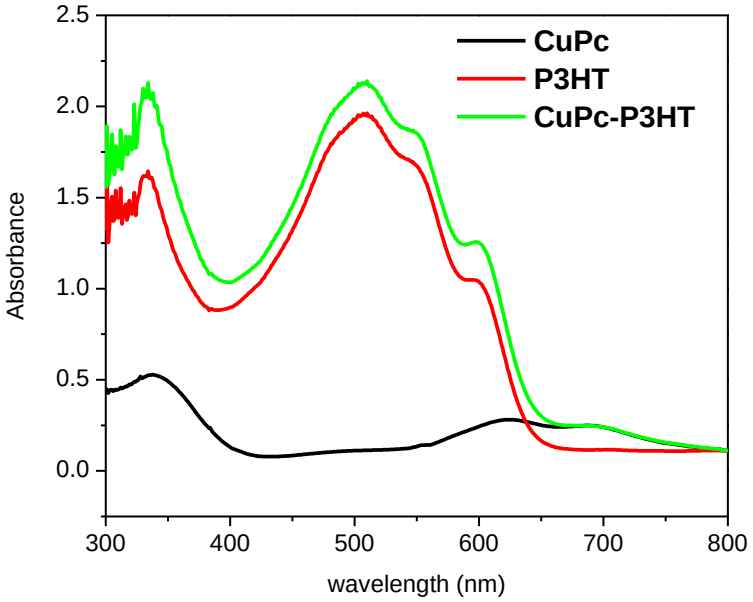

Figure 4.14 Absorption spectra of CuPc single cell, P3HT single cell, and CuPc-P3HT tandem cell.

In order to investigate how tandem solar cells work and what factors contribute to an efficient tandem solar cell performance, we fabricated our single reference cells and assembled them into a tandem solar cell step by step. Figure 4.15 shows the comparison of tandem solar cells under different configurations. A pristine tandem cell without incorporating Au NPs and doping ETL presents an inferior performance. 0.4 V tandem cell V_{oc}, which is even lower than that of a single subcell, indicates that two subcells are not connected in series. That can be ascribed to the accumulated space charge near the interface between two subcells, and space

charge induced inverted electric field would offset the built-in potential across the tandem cell, thus reducing the tandem cell V_{oc}.[38]

We deposited 1 nm gold NP layer at the interface between two subcells to create a charge recombination pathway. However, the tandem cell only shows slight increase on V_{oc}, it implies that either holes are trapped in MoO_3 layer or electrons get trapped in C_{60} layer, causing unbalanced hole/electron ratio at interface. It is reported that MoO_3 was used to replace PEDOT: PSS in polymer solar cell and it has excellent hole mobility;[39] moreover, normally inorganic semiconductor has higher charge carrier mobility than organic semiconductors.[24] It is more likely that electrons transport slowly in C_{60} and cannot recombine with the holes from the bottom cell effectively, and space charge induced V_{oc} reduction still exists.

To increase the electron conductivity of C_{60}, we doped it with a cationic dye rhodamine B as demonstrated in section 4.2. As a result, the tandem cell with RB doped ETL (RB: C_{60} = 0.7:1 weight ratio) exhibits drastically increased V_{oc} from 0.4 V to 0.95V. However, it still presents 7% V_{oc} loss and S-shape J-V curve which corresponds to rather poor FF (35%). This S-shape J-V curve could originate from the counter diode effect at the interface of the two subcells.[40] As the conductivity of C_{60} is increased by doping RB, it becomes comparable to that of MoO_3. The n-type C_{60} and p-type MoO_3 at interface could build an efficient reversed p-n junction against the tandem cell operation, which lowers the V_{oc} and fill factor of the tandem cell.

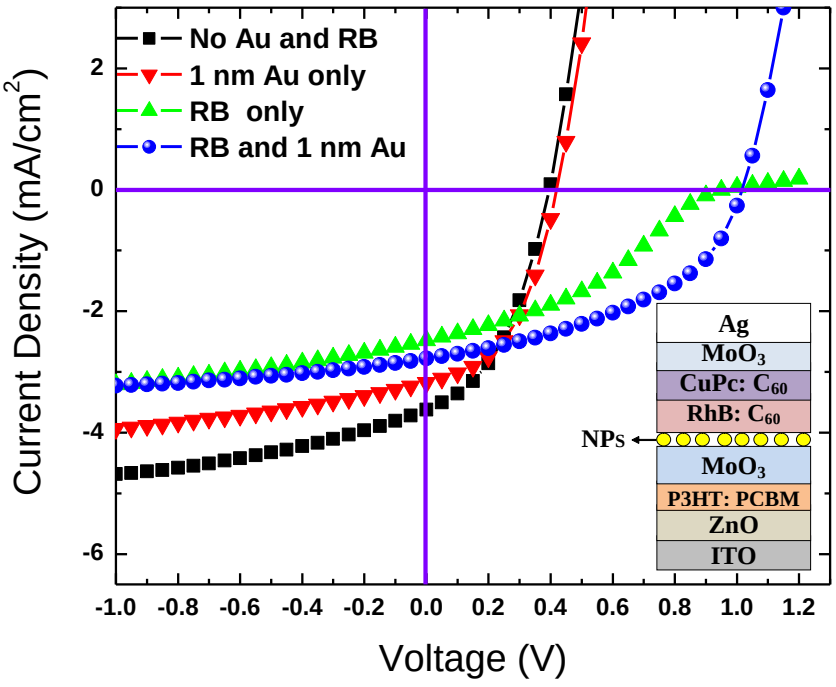

Figure 4.15 J-V curves of tandem solar cells with different cell structures. [41]

The counter diode could be destroyed by inserting a layer of metal NPs acting as charge recombination site, so that electron and hole can recombine effectively. Therefore we combined both optimization methods to fabricate a tandem solar cell with 1 nm Au NP interfacial layer and RB doped ETL, obtained tandem cell presents a further increased V_{oc}, besides the S-shape J-V curve is eliminated and a decent fill factor, 45%, is reached.

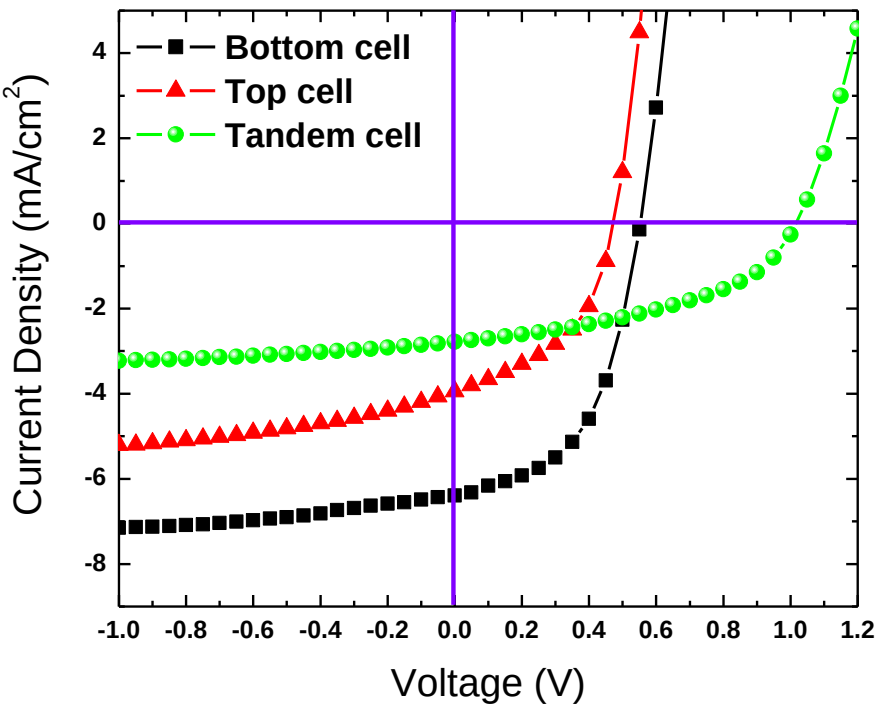

Figure 4.16 J-V curves of single top cell, single bottom cell and tandem solar cell with 70% RB doped C_{60} and 1 nm Au interfacial layer. [41]

The J-V curves comparison between this tandem cell and two reference single cells is shown in Figure 4.16. The small-molecule top cell has a V_{oc} 0.47 V and polymer bottom cell has a higher V_{oc} 0.55V, which accords with the reported values in literature. [23, 30] The tandem solar cell presents a 1.02 V V_{oc} which is the exact summation of two subcells V_{oc}, it indicates that two subcells are indeed connected in series. In this case, the current density from tandem cell should be larger or equal to the current density from two subcells, whichever is smaller.[42] In present tandem cell configuration, small-molecule cell has lower J_{sc} 3.94 mA/cm^2 compared to polymer cell 6.38 mA/cm^2, whereas the tandem cell has J_{sc} 2.78 mA/cm^2, which is 70% of the limiting cell J_{sc}. With regard to fill factor, tandem cell has a 45% FF which is quite close to that of the limiting cell 47%. The above results suggest current tandem cell configuration is a successful design and both metal NPs layer and doping ETL are necessary to make tandem cell functional.

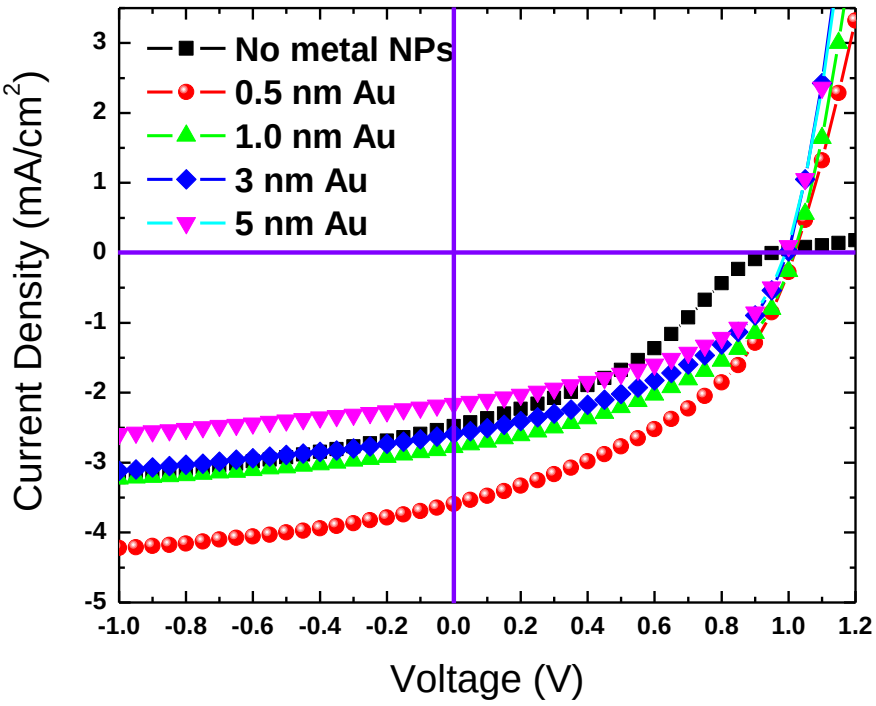

Figure 4.17 J-V curves of tandem solar cells with different gold NPs layer thickness. [41]

In order to further investigate how gold NPs and RB dopant affect tandem cell performance and also aim to optimize hybrid inverted tandem cell, we conducted a series of comparative experiments. Figure 4.17 shows the J-V curves of the tandem cells with different Au NPs layer thickness, here the ETL of all the tandem solar cells was doped with RB. Notably, the incorporation of even 0.5 nm gold NPs layer can eliminate the S-shape of J-V curve and increase the tandem cell V_{oc}. However, with the increase of the gold NPs layer thickness, J_{sc} gradually decreases. According to our device configuration, the incident light will be partially absorbed and scattered by metallic layer after passing through bottom polymer cell, and then impinges on top small-molecule cell. Gold NP is of large scattering cross-section due to surface plasmon resonance,[43] thus even a few nanometer increment on gold thickness could lead to substantial change on light extinction, which in turn impairs the light absorption of the top limiting cell. As a result, the J_{sc} of the top single cell decreases, so does the J_{sc} of the tandem cell.

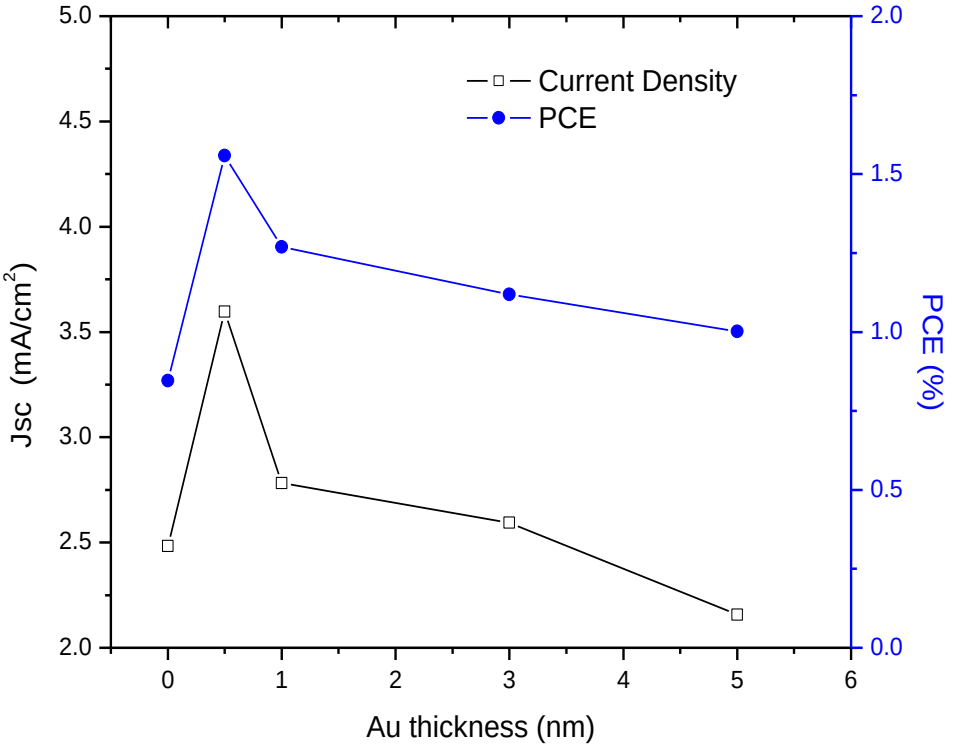

Figure 4.18 J_{sc} and PCE of tandem solar cells with different Au NPs layer thickness.

Figure 4.18 shows the variation of tandem solar cell J_{sc} and PCE with Au NPs thickness, both increase sharply to the peak maximum when Au NPs layer thickness reaches 0.5 nm, and then monotonously decreases. For tandem cell deposited with 5 nm gold NPs layer, its J_{sc} even drops below that of Au NPs free tandem cell. Thus only 0.5 nm Au NPs layer was deposited at the interface of the two subcells in our optimized device.

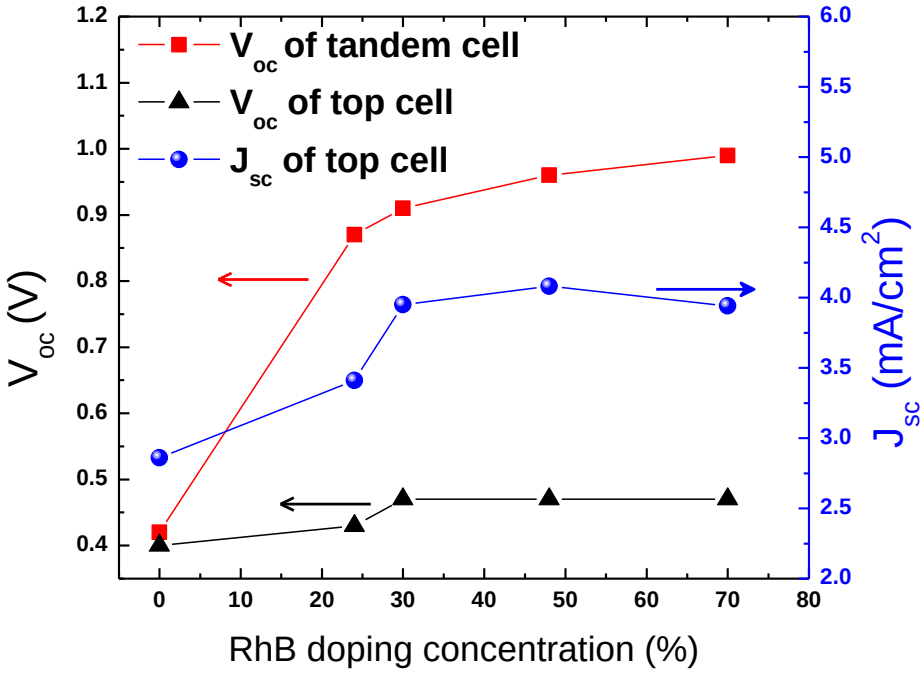

Figure 4.19 V_{oc} and J_{sc} of single top cell and tandem cell vary with RB doping concentration (RB: C_{60}, mass ratio). [41]

Figure 4.19 presents solar cell V_{oc} and J_{sc} variation with RB doping concentration, here all the tandem cells were incorporated with gold NPs layer. Undoped small-molecule top cell shows rather low V_{oc} 0.4 V, which results from unbalanced charge carrier transport in MoO_3 HTL and C_{60} ETL as we interpreted before. When 25% RB is doped in ETL, the V_{oc} of the top cell increases to 0.43 V; with the further increase of RB concentration, top cell V_{oc} elevates to 0.47 V and remains constant. Correspondingly the J_{sc} of the top cell is also enhanced greatly by introducing RB dopant, and tends constant when the doping concentration is above 30%. The synchronous increase of V_{oc} and J_{sc} by doping ETL indicates that the charge carrier extraction efficiency is enhanced and confirms that electron conductivity in C_{60} is indeed increased, 30% RB doping in ETL is enough to maximize the top cell efficiency. With regard to tandem cell, its V_{oc} keeps monotonic increase relation with RB doping concentration, and 70% RB doping concentration is determined to be optimal for tandem cell design.

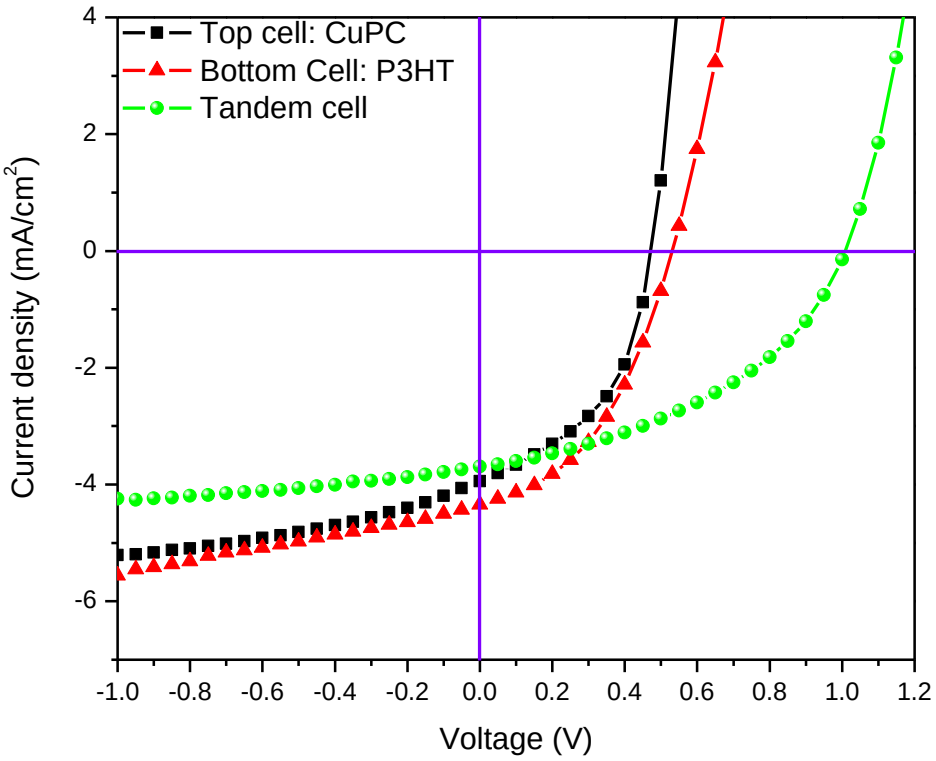

Figure 4.20 J-V curves of optimized tandem solar cell and corresponding single reference cells. [41]

The two single subcells in Figure 4.16 show notable difference on J_{sc}, i.e. excess holes generated from bottom cell would not recombine with electrons from top cell and thus charge the bottom cell. This in turn leads to a reduced performance of the tandem cell.[38] In order to match the J_{sc} from two subcells, we gradually reduced P3HT polymer thickness, and an optimal hybrid inverted tandem cell with structure ITO/ZnO/P3HT: PCBM (75 nm)/ MoO_3(3 nm)/ Au (0.5 nm)/ RB: C_{60} (0.7: 1, 17 nm)/ CuPc:C_{60} (1: 0.7, 51 nm)/MoO_3 (3 nm)/ Ag (100 nm) were fabricated. The detailed tandem cell performance is listed in Table 5. The bottom cell presents slight J_{sc} deviation from that of the top cell. As a result, the J_{sc} of the tandem solar cell is increased remarkably and reaches 94% of the limiting cell J_{sc}, besides null V_{oc} loss is also achieved. (Note the V_{oc} of the single polymer cell drops 0.01V and FF reduces from 52% to 43% due to very thin

active layer structure). As a result, the PCE of the tandem cell reaches 84% of the PCE sum of two subcells.

Table 5 Optimal tandem cell and corresponding single cells performance.[41]

Cell	J_{sc}(mA/cm^2)	V_{oc} (V)	FF(%)	PCE(%)
Bottom	4.34	0.54	43.0	1.00
Top	3.94	0.47	46.6	0.87
Tandem	3.70	1.01	42.3	1.58

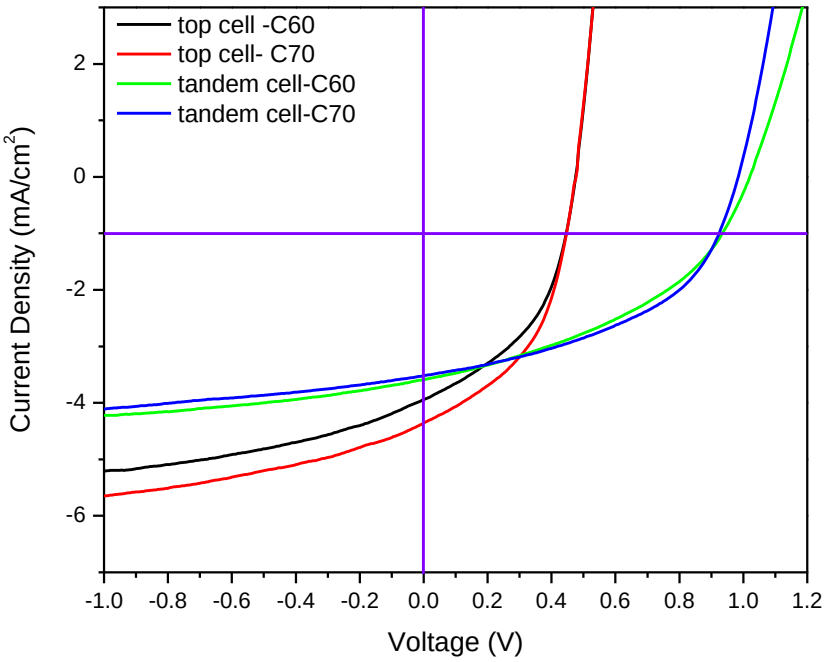

Figure 4.21 J-V curves comparison of tandem cell and top single cell using C_{60} and C_{70} as ETL respectively.

To further optimize the present tandem solar cell, we replaced the C_{60} ETL layer with C_{70} since C_{70} is reported to have higher absorbance in 500~700 nm than C_{60} and is thus considered as a better candidate in improving small-molecule solar cell external quantum efficiency.[44] Figure

4.21 shows the J-V curves of the tandem cell and the top single cell with C_{60} and C_{70} as ETL respectively. Notably when C_{60} layer is replaced by C_{70}, the photocurrent density J_{sc} increases in top single cell from 3.94 mA/cm^2 to 4.36 mA/cm^2. C_{70} can absorb more photons than C_{60} in visible range, thus it contributes more excitons which dissociate at the CuPc/C_{70} interface, similarly as excitons in CuPc dissociate, the J_{sc} is increased by 11%. However, open circuit voltage is not changed as shown in Table 6. V_{oc} is mainly determined by the energy gap between the LUMO of the acceptor and HOMO of the donor, while the LUMO of C_{70} is reported to be the same as that of C_{60},[45] therefore an unchanged V_{oc} is expectable. With regard to the tandem cells, the replacement of C_{60} with C_{70} does not result in higher photocurrent and the V_{oc} of C_{70} cell even decreases slightly, that might result from much lower electron mobility in C_{70}.[44] Two orders of magnitude lower electron mobility in C_{70} would significantly reduce the conductivity of C_{70} even with the N-type rhodmaine B dopant. Thus more space charge would appear at the interface which should be responsible for the slightly reduced V_{oc}. Although the fill factor of C_{70} cell is enhanced leading to 6.4% PCE increase, the V_{oc} of C_{70} cell sacrifices causing imperfect tandem cell performance.

Table 6 Performance of tandem cell and top single cell with C_{60} and C_{70} as ETL respectively.

Cell	J_{sc}(mA/cm^2)	V_{oc} (V)	FF(%)	PCE(%)
Single-C_{60}	3.94	0.47	46.6	0.87
Single-C_{70}	4.36	0.47	47.5	0.99
Tandem-C_{60}	3.60	1.02	42.5	1.56
Tandem-C_{70}	3.51	0.99	47.9	1.66

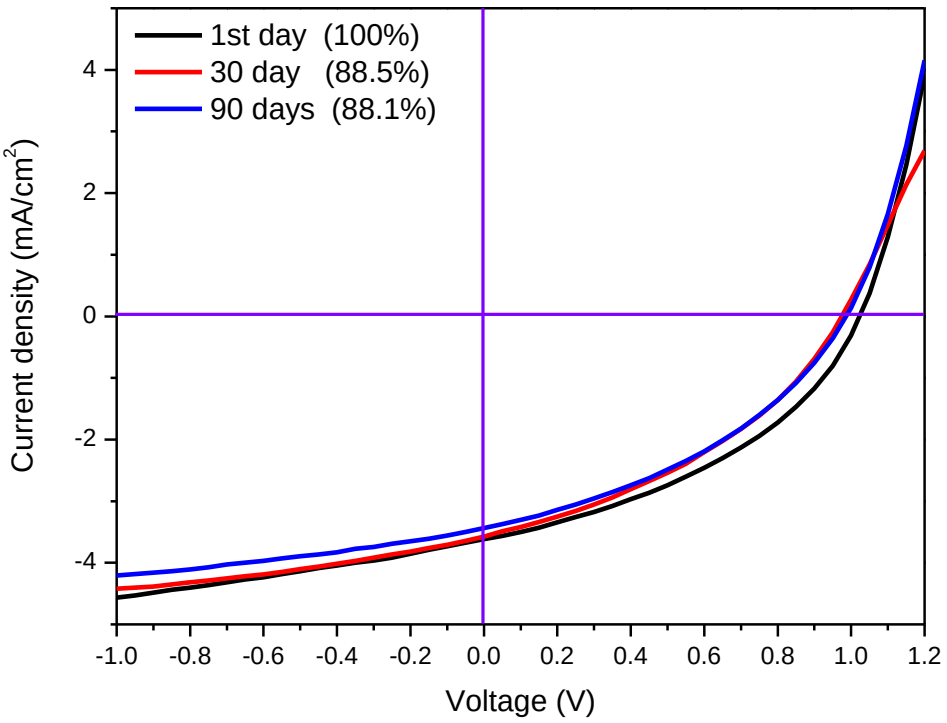

Figure 4.22 J-V curves of tandem cell without encapsulation stored in air for different time period.

The short lifespan is one of the most significant drawbacks of organic solar cells compared to inorganic solar cells, which baffles its practical application. Thus the increase of OSC lifespan is as important as its PCE enhancement. We investigated the air stability of our tandem solar cell as shown in Figure 4.22. Surprisingly even after three-month exposure in the air, our tandem solar cell still remained over 80% of its initial efficiency. Contrary to our tandem solar cell, conventional solar cell normally degrades to 50% of its initial PCE after only one day storage in air. [46] This superior air stability originates from a few advanced designs. First of all, the inverted cell structure with high work function metal silver as top electrode should be mainly responsible for the high air stability. Silver resists the oxidation and thus could remain its conductive metal nature in the air atmosphere. Secondly, MoO_3 is a good barrier preventing oxygen diffusion towards active layer. MoO_3 is known as a p-type semiconductor, oxygen defect

sites apparently exist in the thin film, which reasonably trap the oxygen diffusing through it. Moreover, CuPc is a stable active layer which can also protect the bottom P3HT polymer from degradation.

4.3.4 Conclusion

As a summary, a hybrid inverted tandem solar cell was designed and fabricated. Incorporating metal NPs charge recombination layer and doping ETL are essential for a successful tandem cell performance. By tuning Au NPs layer thickness, RB doping concentration, and P3HT polymer thickness, we optimized the present tandem cell structure, and achieved null V_{oc} loss and high J_{sc} recovery from limiting cell. Cationic dye RB is a good n-type dopant for organic semiconductor, which significantly increases the electron conductivity in C_{60}. Thanks to the additional encapsulation from metal oxide layers, the present hybrid inverted tandem cell shows prominent air stability.

References

[1] Liang, Y.; Xu, Z.; Xia, J.; Tsai, S-T.; Wu, Y.; Li, G.; Ray, C.; Yu, L. Adv. Mater. **2010**, 22, E135.

[2] Sekine, N.; Chou, C-H.; Kwan, W. L.; Yang, Y. Org. Electron. **2009**, 10, 1473.

[3] (a) Lee, J.; Ma, W.; Brabec, C. J.; Yuen, J.; Moon, J.; Kim, J.; Lee, K.; Bazan, G. C.; Heeger, A. J. J. Am. Chem. Soc. **2008**, 130, 3619. (b) Liang, Y.; Feng, D.; Wu, Y.; Tsai, S.; Li, G.; Ray, C.; Yu, L. J. Am. Chem. Soc. **2009**, 131, 7792.

[4] Pillai, S.; Catchpole, K. R.; Trupke, T.; Green, M. A. J. Appl. Phys. **2007**, 101, 093105.

[5] Yoon, W-J.; Jung, K-Y.; Liu, J.; Duraisamy, T.; Revur, R.; Teixeira, F. L.; Sengupta, S.; Berger, P. R. Sol. Energ. Mat. Sol. **2010**, 94, 128.

[6] Temple, T. L.; Mahanama, G. D. K.; Reehal, H. S.; Bagnall, D. M. Sol. Energ. Mat. Sol. C. **2009**, 93, 1978.

[7] Duche, D.; Torchio, P.; Escoubas, L.; Monestier, F.; Simon, J.-J.; Flory, F.; Mathian, G. Sol. Energ. Mat. Sol. C. **2009**, 93, 1377.

[8] Lee, J. H.; Park, J. H.; Kim, J. S.; Lee, D. Y.; Cho, K. Org. Electron. **2009**, 10, 416.

[9] Sekine, N.; Chou, C-H.; Kwan, W. L.; Yang, Y. Org. Electron. **2009**, 10, 1473.

[10] Lee, J. H.; Park, J. H.; Kim, J. S.; Lee, D. Y.; Cho, K. Org. Electron. **2009**, 10, 416.

[11] Kim, H.; So, W. W.; Moon, S. J. J. Korean Phys. Soc. **2006**, 48, 441.

[12] Evanoff Jr, D. D.; Chumanov, G. Chem. Phys. Chem. **2005**, 6, 1221.

[13] Rand, B. P.; Peumans, P.; Forrest, S. R. J. Appl. Phys. **2004**, 96, 7519.

[14] Huang, Y.; Liao, Y.; Li, S.; Wu, M.; Chen, C.; Su, W. Sol. Energ. Mat. Sol. C. **2009**, 93, 888.

[15] Bhattacharyya, S. R.; Chini, T. K.; Datta, D.; Hippler, R.; Shyjumon, I.; Smirnov, B. M. J. Exp. Theor. Phys. **2008**, 107, 1009.

[16] Catchpole, K. R.; Polman, A. Optical Express **2008**, 16, 21794.

[17] Peumans, P.; Forrest, S. R. Appl. Phys. Lett. **2001**, 79, 126.

[18] Xue, J.; Uchida, S.; Rand, B. P.; Forrest, S. R. Appl. Phys. Lett. **2004**, 84, 3013.

[19] Yang, F.; Sun, K.; Forrest, S. R. Adv. Mater. **2007**, 19, 4166.

[20] Zhang, F. J.; Zhao, D. W.; Zhuo, Z. L.; Wang, H.; Xu, Z.; Wang, Y. S. Sol. Energ. Mat. Sol. C. **2010**, 94, 2416.

[21] Shan, M. N.; Wang, S. S.; Bian, Z. Q.; Liu, J. P.; Zhao, Y. L. Sol. Energ. Mat. Sol. C. **2009**, 93, 1613.

[22] Li, G.; Shrotriya, V.; Huang, J.; Yao, Y.; Moriarty, T.; Emery, K.; Yang, Y. Nat. Mater. **2005**, 4, 864.

[23] Zhang, F. J.; Zhao, D. W.; Zhuo, Z. L.; Wang, H.; Xu, Z.; Wang, Y. S. Sol. Energ. Mat. Sol. C. **2010**, 94, 2416.

[24] Shinar, J. Organic Light-emitting Devices **2004**, (Springer Press, New York).

[25] Werner, A. G.; Li, F.; Harada, K.; Pfeiffer, M.; Fritz, T.; Leo, K. Appl. Phys. Lett. **2003**, 82, 4495.

[26] Jorgensen, M.; Norrman, K.; Krebs, F. C. Sol. Energ. Mat. Sol. C. **2008**, 92, 686.

[27] Yu, G.; Gao, J.; Hummelen, J. C.; Wudl, F.; Heeger, A. J. Science **1995**, 270, 1789.

[28] Hiramoto, M.; Suezaki, M.; Yokoyama, M. Chem. Lett. **1990**, 327.

[29]Kim, J. Y.; Lee, K.; Coates, N. E.; Moses, D.; Nguyen, T.; Dante, M.; Heeger, A. J. Science **2007**, 317, 222.

[30] Dennler, G.; Prall, H.; Koeppe, R.; Egginger, M.; Autengruber, R.; Sariciftci, N. S. Appl. Phys. Lett. **2006**, 89, 073502.

[31] Colsmann, A.; Junge, J.; Kayser, C.; Lemmer, U. Appl. Phys. Lett. **2006**, 89, 203506.

[32] Drechsel, J.; Mannig, B.; Kozlowski, F.; Pfeiffer, M.; Leo, K.; Hoppe, H. Appl. Phys. Lett. **2005**, 86, 244102.

[33] Sahin, Y.; Alem, S.; Bettignies, R. D.; Nunzi, J. M. Thin Solid Films **2005**, 476, 340.

[34] Sekine, N.; Chou, C-H.; Kwan, W. L.; Yang, Y. Org. Electron. **2009**, 10, 1473.

[35] Mor, G. K.; Shankar, K.; Paulose, M.; Varghese, O. K.; Grimes, C. A. Appl. Phys. Lett. **2007**, 91, 152111.

[36] Sun, X. W.; Zhao, D. W.; Ke, L.; Kyaw, A. K. K.; Lo, G. Q.; Kwong, D. L. Appl. Phys. Lett. **2010**, 97, 053303.

[37] Hau, S. K.; Yip, H-L.; Chen, K-S.; Zou, J.; Jen, A. K. Y. Appl. Phys. Lett. **2010**, 97, 253307.

[38] Hadipour, A.; Boer, B. D.; Wildeman, J.; Kooistra, F. B.; Hummelen, J. C.; Turbiez, G. R.; Wienk, M. M.; Janssen, A. J.; Blom, P. W. M. Adv. Funct. Mater. **2006**, 16, 1897.

[39] (a) Zhao, D. W.; Sun, X. W.; Jiang, C. Y.; Kyaw, A. K. K.; Lo, G. Q.; Kwong, D. L. Appl. Phys. Lett. **2008**, 93, 083305. (b) Shrotriya, V.; Li, G.; Yao, Y.; Chu, C-W.; Yang, Y. Appl. Phys. Lett. **2006**, 88, 073508.

[40] Pandey, A. K.; Nunzi, J. M.; Wang, H.; Oey, C. C.; Djurisic, A. B.; Xie, M. H.; Leung, Y. H.; Man, K. K.Y.; Chan, W. K. Org. Electron. **2007**, 8, 396.

[41] Liu, F.; Nunzi, J-M. Appl. Phys. Lett. **2011**, 99, 063301.

[42] (a) Hiramoto, M.; Suezaki, M.; and Yokoyama, M. Chem. Lett. **1990**, 19, 327. (b) Braun, A.; Szabo, N.; Schwarzburg, K.; Hannappel, T.; Katz, E. A.; Gordon, J. M. Appl. Phys. Lett. **2011**, 98, 223506.

[43] Hu, M.; Chen, J.; Li, Z.; Au, L.; Hartland, G. V.; Li, X.; Marquez, M.; Xia, Y. Chem. Soc. Rev. **2006**, 35, 1084.

[44] Pfuetzner, S.; Meiss, J.; Petrich, A.; Riede, M.; Leo, K. Appl. Phys. Lett. **2009**, 94, 223307.

[45] Dresselhaus, M. S.; Dresselhaus, G.; Eklund, P. Science of Fullerenes and Carbon Nanotubes **1996** Academic, San Diego.

[46] Hau, S. K.; Yip, H. L.; Bake, N. S.; Zou, J.; O'Malley, K.; Jen, A. K. Y. Appl. Phys. Lett. **2008**, 92, 253301.

Chapter 5
Conclusions and Future work

We have demonstrated the application of surface plasmon in photoluminescence, electroluminescent and photovoltaic devices in Chapter 2, 3, 4 respectively. Some interesting features of surface plasmon have been revealed and more are left to explore. In this chapter, we will summarize the surface plasmon characteristics found in our studies and propose new research directions on surface plasmon application in optoelectronic devices.

5.1 Conclusions

The importance of the separation between metal NPs and dye molecules has been addressed in metal enhanced fluorescence theory. In our photoluminescence study, we validated this theory and successfully increased the europium luminescence by using a polymer spacer which is different from the widely investigated protein and DNA spacers. This fundamental study on photoluminescence enhancement guides us to utilize surface plasmon resonance in layer by layer structure devices such as OLED and solar cell. Fluorescence decay lifetime study indicates the lifetime of the europium complex is reduced, whereas the fluorescence intensity increases. The only explanation to this phenomenon is the radiative decay rate is increased, which originates from the enhanced local E-field induced by surface plasmon resonance. In addition, we investigated the photostability of the chromophore $Eu(fod)_3$ in the proximity of the metal NPs and found that the photobleaching effect is greatly suppressed by the surface plasmon of metal NPs owing to enhanced radiative decay rate. Therefore in our surface plasmon enhanced photoluminescence study, we realized the importance of an optical spacer for photoluminescence

enhancement and the way to choose and employ a spacer. Moreover we also learned that surface plasmon could increase dye molecule photostability.

As our focus shifted to electroluminescence domain, we integrated the surface plasmon resonance into OLEDs. In the Alq_3 SM-OLED study, we have tried various methods to incorporate silver NPs. It turns out enhanced electroluminescence cannot be observed unless metal NPs are deposited underneath the cathode Al electrode. Surface plasmon increased electron injection as well as increased Alq_3 luminescence QE contribute to the EL enhancement. In addition to SM-OLED, we intentionally incorporated silica functionalized silver NPs into the emitting layer of PHOLEDs. The luminous efficiency is significantly increased under low current injection level since the surface plasmon of the Ag NPs can favor exciton formation when the electron number density is low. However, this cannot increase the maximum luminous efficiency of the PHOLED owing to the high QE of $Ir(ppy)_3$. 13 nm or above silica spacer is critical for enhancing PHOLED performance and unfunctionalized Ag NPs result in drastic EL quenching. Moreover, we have grafted rhodamine B molecule onto silica functionalized silver NPs, and the photostability of RB molecule is increased as expected. This hybrid NP has brighter EL compared to the pure RB molecule, and moreover, this hybrid NP is of a much broader EL spectrum than pure RB molecule since surface plasmon favors exciplex formation, this important feature would permit to design a white light OLED from a novel point of view. The absolute EQEs of our OLEDs including SM-OLEDs, PHOLEDs and hybrid OLEDs are quite low compared to literature values, and it mainly results from the fact that the diodes we fabricated were not fully optimized. For instance, we could use UV-Ozone to treat the ITO slides to increase their work functions; besides we could also deposit a layer of LiF between the cathode and the ETL to reduce electron injection barrier. Nevertheless, the motivation of our research is to develop a universal method to increase OLEDs efficiency, the absolute EQEs of OLEDs in our lab could be increased with no doubt provided all the optimization techniques were used.

Based on successful application of metal NPs surface plasmon in OLEDs, we further extended our research scope to organic solar cell. By incorporating silver NPs into P3HT polymer solar cell, we observed both increased and diminished solar cell performance depending on the solar cell layout. Direct contact of Ag NPs with P3HT polymer does not increase device performance since Ag NPs serve as charge recombination sites quenching the excitons although they can increase the polymer absorption. The incorporation of Ag NPs underneath the P3HT polymer layer would result in massive light loss due to large scattering cross-section, and device performance drops significantly. When the metal NPs are deposited over P3HT layer with PEDOT: PSS as spacer, increased PCE is obtained benefitting from increased polymer absorption. Therefore, in order to take advantage of the surface plasmon merits, proper device structural design becomes critical. In addition to P3HT polymer solar cell, we have investigated CuPc small molecule solar cell. By doping RB into C_{60} electron transport layer we double the CuPc-C_{60} BHJ solar cell efficiency due to increased C_{60} conductivity and thus balanced electron and hole extraction. Based on good understanding of P3HT and CuPc solar cells properties, we fabricated a hybrid tandem solar cell consisting of P3HT bottom cell and CuPc top cell. A series connection cannot be established by direct stacking two subcells together due to space charge at the interface. Doping C_{60} ETL layer of the CuPc subcell is critical to diminish the space charge and increase tandem cell V_{oc}. However an S-shaped J-V curve is obtained due to a highly efficient MoO_3-C_{60} counter diode at the interface, leading to poor fill factor of the tandem cell. Au NPs are employed to eliminate the counter diode effect by depositing them at MoO_3 / C_{60} interface since Au NPs are very good charge recombination sites. The optimized tandem solar cell has a V_{oc} which equals the exact summation of the two subcells V_{oc}, the J_{sc} of the tandem cell can reach 94% of the limiting cell J_{sc} by reducing the mismatch between two subcells J_{sc}.

As a summary, we recognized and demonstrated that the surface plasmon of metal NPs can either enhance or quench the luminescence of chromophores depending on the way we

manipulate the spacer layer. This becomes the core of the whole thesis. All the plasmonic OLEDs and plasmonic OSCs were designed and tailored based on that concept. Another important feature of surface plasmon revealed here is that it favors the recombination of charges. Implementation of this concept in organic electronic devices yields the successful application of gold NPs in the tandem solar cells as charge recombination layer and the application of silica coated Ag NPs in PHOLEDs to boost exciton recombination.

5.2 Suggestion for Future work

5.2.1 Elongated NPs in OLEDs

We have studied the silica functionalized spherical Ag NP and its application in phosphorescent OLED. Although 3-fold increase on luminous efficiency was achieved, elongated NPs could in principle result in much higher efficiency increase since the local E-field enhancement from non-spherical metal NPs is much higher than that from spherical ones. Therefore one can fabricate metal nanorod structure and functionalize it with silica shell, here gold nanorod would be a better candidate since its transverse surface plasmon resonance wavelength overlaps more with the emission spectrum of $Ir(ppy)_3$ molecule.

Diverse methods have been developed to synthesize nanorod structure. Pileni et al. reported a seed-mediated technique to synthesize gold nanorod.[1] Firstly, gold seeds with diameter around 3-4 nm are synthesized via reducing $HAuCl_4$ by $NaBH_4$ with the presence of CTAB surfactant. A fresh seed solution is demonstrated to work better for the formation of gold nanorods. The growth solution of nanorods consists of $HAuCl_4$, CTAB, Ag^+ and L-ascorbic acid the reducing reagent, finally certain amount of a gold seeds solution is added into growth solution to finalize the formation of gold nanorod. The yield of gold nanorod structure obtained in this method is reported to be above 90%.

Once one obtains the gold nanorod, one can coat its surface with silica shell as we did in Chapter 3. The silica-coated gold nanorods are expected to further increase the luminous efficiency of the PHOLED under moderate current density as shown in Figure 5.1. In addition, it

will be interesting to study how the aspect ratio of the gold nanorods, which can be readily tuned by changing the ratio between surfactant and $HAuCl_4$, affects the performance of the PHOLED.

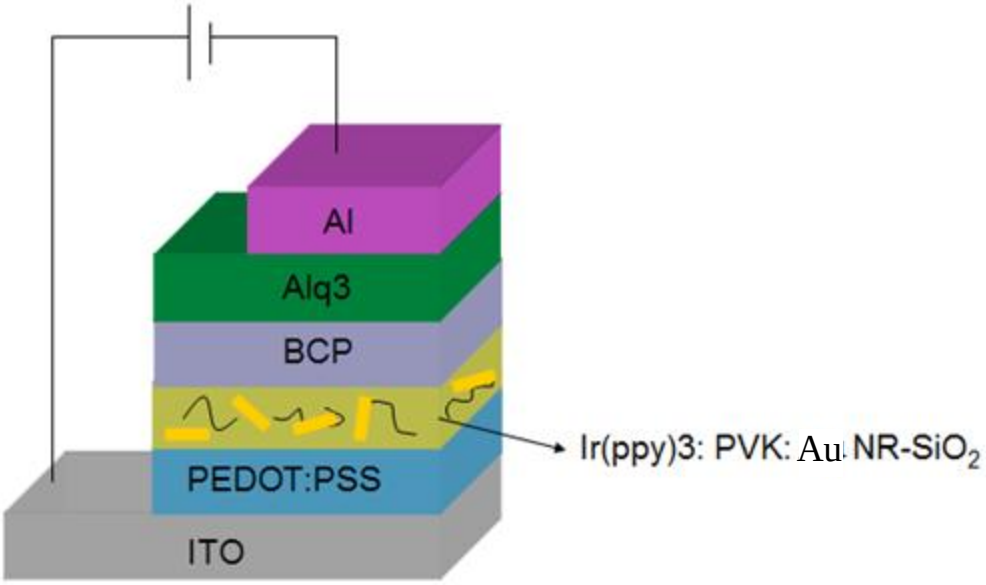

Figure 5.1 Schematic diagram of PHOLED doped with silica coated Au nanorod in emitting layer.

5.2.2 Metal Core-Silica Shell NPs in OSCs

Although many plasmonic organic solar cell prototypes have been proposed in which surface plasmon of metal NPs was predicted to enhance polymer layer absorption and thus increase solar cell efficiency, [2,3] the metallic nanostructures induced exciton quenching effect was always neglected in those models, which can compromise absorption enhancement induced PCE increment. In the worst case those designs could result in significant PCE drop.

As we demonstrated the successful application of the silica coated metal NPs in PHOLEDs; this concept could also be implemented in organic solar cell fabrication. Provided that silica functionalized silver NPs were added into the blend of P3HT and P3BM, on the one hand,

the concentrated E-field from Ag NPs would help polymer layer absorb more photons, improving the photocurrent; on the other hand, unwanted exciton recombination effect could be minimized by the silica insulator coating. Although the introduction of the hybrid metal NPs into a polymer blend would disturb phase separation of the active layer potentially, this adverse effect could be minimized and enhancement on solar cell PCE is feasible if one controls the dose of the silica coated metal NPs well.

A protocol of this metal-silica hybrid NPs enhanced polymer solar cell performance is listed as follows: silver or gold spherical NPs could be synthesized in traditional sodium citrate reducing method,[4] and nanorod structure could be synthesized via template method. The coating of a silica shell can be readily accomplished by adding TEOS solution. The resulting silica coated metal NPs are then mixed with P3HT: PCBM, and the blend is then spin coated on ZnO covered ITO substrate to fabricate an inverted solar cell as shown in Figure 5.2.

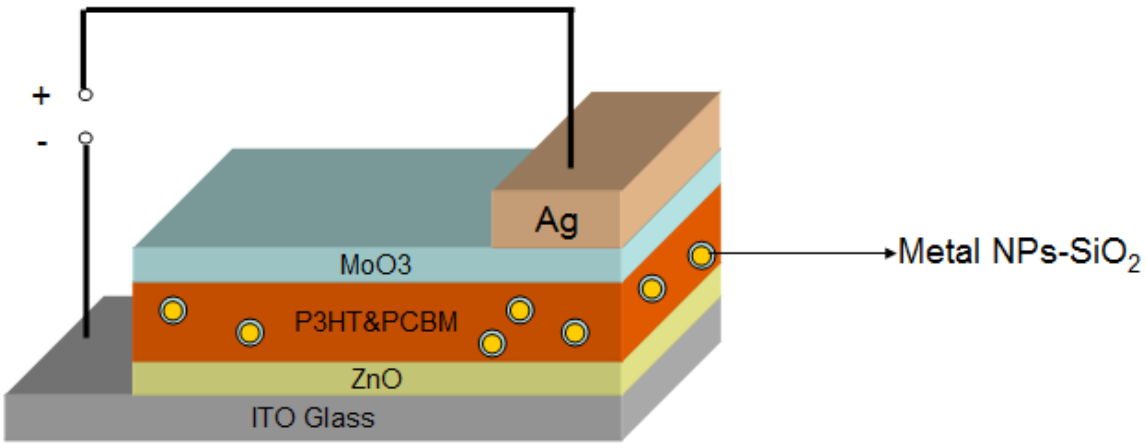

Figure 5.2 Schematic diagram of polymer solar cell doped with silica coated metal NPs

Device performance could be optimized by tuning the doping dose of the silica coated metal NPs as well as the silica shell thickness. Moreover the introduction of metal NPs would

result in high surface roughness in active layer, and lead to a textured organic-metal interface which favors charge extraction.[5] This prototype in principle would favor the polymer solar cell efficiency increase in low cost.

5.2.3 Interdigitated Morphology for OSC Design

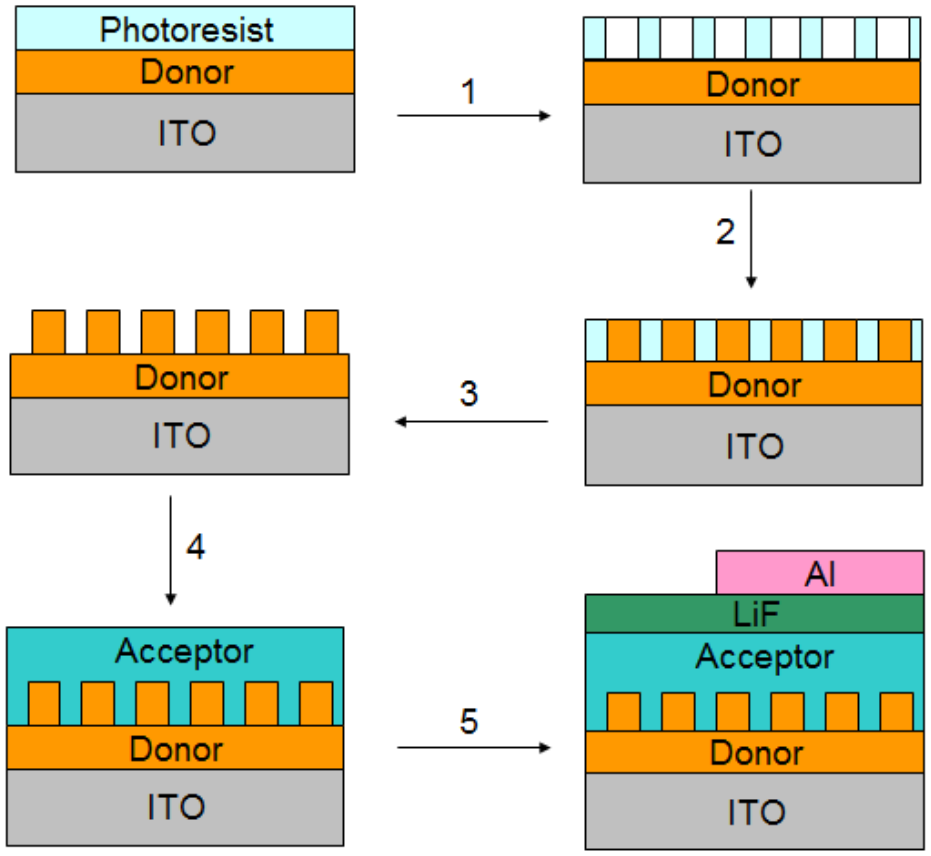

Figure 5.3 Interdigitated structure design for BHJ solar cell using lithography method.

Short exciton diffusion length in organic solar cells greatly restricts the thickness of an active layer and demands good phase separation to achieve high PCE for BHJ solar cells. In order to overcome this barrier, we can fabricate an interdigitated donor-acceptor structure in organic

solar cells via photolithography technique as shown in Figure 5.3. A donor layer is firstly deposited on top of a pre-cleaned ITO glass and then a photoresist layer is deposited over donor layer, here the solvent used for photoresist layer should not dissolve the donor layer. A periodic square array on photoresist ideally with space around 10~20 nm could be created by using extreme ultraviolet lithography, and then the donor molecules are deposited into array. The photoresist template could be washed away using organic solvent. As we previously emphasized, the solvent used here should not swallow the donor layer, thus a nanopole array structure of the donor can retain after washing step. Once one obtains the digitated structure of donor molecules, a layer of acceptor molecules is then deposited to create numerous nano-scale DA junctions. The diffusion of acceptor molecules into the gaps between donor nanopoles becomes critical for efficient BHJ solar cell performance. A solution spin coating method would help the acceptor molecules diffusion provided the used solvent does not dissolve the donor molecules. Vacuum thermal deposition method may be not as efficient as spin coating method; however thermal annealing treatment after acceptor molecules deposition could facilitate the diffusion of the acceptor molecules. Finally a LiF insulator layer as well as Al cathode is deposited to extract the electrons. This prototype demonstrates a universal method to produce interdigitated donor/acceptor microstructure, which would boost the exciton dissociation and increase organic BHJ solar cell PCE significantly.

References

[1] Jiang, X. C.; Pileni, M. P. Colloid. Surface. A **2007**, 295, 228.

[2] Duche, D.; Torchio, P.; Escoubas, L.; Monestier, F.; Simon, J-J.; Flory, F.; Mathian, G. Sol. Eng. Mater. Sol. C. **2009**, 93, 1377.

[3] Williamson, A.; McClean, E.; Leipold, D.; Zerulla, D.; Runge, E. Appl. Phys. Lett. **2011**, 99, 093307

[4] Lee, P. C.; Meisel, D. J. Phys. Chem. **1982**, 86, 3391.

[5] Riedel, B.; Hauss, J.; Aichholz, M.; Gall, A.; Lemmer, U.; Gerken, M. Org. Electron. **2010**, 11, 1172.